

Julius-Maximilians-Universität Würzburg

Institut für Geographie und Geologie

Physische Geographie

Prof. Dr. Heiko Paeth

Future changes in climate means and
extremes in the Mediterranean region
deduced from a regional climate model

Dissertation zur Erlangung des

naturwissenschaftlichen Doktorgrades

der Bayerischen Julius-Maximilians-Universität Würzburg

vorgelegt von

Andreas Paxian

aus Heidelberg

Würzburg 2012

Eingereicht am: 14. Februar 2012

1. Gutachter: Prof. Dr. Heiko Paeth
2. Gutachter: Prof. Dr. Jucundus Jacobeit
der Dissertation

1. Prüfer: Prof. Dr. Heiko Paeth
2. Prüfer: Prof. Dr. Jürgen Rauh
der mündlichen Prüfung

Tag der mündlichen Prüfung: 27. Juni 2012

Doktorurkunde ausgehändigt am:

Abstract

The Mediterranean area reveals a strong vulnerability to future climate change due to a high exposure to projected impacts and a low capacity for adaptation highlighting the need for robust regional or local climate change projections, especially for extreme events strongly affecting the Mediterranean environment. The prevailing study investigates two major topics of the Mediterranean climate variability: the analysis of dynamical downscaling of present-day and future temperature and precipitation means and extremes from global to regional scale and the comprehensive investigation of temperature and rainfall extremes including the estimation of uncertainties and the comparison of different statistical methods for precipitation extremes. For these investigations, several observational datasets of CRU, E-OBS and original stations are used as well as ensemble simulations of the regional climate model REMO driven by the coupled global general circulation model ECHAM5/MPI-OM and applying future greenhouse gas (GHG) emission and land degradation scenarios.

Concerning dynamical downscaling, REMO (0.5°) strongly improves the representation of temperature and precipitation means and extremes in context of the large orographic and land-sea contrasts of the Mediterranean area compared to ECHAM5 (1.875°): larger temperature means over northern Africa, smaller temperature means and extremes over mountain peaks, higher rainfall means and extremes, especially in winter, fine-scale rainfall structures over mountain ranges and coastal regions and decreased frequencies and increased intensities of heavy rainfall reducing the strong area-averaging effects of ECHAM5. But REMO tends to overestimate rainfall means and extremes compared to E-OBS observations. Concerning future changes, REMO shows smaller changes than ECHAM5 in temperature means and extremes over the southern areas and larger changes in rainfall means and extremes with improved topographic details.

Furthermore, principal component analyses depict that present-day temporal evolutions of major mid-latitude circulation modes in ECHAM5 strongly differ from observations probably due to differing initial conditions. Multiple regression analyses reveal that these discrepancies in large-scale modes of variation induce differing

observed and simulated circulation-related temperature and precipitation trends, especially in winter, but improved agreement of circulation-unrelated trends can be stated in most regions. Thus, the only real boundary condition CO_2 emissions of the given model-into-model-approach does not clearly prevail over other Mediterranean drivers in present-day 30-year trends but model predictability mostly increases after removing the impacts of mid-latitude circulation. In the long-term and future time period impacts of mid-latitude circulation mostly decrease and influences of circulation-unrelated drivers, such as GHG, increase probably pointing at improved model predictability.

Additionally, future temperature projections reveal strong and significant warming patterns over the whole Mediterranean, especially in summer for the A1b scenario, and signal-to-noise ratios depict strong GHG signals exceeding impacts of natural variability. The fitting of Generalized Pareto Distribution (GPD) functions yields similar strong future increases over the whole area for daily temperature extremes and aggregated extremes over several days indicating heat waves.

Future rainfall projections depict strong summer and winter drying over the northern and southern Mediterranean, respectively, and winter wetting over the northern parts and signal-to-noise ratios show small GHG signals with strong impacts of internal variability. Future changes in consecutive dry days and heavy rainfall are mostly consistent with trends of precipitation totals and reveal strong agreement between quantile-based extreme indices and GPD return values. But increases in heavy rainfall are more expanded than increases in precipitation totals identifying regions of decreasing totals but increasing extremes with possible broadening of future rainfall distribution functions.

Finally, a dynamical-statistical weather generator including orographic and stochastic terms and a matching of Probability Density Functions (PDF) constructs local virtual rainfall stations from gridded REMO data featuring the final step in downscaling from regional to local scale. These virtual stations overcome typical discrepancies of area-averaged model output of rainfall and rainfall extremes compared to local stations, e.g. overestimated numbers of low-intensity precipitation days and underestimated extreme rainfall intensities. Future changes of virtual station rainfall extremes reveal local climate change information for impact research and slightly stronger increases in winter and less decreases in summer than gridded REMO extremes. These improvements are mainly reached by PDF matching because the calculation of orographic effects is restricted by the small given station database.

Kurzzusammenfassung

Der Mittelmeerraum weist eine starke Vulnerabilität gegenüber dem zukünftigen Klimawandel auf, da für diese Region starke klimatische Auswirkungen vorhergesagt werden, aber nur eine geringe Anpassungsfähigkeit besteht. Daher werden präzise Vorhersagen des regionalen oder lokalen Klimawandels benötigt, v.a. für Extremereignisse, welche den Mittelmeer-Lebensraum stark beeinträchtigen. Die vorliegende Studie untersucht zwei Hauptaspekte der Klimavariabilität im Mittelmeerraum: Zum Einen wird das dynamische Downscaling gegenwärtiger und zukünftiger Mittelwerte und Extremereignisse von Temperatur und Niederschlag von der globalen zur regionalen Skala analysiert. Zum Anderen wird eine umfassende Untersuchung von Temperatur- und Niederschlagsextremen samt Unsicherheitsabschätzung und Vergleich unterschiedlicher statistischer Methoden zur Bestimmung von Niederschlagsextremen durchgeführt. Für diese Untersuchungen stehen verschiedene Beobachtungsdaten von CRU, E-OBS und Messstationen sowie Ensemble-Simulationen des regionalen Klimamodells REMO zur Verfügung, das vom gekoppelten globalen "General Circulation Model" ECHAM5/MPI-OM angetrieben wird und zukünftige Treibhausgasemissions- und Landnutzungsänderungs-Szenarien verwendet.

Hinsichtlich des dynamischen Downscalings verbessert REMO (0.5°) deutlich die Darstellung von Mittel- und Extremwerten von Temperatur und Niederschlag vor dem Hintergrund der starken Topographie und kleinräumigen Land-See-Verteilung im Mittelmeerraum im Vergleich zu ECHAM5 (1.875°): REMO zeigt höhere Temperaturmittel über Nordafrika, niedrigere Temperaturmittel und -extreme über Gebirgen, höhere Niederschlagsmittel und -extreme, v.a. im Winter, und kleinräumige Niederschlagsmuster über Gebirgsketten und Küstenregionen. Geringere Häufigkeiten und erhöhte Intensitäten von Starkniederschlägen in REMO bewirken eine Abschwächung der Effekte der starken Gebietsmittelung der groben ECHAM5-Auflösung. Allerdings neigt REMO zu einer Überschätzung der Niederschlagsmittel und -extreme der E-OBS-Beobachtungen. Für die Zukunftsperiode simuliert REMO geringere Veränderungen der Temperaturmittel und -extreme über dem südlichen Mittelmeerraum als ECHAM5 und größere Veränderungen der Niederschlagsmittel

und -extreme mit verbesserten topographischen Details.

Weiterhin zeigen Hauptkomponentenanalysen, dass die gegenwärtigen zeitlichen Entwicklungen der wichtigsten Zirkulationsmodi der Mittelbreiten von ECHAM5 stark von den Beobachtungen abweichen, wahrscheinlich aufgrund von unterschiedlichen Anfangsbedingungen. Durch multiple Regressionsanalysen kann festgestellt werden, dass diese Unterschiede in den großskaligen Variationsmodi v.a. im Winter stark unterschiedliche zirkulationsabhängige Temperatur- und Niederschlagstrends zwischen Modell und Beobachtung hervorrufen. Die zirkulationsunabhängigen Trends zeigen jedoch in den meisten Regionen eine höhere Übereinstimmung. Folglich können sich die CO_2 -Emissionen als einzige reale Randbedingung des vorliegenden “model-into-model-approach” in gegenwärtigen 30-Jahres-Trends nicht klar gegenüber anderen Einflussgrößen des Mittelmeerraums durchsetzen. In den meisten Regionen nimmt die Modellvorhersagbarkeit allerdings zu, wenn die Einflüsse der Mittelbreiten-Zirkulation entfernt werden. Im langfristigen, zukünftigen Zeitraum können meist abnehmende Zirkulationseinflüsse aber zunehmende zirkulationsunabhängige Einflüsse, wie solche von Treibhausgasen, festgestellt werden, was auf eine verbesserte Modelvorhersagbarkeit hinweisen könnte.

Außerdem zeigen zukünftige Temperaturprojektionen starke und signifikante Erwärmungsmuster über dem gesamten Mittelmeerraum, v.a. im Sommer im A1b-Emissionsszenario. Signal-Rausch-Verhältnisse beschreiben starke Treibhausgas-Signale, welche die Einflüsse der natürlichen Variabilität überschreiten. Die Anpassung von Generalisierten Pareto Verteilungen (GPD) ergibt ähnlich starke zukünftige Zunahmen über dem gesamten Gebiet für tägliche Temperaturextreme und aggregierte Extreme über mehrere Tage, welche Hitzewellen beschreiben.

Zukünftige Niederschlagsprojektionen zeigen starke Austrocknungen über dem nördlichen Mittelmeerraum im Sommer und über dem südlichen im Winter sowie Niederschlagszunahmen über den nördlichen Gebieten im Winter. Signal-Rausch-Verhältnisse ergeben geringe Treibhausgas-Signale mit starken Einflüssen interner Variabilität. Zukünftige Veränderungen von Trockenperioden und Starkniederschlägen sind meistens konsistent mit Trends der Niederschlagssummen und zeigen starke Übereinstimmungen zwischen quantil-bezogenen Extremindizes und GPD-Wiederkehrwerten. Zunahmen von Starkniederschlägen sind jedoch weiter verbreitet als Zunahmen des Gesamtniederschlags. Daher lassen sich Mittelmeerregionen mit abnehmenden Niederschlagssummen aber zunehmenden -extremen identifizieren, was auf eine mögliche Verbreiterung der zukünftigen Niederschlagsverteilungsfunktion hinweist.

Schließlich berechnet ein dynamisch-statistischer Wettergenerator anhand von

orographischen und stochastischen Komponenten und einer Anpassung täglicher Verteilungsfunktionen (PDF-Matching) lokale virtuelle Niederschlagsstationen aus aggregierten REMO-Modelldaten. Der Wettergenerator stellt den letzten Schritt des Downscalings von der regionalen zur lokalen Skala dar. Die virtuellen Stationen können typische Diskrepanzen von Niederschlag und Niederschlagsextremen aus gebietsgemitteltem Modelloutput im Vergleich zu lokalen Stationen überwinden, z.B. die Überschätzung der Anzahl von Regentagen und Unterschätzung der Intensität von Extremniederschlägen. Zukünftige Veränderungen der Niederschlagsextreme virtueller Stationen dienen als Vorhersagen des lokalen Klimawandels für Studien der Klimafolgenforschung und zeigen leicht stärkere Zunahmen im Winter und weniger Abnahmen im Sommer als aggregierte REMO-Extreme. Die genannten Verbesserungen werden hauptsächlich durch das PDF-Matching erreicht, weil die Berechnung der orographischen Komponenten für viele REMO-Gitterboxen durch eine geringe Anzahl verfügbarer Niederschlagsstationen eingeschränkt wird.

Contents

Abstract	i
Kurzzusammenfassung	iii
List of Figures	xi
List of Acronyms	xv
1 Introduction and background	1
1.1 Motivation and geographical background	1
1.2 Observations of the present-day Mediterranean climate	5
1.3 Simulations of the present-day and future Mediterranean climate	9
1.4 Major aims of the present study	16
2 Database	20
2.1 Observational database	20
2.1.1 Station data	21
2.1.2 Gridded E-OBS data	22
2.1.3 Gridded CRU data	23
2.1.4 NCEP/NCAR and ERA40 reanalysis data	24
2.1.5 SRTM elevation data	25
2.2 Climate model database	26
2.2.1 Global coupled general circulation model ECHAM5/MPI-OM	27
2.2.2 Regional climate model REMO	29
3 Statistical methods	34
3.1 Analysis of climatological means	34
3.2 Trend analysis	36
3.3 Analysis of variance	40
3.4 Principal component analysis	44
3.5 Multiple regression	48
3.6 Quantile-based extreme indices	52

3.7	Extreme value distributions	55
3.8	Weather generator	59
4	Analysis of temperature and precipitation means and trends	65
4.1	Validation and dynamical downscaling of present-day climate	65
4.1.1	Annual cycle	66
4.1.2	Climate means	67
4.1.3	Validation tests	70
4.1.4	Climate trends	72
4.1.5	Comparison with ERA15-forced REMO simulation	76
4.1.6	Impact of initial conditions on climate trends	78
4.1.7	One-way Analysis of Variance	79
4.2	Dynamical downscaling of long-term climate	81
4.2.1	Annual cycle	81
4.2.2	Climate trends	83
4.2.3	One-way Analysis of Variance	85
4.2.4	Two-way Analysis of Variance	87
5	Impact of mid-latitude circulation on temperature and precipitation	91
5.1	Mid-latitude circulation in present-day climate	92
5.1.1	Observed and simulated mid-latitude circulation variability	92
5.1.2	Impact of mid-latitude circulation on climate	95
5.1.3	Circulation-related and -unrelated climate trends	98
5.1.4	Dependence of simulated circulation variability on initial conditions	104
5.2	Mid-latitude circulation in long-term climate	106
5.2.1	Simulated mid-latitude circulation variability	107
5.2.2	Impact of mid-latitude circulation on climate	107
5.2.3	Circulation-related and -unrelated climate trends	109
6	Quantile-based precipitation extreme indices	112
6.1	Validation and dynamical downscaling of present-day climate	112
6.1.1	Number of precipitation days	113
6.1.2	Maximum number of consecutive dry days	115
6.1.3	Precipitation extreme indices	116
6.1.4	Scale effects and subscale processes	119
6.2	Dynamical downscaling of future climate	120
6.2.1	Number of precipitation days	121

6.2.2	Maximum number of consecutive dry days	122
6.2.3	Precipitation extreme indices	123
7	Temperature and precipitation extremes from a Generalized Pareto Distribution	126
7.1	Validation and dynamical downscaling of present-day climate	126
7.1.1	GPD fit and uncertainty	127
7.1.2	Evaluation of dynamical downscaling	131
7.1.3	GPD parameters	133
7.1.4	GPD return values of different return times and aggregation levels	135
7.2	Dynamical downscaling of future climate	137
7.2.1	GPD fit and uncertainty	138
7.2.2	GPD parameters	140
7.2.3	GPD return values of different return times and aggregation levels	142
8	Precipitation extremes from a weather generator	144
8.1	Validation of the weather generator in present-day climate	145
8.1.1	Precipitation, wind and orography input data	145
8.1.2	Orographic term	148
8.1.3	Precipitation distribution of virtual station data	149
8.1.4	Precipitation characteristics of virtual station data	151
8.2	Precipitation extremes of present-day climate	153
8.2.1	GPD return values and parameters	154
8.2.2	GPD return values of selected stations	156
8.3	Precipitation extremes of future climate	157
8.3.1	GPD return values and parameters	158
8.3.2	GPD return values of selected stations	159
9	Synthesis	161
9.1	Summary and Discussion	161
9.2	Conclusions and Outlook	173
	Bibliography	181

List of Figures

1.1	The Mediterranean area: orography and sea-depth	4
2.1	REMO model domain	31
4.1	Annual cycle of temperature and precipitation from E-OBS, CRU, REMO and ECHAM5 in 1961-1990	67
4.2	Validation of climatological temperature means from REMO and ECHAM5 with E-OBS in 1961-1990	68
4.3	Validation of climatological precipitation means from REMO and ECHAM5 with E-OBS in 1961-1990	70
4.4	Results of the validation tests for temperature and precipitation from REMO with E-OBS in 1961-1990	71
4.5	Validation of temperature trends from REMO and ECHAM5 with E-OBS in 1961-1990	74
4.6	Validation of precipitation trends from REMO and ECHAM5 with E-OBS in 1961-1990	75
4.7	Validation of temperature and precipitation trends from REMO 5.0 and REMO 5.7 with E-OBS in 1980-2000	77
4.8	Seasonal trends of different REMO ensemble members for tempera- ture and precipitation in 1961-1990	79
4.9	One-way analysis of variance for REMO and ECHAM5 temperature and precipitation in 1961-1990	80
4.10	Annual cycle of temperature and precipitation for REMO and ECHAM5 in 1961-1990 and 2021-2050	82
4.11	Comparison of temperature trends from REMO and ECHAM5 in 1961-2050	83
4.12	Comparison of precipitation trends from REMO and ECHAM5 in 1961-2050	84
4.13	One-way analysis of variance for REMO temperature from different emission scenarios in 1961-2050	86

4.14	One-way analysis of variance for REMO precipitation from different emission scenarios in 1961-2050	87
4.15	Two-way analysis of variance for REMO and ECHAM5 temperature in 1961-2050	88
4.16	Two-way analysis of variance for REMO and ECHAM5 precipitation in 1961-2050	89
5.1	Mid-latitude large-scale modes of variation of NCEP and ECHAM5 in 1961-1990	93
5.2	Results of cross-validated stepwise multiple regression based on E-OBS or REMO predictands and NCEP or ECHAM5 predictors for temperature in 1961-1990	96
5.3	Results of cross-validated stepwise multiple regression based on E-OBS or REMO predictands and NCEP or ECHAM5 predictors for precipitation in 1961-1990	97
5.4	Comparison of circulation-related and circulation-unrelated temperature trends in 1961-1990 between REMO and E-OBS	100
5.5	Comparison of circulation-related and circulation-unrelated precipitation trends in 1961-1990 between REMO and E-OBS	101
5.6	Comparison between original, circulation-related and circulation-unrelated spring temperature trends of E-OBS in 1961-1990	103
5.7	Winter NAO time series of the ECHAM5 ensemble mean, its ensemble members and NCEP during 1961-1990	105
5.8	One-way analysis of variance results for projected PC time series of ECHAM5 ensemble members for different modes of variation and seasons	106
5.9	Results of cross-validated stepwise multiple regression based on REMO predictands and ECHAM5 predictors for temperature and precipitation in 1961-2050	109
5.10	Comparison of circulation-related and circulation-unrelated temperature and precipitation trends of REMO in 1961-2050	110
6.1	Validation of the number of rain days from REMO and ECHAM5 with E-OBS for different thresholds in 1961-1990	114
6.2	Validation of the maximum number of consecutive dry days (CDD) from REMO and ECHAM5 with E-OBS in 1961-1990	115
6.3	Validation of the number of rain days exceeding the 95% quantile (R95N) from REMO and ECHAM5 with E-OBS in 1961-1990	117

6.4	Validation of the simple daily intensity index of rain days exceeding the 95% quantile (SDII95p) from REMO and ECHAM5 with E-OBS in 1961-1990	118
6.5	Number (R95N) and simple daily intensity index (SDII95p) of rain days exceeding the 95% quantile of REMO on 2.0° resolution in 1961-1990	120
6.6	Change in the number of rain days of REMO and ECHAM5 in 2021-2050 compared to 1961-1990	121
6.7	Change in the maximum number of consecutive dry days (CDD) of REMO and ECHAM5 in 2021-2050 compared to 1961-1990	122
6.8	Change in the number of rain days exceeding the 95% quantile (R95N) of REMO and ECHAM5 in 2021-2050 compared to 1961-1990	124
6.9	Change in the simple daily intensity index of rain days exceeding the 95% quantile (SDII95p) of REMO and ECHAM5 in 2021-2050 compared to 1961-1990	125
7.1	Validation of GPD 1d-20a-RTVs from REMO and ECHAM5 temperature with E-OBS and corresponding variation coefficients in 1961-1990	128
7.2	Validation of GPD 1d-20a-RTVs from REMO and ECHAM5 precipitation with E-OBS and corresponding variation coefficients in 1961-1990	130
7.3	Differences between GPD 1d-20a-RTVs and empirical quantiles of REMO, ECHAM5 and E-OBS for 1961-1990	131
7.4	Difference of GPD 1d-20a-RTVs between REMO and E-OBS and between ECHAM5 and E-OBS on 1.875° for 1961-1990	132
7.5	Validation of GPD parameters from REMO and ECHAM5 summer temperature with E-OBS in 1961-1990	134
7.6	Validation of GPD parameters from REMO and ECHAM5 winter precipitation with E-OBS in 1961-1990	135
7.7	GPD return values of E-OBS, REMO and ECHAM5 temperature for different return times and aggregation levels in 1961-1990	136
7.8	GPD return values of E-OBS, REMO and ECHAM5 precipitation for different return times and aggregation levels in 1961-1990	137
7.9	GPD 1d-20a-RTV change of REMO and ECHAM5 temperature in 2021-2050 compared to 1961-1990	138
7.10	GPD 1d-20a-RTV change of REMO and ECHAM5 precipitation in 2021-2050 compared to 1961-1990	140
7.11	GPD parameter change of REMO and ECHAM5 summer temperature and winter precipitation for 2021-2050 compared to 1961-1990	141

7.12	GPD RTV change of REMO and ECHAM5 temperature and precipitation for different return times and aggregation levels in 2021-2050 compared to 1961-1990	142
8.1	Precipitation, wind and orography input data of original stations and REMO for the application of the weather generator in 1960-2000 . . .	146
8.2	Validation of Gamma (Γ) distributions of daily rainfall from REMO, PDF matching and full weather generator with original stations for selected stations in January and July of 1960-2000	150
8.3	Validation of characteristics of daily rainfall from REMO, PDF matching and full weather generator with original stations for selected stations in January and July of 1960-2000	153
8.4	Validation of GPD 1d-20a-RTVs and third GPD parameter for precipitation from PDF matching with original stations in 1961-1990 . .	155
8.5	GPD return values for precipitation from original stations, PDF matching, full weather generator, E-OBS, REMO and ECHAM5 for selected stations in 1961-1990	157
8.6	GPD 1d-20a-RTV change for precipitation from PDF matching and full weather generator in 2021-2050 compared to 1961-1990	159
8.7	GPD 1d-RTV change for precipitation from PDF matching, full weather generator, REMO and ECHAM5 for different return times and selected stations in 2021-2050 compared to 1961-1990	160

List of Acronyms

AR4	Fourth Assessment Report
CH_4	Methane
CO_2	Carbon Dioxide
CRU	Climatic Research Unit
DFG	Deutsche Forschungsgemeinschaft - German Research Foundation
DKRZ	Deutsches Klimarechenzentrum - German Climate Computing Centre
DWD	Deutscher Wetterdienst - German Weather Service
EA-Jet	East Atlantic Jet (pattern)
EA	East Atlantic (pattern)
EA/WR	East Atlantic/West Russia (pattern)
ECA&D	European Climate Assessment & Dataset (project)
ECMWF	European Centre for Medium-Range Weather Forecasts
EMULATE	European and North Atlantic daily to MULTidecadal climATE variability (project)
ENSO	El Niño-Southern Oscillation
EOF	Empirical Orthogonal Function
EROS	Earth Resources Observation and Science (Center)
ESF	European Science Foundation
ETOPO5	Earth Topography Five Minute Grid (dataset)
EU-FP5	European Commission's 5th Framework Program
EU-FP6	European Commission's 6th Framework Program
FAO	Food and Agriculture Organization
GCM	General Circulation Model
GEV	Generalized Extreme Value (distribution)
GHG	Greenhouse Gas
GLCC	Global Land Cover Characterization
GLOWA-JR	Global Change and the Hydrological Cycle Jordan River (project)

GPD	Generalized Pareto Distribution
GTOPO30	Global 30 Arc-Second Elevation Dataset
HOPE	Hamburg Ocean Primitive Equation (model)
IDW	Inverse Distance Weighting
IMPETUS	Integrated Approach to the Efficient Management of Scarce Water Resources in West Africa (project)
IMSL	International Mathematics and Statistics Library
IPCC	Intergovernmental Panel on Climate Change
JPL	Jet Propulsion Laboratory
KLIWEX-MED	Klimawandel und Extremereignisse im Mittelerranen Großraum - Climate change and Extreme events in the Mediterranean Basin (project)
M&D	Model and Data (group)
MedCLIVAR	Mediterranean CLimate and VARIability and Predictability
MO	Mediterranean Oscillation
MOI	Mediterranean Oscillation Index
MOS	Model Output Statistics
MPI-OM	Max-Planck Institute ocean model
MPIM	Max Planck Institute for Meteorology
NAO	North Atlantic Oscillation
NASA	National Aeronautics and Space Administration
NCEP/NCAR	National Centers for Environmental Prediction/National Center for Atmospheric Research
NGA	National Geospatial-Intelligence Agency
NO_2	Nitrogen Dioxide
OASIS	Ocean-Atmosphere-Sea Ice-Soil (coupler)
PC	Principal Component
PCA	Principal Component Analysis
PDF	Probability Density Function
PHC	Polar science center Hydrographic Climatology
RCM	Regional Climate Model
SCAND	Scandinavian (pattern)
SIR-C	Spaceborne Imaging Radar-C
SRES	Special Report on Emission Scenarios
SRTM	Shuttle Radar Topography Mission
STARDEX	Statistical and regional dynamical downscaling of extremes for European regions (project)

SZ	Subtropical Zonal (pattern)
UN	United Nations
UNEP	United Nations Environment Programme
USGS	United States Geological Survey
WDCC	World Data Center for Climate
WMO	World Meteorological Organisation
X-SAR	X-Band Synthetic Aperture Radar

1 Introduction and background

The introductory chapter describes the motivation of this study and the geographical background of the Mediterranean area including basic climatic features as well as socio-economic and ecologic vulnerabilities to climate variability in the first section. The second section presents recent scientific studies on observed trends of temperature, precipitation and corresponding extremes, influences of large-scale mid-latitude or tropical variability and possible impacts of human activities in present-day times. Then, numerical climate models are introduced and previous works on simulations of global general circulation models and regional climate models in the Mediterranean area are presented in the third section including the validation of present-day means and trends and the projection of future trends concerning temperature, precipitation and corresponding extremes with some closing remarks on general difficulties of extreme value analysis. Finally, the last section describes the framework, main aims and layout of the prevailing study.

1.1 Motivation and geographical background

Multiple meteorological or climate extreme events in the Mediterranean area exerted a very strong influence on society, economy and ecology in the recent decades and deeply entered the focus of public attention, media, politics and the scientific community. The most striking example is probably the prolonged European heat wave of summer 2003 which reached record-breaking temperatures over the western Mediterranean (GARCÍA-HERRERA et al., 2010), e.g. 47.3°C in Portugal (TRIGO et al., 2006a), indicating very likely the hottest summer since at least 500 years (LUTERBACHER et al., 2004). The heat wave caused 40,000 casualties over western and central Europe (GARCÍA-HERRERA et al., 2010) due to high night-time temperatures and large relative air humidities impacting on human health (FISCHER and SCHÄR, 2010), extended forest fires burning 5% of the Portuguese territory (TRIGO et al., 2006a) and agricultural losses of approximately 10 billion US dollars (MUNICH RE, 2004). GARCÍA-HERRERA et al. (2010) indicate a persistent blocking pattern over western Europe and decreased winter and spring soil moistures over

central Europe as main forcing mechanisms and STOTT et al. (2004) suppose that past anthropogenic warming increased the probability of such heat waves by factor two. Further examples describe heavy precipitation events over the Mediterranean area: the extra-tropical cyclone resulting from extra-tropical transition of Tropical Storm Leslie caused persistent extreme rainfall exceeding 700mm over Piedmont, Italy, in 13-16 October 2000 associated with extended flooding, landslides and damage to infrastructure over the whole Po valley (TURATO et al., 2004). In 2009, the winter storm Klaus induced heavy rainfall over France and Spain and losses of 5,100 million US dollars (LIBERATO et al., 2011; MUNICH RE, 2010) and most recently in autumn 2011, two weeks of prolonged heavy rainfall over northern Italy and southern France with river flooding, landslides and 16 casualties were visually entitled by the media as “tsunami of Genoa” (SZ, 2011). Generally, 122 extreme flooding events have been stated over the Euro-Mediterranean region in 1970-2006 causing total losses of 140 billion US dollars (BARREDO, 2009). Concerning dry periods, Iberia experienced strongly decreased rainfall from October 2004 to September 2005 because of reduced cyclones numbers and wet weather types due to a positive winter NAO and intense spring blocking conditions denoting the strongest drought of the last 140 years with intensively decreased agricultural and hydroelectricity production (GARCÍA-HERRERA et al., 2007). Another intense drought affected central and eastern Spain in 2008 causing dried water reservoirs and shortage of drinking water which resulted in public and private water use restrictions and water transports via trucks, ships or pipelines (GOODMAN, 2008). In Greece, severe droughts induced expanded fires burning 275,000 hectares of agricultural land and forests in 2007. Over the last 30 years, the total economic impacts of droughts for the former EU15 countries are estimated to 85 billion Euros (AUGUST and GEIGER, 2008). Thus, extreme events like heat waves, heavy precipitation, flooding or droughts severely influence the Mediterranean society, economy and ecology (FOWLER and KILSBY, 2003). Consequently, they are particularly regarded in climate studies on the impacts of anthropogenic climate change (MEEHL et al., 2000) because robust measures of the sensitivity of extreme events are needed to provide detailed information for political decision-makers and local stakeholders of the Mediterranean area in order to implement adequate measures for the mitigation and adaptation to climate change (CHANGNON, 2003).

Following the traditional climate classification of KÖPPEN (1936) the term “Mediterranean climate” characterises several similar climate regions on the globe determined by wet mild winters and dry warm or hot summers on the western sides of large continental masses between 30° and 40° latitude (LIONELLO et al., 2006b).

This study investigates the “real” Mediterranean area lying in the transition zone between the large continents Europe, Africa and Asia (Fig. 1.1). Besides the typical winter rainfall maximum several Mediterranean regions reach maxima in spring, e.g. parts of the Iberian Peninsula, or autumn, e.g. northern Italy or Dalmatia (ENDLICHER, 2000). The spatial temperature and precipitation distribution features a general north-south gradient revealing coolest and wettest regions over southern Europe and Turkey and warmest and driest regions over northern Africa and Arabia. The seasonal and spatial distribution of Mediterranean temperature and precipitation is further deepened in the validation part of this study (see subsection 4.1.2). Several specific characteristics make the climate of the Mediterranean area unique: The first particularity is the relatively large and deep semi-enclosed Mediterranean Sea which is connected to the global oceans via the narrow Gibraltar Strait (LIONELLO et al., 2006b). This concentration basin with evaporation exceeding freshwater input (TSIMPLIS et al., 2006) serves as source of moisture and heat reservoir for neighbouring land masses (LIONELLO et al., 2006b) and enhances cyclonic development (LIONELLO et al., 2006a). The Mediterranean Sea circulation consists of three main thermohaline cells located in the whole, western and eastern basins (TSIMPLIS et al., 2006) and even influences the Atlantic overturning circulation (ARTALE et al., 2006). Furthermore, the Mediterranean area reveals strong orographic features, e.g. the Alps, Pyrenees, Atlas or Anatolian mountains, and complex land-sea distribution patterns with many islands and peninsulas resulting in a spatially heterogeneous morphology strongly impacting on both atmospheric and sea circulation. Thus, very different climatic and environmental regions can be found from hot arid deserts in the south to humid mountains with permanent glaciers in the north (LIONELLO et al., 2006b). Additionally, the Mediterranean area lies in the transition zone between the mid-latitude and subtropical climate zones revealing both impacts of mid-latitude circulation variability mostly over the northern parts and influences of tropical variability over the southern parts (cf. ALPERT et al. (2006); TRIGO et al. (2006b), see further below). Finally, the Mediterranean area has been settled and influenced by several highly populated and advanced cultures since 2,000 BC (LIONELLO et al., 2006b) and suffered from probably the first large-scale human impact on climate, i.e. the expanded deforestation in Roman and Greek times influencing the atmospheric circulation and causing enhanced drying over the whole area (REALE and DIRMEYER, 2000; REALE and SHUKLA, 2000; GAERTNER et al., 2001).

The need for investigating present-day and future Mediterranean climate and extremes is enforced by the strong socio-economic and ecologic vulnerability of the

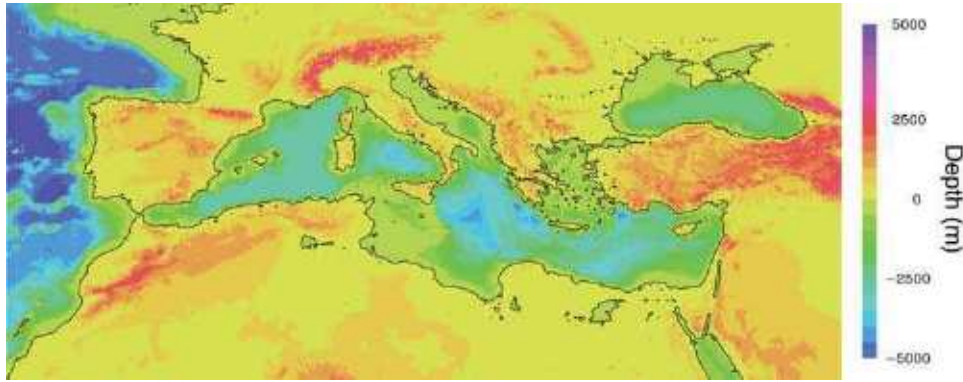


Figure 1.1: The Mediterranean area: orography and sea-depth [m], modified following LIONELLO et al. (2006b).

Mediterranean area to impacts of climate variability: Around 400 million people live in the densely populated Mediterranean area (LIONELLO et al., 2006b) which suffers from strong socio-economic contrasts between the northern parts and the southern and eastern parts concerning per capita Gross Domestic Product, energy supply and CO_2 emissions (PLAN BLEU, 2009). The population of the south-eastern countries is strongly and rapidly growing and urbanizing causing over-exploitation of natural resources like water and land and thus, desertification with weakening land productivity (PLAN BLEU, 2005). Water availability is already limited and projected to further decrease in future time periods, especially over the southern regions (see below), but 40% and 80% of the total water demand is applied exclusively for irrigation in the northern and south-eastern countries, respectively. This strong dependence on irrigation water worsens the socio-economic vulnerability of the Mediterranean area to climate variability. Lacking wastewater treatment in cities further highlights the problem of water quality (PLAN BLEU, 2005, 2009). Summer droughts like the 2003 hot and dry spell induce water shortages during the growing season causing damage to agricultural crops and mortality of animal stocks (LIONELLO et al., 2006b). Thus, the agricultural production recently decreased over northern Africa due to drought impacts and increased urbanization (IAASTD, 2008) resulting in the dependence of the south-eastern Mediterranean countries to import virtual water (FERNANDEZ and ENGREF, 2007). Furthermore, Mediterranean rainfall variability impacts on hydroelectricity production representing on average 35% and 20% of the Portuguese and Spanish total electricity production (TRIGO et al., 2004). Rapidly growing cities and tourist destinations on the shore reveal strong vulnerabilities to sea level rise and intense warming strongly impacting on the Mediterranean economy because the Mediterranean area receives 30% of the global international tourism (PLAN BLEU, 2005, 2009). But strongest socio-economic impacts can be stated by meteorological

extreme events like mentioned before, especially in densely populated areas (LIONELLO et al., 2006b). Finally, Mediterranean warming and drying enhances the risks of forest fires and soil or land degradation and endangers the biodiversity of plants and animals due to displacement of habitats and extinction or invasion of species. Deltas and coastal areas are especially vulnerable to sea level rise and wave activity (PLAN BLEU and EUROPEAN INVESTMENT BANK (EIB), 2008). Thus, the Mediterranean area features a high exposure to socio-economic and ecologic climate change impacts due to present-day as well as future projected strong warming and drying associated with heat waves, droughts and floods which is highlighted further below and a low capacity for adaptation due to dense population, strong dependence on limited natural resources and partly limited financial and technical capacities. This results in a strong vulnerability of the Mediterranean area to climate change, especially for the south-eastern countries (LIONELLO et al., 2006b; HOFF, 2008; PLAN BLEU and EUROPEAN INVESTMENT BANK (EIB), 2008).

1.2 Observations of the present-day Mediterranean climate

Large present-day seasonal temperature and precipitation trends over the Mediterranean region are found in several meteorological observations such as stations, radiosondes, aircrafts or satellites: For the whole 20th century, but especially for the early and last decades, GIORGI (2002) finds a significant warming trend in winter and summer over the whole Mediterranean area based on gridded station datasets. For the second half of the 20th century, a significant warming is obvious in the western Mediterranean in summer and winter and a slight cooling over the eastern parts (JACOBET, 2000; XOPLAKI, 2002). Recent warming trends initiated around 1980 in the western Mediterranean and only around 1990 in the eastern Mediterranean area (MIRANDA and TOMÉ, 2009) being especially strong in summer with several regions lacking significant trends in winter (TORETI, 2010). Concerning precipitation, winter wetting and drying patterns are prominent over the western and eastern Mediterranean in the 20th century, respectively (GIORGI, 2002). For the second half of the 20th century, the prevailing winter rainfall trend is negative but mostly not significant due to high interannual precipitation variability (XOPLAKI, 2002). Mainly in the last two to three decades of the 20th century an area-wide decrease of winter and spring precipitation is observed in the western Mediterranean, in particular over the Iberian Peninsula (JACOBET, 2000; GOODESS and JONES, 2002; GARCÍA et al., 2007; DEL RÍO et al., 2010). But also positive rainfall trends

are found, e.g. in the south-eastern Mediterranean (JACOBEIT et al., 2007) or in the western Iberian Peninsula from August to October (JACOBEIT, 2000; DEL RÍO et al., 2010). Overall, the most recent winter decades are found to be the driest and warmest since 500 years (LUTERBACHER et al., 2004; PAULING et al., 2006).

Concerning present-day trends of extreme events, many observed changes in temperature extremes are strongly consistent with present-day mean temperature trends revealing mainly warming patterns of Mediterranean extreme indices for daily minimum and maximum temperatures in summer and winter (KLEIN TANK and KÖNNEN, 2003; KOSTOPOULOU and JONES, 2005; MOBERG et al., 2006): Increasing numbers of warm days or nights and decreasing numbers of cold days or nights are found over the Iberian Peninsula (BRUNET et al., 2007; RODRÍGUEZ-PUEBLA et al., 2010), increasing numbers of tropical nights over Italy (TORETI and DESIATO, 2008) and Greece (KIOUTSIUKIS et al., 2010) and increasing numbers of hot summer days or nights over the eastern Mediterranean (KUGLITSCH et al., 2010). In winter, increasing numbers of very hot days and decreasing numbers of very cold nights over the whole Mediterranean are smaller and less uniform than in summer revealing some opposite trends over Turkey (EFTHYMIADIS et al., 2011). Besides extreme indices as well the fitting of a Generalized Pareto Distribution (GPD) reveals mostly increases in intensity and frequency of hot summer temperature extremes and rather decreases or no change patterns of corresponding cold winter extremes (NOGAJ et al., 2006). KIOUTSIUKIS et al. (2010) finds increasing return values of minimum and maximum temperatures over Greece in fitting both GPD and Generalized Extreme Value (GEV) distribution functions. Finally, increasing numbers, durations and intensities of summer heat waves are identified over the western (DELLA-MARTA et al., 2007) and eastern Mediterranean area (KUGLITSCH et al., 2010).

For precipitation extremes, observed trends of dry periods are generally consistent over the Mediterranean area but recent trends of heavy rainfall are rather controversial in different studies and less consistent with present-day Mediterranean drying: Over the Iberian Peninsula, ALPERT (2002) identifies increases of heavy rainfall exceeding 64mm but RODRIGO (2010) and LÓPEZ-MORENO et al. (2010) find decreasing or no significant trends in the occurrence of rainfall extremes exceeding the 95th and 90th percentiles, respectively. GALLEGO et al. (2006) and RODRIGO and TRIGO (2007) reveal as well decreasing heavy rainfall events. Over Italy, ALPERT (2002) and KOSTOPOULOU and JONES (2005) state increasing frequencies of torrential rainfall exceeding 128mm and intense rainfall events, respectively. Over the Balkans and Turkey, KOSTOPOULOU and JONES (2005) find decreasing occurrences of intense rainfall events but NORRANT and DOUGUÉDROIT (2006) increasing heavy

rainfall over Greece. Furthermore, fitting the GPD function to rainfall stations for the 1950-2006 extended winter season TORETI et al. (2010) find maxima of the 5-year ($>100\text{mm}$) and 50-year return values ($>250\text{mm}$) over coastal regions of Portugal, eastern Spain, western Balkans and western and northern Turkey and no significant changes or decreases in the occurrence of rainfall extremes. The latter result is conformed by KIOUTSIUKIS et al. (2010) for 5-year GPD and GEV return values over Greece. TRENBERTH et al. (2007) conclude that changes in rainfall extremes for higher return times are generally rather consistent with those for lower return values or more robust percentile estimates. Additionally, TORETI et al. (2010) find connections of western and eastern Mediterranean heavy rainfall events with intense Genoa cyclones and Cyprus lows, respectively, which are related to the smaller Mediterranean cyclonic branch of the north Atlantic storm track (LIONELLO et al., 2006a). The observed overall cyclone frequency does not significantly change in present-day times but the intensity of most intense cyclones decreases (TRIGO et al., 2000). Finally, due to decreasing Mediterranean rainfall in the late 20th century the frequency and persistency of severe droughts increases over the western (GARCÍA-HERRERA et al., 2007) and eastern Mediterranean (XOPLAKI et al., 2004) where KOSTOPOULOU and JONES (2005) find as well increasing maximum numbers of consecutive dry days.

Major parts of the observed Mediterranean temperature and precipitation trends can be explained by natural variability due to variations of large-scale atmospheric circulation patterns: The influence of mid-latitude circulation is largest over the western Mediterranean in winter when mid-latitude cyclone variability is greatest. In summer, both mid-latitude and tropical climate dynamics have to be considered (ALPERT et al., 2006; TRIGO et al., 2006b). The most important mid-latitude mode of atmospheric variation is the North Atlantic Oscillation (NAO) which strongly influences precipitation over the Iberian Peninsula (ULBRICH et al., 1999; GOODESS and JONES, 2002) and Turkey (TÜRKEKES and ERLAT, 2005) and, to a lower extent, temperature over the eastern Mediterranean (BEN-GAI et al., 2001; XOPLAKI, 2002). A positive NAO index correlates with cooling patterns over northern Africa, Near East and Turkey and drying patterns over southern Europe due to a northerly shift of North Atlantic storm tracks in winter (CULLEN and DEMENOCAL, 2000; TRIGO et al., 2002, 2004). The observed winter NAO index shows generally positive trends since the 1960s (JACOBET et al., 2001) and strong increases in the 1980s and 1990s (HURRELL, 1995) leading to corresponding trends in Atlantic storm tracks and Mediterranean cyclogenesis (TRIGO et al., 2000) and to strong decreases of Mediterranean rainfall (QUADRELLI et al., 2001; XOPLAKI et al., 2004; JACOBET et al.,

2007). But since the end of the 20th century the NAO slightly weakened (STEPHENSON et al., 2006). In addition, the Mediterranean Oscillation (MO, CONTE et al. (1989); BRUNETTI et al. (2002); DÜNKELOH and JACOBET (2003)) can be identified as regional manifestation of the NAO showing opposite pressure conditions between the western and eastern Mediterranean. DÜNKELOH and JACOBET (2003) point out that winter drying over the western and central Mediterranean is related to high pressure situations of an increasing long-term MO trend. Further major mid-latitude modes of variation account for Mediterranean temperature and precipitation variability: KRICHAK and ALPERT (2005b,a) explain the observed Mediterranean drying by the combined effect of increasing NAO and East Atlantic/West Russia (EA/WR) patterns and XOPLAKI (2002) shows positive correlation of the EA/WR pattern with winter rainfall over the Near East and eastern Turkey and negative correlation over southern Europe. The East Atlantic (EA) pattern presents even higher impacts on winter temperature than the NAO in the western Mediterranean (SÁENZ et al., 2001), and the Scandinavian (SCAND) pattern is related to winter rainfall in the eastern and western Mediterranean (QUADRELLI et al., 2001) and leads to distinct cyclogenesis and positive correlations with winter precipitation over Italy (XOPLAKI, 2002). Besides, some other mid-latitude modes influencing the Mediterranean area during different seasons are the regional Western Mediterranean Oscillation (MARTIN-VIDE and LOPEZ-BUSTINS, 2006), the Eastern Mediterranean pattern in winter (HATZAKI et al., 2007), the East Atlantic Jet pattern in summer (EA-Jet, DÜNKELOH and JACOBET (2003)) and the Mediterranean Meridional Circulation which is related to the oceanographical peculiarity of the Eastern Mediterranean Transient (JACOBET and DÜNKELOH, 2005).

Furthermore, several impacts of tropical climate dynamics on Mediterranean temperature and rainfall variability are identified: The El Niño-Southern Oscillation (ENSO) over the tropical Pacific is found to influence eastern Mediterranean rainfall in winter (PRICE et al., 1998) as well as western Mediterranean rainfall mainly in spring and autumn (MARIOTTI, 2002; MARIOTTI et al., 2005) whereas the latter influence is linked to the Mediterranean Oscillation in late summer to early autumn (SEUBERT, 2010). Relationships with the Asian and African monsoon variability are predominantly identified over the eastern Mediterranean in summer (RODWELL and HOSKINS, 1996; RAICICH et al., 2003; ZIV et al., 2004) but some negative correlations are found between western Mediterranean rainfall and Sahel precipitation in summer probably due to remote ENSO impacts (SEUBERT, 2010). Finally, Mediterranean summer temperature means and extremes such as heat waves are influenced by persistent anticyclonic regimes and blocking conditions with large positive geopotential

anomalies over whole Europe and the Mediterranean area featuring subsidence and stability and deflecting Atlantic storms away from southern Europe which further enhances summer dryness (XOPLAKI et al., 2003; PAL et al., 2004; CASSOU et al., 2005; CARRIL et al., 2008).

Finally, some parts of the observed Mediterranean temperature and precipitation variability may be related to human activities in present-day times: Major impacts are exerted by increasing atmospheric Greenhouse Gas (GHG) concentrations, like CO_2 , CH_4 or NO_2 , due to anthropogenic emissions from fossil fuel burning. These increasing atmospheric trace gases enhance the natural GHG effect which warms the surface air layers in partially absorbing long-wave emissions of the Earth's surface and emitting them back (WEISCHET and ENDLICHER, 2008; JACOBEIT, 1994). This additional surface warming strongly impacts on several other climate variables, e.g. rainfall (see further below). Influences of anthropogenic emissions on the radiation budget have already been postulated at the end of the 19th century (ARRHENIUS, 1926) but the recent scientific and public discussion on the anthropogenic enhancement of the natural GHG effect did not start before the mid of the 20th century (BUDYKO et al., 1987; FLOHN, 1985). Further impacts on the Earth's radiation budget and strong interactions with clouds are stated for increasing atmospheric concentrations of carbonaceous and sulphate aerosols from anthropogenic fossil fuel and biomass burning (PENNER et al., 1998). Additionally, Mediterranean climate variability may be related to anthropogenic land cover changes which intensively alter land surface processes, e.g. expanded agriculture or deforestation (ZAMPIERI and LIONELLO, 2011), reduced soil moisture (ROWELL and JONES, 2006) and desertification or soil degradation (FEDDEMA and FREIRE, 2001). In particular, SENEVI-RATNE et al. (2006) and FISCHER et al. (2007) highlight the strong impacts of decreasing winter or spring soil moistures on summer heat waves over southern Europe, like during the 2003 European heat wave. Thus, multiple studies investigate the impacts of human activities on Mediterranean climate variability in present-day and future time periods in context of natural variability, such as large-scale atmospheric circulation dynamics, in applying numerical climate models like the following section shows.

1.3 Simulations of the present-day and future Mediterranean climate

In order to understand the physical processes determining climate and to project future climate change under increasing atmospheric GHG concentrations numeri-

cal models are applied (VON STORCH et al., 1999; CUBASCH and KASANG, 2000): Global General Circulation Models (GCMs) simulate the various components and processes of the climate system including its general circulation at the global scale. In their dynamical core the major fluxes of the main climate components, i.e. atmosphere and ocean, are described by differential equations of the prognostic variables temperature, pressure, flux velocities, atmospheric humidity and oceanic salinity based on the basic principles on conservation of mass, energy and momentum. These complex non-linear differential equations cannot be solved analytically and their solutions are estimated by numerical approximations. Therefore, the spatial and temporal climate continuum is discretised to a horizontal grid of mostly spectral resolution and several atmospheric and oceanic vertical levels featuring climate variations on discrete time steps. Sub-grid scale climate processes, e.g. radiation, turbulence, convection, clouds or rainfall, are not resolved by the model and are described by parameterisations which apply empirical or physical relationships to resolved large-scale processes. After the initial state of every variable at every atmospheric and oceanic grid box has been defined by observational data and the boundary conditions at sea floor, top of the atmosphere and land surface, e.g. topography, albedo, soils or vegetation cover, have been prescribed for all time steps the integration of the climate model can be started and the differential equations are solved for every variable at every time step and grid box. The atmospheric and oceanic components of the climate system are often simulated in two separate GCMs and coupled in exchanging simulated fluxes of mass, energy and momentum. In addition to the simulation of the natural climate variability, specific external forcings can be defined, e.g. increasing atmospheric GHG concentrations, in order to estimate the sensitivity of the climate system to such external forcings (VON STORCH et al., 1999; CUBASCH and KASANG, 2000). Thus, different future emission scenarios of anthropogenic GHG and aerosols describing possible future developments of population growth, society, economy and technology have been constructed in the Special Report on Emission Scenarios (SRES, NAKICENOVIC and SWART (2000)) of the Intergovernmental Panel on Climate Change (IPCC), an international scientific committee founded by the World Meteorological Organisation (WMO) and the United Nations Environment Programme (UNEP) to assess climate change and corresponding socio-economic and ecologic impacts (IPCC, 2011). The most commonly used emission scenarios B1, A1b and A2 project atmospheric CO_2 concentrations of approximately 550, 700 and 850ppm in 2100, respectively, ranging from optimistic to rather pessimistic views of the future evolution of anthropogenic GHG emissions (GIORGI and COPPOLA, 2009).

But before future climate change is projected the modelling skill of GCMs is proved in validating simulations of present-day climate variability with observations: The global coupled atmosphere-ocean GCM simulations of the fourth Assessment Report (AR4) of the IPCC have been reviewed for the Mediterranean area by GIORGI and LIONELLO (2008) who report general good agreement of present-day temperature and precipitation means with gridded observations yielding maximum biases of mostly 1°C and 20%, respectively. But orography is strongly smoothed and insufficiently represented due to coarse GCM grid resolution ($\sim 120\text{-}450\text{km}$) resulting in warm and dry bias over mountain peaks and corresponding cold bias in neighbouring regions compared to observations (GIORGI and COPPOLA, 2009). Thus, the complex orography and land-sea contrast of the Mediterranean area strongly complicate climate modelling with global GCMs on regional scale and make the use of Regional Climate Models (RCMs) indispensable. RCMs resolve more small-scale climate features than GCMs due to larger spatial resolutions ($\sim 50\text{km}$) but reveal only regional model grids because of limited computer resources and are thus, nested into coarser-grid GCMs to obtain the necessary lateral boundary forcing (VON STORCH et al., 1999; CUBASCH and KASANG, 2000). Several scientific studies evaluate the performance of recent RCM simulations over the Mediterranean area and investigate possible improvements compared to driving GCM simulations: Within the PRUDENCE project (CHRISTENSEN and CHRISTENSEN, 2007), JACOB et al. (2007) validate ten RCMs driven by the GCM HadAM3H with observations revealing cold and dry bias in winter and warm and dry bias in summer relatively consistent over all RCMs and mostly smaller biases than GCMs in winter but less improvement of GCM biases in summer. GIORGI and COPPOLA (2009) compare two ensembles of GCMs and RCMs and find strongly differing temperature biases but equal patterns of rainfall biases with smaller summer rainfall biases in RCMs than in GCMs. The validation of 13 RCMs of the more recent ENSEMBLES project (CHRISTENSEN et al., 2008) with observations confirms warm bias in summer and dry bias in winter for many RCMs. Generally, RCMs produce more small-scale details over mountainous and coastal areas than GCMs (GIORGI and LIONELLO, 2008; GIORGI and COPPOLA, 2009) and are often able to reduce the corresponding large systematic GCM biases. Further added values of dynamical downscaling from global to regional scale can be stated: an improved representation of surface wind speeds and directions, especially over complex orography (SOTILLO et al., 2005), a larger and more dynamic water cycle with more realistic rainfall and river discharge (SANCHEZ-GOMEZ et al., 2009; ELGUINDI et al., 2009) and improved rainfall extremes due to a more realistic representation of the upper tails of the rainfall distri-

bution function (DEQUE and SOMOT, 2008). Thus, RCMs strongly improve climate modelling over areas with large regional impacts of orography, land-sea contrast or land use (WANG et al., 2004) which intensely highlights the need for regional climate modelling in the Mediterranean area.

Concerning the validation of present-day temperature and precipitation trends, GIORGI and LIONELLO (2008) report that the global coupled GCM simulations of the IPCC AR4 are able to capture the observed summer and winter warming as well as summer drying but the observed strong winter drying is not reproduced. However, this does not necessarily point to poor model performance in projecting GHG related climate change but could be explained by the strong NAO increase in the 1980s and 1990s, an observed random multidecadal natural variability event which is not reproduced by the GCMs without realistic initialisation of the global oceans. OSBORN (2004) states that many GCMs are still not able to reproduce the present-day amplitude of interannual variability and multidecadal trends of observed large-scale atmospheric modes. Furthermore, GCMs strongly control the interdecadal variability of large-scale circulation of nested RCMs in model-into-model-approaches, especially in winter (GIORGI et al., 2004a; GIORGI and LIONELLO, 2008). Thus, simulations of the RCM REMO (JACOB, 2001; JACOB et al., 2007) driven by the global coupled GCM ECHAM5/MPI-OM (ROECKNER et al., 2003) are not able to reproduce the interdecadal observed drought tendency of the Sahel Zone in 1960-2000 because of lacking atmosphere-vegetation feedbacks and different lower oceanic boundary conditions in the driving GCM (PAETH et al., 2009). Nevertheless, climate models are able to capture present-day trends of seasonal temperature and precipitation if forced by observed boundary conditions, e.g. if REMO is driven by global ECMWF ERA15 reanalyses and analyses in the 1979-2003 period (GIBSON et al., 1997), the main characteristics of observed means, trends and large-scale circulation are captured in tropical West Africa (PAETH et al., 2005) and the Mediterranean region (PAETH and HENSE, 2005). This highlights the strong dependence of simulated present-day trends on initial and boundary conditions.

After the validation of present-day GCM and RCM simulations future climate change projections over the Mediterranean area are regarded: The IPCC AR4 presents land-only future temperature and precipitation changes for the A1b emission scenario of 2080-2099 compared to 1980-1999 derived from the multi-model dataset of 21 global coupled atmosphere-ocean GCMs and area-averaged over sub-continental regions (CHRISTENSEN et al., 2007): the Mediterranean region experiences area-averaged multi-model median changes of 4.1°C (3.7-5.0°C) in summer and 2.6°C (2.5-3.3°C) in winter for temperature and -24% (-35- -14%) in summer and

-6% (-10- -1%) in winter for precipitation. The values in brackets denote the range of future changes containing 50% of all investigated models. In their review of 17 global GCM simulations of the IPCC AR4 for the Mediterranean area, GIORGI and LIONELLO (2008) find similar results and strong agreement of the selected simulations in future Mediterranean warming and drying for the A1b scenario of 2071-2100 compared to 1961-1990: warming reaches 2-3.5°C in winter and 3-5°C in summer, especially over Spain and the Balkans, and rainfall reduction reaches -40% over the northern Mediterranean in summer and -30% over the southern Mediterranean in winter with some small increases over the Middle East in summer and the northern parts in winter. The A2 and B1 scenarios reveal larger and smaller warming and drying patterns, respectively. These future GCM projections of Mediterranean warming and drying are substantially confirmed by investigations of RCM ensembles in recent European projects: ten RCMs forced by four global coupled GCMs in PRUDENCE (CHRISTENSEN and CHRISTENSEN, 2007; GIORGI and COPPOLA, 2009) and 16 RCMs driven by eight global coupled GCMs in ENSEMBLES (GOOD-ESS et al., 2009). RCMs mostly agree with GCMs in the projected warming which is larger in summer than in winter and increases with higher intensity of radiative forcing (GIORGI et al., 2004b). They reveal similar summer drying patterns and high uncertainties of winter rainfall changes because the extension of winter wetting over the northern Mediterranean strongly depends on GCM boundary conditions (RÄISÄNEN et al., 2004). But RCMs reveal generally more small-scale orographic and coastline features of future temperature and precipitation changes than GCMs (GIORGI and LIONELLO, 2008; GIORGI and COPPOLA, 2009). Finally, future Mediterranean warming and drying with some increases of winter rainfall over the north-western parts is as well confirmed by statistical downscaling approaches (HERTIG and JACOBET, 2008a,b).

The projected future Mediterranean surface warming can be related to the anthropogenic enhancement of the natural GHG effect due to increasing atmospheric GHG concentrations like mentioned before. The projected strong drying can be explained by direct thermodynamic consequences of a warmer atmosphere with increased atmospheric water vapour contents and large-scale water vapour transports producing generally wetter tropics and dryer subtropics (CHRISTENSEN et al., 2007). Additionally, Mediterranean winter drying is enhanced by the poleward expansion of subtropical high pressure systems and the corresponding displacement of mid-latitude westerly winds and North Atlantic storm tracks (CHRISTENSEN et al., 2007) which is described by positive winter NAO trends projected in several climate model simulations for the 21st century (ULBRICH and CHRISTOPH, 1999; COPPOLA et al.,

2005; STEPHENSON et al., 2006). But future projections of Mediterranean storm tracks reveal several uncertainties: Decreasing future annual storm track intensities are stated but as well increasing numbers of cyclones in summer (LIONELLO et al., 2008) and increasing extreme cyclone intensities even forming tropical cyclones can be seen (GAERTNER et al., 2007). Impacts of future warming and drying on the Mediterranean water cycle over land areas feature decreasing soil moisture, river discharge and evapotranspiration due to drier land surfaces which strongly reduces fresh water availability (MARIOTTI et al., 2008). Overall, GIORGI (2006) identifies the Mediterranean area as a primary climate change hot spot, i.e. one of the most vulnerable or responsive regions to future changes in mean and variability of temperature and precipitation.

Future changes of Mediterranean temperatures extremes are consistent to present-day observed changes. GCM and RCM simulations project warming of extreme indices of both daily minimum and maximum temperatures (CLARK et al., 2006; DIFFENBAUGH et al., 2007; KJELLSTRÖM et al., 2007) and larger frequencies, durations and intensities of heat waves in the Mediterranean area, especially in summer (MEEHL and TEBALDI, 2004; CLARK et al., 2006; BENISTON et al., 2007; FISCHER and SCHÄR, 2010), due to large future increases of both temperature means and variabilities in summer (FISCHER and SCHÄR, 2009). In fitting GPD functions to daily RCM temperature data, PAETH and HENSE (2005) find increasing 1-year return values of temperature extremes over the western and eastern Mediterranean area until 2020. Statistical downscaling reveals as well mainly future increases of the 5th percentile of winter minimum temperatures and 95th percentile of summer maximum temperatures except small decreases over some western Mediterranean regions (HERTIG et al., 2010).

But GCM and RCM simulations are generally controversial in projecting future climate change of Mediterranean heavy rainfall, especially in summer, suggesting both increases and decreases because of increased atmospheric water vapour and reduced number of rain days, respectively (CHRISTENSEN et al., 2007): SEMMLER and JACOB (2004) state increasing 10-year and 20-year GEV return values for daily precipitation over the central Mediterranean area and GOUBANOVA and LI (2007) find increasing precipitation extremes over the northern Mediterranean area in winter but small decreases or no change patterns in summer in fitting GEV functions to seasonal extremes. Similar patterns are described by GAO et al. (2006) revealing increasing and decreasing heavy rainfall over the north-western and south-western Mediterranean in winter, respectively, and mixed patterns over southern Europe in summer. But CHRISTENSEN and CHRISTENSEN (2003) denote increasing intensities

of heavy summer rainfall episodes for several days causing severe river flooding over the western parts except Portugal and decreases over the eastern parts. PAETH and HENSE (2005) reveal inhomogeneous change patterns for 1-year GPD return values of daily precipitation with probably decreasing winter and increasing summer rainfall extremes over the western and eastern Mediterranean until 2020, respectively. Instead, FREI et al. (2006) show decreases or insignificant changes of winter rainfall extremes and large inter-model differences in summer over southern Europe in a model comparison study of six European RCMs analysing GEV return values of daily precipitation. BENISTON et al. (2007) find mostly decreases of heavy winter and summer rainfall over southern Europe in RCM simulations of the PRUDENCE project with change intensities and patterns being rather sensitive to the selection of RCMs and driving GCMs, respectively. Thus, strong differences and inconsistencies are found in future simulations of Mediterranean rainfall extremes but large agreement can be stated in future GCM and RCM projections of Mediterranean dry periods revealing decreasing numbers of rain days (FREI et al., 2006) and increasing numbers and durations of dry spells with strengthening risk of droughts (VOSS et al., 2002; TEBALDI et al., 2006; BENISTON et al., 2007) consistent to present-day observed changes. PAL et al. (2004) and GAO et al. (2006) find increasing frequencies of both severe drought and flood events at least in summer and identify a broadening of the daily rainfall distribution function over the Mediterranean area.

Generally, the statistical analysis of extreme events reveals many uncertainties and difficulties because very rare events are regarded. Thus, the investigation of extremes at the upper distribution tails is very sensitive to sampling errors (PALMER and RÄISÄNEN, 2002) affecting both the assessment of distinct percentiles and the parameter estimation in fitting extreme value distributions to sample data. PAETH and HENSE (2005) highlight the need for large sample sizes, appropriate statistical distributions and a Monte Carlo sampling approach to evaluate the uncertainty of the corresponding return value estimate. LANA et al. (2006) find that the GPD fits the empirical distribution of dry periods over the Iberian Peninsula better than the GEV distribution. Generally, often moderate instead of very rare extremes are selected to increase the quantity of events for more accurate statistical analysis (HERTIG et al., 2012). But daily station data feature low spatial and temporal coverage and reveal missing values and inhomogeneities probably causing artificial trends (DELLA-MARTA and WANNER, 2006) which both complicate the analysis of extreme events. Instead, climate model data do not contain spatial and temporal gaps or inhomogeneities but several deficiencies can be stated in gridded simulations of extreme events (MEARNS et al., 1995), e.g. differing daily rainfall probability

functions compared to local stations with overestimated numbers of low-intensity rain days and underestimated numbers of high-intensity rain days (ZOLINA et al., 2004) or uncertain parameterisations of convection, clouds or rainfall (ERRICO et al., 2001). Several statistical post-processing approaches prevail to correct systematic deficiencies of climate model data in simulating extreme events: First, systematic model errors can be statistically corrected with observations applying model output statistics (MOS), i.e. relationships between observed rainfall and simulated model variables (GLAHN and LOWRY, 1972; HANSEN and EMANUEL, 2003; PAETH and HENSE, 2003; PAETH, 2010). Furthermore, extreme events can be simulated indirectly by statistical downscaling from large-scale circulation patterns to local extremes which has been done in several Mediterranean studies (HERTIG et al., 2010, 2012). Finally, a dynamical-statistical weather generator (PAETH and DIEDERICH, 2010) includes both statistical and physical adjustments of simulated precipitation to observations and produces local virtual rainfall stations from gridded model data.

1.4 Major aims of the present study

The international MedCLIVAR (Mediterranean CLimate and VARiability and Predictability) programme is founded by the European Science Foundation (ESF) and established to coordinate scientific research on the Mediterranean climate involving the estimation of observed climate variability and extremes, the understanding of major climatic and oceanic processes and the projection of future climate change (MEDCLIVAR, 2011). Within the MedCLIVAR framework, the research project KLIWEX-MED (Klimawandel und Extremereignisse im Mediterranen Großraum - Climate change and Extreme events in the Mediterranean Basin) is founded by the German Research Foundation (Deutsche Forschungsgemeinschaft DFG) and carried out in cooperation of the Institute of Geography and Geology of the University of Würzburg and the Institute of Geography of the University of Augsburg. It aims to construct probabilistic estimations of regional climate change in the Mediterranean Basin with special focus on meteorological and climatic extreme events which are investigated by several dynamical and statistical methods: directly from global GCMs and RCMs, indirectly from statistical downscaling based on transfer functions and synoptical approaches and indirectly from a dynamical-statistical weather generator based on RCM data.

The present study was carried out within the framework of the KLIWEX-MED project and investigates two major topics of the Mediterranean climate variability: The first main aim is to analyse the present-day and future variability of Mediter-

anean temperature and precipitation means and extremes from high-resolution RCM simulations and to investigate if the dynamical downscaling from global to regional scale improves the corresponding deficiencies of coarse-grid GCM simulations. Several biases of GCM simulations compared to observations and added values of regional climate modelling concerning Mediterranean temperature and precipitation means have been presented in this chapter. But the focus of this study is particularly laid on dynamical downscaling of temperature and precipitation extreme values over the Mediterranean area where strong heterogeneity of orography and land-sea contrast make the application of high-resolution RCM simulations indispensable. Thus, ensemble simulations of the regional climate model REMO (JACOB, 2001; JACOB et al., 2001, 2007) driven by the global coupled general circulation model ECHAM5/MPI-OM (ROECKNER et al., 2003; JUNGCLAUS et al., 2006) are analysed applying both future GHG emission and land degradation scenarios.

The second main aim features the application and comparison of several statistical methods of extreme value analysis for Mediterranean precipitation, i.e. quantile-based extreme indices, the fitting of GPD functions and a dynamical-statistical weather generator, in order to capture this highly uncertain topic from different methodical ways closely following the recommendations of the European STARDEX project (Statistical and regional dynamical downscaling of extremes for European regions, HAYLOCK (2005)). Several methodological difficulties and uncertainties of the statistical analysis of extreme events for both observations and climate model simulations have been described in this chapter and previous studies on present-day and future precipitation extremes over the Mediterranean area reveal strong disagreement. Due to more consistency and less uncertainty in previous studies Mediterranean temperature extremes are exclusively estimated by the fitting of GPD functions. Thus, this study performs a comprehensive investigation of present-day and future Mediterranean temperature and precipitation extreme events with thorough estimation of corresponding uncertainties and further applies and compares a broad spectrum of different statistical methods for precipitation extremes to clarify the corresponding uncertainty and inconsistency of previous studies.

In the following, the layout of this study is presented and the topics of the main chapters are shortly described. The second and third chapter give an overview of the various Mediterranean observational, GCM and RCM datasets and the different statistical methods applied in this study for the analysis of Mediterranean temperature and precipitation means and extreme events, respectively.

The fourth chapter presents the probabilistic investigation of present-day and future variability of Mediterranean temperature and precipitation containing the anal-

ysis of climatological means and trends and the quantification of the corresponding signal-to-noise ratios via analyses of variance from the prevailing REMO and ECHAM5/MPI-OM ensembles of model simulations. These model results are intensively validated with observations in the present-day time period, future climate change projections are presented and dynamical downscaling from global to regional scale is analysed in both present-day and future times. Seasonal and regional differences are investigated as well as the political scope of action given by different future emission scenarios. Thus, this chapter provides the necessary background for the analysis of Mediterranean extreme events.

The fifth chapter investigates the present-day impacts of mid-latitude circulation dynamics on Mediterranean temperature and precipitation variability for both models and observations in order to closer evaluate the discrepancies between observed and simulated present-day trends stated in the chapter before. Large-scale modes of variation from mid-latitude circulation are determined via *s*-mode Principal Component Analysis (PCA) and relationships to Mediterranean temperature and precipitation are found via cross-validated stepwise multiple regression. Furthermore, the impacts of large-scale circulation and residual circulation-unrelated drivers, e.g. GHG, are separated to find out whether the predictability of the given model-into-model approach with the only real boundary condition CO_2 increases after removing the influences of mid-latitude circulation variability on Mediterranean temperature and precipitation. Finally, similar analyses are performed for the whole REMO simulation period to investigate the impacts of mid-latitude circulation dynamics in long-term and future time periods.

The following three chapters present different statistical approaches of investigating the Mediterranean precipitation and temperature extremes. The sixth chapter determines four different precipitation extreme indices based on empirical quantiles describing both frequency and intensity of extreme rainfall events and consecutive dry days as measure for the analysis of Mediterranean dry periods. In order to avoid different uncertainty levels in context of differing present-day and future sample sizes of rain days both present-day and future extreme indices are based on a fixed present-day quantile threshold and days per season exceeding this threshold are counted. The resulting precipitation extremes of REMO and ECHAM5/MPI-OM are validated with observations in present-day times, future projections are performed and possible added values of dynamical downscaling are investigated in both present-day and future times. The focus of this chapter is laid on precipitation because dynamical and statistical downscaling techniques for Mediterranean rainfall extremes are compared in context of the KLIWEX-MED cooperation.

The seventh chapter describes the Mediterranean temperature and precipitation extremes produced by matching GPD functions to the daily observational and model data. Return values for several return times are built as well as return values for aggregated temperature and precipitation datasets over several days which indicate longer-term heat waves and wet periods. The uncertainties of the GPD return value estimates are assessed by a parametric bootstrap sampling approach which further provides a measure to evaluate the significance of future climate change. The REMO and ECHAM5/MPI-OM temperature and precipitation extremes are validated with observations in the present-day time period and projections of future climate change are performed for different emission scenarios of the future time period. Furthermore, dynamical downscaling from global to regional scale is analysed in both present-day and future time periods.

The eighth chapter presents Mediterranean rainfall extremes built by a dynamical-statistical weather generator considering orographic influences of windward and lee effects, a stochastic part describing the spatial spread within a climate model grid box and a matching of simulated Probability Density Functions (PDF) to observed daily distributions. This analysis is only performed for precipitation because simulated area-averaged rainfall strongly overestimates numbers of rain days and underestimates daily rainfall intensities compared to local stations and the prevailing weather generator is able to improve such deficiencies. Thus, the performance of the weather generator is investigated in present-day climate and the resulting virtual precipitation stations derived from gridded REMO data are directly evaluated with original stations at the local scale. Then, rainfall extremes from both virtual and original stations are constructed by fitting GPD functions similar to the previous chapter. Precipitation extremes of virtual stations are validated with original stations in the present-day time period and climate change projections for different emission scenarios of the future time period are performed. Furthermore, comparisons to former gridded observational and simulated rainfall extremes of REMO and ECHAM5/MPI-OM are done.

Finally, the ninth chapter shortly summarizes the main findings of this study and discusses them in the context of previous research studies on Mediterranean temperature and precipitation means and extremes. Furthermore, some major conclusions for the Mediterranean climate are drawn from these findings and a short outlook presents main uncertainties of this study and several aspects requiring further research work.

2 Database

This chapter describes the various Mediterranean climate datasets applied in this study for the analysis of temperature and precipitation means and extremes in present-day and future time periods. Generally, the most recent observational and climate model datasets that have been available at the beginning of this study are used. The first section presents the observational database including station data, gridded observations, reanalysis datasets and elevation data mainly for the validation of climate model results in the present-day time period. The second section describes the considered model simulations of the global coupled general circulation model ECHAM5/MPI-OM and the regional climate model REMO for the analysis of dynamical downscaling from global to regional scale and the investigation of future climate change. The close description of the selected time periods and the distinct geographical extent of the Mediterranean region under consideration is given in section 3.1 of the methods chapter for all observational and model datasets applied in this study.

2.1 Observational database

The observational datasets are used to describe the climatic characteristics of the present-day time period and serve for the validation and calibration of climate model results before future projections are performed. But observed datasets often feature low spatial and temporal coverage with missing values and reveal several deficiencies, like errors in station measurement, erroneous spatial coordinates of station location and inhomogeneities in time series due to changing station environment or geographical position, observation practices or instruments, i.e. non-climatic breaks (HAYLOCK et al., 2008; HOFSTRA et al., 2009). Furthermore, local station information needs to be transformed to larger area average values by spatial interpolation to be appropriate for the validation of model grid box values. But spatial interpolation features as well several limitations due to larger uncertainties in areas of low station density or complex topography and for variables with high spatial variability, e.g. precipitation (HOFSTRA et al., 2009). Reanalysis data suffer from deficiencies

of the specific data assimilation system (UPPALA et al., 2005). Nevertheless, despite all inaccuracies or limitations of observations there is no real alternative for representing the present-day climate conditions. Thus, observations are applied for the validation of climate models but the corresponding uncertainties have always to be kept in mind. The following subsections present the observational data applied in this study for model validation, analysis of mid-latitude circulation or as input data for the dynamical-statistical weather generator: station data gathered from several projects, gridded E-OBS and CRU observational datasets, NCEP/NCAR and ERA40 reanalysis data and the SRTM elevation dataset.

2.1.1 Station data

In total, the KLIWEX-MED cooperation has collected a dataset of 201 daily temperature and 330 daily precipitation station records in the Mediterranean area mainly used for model validation and calibration. 81 temperature and 102 precipitation stations remain for subsequent analyses after testing homogeneity following WIJNGAARD et al. (2003) and applying data completeness tests slightly modified from MOBERG and JONES (2005) further described in section 3.1. In this study, only the daily precipitation stations are used as input data for the dynamical-statistical weather generator revealing highest station density over the Iberian Peninsula and the Near East and several stations over the central Mediterranean area but only two stations over the whole northern Africa (cf. Fig. 8.1). In the following, the projects from which the station data have been collected are shortly presented:

The European Climate Assessment & Dataset (ECA&D, KLEIN TANK et al. (2002)) project holds daily station time series of surface air temperature and precipitation from 56 participating national meteorological and hydrological services, observatories and research institutes from European and Mediterranean countries with main focus on the analysis of extremes. The station data are quality controlled and tested for homogeneity but not completely homogenised. Furthermore, they may be blended, i.e. temporal gaps are filled by adjacent station data within 25 km distance, and updated with non-validated synoptical messages for most recent years (ECA&D, 2011).

The European and North Atlantic daily to MULTidecadal climATE variability (EMULATE) research project of the European Commission's 5th Framework Program (EU-FP5) focuses on creating daily historic sea level pressure grids over Europe and the extratropical Atlantic from 1850 until today and on investigating correlations between atmospheric circulation patterns, sea surface temperature and surface climate variables over Europe (LISTER, 2007). Within this project a database of

long-term daily European temperature and precipitation station records starting before 1901 has been collected from several meteorological services and datasets of 26 countries. Basic data quality checks have been performed but no overall homogeneity assessment (MOBERG et al., 2006).

The international Global Change and the Hydrological Cycle Jordan River (GLOWA JR) Project investigates water availability and sustainable water management in the water scarce Jordan River basin under climate and global change (GLOWA, 2011). In the Upper Jordan Catchment the physically based hydrological model WaSiM analyses terrestrial water balance, river discharge and interplay between surface and groundwater utilising information from several daily precipitation and climatological station records over Israel, Syria, Lebanon and Jordan (KUNSTMANN et al., 2006).

In particular, several station time series have been gathered from cooperation with scientists of the international MedCLIVAR programme which coordinates research on the Mediterranean climate and has already been described in section 1.4 of the introduction chapter (MEDCLIVAR, 2011).

2.1.2 Gridded E-OBS data

The ENSEMBLES project (ENSEMBLES, 2011) of the European Commission's 6th Framework Program (EU-FP6) aims at designing an ensemble prediction system for future climate change at seasonal, decadal and centennial time scales applying regional and global Earth System models. For validation, an independent high-resolution gridded observational dataset has been produced called E-OBS Version 2.0 dataset (HAYLOCK et al., 2008). The land-only dataset covers the surface climate variables daily mean, maximum and minimum temperatures and daily precipitation sum over whole Europe and parts of northern Africa from 21° N to 75° N and from 49° W to 68° E at four different grid versions for the time period 1950-2008: regular 0.25° and 0.5° geographical grids and 0.22° and 0.44° rotated pole grids with North Pole located at 39.25° N and 162° W commonly applied for many ENSEMBLES RCMs (ECA&D, 2009). For this study, daily mean temperature and precipitation sum on the regular 0.5° grid (~50km) is selected for model validation in agreement with the resolution of prevailing CRU and REMO datasets.

The E-OBS dataset has been interpolated from daily station time series of the ECA&D project (KLOK and KLEIN TANK, 2008). The station network contains more than 2,000 stations with highest density over Ireland, Switzerland and the Netherlands and lowest station density over the southern and eastern Mediterranean area. Station data is quality controlled but not completely homogenised and also

potentially inhomogeneous station data are applied for interpolation in order to sustain high station network density (HOFSTRA et al., 2010). The interpolation process is performed in three steps (HAYLOCK et al., 2008): first, monthly temperature means and precipitation totals are interpolated to a 0.1° rotated pole grid via three-dimensional thin plate splines. Then, corresponding daily anomalies are interpolated to the same grid using different kriging techniques for temperature, precipitation occurrence and magnitude. Finally, monthly and daily values of the finer 0.1° grid are combined and area averaged to the four different coarser grid resolutions mentioned before. The last step is performed to be more comparable to the statistics of area average RCM output at equal resolution, e.g. concerning the rainfall occurrence distribution or intensities of extremes being strongly smoothed by both interpolation of daily anomalies and area averaging. Besides best estimate values elevation files and daily standard errors are available for each grid box. The latter describe the combined uncertainty of both daily and monthly interpolation and strongly depend on season and station density revealing maximum errors of 0.06°C and 7mm for temperature and precipitation over Turkey and northern Africa in winter (HAYLOCK et al., 2008).

But the gridded E-OBS dataset features several inaccuracies due to errors in underlying station data or limitations of the interpolation method: BEGERT et al. (2008) assess the homogeneity of the underlying station data and find only 20% and 59% of the mean temperature and precipitation station time series to be homogeneous in the time period 1960-2004, respectively. Such inhomogeneous station time series induce many inhomogeneities in the gridded E-OBS dataset (HOFSTRA et al., 2009). In investigating different station network densities HOFSTRA et al. (2010) show that daily E-OBS temperature and precipitation are over-smoothed in areas with low station density, i.e. interpolated values are reduced in comparison to real area-averages, especially for higher percentile extremes. Finally, HOFSTRA et al. (2009) find that the available interpolation standard deviation underestimates the real uncertainty caused by daily and monthly interpolation.

2.1.3 Gridded CRU data

The CRU TS 2.1 dataset from the Climatic Research Unit (CRU, MITCHELL and JONES (2005)) offers long-term monthly observational time series from 1901 to 2002 on a regular high-resolution 0.5° grid over all global land masses except Antarctica. It has been built from updated and revised meteorological station records in interpolating the station anomalies following NEW et al. (2000) and combining them with gridded climate normals for the baseline period 1961-1990 (NEW et al., 1999) to ar-

rive at absolute monthly climate grids. In regions without adjacent stations within the correlation decay distance, e.g. 1200 km for temperature and 450 km for precipitation, interpolated absolute values are relaxed towards the climate normals (NEW et al., 2000). A refined automated iterative method for inhomogeneity detection and correction using reference time series from neighbouring stations enables the construction of homogenous long-term station time-series with reduced data fragmentation. Nine climate variables are available, e.g. precipitation and daily mean, minimum or maximum temperature (MITCHELL and JONES, 2005). Additional files describe the number of adjacent stations within the correlation decay distance of a grid box revealing high and low station density over the northern and southern Mediterranean area in all seasons, respectively, and give information on the 0.5° grid elevation and land-sea-mask applied (MITCHELL, 2011). The independent observational CRU datasets are complete in space and time and appropriate for validation of climate model data (NEW et al., 2000). But they are just best estimates of the observed spatial climate pattern in time and suffer from shortcomings in time series analysis like the relaxation to climate normals and impacts of changing station networks in time, especially in regions with sparse station density (MITCHELL, 2011). In this study, the monthly CRU precipitation and mean temperature data on 0.5° grid resolution are applied for model validation of means and trends additionally to E-OBS data to estimate the prevailing uncertainties in observations.

2.1.4 NCEP/NCAR and ERA40 reanalysis data

The reanalyses of the National Centers for Environmental Prediction/National Center for Atmospheric Research (NCEP/NCAR, KALNAY et al. (1996), KISTLER et al. (2001)) are global atmospheric fields without gaps which have been processed from observational data of the land surface, ships, radiosondes, aircrafts or satellites from different countries or institutions applying quality controls and a global data assimilation system. For this kind of dynamical interpolation a state-of-the-art operational forecast model with spectral horizontal resolution T62 ($\sim 210\text{km}$) and 28 vertical levels has been used remaining unchanged during the whole project in order to avoid artificial jumps due to a changing assimilation system. Further inhomogeneities coming along with changes in the observing systems can be prevented by parallel reanalysis with inclusion and exclusion of the new observations over one year (KALNAY et al., 1996; KISTLER et al., 2001). The reanalysis products are daily and monthly global atmospheric fields of several variables, e.g. geopotential heights, horizontal winds, temperature and relative humidity, at surface and 17 pressure levels from 1000 to 10hPa in 2.5° horizontal resolution for the time period 1948 until today (EARTH SYS-

TEM RESEARCH LABORATORY, 2011). In this study, the NCEP/NCAR reanalysis dataset is applied to determine observed mid-latitude circulation variability from 2.5° sea level pressure data because we aim at including the influence of the whole North Atlantic circulation dynamics on the Mediterranean area which lies outside the European E-OBS grid. In the following, the NCEP/NCAR reanalysis dataset is called NCEP reanalyses.

The European Centre for Medium-Range Weather Forecasts (ECMWF) has produced the ERA40 reanalysis data (UPPALA et al., 2005) from several meteorological observations during mid-1957 to mid-2002 such as radiosondes, aircrafts, ocean-buoys and surface platforms including satellites since the 1970s which particularly improve observations over the southern hemisphere. The data assimilation system of the second-generation ERA40 reanalyses includes several improvements in operational forecasting, e.g. spectral horizontal resolution T159 ($\sim 125\text{km}$) and 60 vertical levels, since the implementation of the first-generation systems of ERA15 (15-year ECMWF reanalyses for 1979-1993, GIBSON et al. (1997)) and NCEP reanalyses in the mid-1990s revealing several limitations and problems. Thus, ERA40 provides better reanalysis fields with higher horizontal and vertical resolution and with a wider range of variables, e.g. ocean waves and ozone, strongly appropriate for studies on climate variability (UPPALA et al., 2005): global surface fields, e.g. for radiation, pressure, temperature, winds, clouds, precipitation, runoff or sea-ice, and global fields at 23 pressure levels from 1000 to 1hPa, e.g. for geopotential, temperature, winds or humidity, available four times daily at 2.5° horizontal grid resolution (ECMWF, 2011). In this study, the 10m zonal and meridional wind fields of ERA40 reanalysis data at 2.5° resolution are applied as input data for the orographic term of the dynamical-statistical weather generator.

2.1.5 SRTM elevation data

The Earth Resources Observation and Science (EROS) Center of the United States Geological Survey (USGS) offers several regional and global raster elevation datasets on different resolutions. The digital topographic map applied for the orographic term of the weather generator of this study is derived from the Shuttle Radar Topography Mission (SRTM) Finished Grade Data (FARR et al., 2007; USGS EROS, 2011). This international remote sensing radar project has been operated in cooperation of the National Geospatial-Intelligence Agency (NGA), the National Aeronautics and Space Administration (NASA) and the Italian and German Space Agencies. The space shuttle Endeavour performed 176 orbits on 11 days in February 2000 covering 80% of the Earth's land masses lying between 56° S and 60° N at spatial resolution

of 1 arc-second ($\sim 30\text{m}$). Surface elevation data is derived from single-pass radar interferometry which calculates the difference between two radar signals measured simultaneously at two antennas on board and on a 60 m mast outside the space shuttle imaging earth surface at different angles. Hardware of both Spaceborne Imaging Radar-C (SIR-C) and X-Band Synthetic Aperture Radar (X-SAR) was applied (FARR et al., 2007; USGS EROS, 2011). C-band SRTM raw data were processed at the Jet Propulsion Laboratory (JPL, RAMIREZ (2009)) and Finished Grade data were produced by levelling water bodies, correcting coastlines and single elevation errors and completing small areas of missing values. The SRTM Finished Grade raster elevation data are publicly available in 1° data sectors with non-US regions interpolated to 3 arc-second ($\sim 90\text{m}$) resolution for global coverage (USGS EROS, 2011).

2.2 Climate model database

The design and functionality of climate models has already been presented in detail in section 1.3 of the introduction chapter. Compared to observational data climate models offer several essential advantages (PAETH and HENSE, 2005): They provide continuous data on a regular geographical grid and do not feature gaps due to instrumental errors, inhomogeneities due to change of measuring conditions or uncertainties due to interpolation over areas of low station density. Furthermore, future climate evolutions can be projected and external forcings, e.g. anthropogenic GHG emissions or land use change, can be prescribed to investigate the sensitivity of the climate system to such forcings (PAETH and HENSE, 2005). But in analysing and interpreting present-day and future climate model simulations one should be aware of the important deficiencies and uncertainties of climate modelling (VON STORCH et al., 1999; CUBASCH and KASANG, 2000): Basic problems feature possible long-term climate drifts of coupled atmosphere-ocean models which can be corrected by adjusting the corresponding exchange fluxes and the cold start problem denoting the importance to consider in set-up and interpretation of climate simulations that slowly responding components of the climate system, such as the ocean, need some decades to reach their equilibrium state. Furthermore, small-scale climate processes are often neglected in discretisation due to limited computer resources or insufficiently represented in parameterisation causing systematic model errors (VON STORCH et al., 1999; CUBASCH and KASANG, 2000), e.g. deficient parameterisations of clouds and convection (ERRICO et al., 2001) or overestimations and underestimations of numbers of low-intensity and high-intensity rainfall events in area-averaged

simulations, respectively (ZOLINA et al., 2004). Finally, the unknown initial states of atmosphere and ocean, differing model formulations of various climate models and the unknown future evolution of anthropogenic GHG emissions induce uncertainties which are captured by constructing ensembles of climate model simulations for different initial conditions, climate models or emission scenarios (VON STORCH et al., 1999; CUBASCH and KASANG, 2000). Thus, the following sections present the global coupled general circulation model ECHAM5/MPI-OM and the regional climate model REMO driven by ECHAM5/MPI-OM which provide the model simulations of Mediterranean temperature and precipitation applied in this study for model validation in present-day times, projection of future climate change and investigation of dynamical downscaling from global to regional scale.

2.2.1 Global coupled general circulation model ECHAM5/MPI-OM

The global coupled atmosphere ocean model ECHAM5/MPI-OM (JUNGCLAUS et al., 2006) has participated at the IPCC AR4 and consists of the atmospheric component ECHAM5 (ROECKNER et al., 2003, 2006) and the ocean-sea ice component Max-Planck Institute Ocean Model (MPI-OM, MARSLAND (2003)) which are coupled by the Ocean-Atmosphere-Sea Ice-Soil (OASIS) coupler (VALCKE et al., 2003): the ocean delivers sea surface temperature, surface velocity, sea ice concentration and thickness and snow depth to the atmosphere which passes atmospheric freshwater fluxes including glacier calving and river runoff to the ocean (JUNGCLAUS et al., 2006).

The atmospheric General Circulation Model (GCM) ECHAM5 (ROECKNER et al., 2003, 2006) has been designed for climate research at the Max Planck Institute for Meteorology (MPIM) based on the spectral weather forecast model of the ECMWF (SIMMONS et al., 1989). The GCM ECHAM5 features several improvements in comparison to its precursor model ECHAM4 (ROECKNER et al., 1996) concerning the schemes for flux-form semi-Lagrangian transport, longwave radiation and cloud microphysics, the representation of land surface processes and subgrid-scale orographic effects and the cloud cover parameterisation. Furthermore, the prognostic variables for cloud water and ice have been separated, the number of spectral bands has been raised and new land surface parameters have been applied in ECHAM5 (ROECKNER et al., 2003). The prognostic variables of the spectral dynamical core are vorticity, divergence, temperature, logarithm of surface pressure, specific humidity, cloud water and cloud ice (MPIM, 2005; ROECKNER et al., 2006). Different horizontal resolutions are available from T21 to T159 and the standard ECHAM5

configuration features 19 or 31 vertical levels up to 10hPa for tropospheric studies. The middle-atmosphere MAECHAM5 configuration even shows 39 or 90 vertical levels up to 0.1hPa (ROECKNER et al., 2003). Furthermore, ECHAM5 is able to include sub-model extensions, e.g. for atmospheric chemistry or aerosols (MPIM, 2011a). Finally, multiple input files are applied to define the initial state of the atmosphere, the boundary conditions at the land and ocean surface, i.e. surface albedo, orography, soils, vegetation, snow, sea surface temperature and sea ice concentration, the ozone distribution and the initialization of subgrid-scale parameterisations before beginning the model integration (cf. MPIM (2011a)).

The ocean GCM MPI-OM (MARSLAND, 2003) originates from the Hamburg Ocean Primitive Equation (HOPE) model (WOLFF et al., 1997) and follows the hydrostatic and Boussinesq assumptions. It contains a dynamic-thermodynamic sea ice model and improved parameterisations of subgrid-scale processes, e.g. a bottom boundary layer scheme for slope convection (MPIM, 2011b; MARSLAND, 2003). Prognostic variables and tracers are velocities, temperature, salinity, surface elevation, ice thickness, concentration and velocities and snow depth (MPIM, 2005). MPI-OM features 40 vertical layers and applies an orthogonal curvilinear grid where grid poles can be located arbitrarily. This might help removing the numerical singularity due to converging meridians at the geographical North Pole and increasing horizontal resolution in regions of deep water formation (JUNGCLAUS et al., 2006). The sub-model extension HAMOCC is able to further model biogeochemistry in ocean waters and sediments (MPIM, 2011b). Temperature and salinity initial data and atmospheric boundary conditions are gained from the gridded Polar science center Hydrographic Climatology (PHC, ERMOLD and STEELE (2005)) and topography has been derived from the Earth Topography Five Minute Grid (ETOPO5) dataset from NATIONAL GEOPHYSICAL DATA CENTER (1988).

The 6-hourly ECHAM5/MPI-OM simulations applied in this study have been performed for the IPCC AR4 and collected from the World Data Center for Climate (WDCC) maintained by the Model and Data group (M&D) hosted at the MPIM Hamburg in cooperation with the German Climate Computing Centre (Deutsches Klimarechenzentrum DKRZ) (MODEL&DATA, 2008). ECHAM5 has been operated in spectral horizontal resolution T63 (192x96 grid boxes globally) equalling approximately a 1.875° geographical grid with 31 vertical layers up to 10hPa (MPIM, 2005). The MPI-OM features 40 vertical layers and a 1.5° average horizontal resolution with grid poles over central Antarctica and Greenland resulting in high resolution (15 km) over the deep water formation areas of Greenland, Labrador and the Weddell Sea and low resolution (184 km) over the Pacific (JUNGCLAUS et al., 2006). The sim-

ulations cover the time period 1860-2100. The forcing is transient with observed GHG emissions (e.g. CO_2 , CH_4 , NO_2 , ozone) and sulphates for 1860-2000 in the 20th century simulation (20C3M) and the IPCC SRES A1b and B1 emission scenarios (NAKICENOVIC and SWART, 2000) for 2001-2100 identifying a business-as-usual and a mitigation future scenario, respectively. The long-lived GHG concentrations are given as global annual means. Ozone and sulphate aerosols are prescribed with higher spatial and temporal resolution (MODEL&DATA, 2008). For 20C3M and both future scenarios three different ensemble members are available which have been initialized by different years of the long-term pre-industrial control experiment with constant well-mixed GHG concentrations at 1860 levels characterising a typical non-drifting climate state of the mid 19th century (MODEL&DATA, 2008). In this study, temperature and precipitation data of ECHAM5/MPI-OM are applied for the analysis of the Mediterranean means and extremes in present-day and future time periods and sea level pressure data for the investigation of mid-latitude circulation variability.

2.2.2 Regional climate model REMO

A GCM like ECHAM5 with horizontal resolution of about 1.875° (~ 150 - 200 km) is not able to resolve the high heterogeneity of orography and land-sea contrast in the Mediterranean area, e.g. the Apennine Mountains, Crete, the Balearic Islands or the Straits of Gibraltar, Messina and Bosphorus, making the use of a high-resolution Regional Climate Model (RCM) indispensable. RCMs operate similarly to GCMs but present limited area models of finer resolution. Thus, atmospheric forcing data from GCMs or global observations are needed to force RCM lateral boundaries (PAETH, 2005).

In this study, the hydrostatic regional climate model REMO (JACOB, 2001; JACOB et al., 2001, 2007) is applied which has been developed at MPIM based on the previous numerical weather prediction model Europa-Modell (MAJEWSKI, 1991) of the German Weather Service (Deutscher Wetterdienst DWD). It has been generated for atmospheric simulations at the synoptic scale and further adapted to regional climate modelling (JACOB, 2001). The prognostic variables of its dynamical kernel are surface pressure, temperature, horizontal wind components, water vapour and cloud water content (JACOB et al., 2001; JACOB, 2011). The corresponding model equations are projected on a regular geographical grid with the vertical coordinate following the surface terrain (PAETH et al., 2005). Subgrid-scale atmospheric processes, e.g. radiation, convection or clouds, are not resolved and need to be parameterised. REMO can apply two different physical parameterisation schemes

DWD and ECHAM4 physics in order to enable applications in weather forecast and climate modelling mode, respectively (JACOB, 2011). In climate mode, the physical parameterisations are derived from the GCM ECHAM4 (ROECKNER et al., 1996) adapted to the finer REMO scale. The mass flux scheme by TIEDTKE (1989) is applied for moist convection and a 5-layer soil model down to 10m depth for land surface processes. But lateral ground water flows are not considered (PAETH, 2005). The REMO version 5.7 used here additionally features a fractional land-sea mask and an enhanced land surface scheme (PAETH et al., 2009).

The 6-hourly REMO simulations used in this study (PAETH et al., 2009) have been performed during the German IMPETUS project (Integrated Approach to the Efficient Management of Scarce Water Resources in West Africa, CHRISTOPH et al. (2004)). Therefore, the model domain is centred over Africa further covering the adjacent Mediterranean Basin and Arabian Peninsula and extends from 30° W to 60° E and from 15° S to 45° N (Fig. 2.1) with a horizontal resolution of 0.5° (181 x 121 grid boxes) and 20 hybrid vertical levels up to 25km height (PAETH et al., 2009). The REMO simulations are nested into simulations of the coupled GCM ECHAM5/MPI-OM (ROECKNER et al., 2003; JUNGCLAUS et al., 2006) with transient forcing for the time period 1960-2050. Generally, in such model-into-model approaches the RCM might suffer from uncertainties or errors in the global GCM (PAETH et al., 2009). The REMO model is operated in climate mode: The simulation area is once initialized by all forcing data when starting the integration and then, in subsequent time steps lateral atmospheric and lower oceanic boundary data of ECHAM5/MPI-OM are prescribed every six hours (PAETH et al., 2005). The impact of the lateral boundary forcing decreases exponentially in a boundary zone of eight grid box rows allowing REMO to evolve its own dynamics in the central model domain (JACOB, 2001; PAETH et al., 2005). By restraining the relaxation of humidity and temperature at the lateral boundaries in outward directed atmospheric flows artificial precipitation due to lateral boundary effects can be constrained to the outmost two to three lateral grid box rows of the model domain (PAETH et al., 2005). The original REMO model has been designed for extratropical regions. Thus, in the REMO version 5.7 used here some model parameters have been adjusted to the tropical-subtropical atmospheric conditions of West Africa, e.g. the lower cloud thickness threshold is lifted in the convection scheme (PAETH et al., 2005).

During 1960-2000 observed GHG emissions and sulphate aerosol conditions are applied consistent to the transient ECHAM5/MPI-OM forcing. Due to limited computational resources only direct sulphate aerosol effects are considered but no complex aerosol model including further aerosol processes (PAETH et al., 2009). Land

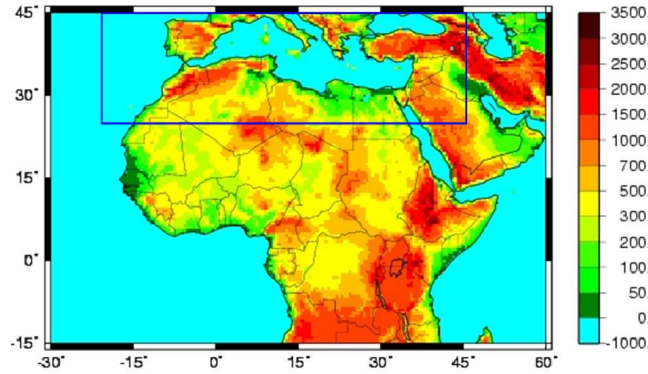


Figure 2.1: Full model domain and orography [m] of the given REMO simulations on 0.5° resolution with the blue frame denoting the Mediterranean area of investigation, modified following PAETH (2005).

surface parameters, e.g. orography, soils, vegetation and albedo, are derived from NOAA data and from the Global 30 Arc-Second Elevation Dataset (GTOPO30) of the USGS with idealized annual cycle but without interannual variations characterising constant land cover conditions representative for this time period (HAGEMANN et al., 1999). For 2001-2050 the IPCC SRES A1b and B1 emission scenarios (NAKICENOVIC and SWART, 2000) are considered consistent to ECHAM5/MPI-OM. Corresponding transient scenarios of high-resolution land cover change are derived from a stochastic land use change model (PAETH et al., 2009) following estimates on future population growth and urbanization by the United Nations (UN) and projected deforestation and desertification rates by the Food and Agriculture Organization (FAO) over the African part of the model domain. The land use change model is applied to a $1 \times 1 \text{ km}^2$ land cover classification of the USGS GLCC (Global Land Cover Characterization) and results in a plausible scattered pattern of tropical African land degradation which is transformed to REMO land surface parameters on 0.5° resolution. Maximum changes in forest and vegetation cover in 2000-2050 due to deforestation and desertification processes are found over the western and central tropical Africa and over the southern Sahel, respectively. But hardly any changes can be stated in the Mediterranean area except over the Atlas mountains and the Nile river. B1 changes are slightly lower than A1b results due to higher efficiency and less expansion in agriculture. However, no completely interactive vegetation feedbacks on future climate changes are applied (PAETH et al., 2009). Nevertheless, the prevailing scenarios feature a rather complex set-up of future boundary conditions covering both radiative heating and land cover change. For the 20th-century simulation and each future scenario three ensemble members following different initial conditions have been performed corresponding to the three considered ECHAM5/MPI-OM ensemble members in order to capture the uncertainty of unknown initial conditions

(PAETH et al., 2009).

In this study, the Mediterranean section of REMO is selected as the region extending from 20° W to 45° E and 25° N to 44° N (181 x 119 grid boxes) identified by the blue frame in Fig. 2.1. The selected Mediterranean sections for the other climate datasets are described in section 3.1. The Mediterranean area of investigation is located near the northern border of the REMO model domain because the REMO simulations are centred over Africa which might probably cause lateral boundary effects such as artificial rainfall. Therefore, two grid point rows are removed from the northern rim to avoid such artificial boundary effects. REMO version 5.7 temperature and precipitation data on 0.5° resolution are applied for the investigation of Mediterranean means and extremes in present-day and future time periods and horizontal wind data for the orographic term of the weather generator.

For general validation of the prevailing REMO model with observations in the present-day time period usually simulations driven by reanalysis data are applied containing all observed boundary forcings necessary for reproducing observed climate variability. Thus, one single 25-year simulation of REMO version 5.0 is further derived (PAETH et al., 2005) which is forced by realistic lower oceanic and lateral atmospheric boundary conditions from the global ECMWF ERA15 reanalyses for the time period 1979-1993 (GIBSON et al., 1997) and corresponding ECMWF analyses for 1994-2003. But a slight warm bias of the prescribed ERA15 sea surface temperatures over the tropical Atlantic and Indian Oceans has been systematically corrected (PAETH et al., 2005). When performing these RCM simulations the longer-term ERA40 reanalysis dataset was not yet provided by ECMWF (PAETH, 2005). The slightly older REMO version 5.0 is generally equal to version 5.7 applied above except for the lack of a fractional land-sea mask and some improvements in the land surface scheme (PAETH et al., 2009). Validation studies reveal that this REMO 5.0 simulation generally reproduces the main characteristics of observed means and large-scale circulation including observed trends and interannual variability over tropical West Africa (PAETH et al., 2005) as well as over the Mediterranean region (PAETH and HENSE, 2005). But REMO systematically underestimates Sub-saharan precipitation due to coarse resolution of Guinean Coast orography (PAETH et al., 2005) and is not able to simulate small-scale rainfall processes (PAETH and HENSE, 2005) like convective-orographic summer storms, sea breezes or back-door cold fronts, i.e. easterly advections from the Mediterranean Sea, which are essential for western Mediterranean precipitation (MILLÁN et al., 2005a,b). In this study, the temperature and precipitation data of the ERA15 forced REMO 5.0 simulation on 0.5° resolution are applied for general model validation and for comparison to

corresponding values of the REMO 5.7 simulations driven by ECHAM5/MPI-OM. In all following chapters, the coupled model simulations of ECHAM5/MPI-OM are called ECHAM5 simulations.

3 Statistical methods

This chapter presents the statistical methods applied in this study for the investigation of the temperature and precipitation means and extremes in the Mediterranean area in present-day and future time periods. All presented methods are basic analysis tools of statistical climatology extensively described in several established statistical textbooks (SACHS, 1997; BAHRENBERG et al., 1999; VON STORCH and ZWIERS, 1999; COLES, 2001; SCHÖNWIESE, 2006; WILKS, 2006; RINNE, 2008; BORTZ and SCHUSTER, 2010). Thus, the following sections describe the analyses of climatological means and trends and one-way and two-way analyses of variance to evaluate the signal-to-noise ratios of the trends. The principal component analysis and multiple regression analysis are used for determining the impacts of mid-latitude circulation on Mediterranean temperature and precipitation. Finally, quantile-based extreme indices, extreme value distributions and the weather generator present appropriate tools for the analysis of extreme events. Every section first explains the main procedure and basic features of the statistical method under consideration and then describes the exact form or modification in which this method is applied in the prevailing study.

3.1 Analysis of climatological means

The following specifications on selected time periods and on the spatial extent of the Mediterranean region under consideration are valid for all following investigations. First, the choice of the time periods is limited by the REMO simulation period of 1960-2050. Thus, the climate normal periods 1961-1990 and 2021-2050 at the beginning and end of the REMO period are chosen as present-day time period for validation of model simulations and as future time period for investigating future climate change, respectively. The long-term period 1961-2050 is selected for long-term analysis of trends and variance allowing the simulated GHG signal to emerge from interdecadal variability. Furthermore, the Mediterranean section is set to the region extending from 20° W to 45° E and 25° N to 44° N for the E-OBS, CRU and REMO datasets on 0.5° resolution (181 x 119 grid boxes) according to the limited

model domain of REMO (cf. subsection 2.2.2, Fig. 2.1). As the original CRU and E-OBS 0.5° geographical grids are shifted by 0.25° in both zonal and meridional directions compared to the REMO model grid both observational grids are linearly interpolated to the REMO grid for reasons of comparability, i.e. one new CRU or E-OBS grid box is derived from those four old grid boxes not featuring missing values. The corresponding Mediterranean section of ECHAM5 on 1.875° resolution is defined by 20.625° W to 45° E and 25.18° N to 45.7° N (36 x 12 grid boxes). Furthermore, only Mediterranean land areas are investigated but no grid boxes over the Atlantic Ocean or Mediterranean Sea because both observational datasets for validation are only available over land masses and REMO is forced by simulated sea surface temperatures from ECHAM5 not including feedbacks to the global model over the oceans, i.e. no added values from dynamical downscaling can be expected except for improved resolution.

First, 6-hourly REMO and ECHAM5 model output is aggregated to reach daily temperature means and rainfall sums. From monthly CRU, daily E-OBS, REMO and ECHAM5 data seasonal temperature means and precipitation sums of spring (March-April-May MAM), summer (June-July-August JJA), autumn (September-October-November SON) and winter (December-January-February DJF) are calculated applying December values from corresponding previous years. Furthermore, seasonal climatological means of these temperature means and rainfall sums are computed over the present-day time period 1961-1990 for all models and observations in order to allow the validation of simulated with observed climatological means and the investigation of dynamical downscaling from ECHAM5 to REMO. For both models, the ensemble means of three ensemble members are regarded in order to capture the uncertainty of unknown initial conditions. The new daily E-OBS dataset is generally preferred for representing observations in this study but for the validation of seasonal means and trends also the popular monthly CRU observations are applied offering additional information on northern Africa and the Middle East and allowing for some measure of uncertainty for observed results. Due to time lacks in E-OBS observational data only those grid boxes are considered which fulfil the following standards for completeness of observational time series slightly modified from MOBERG and JONES (2005): A complete month contains two missing days maximally, a complete season contains no missing months, and a complete time series no missing seasons in the given time period. Following these rules several E-OBS grid boxes over northern Africa, Near East and Turkey are deleted in different seasons. For those grid boxes with missing values fulfilling these standards the seasonal precipitation sums are calculated from all days with rainfall data and

extrapolated to all days of the whole time period.

The following two statistical tests investigate if two samples of sample size n originate from the same population concerning sample means \bar{x}_1 and \bar{x}_2 and variances s_1^2 and s_2^2 . The preconditions are normal distributed samples for both tests (see section 3.2 for corresponding test) and no significantly different sample variances for the sample mean test. The two null hypotheses $H_0 : s_1^2 = s_2^2$, i.e. sample variances originate from same population, and $H_0 : \bar{x}_1 = \bar{x}_2$, i.e. sample means originate from same population, are tested on a significance level of 5%. The test statistic for variances is defined by $\hat{F} = s_1^2/s_2^2$ or vice versa if $s_1 < s_2$ and F-distributed with $(n-1, n-1)$ degrees of freedom. The test statistic for sample means \hat{t} is tested via two sided t-test with $(2n-2)$ degrees of freedom and determined by (SCHÖNWIESE, 2006):

$$\hat{t} = \frac{|\bar{x}_1 - \bar{x}_2|\sqrt{n}}{\sqrt{s_1^2 + s_2^2}} \quad (3.1)$$

In this study, the mentioned statistical tests are applied separately per grid box and season for the validation of Mediterranean temperature and precipitation from REMO ensemble mean with E-OBS data in the present-day time period 1961-1990 in order to test if the corresponding sample means and variances originate from the same population. Furthermore, the sample mean t-test is applied to check the significance of future change of consecutive dry days and quantile-based precipitation extreme indices from REMO and ECHAM5 in 2021-2050 compared to 1961-1990. The author is aware that the precipitation extreme data are mostly not normally distributed but the t-test is not very sensitive towards the violation of this precondition (VON STORCH and ZWIERS, 1999). Due to possible uncertainties arising from this fact the t-test is regarded as indicator, but not as distinct measure, for the significance of future changes in rainfall extremes and the interpretation of significance is performed with caution.

3.2 Trend analysis

The simple linear regression analysis describes the linear relationship between an independent predictor variable X and a dependent predictand variable Y . In this study, linear regression is applied for analysing present-day and long-term trends of temperature and precipitation time series in the Mediterranean area. The relationship between the realisations x_i and y_i of the random variables X and Y for $i=1, n$ time steps is determined by the linear statistical model (VON STORCH and ZWIERS,

1999; SCHÖNWIESE, 2006; WILKS, 2006):

$$y_i = a_0 + a_1 \cdot x_i + \epsilon_i \quad (3.2)$$

The regression coefficients a_0 and a_1 describe the intercept and slope parameter of the straight linear regression line between X and Y, respectively. The residuals ϵ_i determine stochastic errors of zero mean or impacts of further predictors which are not explained by the linear regression. The major preconditions of linear regression are normal distribution of original data samples and normal distribution and independence, i.e. absence of autocorrelation, of residuals which are proved by two statistical tests described further below. The regression coefficients \hat{a}_0 and \hat{a}_1 are estimated from the given data samples in determining the optimal regression line with minimal vertical distance to all sample data points by least square fit, i.e. minimising the sum of squared errors of linear regression defined by (VON STORCH and ZWIERS, 1999; SCHÖNWIESE, 2006; WILKS, 2006):

$$SS\varepsilon = \sum_{i=1}^n (y_i - \hat{a}_0 - \hat{a}_1 \cdot x_i)^2 \quad (3.3)$$

The minimisation of $SS\varepsilon$ is performed by computing the roots of the partial derivatives of $SS\varepsilon$ with respect to \hat{a}_0 and \hat{a}_1 . The solution of the resulting two normal equations reveals that the estimated slope parameter \hat{a}_1 equals the covariance of X and Y normed by the variance of X (VON STORCH and ZWIERS, 1999; WILKS, 2006):

$$\hat{a}_1 = \frac{\sum_{i=1}^n (x_i - \bar{x})(y_i - \bar{y})}{\sum_{i=1}^n (x_i - \bar{x})^2} \quad (3.4)$$

The corresponding regression intercept \hat{a}_0 is estimated by $\hat{a}_0 = \bar{y} - \hat{a}_1 \cdot \bar{x}$. The total sum of squares $SST = \sum_{i=1}^n (y_i - \bar{y})^2$ of the variable Y can be separated into the sum of squares due to regression $SSR = \sum_{i=1}^n (\hat{a}_0 + \hat{a}_1 x_i - \bar{y})^2$, i.e. the variability explained by the linear regression line, and into the sum of squared errors $SS\varepsilon$, i.e. the deviations from that line. Thus, the coefficient of determination $R^2 = SSR/SST$ determines the proportion of total variability of Y accounted for by linear regression with X and can be computed from multiplying the squared slope parameter \hat{a}_1 with the variance of X normed by the variance of Y. Furthermore, R^2 equals the square of the linear Pearson product-moment correlation coefficient r between X and Y, i.e. the covariance of X and Y normed by the single standard deviations of X and Y, which describes the strength and direction of the relationship between X and Y (VON STORCH and ZWIERS, 1999; SCHÖNWIESE, 2006; WILKS, 2006).

The significance of the slope parameter of linear regression is checked in testing

the null hypothesis $H_0 : a_1 = 0$ via t-test. The test statistic \hat{t} with $(n-2)$ degrees of freedom relates the estimated slope parameter \hat{a}_1 to the corresponding standard error applying the variances of X and Y slightly modified to VON STORCH and ZWIERS (1999) and WILKS (2006):

$$\hat{t} = \frac{\hat{a}_1}{\sqrt{\frac{\text{var}(Y) - \hat{a}_1^2 \cdot \text{var}(X)}{\text{var}(X) \cdot (n - 2)}}} \quad (3.5)$$

In this study, seasonal trends of Mediterranean temperature and precipitation over the present-day time period 1961-1990 are computed for E-OBS, CRU, REMO and ECHAM5 for reasons of present-day validation and analysis of dynamical downscaling similar to the climatological means. Thereby, the ensemble means of REMO and ECHAM5 are analysed in order to capture the uncertainty given by differing initial conditions of different ensemble members. Furthermore, long-term trends are constructed for A1b and B1 emission scenarios of REMO and ECHAM5 during the long-term period 1961-2050, i.e. the whole simulation time of REMO, representing a period probably long enough to allow the impacts of the GHG effect to emerge from background interdecadal variability. For present-day and long-term trends, significance is tested two-tailed at a significance level of 5% and the temperature and precipitation changes displayed in all plots of this study result from multiplying the estimated slope parameters of linear regression, i.e. the changes per time unit, by the number of years of the considered time period. In the following, two statistical tests for proving the preconditions of linear regression analysis are presented.

The Kolmogorov-Smirnov goodness of fit test is performed to test if a given data sample originates from a certain theoretical distribution, e.g. if the original data sample and trend residuals of linear regression are normally distributed. This popular test is independent of certain distributions, requires only little computing time and is also appropriate for smaller data samples. But the test statistic is derived from one single maximum value only which might be a disadvantage considering the problem of outliers. The parameters of the theoretical distribution function $F_0(x)$ are determined from the data sample, e.g. sample mean and standard deviation for the normal distribution, resulting in a rather conservative test. If the sample standard deviation equals zero the corresponding test result is declared as missing value. The empirical distribution function $F_n(x)$ of the ordered data sample x_i for $i = 1, 2, \dots, n$ with sample size n is defined by i/n for $x_i \leq x < x_{i+1}$ for $i = 1, 2, \dots, n - 1$. Furthermore, $F_n(x) = 0$ is valid for $x < x_1$ and $F_n(x) = 1$ for $x \geq x_n$. The null hypothesis $H_0 : F_n(x) = F_0(x)$, i.e. the empirical sample fits

the theoretical distribution, is tested with the test statistic D_n and rejected if D_n exceeds the corresponding critical values from literature for a given significance level (SACHS, 1997; VON STORCH and ZWIERS, 1999; SCHÖNWIESE, 2006; RINNE, 2008):

$$D_n = \sup_x (|F_n(x) - F_0(x)|) \approx \max_{1 \leq i \leq n} (|F_n(x_i) - F_0(x_i)|; |F_n(x_{i-1}) - F_0(x_i)|) \quad (3.6)$$

In this study, the Kolmogorov-Smirnov test is applied at a significance level of 5% to test if the precondition of linear regression for trend analysis is fulfilled and both sample data and trend residuals are normally distributed. Furthermore, the test is performed for every GPD fit in extreme value analysis (see section 3.7) to investigate if the fitted theoretical GPD function matches the empirical distribution function of the original data sample.

The second major precondition for linear regression analysis is independence within the trend residuals, i.e. the absence of autocorrelation. Autocorrelation describes stochastic dependences within time series, i.e. endogenous interactions causing similar relationships between temporally neighbouring values over time, which disrupt the performance of statistical methods and induce misinterpretations. The precondition for analysing autocorrelation within a time series is stationarity, i.e. temporal homogeneity of mean and variance. Thus, the linear trend of the given time series has to be removed for this investigation. The stochastic dependence per step size k within a time series of sample size n describes the relationship between the original variable $X[k] = x(t_1), x(t_2), \dots, x(t_{n-k})$ and the variable $X(k) = x(t_{1+k}), x(t_{2+k}), \dots, x(t_n)$ shifted by k . Thus, the sample size n decreases to $n-k$ for analysis of autocorrelation and further decreases for increasing step size k . The kind and strength of this stochastic dependence can be determined by normalizing the covariance per step size k between these variables $X[k]$ and $X(k)$ by the variance of X . This normalized covariance determines the autocorrelation function $\rho(k)$ per step size k . Usually stationarity of the given time series is not completely fulfilled and the autocorrelation function is estimated analogous to the correlation coefficient of Pearson by (BAHRENBERG et al., 1999; SCHÖNWIESE, 2006):

$$r^*(k) = \frac{\text{cov}(X[k], X(k))}{\sqrt{\text{var}(X[k]) \cdot \text{var}(X(k))}} \quad (3.7)$$

The autocorrelation function lies between -1 and 1 denoting alternating and concordant stochastic dependences and equals 1 for $k=0$ due to correlation of two identical time series. The significance of the autocorrelation function is estimated per step size k by testing the null hypothesis $H_0 : \rho(k) = 0$, i.e. no autocorrelation pre-

vails. The test statistic $g(k) = |r^*(k)/\sigma_{r^*(k)}|$ is approximatively standard normally distributed with the standard error $\sigma_{r^*(k)}$ estimated by (BAHRENBERG et al., 1999; SCHÖNWIESE, 2006):

$$s_{r^*(k)} = \frac{\sqrt{1 + 2 \cdot \sum_{j=1}^{k-1} r^*(j)^2}}{\sqrt{n}} \quad (3.8)$$

For $k=1$ the sum within this equation is defined as zero. Often the autocorrelation function decreases with increasing step size k . The length of the temporal memory of a time series is defined by the maximum step size with consecutively significant values of the autocorrelation function $\rho(k)$. In order to maintain large data samples the analysis of the autocorrelation function is calculated for maximum step sizes of $n/4$ only (BAHRENBERG et al., 1999; SCHÖNWIESE, 2006). The maximum step size for a two-tailed test at a significance level of 10% is used to test the independence of the trend residuals in trend analysis as precondition for linear regression and is furthermore applied to reduce the number of degrees of freedom in significance testing for the one-way and two-way analyses of variance due to stochastic dependence in the given data sample (see section 3.3).

3.3 Analysis of variance

The univariate analysis of variance investigates if the different categories of a discrete independent variable X impact significantly on the variance of a continuous dependant variable Y similar to linear regression analysis regarding linear relationships between two continuous variables (BAHRENBERG et al., 1999; VON STORCH and ZWIERS, 1999; SCHÖNWIESE, 2006; BORTZ and SCHUSTER, 2010). Concerning the one-way analysis of variance, the values of the dependant variable y_{ij} of reference unit $i = 1, \dots, n_i$ and category $j = 1, \dots, n_j$ can be represented by the linear statistical model of VON STORCH and ZWIERS (1999):

$$y_{ij} = \mu_j + \epsilon_{ij} = \mu + \beta_j + \epsilon_{ij} \quad (3.9)$$

Thereby, the fixed effects model is chosen which includes the reproducible impacts of fixed treatment effects, i.e. all categories are known and no random effects occur. μ and μ_j present the total mean of Y and the mean of all values of Y belonging to category j , respectively. Both means can be estimated by the corresponding arithmetic sample means \bar{y} and \bar{y}_j . The so-called treatment effect of X on Y determined by $\beta_j = \mu_j - \mu$ represents the systematic variance between the categories and ϵ_{ij} the residual random variance within the categories which is independent of

X (BAHRENBERG et al., 1999; VON STORCH and ZWIERS, 1999). In climatology, the one-way analysis of variance often investigates the signal-to-noise ratio of an external boundary forcing, e.g. increasing CO_2 concentrations, of a climatic variable y_{ij} , e.g. temperature or precipitation, over different time steps j in context of the internal variability of different ensemble runs i with varying initial conditions (VON STORCH and ZWIERS, 1999; PAETH and HENSE, 2002).

For this purpose, the total variance of Y , i.e. the sum of squared deviations SS_t between y_{ij} and \bar{y} , is partitioned into the sum of squares of the treatment effect SS_β and the residual variance SS_ϵ with $SS_t = SS_\beta + SS_\epsilon$ (BAHRENBERG et al., 1999; VON STORCH and ZWIERS, 1999):

$$SS_\beta = \sum_{i=1}^{n_i} \sum_{j=1}^{n_j} (\bar{y}_j - \bar{y})^2 \quad (3.10)$$

$$SS_\epsilon = \sum_{i=1}^{n_i} \sum_{j=1}^{n_j} (y_{ij} - \bar{y}_j)^2 \quad (3.11)$$

Since the simple coefficient of determination SS_β/SS_t is very optimistic in determining the proportion of total variance of the variable Y explained by the treatment effect an adjusted version \hat{R}^2 [%] from VON STORCH and ZWIERS (1999) is applied which is less optimistic because the internal variability included in SS_β is removed. If sampling variability induces \hat{R}^2 values smaller than zero or larger than one, \hat{R}^2 is set to zero or one, respectively (BAHRENBERG et al., 1999; VON STORCH and ZWIERS, 1999). The variance explained by the treatment effect is determined using $n = n_i \cdot n_j$:

$$\hat{R}^2 = \frac{SS_\beta - SS_\epsilon \cdot (n_j - 1)/(n - n_j)}{SS_t} \quad (3.12)$$

The residual variance due to internal variability is derived from removing the variance accounted for by the treatment effect from total variance. The significance of the treatment effect is analysed in testing the null hypothesis $H_0: \beta_1 = \dots = \beta_{n_j} = 0$, i.e. X and Y are independent, via F-test. The test statistic \hat{F} with $(n_j - 1, n - n_j)$ degrees of freedom compares treatment effect and residual variance (BAHRENBERG et al., 1999; VON STORCH and ZWIERS, 1999):

$$\hat{F} = \frac{SS_\beta/(n_j - 1)}{SS_\epsilon/(n - n_j)} \quad (3.13)$$

The two-way analysis of variance extends the previous approach in order to estimate the impact of two discrete independent variables on a continuous dependant

variable Y (BAHRENBERG et al., 1999; VON STORCH and ZWIERS, 1999; SCHÖN-
WIESE, 2006; BORTZ and SCHUSTER, 2010). In climatology, this extended approach
often analyses the impacts of both external forcing over different time steps and
model physics of different climate models and derives a signal-to-noise ratio of a
common climate change signal across all models against systematic model differences
and internal model variability (PAETH and HENSE, 2002; PAETH and POLLINGER,
2010). In this study only one RCM and one GCM are analysed. Thus, the two-way
analysis of variance is applied to the impacts of different time steps and emission
scenarios of one model. The following linear fixed effects model of VON STORCH
and ZWIERS (1999) explains the values of the dependent variable y_{ijk} of the two
categories $i = 1, \dots, n_i$ (emission scenarios) and $j = 1, \dots, n_j$ (time steps) and the
reference unit $k = 1, \dots, n_k$ (ensemble runs):

$$y_{ijk} = \mu + \alpha_i + \beta_j + \gamma_{ij} + \epsilon_{ijk} \quad (3.14)$$

μ identifies the total mean of Y , $\alpha_i = \mu_i - \mu$ the so-called block effect due to
different emission scenarios, $\beta_j = \mu_j - \mu$ the treatment effect due to different time
steps and $\gamma_{ij} = \mu_{ij} - \mu_i - \mu_j + \mu$ the interaction effect between block and treatment
effects, i.e. the time dependent impact of emission scenarios, which can include
slow processes internal to the climate system. The terminology originates from the
classical agricultural setting where different treatments, e.g. tillage operations, are
applied to different blocks of land, e.g. with varying fertility. μ_i , μ_j and μ_{ij} identify
the means of all values belonging to category i , category j and to both categories
 i and j and can be estimated by the arithmetic sample means \bar{y}_i , \bar{y}_j and \bar{y}_{ij} , like \bar{y}
serves as unbiased estimator for the total mean μ . ϵ_{ij} again represents the random
residual variance within the categories (BAHRENBERG et al., 1999; VON STORCH
and ZWIERS, 1999; BORTZ and SCHUSTER, 2010).

The decomposition of the sum of squares of the total variance $SS_t = SS_\alpha + SS_\beta +$
 $SS_\gamma + SS_\epsilon$ yields four independent components (VON STORCH and ZWIERS, 1999):

$$SS_\alpha = \sum_{i=1}^{n_i} \sum_{j=1}^{n_j} \sum_{k=1}^{n_k} (\bar{y}_i - \bar{y})^2 \quad (3.15)$$

$$SS_\beta = \sum_{i=1}^{n_i} \sum_{j=1}^{n_j} \sum_{k=1}^{n_k} (\bar{y}_j - \bar{y})^2 \quad (3.16)$$

$$SS_\gamma = \sum_{i=1}^{n_i} \sum_{j=1}^{n_j} \sum_{k=1}^{n_k} (\bar{y}_{ij} - \bar{y}_j - \bar{y}_i + \bar{y})^2 \quad (3.17)$$

$$SS_\epsilon = \sum_{i=1}^{n_i} \sum_{j=1}^{n_j} \sum_{k=1}^{n_k} (y_{ijk} - \bar{y}_{ij})^2 \quad (3.18)$$

The contributions \hat{R}_α^2 , \hat{R}_β^2 , \hat{R}_γ^2 and \hat{R}_ϵ^2 [%] to total variance of Y accounted for by the block, treatment and interaction effects and the residual variance, respectively, are again derived following the adjusted coefficients of determination (VON STORCH and ZWIERS, 1999; PAETH and POLLINGER, 2010) with $n = n_i \cdot n_j \cdot n_k$:

$$\hat{R}_\alpha^2 = \frac{SS_\alpha - SS_\epsilon \cdot (n_i - 1)/(n - n_i \cdot n_j)}{SS_t} \quad (3.19)$$

$$\hat{R}_\beta^2 = \frac{SS_\beta - SS_\epsilon \cdot (n_j - 1)/(n - n_i \cdot n_j)}{SS_t} \quad (3.20)$$

$$\hat{R}_\gamma^2 = \frac{SS_\gamma - SS_\epsilon \cdot (n_i - 1) \cdot (n_j - 1)/(n - n_i \cdot n_j)}{SS_t} \quad (3.21)$$

$$\hat{R}_\epsilon^2 = \frac{SS_\epsilon \cdot (n - 1)/(n - n_i \cdot n_j)}{SS_t} \quad (3.22)$$

The first three coefficients explain the variance between the different categories: \hat{R}_β^2 identifies the climate change signal due to external boundary forcing, i.e. the part of total variance accounted for by a common temporal trend over all runs and scenarios. \hat{R}_α^2 and \hat{R}_γ^2 describe the time-independent and time-dependant impacts of different emission scenarios, respectively. Instead, \hat{R}_ϵ^2 holds the internal variability within the categories due to single model simulations with different initial conditions (VON STORCH and ZWIERS, 1999; PAETH and HENSE, 2002; PAETH and POLLINGER, 2010).

The significance is checked separately for block, treatment and interaction effects. Three null hypotheses $H_0: \alpha_1 = \dots = \alpha_{n_i} = 0$, $H_0: \beta_1 = \dots = \beta_{n_j} = 0$ and $H_0: \gamma_{1,1} = \dots = \gamma_{n_i, n_j} = 0$ are tested via F-test using the test statistics \hat{F}_α , \hat{F}_β and \hat{F}_γ with $(n_i - 1, n - n_i \cdot n_j)$, $(n_j - 1, n - n_i \cdot n_j)$ and $(n_i \cdot n_j - n_i - n_j + 1, n - n_i \cdot n_j)$ degrees of freedom, respectively (BAHRENBERG et al., 1999; VON STORCH and ZWIERS, 1999):

$$\hat{F}_\alpha = \frac{SS_\alpha/(n_i - 1)}{SS_\epsilon/(n - n_i \cdot n_j)} \quad (3.23)$$

$$\hat{F}_\beta = \frac{SS_\beta/(n_j - 1)}{SS_\epsilon/(n - n_i \cdot n_j)} \quad (3.24)$$

$$\hat{F}_\gamma = \frac{SS_\gamma/(n_i \cdot n_j - n_i - n_j + 1)}{SS_\epsilon/(n - n_i \cdot n_j)} \quad (3.25)$$

In this study, the one-way analysis of variance is applied to the three ensemble members of both REMO and ECHAM5 to analyse the signal-to-noise ratio in the

temperature and precipitation simulations of the present-day time period 1961-1990 and the long-term period 1961-2050 for each A1b and B1 emission scenario separately. Significance is tested two-tailed at a significance level of 10%. Furthermore, the two-way analysis of variance is performed to find the common GHG signal of both emission scenarios and determine time dependent and independent differences in corresponding signals for 1961-2050. Finally, all these investigations are repeated for 10-year REMO running means, i.e. REMO ensemble member data is averaged over 10 years with the 10-year time window moving continuously through the data of reduced sample size, in order to increase the GHG signal on the interdecadal time scale by smoothing the noise of interannual variations. But the stochastic dependences within these running means reduce the amount of independent time samples and impact on significance tests, e.g. of the analysis of variance (BAHRENBURG et al., 1999). Thus, the autocorrelation function (see section 3.2) is calculated per season and grid box for the trend residuals of the REMO running means averaged over all runs and scenarios. The maximum step size M with significant values of the autocorrelation function is applied to reduce the number of degrees of freedom by multiplication with $1/(M+1)$ for the estimation of the critical F-test values but not for the calculation of the explained variances or test statistics (PAETH and POLLINGER, 2010). The average maximum step sizes over the Mediterranean area lie around 1-3 years with local maxima of 4-5 years for temperature and precipitation in the present-day time period and for both future scenarios.

3.4 Principal component analysis

The multivariate Principal Component Analysis (PCA), also called Empirical Orthogonal Function (EOF) Analysis, enables the reduction of a complex dataset containing a multitude of correlated climatic variables to a smaller subspace of combined variables describing groups of similar variations which cover the main essential variance. These new variables are stochastic independent and orthogonal to each other but physical interpretation is often limited due to variable combinations and the constraint of orthogonality. The PCA assumes that the total variance of the original data can be completely reproduced by a linear combination of all new variables, called principal components, and corresponding fixed weights, called eigenvectors (BAHRENBURG et al., 1999; VON STORCH and ZWIERS, 1999; SCHÖNWIESE, 2006; WILKS, 2006). Besides combining several variables of a dataset the PCA can also be applied to different spatial units of a single variable to generate large-scale spatial patterns of centres with particular variation denoted in the following as modes of

variation (JACOBET et al., 1998; VON STORCH and ZWIERS, 1999), like it is done in this study for sea level pressure.

Given a data matrix \mathbf{X} of a certain climatic field variable, e.g. sea level pressure, of dimension $(n \times m)$ with $j = 1, m$ spatial units over $i = 1, n$ reference units, i.e. time steps, the data anomaly matrix \mathbf{X}' is built in subtracting from x_{ij} the corresponding temporal means \bar{x}_j . The corresponding covariance matrix \mathbf{S} describes the covariability between all spatial units m . In order to identify the main large-scale modes of variation with highest variance, this study conducts the PCA on the covariance matrix \mathbf{S} which highlights different variances of different spatial units in contrast to the correlation matrix which contains equal weights for all spatial units (VON STORCH and ZWIERS, 1999; WILKS, 2006):

$$\mathbf{S}_{(m \times m)} = \frac{1}{n-1} \cdot \mathbf{X}'^T_{(m \times n)} \cdot \mathbf{X}'_{(n \times m)} \quad (3.26)$$

Following the eigenvalue problem $\mathbf{A} \cdot e = \lambda \cdot e$ the eigenvectors e of a quadratic and symmetric matrix \mathbf{A} with corresponding eigenvalues λ are orthogonal. In order to find orthogonal principal components from \mathbf{X}' the eigenvector matrix \mathbf{E} of m eigenvectors over m spatial units is determined from the quadratic and symmetric covariance matrix \mathbf{S} . The eigenvalue matrix $\mathbf{\Lambda}$ is a diagonal matrix holding the m eigenvalues corresponding to the m eigenvectors of \mathbf{E} (VON STORCH and ZWIERS, 1999; WILKS, 2006):

$$\mathbf{S}_{(m \times m)} = \mathbf{E}_{(m \times m)} \cdot \mathbf{\Lambda}_{(m \times m)} \cdot \mathbf{E}^T_{(m \times m)} \quad (3.27)$$

The extraction of such pairs of eigenvalues and eigenvectors can be done by mathematical algorithms, e.g. by solving a characteristic polynomial of degree m (VON STORCH and ZWIERS, 1999). In this study, the eigenvalue problem is technically solved by software implementations of the International Mathematics and Statistics Library (IMSL, ROGUE WAVE SOFTWARE (2011)). In the m -dimensional coordinate space the first eigenvector is oriented towards the direction of the maximum variance of the data anomaly matrix \mathbf{X}' . All following eigenvectors are directed orthogonally to it and to each other and form the rotated axes of a new cartesian coordinate system for \mathbf{X}' . The spatial elements of a certain eigenvector, called loadings, illustrate which spatial units contribute to the corresponding principal component thus, graphically displaying spatial \mathbf{X}' patterns of simultaneous variations (VON STORCH and ZWIERS, 1999; SCHÖNWIESE, 2006; WILKS, 2006).

The principal components are built by linear combinations of the original variables, i.e. the spatial units, aiming at explaining as much variance of the original data anomaly matrix \mathbf{X}' as possible. This is especially effective if high correlations

of original spatial units prevail. The matrix \mathbf{U} of m principal components over n time steps is determined by the projection of the data anomaly matrix \mathbf{X}' onto the m eigenvectors of matrix \mathbf{E} (VON STORCH and ZWIERS, 1999; WILKS, 2006):

$$\mathbf{U}_{(n \times m)} = \mathbf{X}'_{(n \times m)} \cdot \mathbf{E}_{(m \times m)} \quad (3.28)$$

The principal component elements of \mathbf{U} , called scores, form a time series identifying the common temporal evolution of all spatial units belonging to the pattern of simultaneous variation of the corresponding eigenvector. The principal components are sorted by the amount of variance of \mathbf{X}' which they explain with the first principal component holding the maximum. They are uncorrelated with each other and may serve as predictors for multiple regression analyses. The corresponding eigenvector loadings and eigenvalues contribute to the physical interpretation of principal components revealing information on spatial patterns and importance e.g. of atmospheric modes of variation. The eigenvalue matrix $\mathbf{\Lambda}$ above is the covariance matrix of the principal components and the eigenvalues identify the variance of the corresponding principal component. The total variance of \mathbf{X}' equals the sum of all eigenvalues λ_j of the independent principal components $j = 1, m$ and thus, the variance R_k^2 [%] of \mathbf{X}' accounted for by a certain principal component k is identified by (VON STORCH and ZWIERS, 1999; WILKS, 2006):

$$R_k^2 = \frac{\lambda_k}{\sum_{j=1}^m \lambda_j} \quad (3.29)$$

In this study, s-mode PCA is applied to seasonally averaged NCEP and ECHAM5 sea level pressure anomalies of 1961-1990 in order to compare observed and simulated large-scale mid-latitude circulation dynamics. The eigenvector loading maps and principal component (PC) time series of the leading ten PCs are used to represent the spatial structure and temporal evolution of the most important modes of variation. These PCs explain over 90% of total sea level pressure variance of NCEP and ECHAM5 in every season and are thus, considered to cover the essential part of circulation variability necessary for this study. The modes of variation of ECHAM5 are derived from ensemble mean values because they are related via multiple regression analysis (see section 3.5) to temperature and precipitation trends of REMO which are based on ensemble means in order to capture the corresponding uncertainty of different initial conditions (see section 3.2). For better comparison, the 1.875° ECHAM5 sea level pressure anomalies are interpolated to the 2.5° resolution of the NCEP reanalysis data by quadratic spline interpolation. In this interpola-

tion method, every new grid box value is calculated by quadratic polynomials using the nearest old grid box value and old grid box gradients in zonal, meridional and diagonal directions in direct vicinity of the new grid box. The quadratic spline interpolation produces good results for sea level pressure but tends to slightly overestimate extreme values. The geographical area considered for mid-latitude circulation extends from 70° W to 50° E and from 20° N to 70° N in order to include the impacts of North Atlantic circulation dynamics being essential for the Mediterranean region (cf. chapter 1). This area results from sensitivity tests with different area sizes of NCEP reanalysis data by showing highest accordance with teleconnection patterns from literature which are obtained from fields covering the whole northern hemisphere north of 20° N (BARNSTON and LIVEZEY, 1987; NOAA-CPC, 2010).

During PCA sea level pressure anomalies are weighted by the square root of cosine of latitude in order to consider different sizes of spatial units and if required eigenvector loading maps and PC time series of resulting PCs are inverted, i.e. multiplied by -1, to match the agreement on modes of variation from literature (BARNSTON and LIVEZEY, 1987; NOAA-CPC, 2010). Furthermore, different eigenvector scaling conventions are applied for PC time series and eigenvector loadings in the PC plots of the results chapter (see chapter 5): In PC time series plots the eigenvectors have unit length and the variance of each PC equals the corresponding eigenvalue. Instead, in the eigenvector loading plots the eigenvectors are rescaled by multiplication by $\sqrt{\lambda}$ reaching a clearer interpretation of the eigenvector loadings as direct relationships between original data and PCs (WILKS, 2006). In climate research resulting eigenvectors and PCs are often rotated, i.e. spatial and temporal patterns are changed and simplified, in order to ease physical interpretation but at the same time either orthogonality of eigenvectors or independence of PCs is lost (VON STORCH and ZWIERS, 1999; WILKS, 2006). But in this study, the standard unrotated PCA is applied because the unrotated winter NAO of NCEP in 1961-1990 indicates much higher accordance to temporal and spatial patterns of the winter NAO identified in literature (BARNSTON and LIVEZEY, 1987; NOAA-CPC, 2010) than the corresponding rotated NAO. The results of the PCA and multiple regression analysis (see following section) of this study for the present-day time period 1961-1990 are submitted for publication in the International Journal of Climatology (PAXIAN et al., 2011).

Finally, the same analysis is performed for the simulated data in the long-term period 1961-2050 applying A1b and B1 emission scenarios. But for better comparability of patterns the ECHAM5 sea level pressure data of 1961-2050 are projected onto the modes of variation of ECHAM5 data for 1961-1990, i.e. the projected PC

time series are built from ECHAM5 data of 1961-2050 weighted by the square root of cosine of latitude and ECHAM5 eigenvectors of 1961-1990 following equation 3.28. Thus, spatial eigenvector loadings and present-day temporal evolutions of projected PC time series are similar to the present-day modes of variation and future evolution of projected PC time series is added. But projected PC time series are not independent any more and explained variances can not be derived because no real PCA is performed.

3.5 Multiple regression

The multiple regression analysis investigates the influences of several independent predictors on a dependent climatic variable and is performed analogous to the simple linear regression analysis of section 3.2 (BAHRENBERG et al., 1999; VON STORCH and ZWIERS, 1999; WILKS, 2006). In this study, multiple regression is applied to find relationships between seasonal temperature or precipitation as predictand and seasonal large-scale mid-latitude modes of variation resulting from PCA as predictors (cf. PAXIAN et al. (2011)). A modified version of a cross-validated stepwise linear multiple regression model is applied which has been developed by PAETH and HENSE (2003) following VON STORCH and ZWIERS (1999) and further improved and evaluated for several low latitude regions by PAETH et al. (2006). The linear multiple regression model describes the relationship between a predictand time series \vec{y} of dimension n and k predictor time series x_1, \dots, x_k of dimension n building up the predictor matrix \mathbf{X} with units in the additional first column. Standardised time series are used in this study but trends are not removed. The $(k+1)$ -dimensional vector \vec{a} denotes the multiple regression intercept and the coefficients corresponding to the k predictors. The n -dimensional vector $\vec{\epsilon}$ determines the residual of \vec{y} which cannot be reconstructed by the selected predictors (VON STORCH and ZWIERS, 1999; PAETH and HENSE, 2003; PAETH et al., 2006):

$$y_i = a_0 + \sum_{l=1}^k a_l x_{li} + \epsilon_i \quad \text{for } i=1, n \text{ or } \vec{y} = \mathbf{X}\vec{a} + \vec{\epsilon}$$

$$\text{with } \vec{y} = \begin{pmatrix} y_1 \\ \vdots \\ y_n \end{pmatrix}; \mathbf{X} = \begin{pmatrix} 1 & x_{11} & \dots & x_{k1} \\ \vdots & \vdots & & \vdots \\ 1 & x_{1n} & \dots & x_{kn} \end{pmatrix}; \vec{a} = \begin{pmatrix} a_0 \\ \vdots \\ a_k \end{pmatrix} \quad \text{and} \quad \vec{\epsilon} = \begin{pmatrix} \epsilon_1 \\ \vdots \\ \epsilon_n \end{pmatrix} \quad (3.30)$$

The coefficients \vec{a} of the multiple regression model are found by least square fit in minimising the sum of squared errors $SS\epsilon$ which is determined by (VON STORCH

and ZWIERS, 1999):

$$SS\varepsilon = \vec{\varepsilon}^T \vec{\varepsilon} = (\vec{y} - \mathbf{X}\vec{a})^T (\vec{y} - \mathbf{X}\vec{a}) \quad (3.31)$$

This minimisation is done by determining the roots of the partial derivatives of $SS\varepsilon$ with respect to the $k+1$ coefficients a_l . The solutions of the resulting linear system of equations describe the estimated multiple regression coefficients $\hat{\vec{a}}$ (VON STORCH and ZWIERS, 1999):

$$\hat{\vec{a}} = (\mathbf{X}^T \mathbf{X})^{-1} \mathbf{X}^T \vec{y} \quad (3.32)$$

The coefficient of multiple determination R^2 denotes the variance of the predictand time series accounted for by the predictors of the multiple regression model. It is determined by the quotient of the sum of squares due to regression SSR and total variability SST using the identity matrix \mathbf{I} and the matrix \mathbf{U} with all values equalling $1/n$, both of dimension $(n \times n)$ (VON STORCH and ZWIERS, 1999; PAETH and HENSE, 2003):

$$R^2 = \frac{SSR}{SST} = \frac{\vec{y}^T [\mathbf{X}(\mathbf{X}^T \mathbf{X})^{-1} \mathbf{X}^T - \mathbf{U}] \vec{y}}{\vec{y}^T (\mathbf{I} - \mathbf{U}) \vec{y}} \quad (3.33)$$

The multiple regression analysis is performed as stepwise regression screening, i.e. predictors are added to the regression model step by step in order of their importance with respect to the predictand (VON STORCH and ZWIERS, 1999). In the first regression step the predictor matrix \mathbf{X} only consists of the first column with all entries equalling 1. Equation 3.32 determines the corresponding coefficient $a_0 = 1/n \sum_{i=1}^n y_i$, i.e. the multiple regression intercept equals the climatological mean of the predictand \vec{y} . In the second step the most influencing predictor \vec{x}_l is selected as that of all k predictors which holds the maximum coefficient of determination in linear correlation to the predictand \vec{y} . The multiple regression is performed with the predictor matrix \mathbf{X} holding the first column and that of the chosen predictor \vec{x}_l and the corresponding coefficients a_0 and a_1 are determined following equation 3.32. In all following steps the next most influencing predictor \vec{x}_l is chosen by linear correlation to the residual predictand time series $\vec{\varepsilon}$ resulting from all m predictors selected so far until all predictors \vec{x}_l have been selected for multiple regression, i.e. $m = k$ (BAHRENBERG et al., 1999; PAETH and HENSE, 2003; PAETH, 2005):

$$\epsilon_i = y_i - \hat{y}_i = y_i - (a_0 + \sum_{l=1}^m a_l x_{li}) \quad (3.34)$$

This partial correlation solves the problem of multicollinearity when strong corre-

lations between predictors complicate the distinct separation of single predictor influences. As a consequence of multicollinearity all previously determined coefficients a_l may change values with addition of a further predictor in each multiple regression step (BAHRENBURG et al., 1999; PAETH and HENSE, 2003; PAETH, 2005). Furthermore, in each step the variance accounted for by all chosen predictors is calculated allowing the estimation of the explained variance by every new predictor compared to the results of the previous step. Both regression coefficients and explained variances are mostly highest for the first predictors and decrease in size with further regression steps.

In order to avoid overfitting of the statistical model to the given sample the optimal predictor selection in multiple regression analysis is determined by cross validation (MICHAELSEN, 1987; VON STORCH and ZWIERS, 1999). Therefore, predictand and predictor time series are separated into a training dataset for multiple regression analysis and an independent control dataset of nb bootstrap elements for cross validation. After renorming both datasets to anomalies the stepwise multiple regression is performed for the training dataset and the corresponding mean-square error \widehat{MSE}_M between training data predictand y_j and estimated predictand from the regression model \hat{y}_j is built. Furthermore, the mean square error of the control data \widehat{MSE}_C is derived from the control data predictand y_j^B and the estimated predictand \hat{y}_j^B applying multiple regression coefficients of the training data to the control data. Both mean square errors are determined successively in each multiple regression step (VON STORCH and ZWIERS, 1999; PAETH and HENSE, 2003; PAETH et al., 2006):

$$\widehat{MSE}_M = \frac{1}{n - nb} \sum_{j=1}^{n-nb} (y_j - \hat{y}_j)^2 \quad (3.35)$$

$$\widehat{MSE}_C = \frac{1}{nb} \sum_{j=1}^{nb} (y_j^B - \hat{y}_j^B)^2 \quad (3.36)$$

Due to the least square fitting the forecast error of the regression model \widehat{MSE}_M steadily decreases with each additional predictor. The error measure \widehat{MSE}_C instead first decreases denoting physical meaning and reliability of the additional predictors and then at any time increases due to overfitting of the multiple regression model to the training dataset. Thus, the optimal number of predictors is determined by the first minimum of \widehat{MSE}_C and further predictor selection is stopped. But in any case at least one predictor is guaranteed for multiple regression. This stepwise multiple regression analysis with cross validation is repeated in a large number of

iterations with different random bootstraps in order to test the robustness of the relationships found between predictand and predictors (PAETH and HENSE, 2003; PAETH et al., 2006). Averaging the multiple regression results over all iterations reveals difficulties in finding the appropriate average sequence of chosen predictors partly strongly changing with different bootstrap years. Thus, after performance of all iterations, the final results are obtained by a final stepwise multiple regression analysis for the whole dataset without bootstrap selection considering only those predictors that have been identified by cross validation to be robust in at least 50% of all iterations. This robustness threshold only allows the most robust predictors to be correlated to the given predictand. In some cases, none of the given predictors fulfils this condition and the final multiple regression can not be performed (PAXIAN et al., 2011).

In this study, the described statistical model is used to determine the kind and strength of the impact of seasonal NCEP and ECHAM5 large-scale mid-latitude circulation variability on seasonal Mediterranean E-OBS and REMO temperature and precipitation trends in 1961-1990, respectively. The relationships between the predictand time series of temperature or precipitation and the predictor time series of several leading modes of variation are investigated for each Mediterranean grid box and season separately. Like already mentioned in the previous chapter (see section 3.4) the modes of variation of ECHAM5 are built from ensemble mean data adequately to the temperature and precipitation trends of REMO (see section 3.2). For cross validation, 1,000 iterations and six random bootstrap years are applied. For precipitation, only those grid boxes are considered which have more values greater than zero than the number of bootstrap years in order to avoid that after removal of all bootstrap years the resulting dataset contains exclusively zero values causing errors in multiple regression. This condition omits some E-OBS grid boxes over Egypt and the Near East in summer. After 1,000 iterations of multiple regression with cross validation the final stepwise linear multiple regression analysis over 1961-1990 without bootstraps implies the following information at each grid box: the number and sequence of selected predictors, the corresponding regression coefficients of the final multiple regression step, the robustness values as share of 1,000 iterations and the percentage of total temperature or precipitation variance that can be explained by each predictor and by the total of all predictors selected after 1,000 iterations of cross validation (PAXIAN et al., 2011).

In order to separate the impacts of mid-latitude circulation from those of residual influencing factors, e.g. GHGs, original REMO and E-OBS temperature and precipitation time series for 1961-1990 are split into circulation-related and circulation-

unrelated parts following the relationships found in multiple regression. The time series of the circulation-related part is derived by summing up the PC anomaly time series of all predictors selected in cross-validated linear multiple regression multiplied by the corresponding regression coefficients. To transform these anomalies of the circulation-related part back to the original data the time series of the circulation-related part is multiplied by the standard deviation of the original temperature or precipitation time series and the corresponding climatological mean is added. The time series of the circulation-unrelated part results from subtracting the circulation-related part from the original temperature or precipitation time series and adding the corresponding climatological mean. Finally, the seasonal trends of the time series of both circulation-related and circulation-unrelated parts are calculated and the same two-tailed significance test is applied as for the original time series (PAXIAN et al., 2011). The same investigation is performed for the long-term period 1961-2050 in order to analyse the future evolution of present-day modes of variation and their impacts on Mediterranean temperature and precipitation variability.

3.6 Quantile-based extreme indices

A first way to analyse very rare extreme events of a certain data sample is to determine the $q[\%]$ quantiles of the data distribution function which describe the threshold values that $q[\%]$ of the ordered sample fall below and thus, $1-q[\%]$ exceed (BAHRENBERG et al., 1999; SCHÖNWIESE, 2006). Given such an ordered sample x_1, \dots, x_n of size n with $x_1 \leq x_2 \leq \dots \leq x_n$ the $q[\%]$ quantile M_q is derived by an empirical approach of MOBERG et al. (2006) following BAHRENBERG et al. (1999) with k rounded down from $k = nq/100$:

$$M_q = \frac{(100 - q)x_k + qx_{k+1}}{100} \quad (3.37)$$

Extreme indices can be quantiles itself or quantile-based (MOBERG et al., 2006). This analysis of quantile-based extreme indices is part of a KLIWEX-MED cooperation comparing dynamical and statistical downscaling approaches for precipitation extreme events (see chapter 9, (HERTIG et al., 2012)). Thus, the focus is laid on quantile-based precipitation extreme indices in this chapter. A rather moderate quantile for extremes, i.e. the 95% quantile, is considered for the investigation of daily precipitation sums because the consequential larger quantity of extreme events allows accurate statistical analysis (HERTIG et al., 2012), especially considering the dry areas of the southern Mediterranean area.

In order to eliminate numerical noise in precipitation climate model output only rain days with rainfall sums larger than 0.1mm are analysed (MOBERG et al., 2006). But different climate conditions in present-day and future time slices might induce differing sample sizes of rain days causing different uncertainty levels and thus, complicating comparisons. Therefore, a fixed quantile threshold is defined for the present-day reference period. Both future and present-day extreme indices are based on this reference quantile counting days per season exceeding this threshold. The present-day and future time period are defined as 1961-1990 and 2021-2050 according to previous chapters. The reference quantile is derived per day applying a 5-day window including neighbouring values for the whole reference period, i.e. $5 \cdot 30 = 150$ values prevail for quantile calculation (MOBERG et al., 2006). In this study, two seasonal quantile-based precipitation extreme indices are chosen to investigate both frequency and intensity of precipitation extreme events: the number of days (R95N [days]) and mean daily rainfall amount of days exceeding the 95th quantile threshold (simple daily intensity index SDII95p [mm]). Furthermore, the whole rainfall amount from these extreme days exceeding the 95th quantile threshold (R95AM [mm]) and the share of this extreme rainfall amount in total rainfall amount (R95T [%]) are computed (MOBERG et al., 2006; HERTIG et al., 2012). Finally, for the investigation of Mediterranean dry periods the maximum number of consecutive dry days (CDD [days]) with rainfall amounts smaller than 1mm is regarded. Thereby, the threshold for rain days applied for CDD is larger than that for the quantile-based extreme indices (MOBERG et al., 2006).

If the same data of the reference period is used for both estimating the reference quantile and the threshold exceedances, the resulting quantile-based extreme index time series can suffer from artificial inhomogeneous breaks at the beginning and end of the reference period strongly distorting trend analysis. Such inhomogeneities can be avoided by applying a bootstrap resampling procedure following ZHANG et al. (2005) for the estimation of threshold exceedances in the reference period. This technique leaves out for the calculation of the reference quantile in each case the particular year for which threshold exceedances are counted and duplicates another one to reach the full number of reference period years. Every reference period year is duplicated once for quantile threshold calculation and all resulting quantile thresholds are averaged. Therefore, an individual reference quantile is obtained for every day of every reference period year. Counting exceedances of the future period over the reference threshold is performed without this bootstrap technique, i.e. applying data of the whole reference period for estimating the reference quantile (MOBERG et al., 2006).

Within the EMULATE (EU-funded project, <http://www.cru.uea.ac.uk/projects/emulate>) Work Package 4 a Fortran routine has been developed to compute quantile-based extreme indices following the method described above (MOBERG et al., 2006) which is used here with some modifications. In this study, the mentioned seasonal precipitation extremes are calculated for E-OBS, REMO and ECHAM5 in the present-day time period 1961-1990 and for the A1b and B1 emission scenarios of both models in the future time period 2021-2050. For the models, only the first ensemble member and not the ensemble mean is investigated to reach comparability with the statistical downscaling approach in the KLIWEX-MED cooperation performed with the first ECHAM5 ensemble member only. The reference period for the quantile-based extreme indices equals the present-day time period 1961-1990. Thus, for the estimation of threshold exceedances of the present-day time period the bootstrap technique of ZHANG et al. (2005) is applied but not for the exceedances of the future time period. The resulting seasonal CDD and precipitation extreme index time series are averaged over 1961-1990 and 2021-2050 and future changes are computed. The significance of future change is checked with a two tailed t-test at a significance level of 5%.

Several missing value criteria for the calculation of extreme indices and CDD are applied in this study accounting for the strong dryness of the Mediterranean area (cf. MOBERG et al. (2006); HERTIG et al. (2012)): If more than one missing value is prominent in daily input data per month, all corresponding extreme indices of that grid box and season are removed. For the quantile-based precipitation extreme indices, quantiles are not computed if less than two extremes are available for calculation. If a certain quantile of any day and year of the reference period with or without applying the bootstrap resampling procedure is defined as missing value, the quantile-based extreme indices of the corresponding grid box and season are removed for both present-day and future time periods. The threshold for quantile calculation is really small in order to gather information even on dry southern Mediterranean regions in summer but the corresponding high uncertainty is balanced by averaging the quantile thresholds over all years of the reference time period in bootstraps sampling and counting threshold exceedances over all days per season and averaging them over all years of the time period. This criterion deletes several grid boxes in Africa, Arabia and southern Europe in summer. For CDD, a grid box is removed in a certain season if no rain day prevails in that season over all years of the present-day time period deleting many E-OBS grid boxes over Egypt and Israel in summer. Finally, if the precipitation extreme value of a certain year is missing, the present-day mean and future change of the corresponding grid box and

season are defined as missing value.

3.7 Extreme value distributions

Another way to investigate extreme values is to fit a statistical distribution to the upper tail of the sample distribution (COLES, 2001; SMITH, 2003; WILKS, 2006). In contrast to the quantile approach the matching of a distribution function reduces the sampling errors (SCHÖNWIESE, 2006) and allows the extrapolation to higher quantiles lying outside the sample period. However, the resulting extreme values suffer from uncertainties in fitting the appropriate statistical distribution and corresponding parameters. Usually, the Normal distribution is not appropriate to match the upper tails of a sample distribution, especially of precipitation extremes (HOSKING, 1990). Several statistical distributions are applied to match daily climatological extremes depending on the choice of extreme events (COLES, 2001; SMITH, 2003; WILKS, 2006): Independent block maxima occurring once in a certain time period, e.g. year or season, are fitted by the Generalized Extreme Value (GEV) distribution. Instead, in the peaks-over-threshold approach all extremes exceeding a certain threshold regardless the time of occurrence are matched by the Generalized Pareto Distribution (GPD). Usually, this decision depends on what kind of extreme data are available.

According to the central limit theorem describing the normal distribution as approximation of the distribution of sample means the extremal types theorem justifies the GEV as limiting distribution of block maxima z_1, \dots, z_n (COLES, 2001) defined on $\{z : 1 + \xi(z - \mu)/\sigma > 0\}$ with $\sigma > 0$:

$$G(z) = \exp \left\{ - \left[1 + \xi \left(\frac{z - \mu}{\sigma} \right) \right]^{-1/\xi} \right\} \quad (3.38)$$

The distribution function contains a location parameter μ , a scale parameter σ and a shape parameter ξ and combines the three different types of extreme value distributions: the Gumbel ($\xi = 0$), Fréchet ($\xi > 0$) and Weibull ($\xi < 0$) distributions (COLES, 2001).

Using only block maxima for modelling extremes is a wasteful approach, and regarding the distribution of threshold excesses is more appropriate if time series of daily data are given (COLES, 2001). Given the independent measurements x_1, \dots, x_n the GPD function is the approximative distribution of excesses $y_i = x_i - u$ over a

large enough threshold u :

$$H(y) = 1 - \left(1 + \frac{ky}{\tilde{\alpha}}\right)^{-1/k} \quad (3.39)$$

The distribution is defined on $\{y : y > 0 \text{ and } (1 + ky/\tilde{\alpha}) > 0\}$ with $\tilde{\alpha} = \alpha + k(u - \zeta)$ (COLES, 2001). It is described by three specific parameters of location ζ , scale α and shape k indicating the mean, dispersion and skewness of the distribution, respectively (PAETH and HENSE, 2005), and equalling those of the associate GEV distribution. If $k > 0$, the GPD is called long-tailed without upper limit. If $k = 0$, the distribution shows an unbounded exponential developing. If $k < 0$, the GPD reaches a finite upper endpoint being called short-tailed (COLES, 2001; SMITH, 2003).

The choice of the threshold is difficult enhancing either bias or variance. If chosen too high, too little data exceeding the threshold remains for reliable parameter estimation causing high variance. If chosen too low, the exceedance data violates the asymptotic motivation of the GPD provoking high bias. Standard methods, e.g. the mean residual life plot, search the lowest threshold possible for an appropriate model fitting (COLES, 2001; SMITH, 2003). PAETH and HENSE (2005) compare several 85%-95% quantile thresholds and find the resulting location and shape parameters to increase with higher thresholds causing higher values and weaker slope of the cumulative GPD. Similar problems are prevailing for the choice of the block size for block maxima (COLES, 2001).

Several methods are applied to estimate the GPD parameters from a given data sample: graphical, moment-based and likelihood-based techniques (COLES, 2001; SMITH, 2003; WILKS, 2006). Here, the author uses the method of L-moments (HOSKING, 1990) based on the linear combination of order statistics because they describe a wide number of statistical distributions, yield less bias when estimated from small data samples and show higher robustness concerning outliers. The L-moments can be interpreted as location, scale, skewness and kurtosis of a statistical distribution similar to the central moments. Their estimators are determined from an ordered data sample (x_1, \dots, x_N) with $x_1 < x_2 < \dots < x_N$ (PAETH and HENSE, 2005):

$$\hat{\lambda}_1 = \frac{1}{N} \sum_i x_i \quad (3.40)$$

$$\hat{\lambda}_2 = \frac{1}{2} \binom{N}{2}^{-1} \sum_{i>j} \sum_j (x_i - x_j) \quad (3.41)$$

$$\hat{\lambda}_3 = \frac{1}{3} \binom{N}{3}^{-1} \sum_{i>j} \sum_{j>k} \sum_k (x_i - 2x_j + x_k) \quad (3.42)$$

$$\hat{\lambda}_4 = \frac{1}{4} \binom{N}{4}^{-1} \sum_{i>j} \sum_{j>k} \sum_{k>l} \sum_l (x_i - 3x_j + 3x_k - x_l) \quad (3.43)$$

The estimators for the three GPD parameters of location $\hat{\zeta}$, scale $\hat{\alpha}$ and shape \hat{k} are derived from the L-moments above and the Euler's constant γ (PAETH and HENSE, 2005):

$$\hat{k} = \frac{\hat{\lambda}_1}{\hat{\lambda}_2} - 2 \quad (3.44)$$

$$\hat{\alpha} = (1 + \hat{k})\hat{\lambda}_1 \quad (3.45)$$

$$\hat{\zeta} = \hat{\lambda}_1 + \hat{\alpha}\gamma \quad (3.46)$$

After having fit the theoretical GPD function to the given sample data the return values R_T of daily extremes at return times T are determined as $(1 - \frac{1}{T})$ quantiles of the cumulative GPD function from the estimators of the GPD parameters (PAETH and HENSE, 2005):

$$R_T = \hat{\zeta} + \hat{\alpha} \frac{1 - (1 - (1 - \frac{1}{T}))^{\hat{k}}}{\hat{k}} \quad (3.47)$$

If T is given in years, the corresponding R_T are called T -year return values, i.e. they are exceeded at an average once every T years. If more than one data point per year prevails, the return time T has to be multiplied by the average number of data points exceeding the threshold u per year, e.g. the quantile for a 10-year return value with 10 data points exceeding u per year is $\frac{1}{100}$.

However, uncertainties in matching GPD parameters to small data samples involve big shortcomings in the resulting return value estimates, especially concerning high quantile extremes. These return value uncertainties are assessed by a parametric bootstrap sampling approach (KHARIN and ZWIERS, 2000; PARK et al., 2001; PAETH and HENSE, 2005) which derives M new data samples of the same size N than in the original GPD fit randomly chosen from the GPD quantile function matched to the original sample and estimates the corresponding return value for each new sample following the equations above. With the resulting return value estimates being asymptotically normal distributed (PARK et al., 2001) the corresponding standard deviation of all bootstrap samples serves as standard error of the final return value. Furthermore, this standard error can be used to evaluate the significance of future climate change. Significance at the 1% level is found if the 90% return value confidence intervals of a present-day and a future time period do not overlap (KHARIN and ZWIERS, 2000; PAETH and HENSE, 2005).

PAETH and HENSE (2005) determine the GPD standard error of the return value

for every quantile threshold from 85%-95% and choose as final return value the result of that quantile threshold with minimum standard error. They find that the bootstrap sampling seems to yield higher impact on return value estimates than the choice of the quantile threshold. Some sensitivity tests following this approach do not yield any clear physical pattern of quantile thresholds with lowest standard errors over the Mediterranean area in all seasons and for both temperature and precipitation. In order to capture both uncertainties of small data samples and quantile threshold choice in this study the final return value and standard error are defined as mean and standard deviation of the return values of all quantile thresholds and bootstraps. The corresponding GPD parameters are averaged over all quantile thresholds and bootstraps as well.

In this study, the GPD fit is performed for daily temperature and precipitation of REMO and ECHAM5 for the present-day and future time periods 1961-1990 and 2021-2050 for each season and model run separately and the GPD results are averaged over all runs to yield the ensemble mean results. The E-OBS dataset is matched only for 1961-1990. In contrast to the previous chapter, the GPD analysis is performed separately for present-day and future time periods and different sample sizes may cause different uncertainty levels of GPD estimates. But these uncertainty levels are quantified for each time period by the parametric bootstrap sampling and considered in comparison. The return values, standard errors and GPD parameters for different return times are estimated like mentioned above over the 11 quantile thresholds 85%-95% and 100 parametric bootstraps. The relative uncertainties of return values are described by variation coefficients which norm the GPD standard errors by the magnitudes of the return values compared to the corresponding seasonal climatological temperature means or precipitation sums related to one day. The corresponding return times are chosen to be 5, 10, 15, 20, 25 and 30 years. Return values of smaller return times, e.g. one year, cannot be calculated because in several Mediterranean grid boxes the average number of extreme days per year exceeding the given quantile thresholds is smaller than one. Higher return values exceed the given time period length and cause large variation coefficients, especially for precipitation over the southern Mediterranean in summer. Every single GPD fit is only performed with at least six extreme days exceeding the quantile threshold over all years. This sample size threshold is quite small and might cause uncertain GPD fits. But this study aims at analysing temperature and precipitation extremes in the Mediterranean area which features partly very few rain days, especially over the southern and eastern Mediterranean in summer. Thus, the author decided to perform GPD fits also for small data samples in order to cover larger regions of the

Mediterranean area but to further estimate the corresponding GPD uncertainty via parametric bootstrap sampling instead of removing such grid boxes.

Two methods of validating the resulting GPD return values with empirical data are applied: First, a Kolmogorov-Smirnov test (see section 3.2) is performed for every GPD fit at a significance level of 10% to test if the fitted theoretical cumulative GPD function matches the empirical distribution function of the original data sample. The final Kolmogorov-Smirnov test result per grid box, season and time period is negative and corresponding GPD results are removed if any of the corresponding test results of all quantile thresholds, bootstraps or model runs is negative. Furthermore, the final GPD return values are validated with corresponding empirical quantiles of equal return times averaged over all quantile thresholds and model runs. This averaging agrees with the GPD fitting procedure and smoothes the partly strongly differing empirical quantiles of different quantile thresholds. Thus, the equ. 3.37 for calculating data sample quantiles of the previous chapter is applied to the original data sample for those quantiles used in equ. 3.47 to compute GPD return values of certain return times from the cumulative GPD function. The validation with average seasonal empirical block maxima, i.e. average maxima of original data sample blocks over the whole time period with block lengths equalling the GPD return times, is very uncertain because several data blocks in the southern Mediterranean in summer yield maxima of zero precipitation.

Finally, in order to investigate the GPD return values of longer-term wet or warm periods the original daily datasets are aggregated over several days (5, 11, 21, and 31 days) in averaging temperature and summing up precipitation values before performing the GPD analysis. Dry or cold spells are not considered here because only extremes of the upper distribution tails are analysed. Aggregated E-OBS data are declared as missing value if any missing value is used for aggregation. If single rain days occur surrounded by many rainless days, e.g. over the southern Mediterranean in summer, aggregation of daily precipitation may lead to several aggregated days of equal rainfall amounts. But the GPD fit reveals systematic problems if all extreme days exceeding the quantile threshold yield equal rainfall amounts. Thus, such aggregated rainfall days of equal amounts are not removed but the GPD fit is only performed if at least six extreme days with differing rainfall amounts prevail.

3.8 Weather generator

Rainfall features strong variations in time and space and rainfall simulation strongly depends on the given model resolution. Simulated grid box precipitation data are

area average values and differ from local station data in statistical properties: gridded climate model output creates too many rain days of too little intensity thus, underestimating daily mean and extreme intensity and variability of local rainfall and proportion of rainless days (ZOLINA et al., 2004; PAETH and DIEDERICH, 2010). Even gridded observational data feature smoothed rainfall extreme intensities in comparison to local station values due to spatial interpolation (HAYLOCK et al., 2008).

This problem of comparing gridded model and local station rainfall data can be solved by a dynamical-statistical weather generator (PAETH and DIEDERICH, 2010) which creates virtual station data from gridded RCM rainfall output applying orographic information on windward and lee effects, a stochastic term describing the spatial spread of local rainfall within a model grid box and a matching of the simulated Probability Density Functions (PDF) to observed distributions. FUNK et al. (2003) and SALATHE (2005) have already applied physical or orographic downscaling approaches and WILKS (1999) a stochastic weather model generating random daily local weather events resembling realistic station data. The prevailing approach combines these common methods of statistical-dynamical downscaling and produces virtual precipitation station data strongly agreeing with the statistical properties of original stations, particularly revealing less weak rain days and higher daily extreme intensities. Furthermore, all predictors originate from climate model output allowing the application of the weather generator to future time periods assuming the temporal stationarity of the relationships found in the orographic term, stochastic term and PDF matching (PAETH and DIEDERICH, 2010). This weather generator has been successfully applied for impact studies on hydrology and soil erosion in West Africa (BUSCHE et al., 2005). In this study, the setup of the presented weather generator is performed by means of 102 original precipitation stations of the Mediterranean area collected from several projects and tested for homogeneity and completeness (cf. subsection 2.1.1) over the extended present-day time period 1960-2000. The relationships found for observations are applied to gridded REMO rainfall data of the whole time period 1961-2050 to derive local virtual rainfall stations, separately for each model ensemble member. In the following, the basic elements of the weather generator are described in detail.

The orographic term describes the statistical relationship between daily precipitation sum and orography via linear regression (GOLDBERG and BERNHOFER, 2000). First, elevation values of original stations are derived from a high-resolution orography obtained from the SRTM Finished Grade Data of the USGS (USGS EROS, 2011) at 90m resolution. The corresponding REMO grid box elevation values are

averaged over all 90m SRTM elevation grid boxes within these REMO grid boxes. Then, zonal and meridional orographic gradients are calculated for each station over 11 SRTM elevation grid boxes ($\sim 1\text{km}$) in west-east and south-north direction by means of linear trend regression coefficients and normed to 100m. The orographic gradients of the corresponding REMO grid boxes are computed adequately over three grid box elevation values ($\sim 150\text{km}$). The orographic distances are taken from PAETH and DIEDERICH (2010) and a systematical variation of the station orographic distance between five ($\sim 500\text{m}$) and 201 SRTM elevation grid boxes ($\sim 18\text{km}$) to find the appropriate orographic distance for the Mediterranean area with maximum explained variance yields no clear maximum of explained variances over all stations. Thus, the original orographic distances are used. The station anomaly vector of zonal and meridional orographic gradients \vec{g}_j^s of station j respective to the corresponding REMO grid box mean vector is combined with the corresponding daily wind vector $\vec{v}_i^e(t)$ of grid box i and day t from ERA40 reanalyses (UPPALA et al., 2005) which have been interpolated to the 0.5° REMO model grid by quadratic spline interpolation (cf. chapter 3.4). The resulting positive or negative scalar product $c_j^s(t)$ denotes the orographic wind-ward or lee effect at station j respective to the area average REMO orographic effect, respectively (FUNK et al., 2003; PAETH and DIEDERICH, 2010):

$$c_j^s(t) = \vec{v}_i^e(t) \cdot \vec{g}_j^s \quad (3.48)$$

Then, station rainfall anomalies $\dot{p}_j^s(t)$ are built respective to the observed area average of the corresponding REMO grid boxes generated from averaging all rainfall stations within a certain REMO grid box. A linear regression is performed between station rainfall anomalies and station orographic effect $c_j^s(t)$ over all days t for each station j separately in order to specify the different orographic impacts at different stations in contrast to PAETH and DIEDERICH (2010) who average this relationship over all stations of their small-size test area in Benin. But this approach is not able to describe temporal differences in the orographic effect on rainfall posing the question if temporal stationarity of this relationship is given for future time periods. Generally, also further deterministic factors influencing the relationship between local and gridded precipitation might be considered in regression, e.g. the distance to the sea (PAETH and DIEDERICH, 2010).

The residual of the linear regression between station rainfall anomalies and station orographic effect over all days per station remains unexplained. But assuming ergodicity of the prevailing dynamical system this temporal rainfall variation of a certain station can be applied to estimate the spatial rainfall variance in the corresponding grid box, e.g. caused by local convective precipitation events. Thus, the

statistical characteristics of the residual, i.e. mean and standard deviation, are used to define the stochastic term: Random numbers $\epsilon_j^s(t)$ are drawn for each station j and day t from a Normal distribution fitted to the residual time series and describe the stochastic spatial variability between local station and area average rainfall (PAETH and DIEDERICH, 2010). Since both cumulative distribution and quantile functions of the Normal distribution do not exist in closed analytical form the Normal distributed random numbers are generated by the Box Muller method (WILKS, 2006) which applies polar transformation to create two independent standard Normal distributed variates from two independent uniformly distributed variates generated by an uniform random number generator.

Thus, the virtual station time series $\hat{p}_j^s(t)$ of station j and day t is calculated combining the large-scale simulated REMO precipitation $p_i^m(t)$ of grid box i , the orographic term with linear regression coefficient b_j , simulated REMO horizontal wind vector $\vec{v}_i^m(t)$ and station anomaly vector of orographic gradients \vec{g}_j^s and the stochastic part defined by Normal distributed random numbers $\epsilon_j^s(t)$. Having added these terms the resulting virtual station time series already features less weak precipitation days than the simulated REMO time series. The weather generator is implemented for each month separately to reproduce the observed seasonal cycle (PAETH and DIEDERICH, 2010):

$$\hat{p}_j^s(t) = p_i^m(t) + b_j \cdot \vec{v}_i^m(t) \cdot \vec{g}_j^s + \epsilon_j^s(t) \quad (3.49)$$

Finally, a probability matching is performed (DUDA et al., 2001) because the resulting virtual station time series $\hat{p}_j^s(t)$ do not totally fit the distribution function of observed rainfall data, especially concerning extreme precipitation intensities (PAETH and DIEDERICH, 2010). The virtual station data of daily rainfall below and above the 80% quantile is fitted by the Gamma (Γ) function (DUNN, 2004) and GPD (PAETH and HENSE, 2005), respectively. The Γ distribution alone does not sufficiently represent extreme rainfall events. The relatively low 80% threshold is selected to retain enough extreme rainfall events for performing the GPD fit (PAETH and DIEDERICH, 2010). For both fitted distributions, the parameters are assessed via the method of L-moments (HOSKING, 1990). Then, the statistical transformation of the virtual station data $\hat{p}_j^s(t)$ over all days t of a station j with the cumulative distribution function $F_x(x)$, fitted by Γ function or GPD here, to the final virtual station data $\tilde{p}_j^s(t)$ with observed cumulative distribution function $F_y(y)$ of the corresponding original station j is performed (PAETH and DIEDERICH, 2010):

$$\tilde{p}_j^s(t) = F_y^{-1}(F_x(\hat{p}_j^s(t))) \quad (3.50)$$

The PDF matching is based on the present-day rainfall distribution and if future daily REMO rainfall extremes lie outside the present-day GPD reaching quantile values of 100%, unrealistic high outliers result in final virtual station data. Therefore, such future quantile values of 100% are set to 99.9% in PDF matching being low enough to avoid such unrealistic outliers and high enough to conserve realistic extremes and thus, also the rainfall total. This has been proved by corresponding sensitivity tests. In order to avoid uncertain distribution fits to small data samples the PDF matching is only performed per month and station or corresponding REMO grid box if more than 25 rain days with rainfall exceeding 0.1mm are available for both Γ and GPD fits over all years.

But the number of rain days per month in final virtual station data after PDF matching still overestimates original stations in the present-day time period. Thus, before the PDF matching is performed this difference in numbers of rain days per month is randomly removed from all virtual station days of that month over all years. But this adjustment is only performed for virtual stations with higher number of rain days. Sensitivity tests show that adjusting the average number of rain days does not influence daily rainfall intensity, variability or distribution but station precipitation totals are strongly reduced due to a reduced number of rain days. This discrepancy of rain days is regarded as systematic model error and transferred to the future time period. But if the number of rain days to delete is higher than the future prevailing number of rain days which sometimes occurs in summer, the systematic model error is not stationary over time and can not be transferred from present-day to future conditions. Thus, the corresponding virtual rainfall station is sorted out for that month of the future time period.

Generally, such statistical post-processing approaches are cost efficient tools to correct systematic model errors (HANSEN and EMANUEL, 2003; KANG et al., 2004) resulting from deficient model physics, e.g. parameterisation of clouds and convection (ERRICO et al., 2001), when model improvements are too difficult or too expensive but appropriate input data for impact research is needed. Systematic RCM errors at the monthly scale can be corrected and adjusted to observations by Model Output Statistics (MOS), i.e. a linear multiple regression analysis with observed rainfall as predictand and dynamical near-surface RCM output variables as predictors (GLAHN and LOWRY, 1972; PAETH and HENSE, 2003). For example, PAETH (2010) corrects simulated sub-Saharan rainfall amounts underestimating observed values. But since such MOS approaches can not be applied for daily precipitation values due to lacking phase relationship between daily simulated and observed rainfall (PAETH, 2010) the statistical post-processing for daily precipitation is per-

formed by a weather generator like described before. Major uncertainties of both approaches arise from the inaccuracies of the given observational datasets.

4 Analysis of temperature and precipitation means and trends

This chapter presents the analysis of the Mediterranean temperature and precipitation means and trends in present-day and future times providing the necessary background for the analysis of extreme events in the following chapters 6, 7 and 8. The present-day time period 1961-1990 is selected for validation of model simulations and the future time period 2021-2050 for determining possible future climate change. Additionally, the long-term period 1961-2050 is applied for long-term analysis of trends and variance. For both present-day validation and future projection, added values of dynamical downscaling from the global general circulation model ECHAM5 on 1.875° to the regional climate model REMO on 0.5° are investigated and evaluated. Thus, the annual cycle and seasonal climatological means and trends of Mediterranean temperature and precipitation are analysed in both present-day and future times applying validation tests for simulated present-day means and variances. Present-day seasonal trends of REMO forced by ECHAM5 are compared with a REMO simulation driven by ERA-15 reanalyses and impacts of differing initial conditions in different REMO ensemble members on seasonal trends are investigated to understand differences between simulated and observed present-day trends. Finally, one-way and two-way analyses of variance are applied for the present-day and long-term periods to evaluate the signal-to-noise ratio of the corresponding seasonal temperature and precipitation trends. Thus, the following two sections present the corresponding results for the present-day time period and the long-term and future time period.

4.1 Validation and dynamical downscaling of present-day climate

This section describes the results of the investigation of Mediterranean temperature and precipitation means and trends in the present-day time period 1961-1990. High-resolution REMO simulations are validated with observations and compared

with coarse grid ECHAM5 simulations to reveal added values of dynamical down-scaling. Thus, the following subsections present the annual cycle, seasonal means, two validation tests for simulated means and variances and seasonal trends for both temperature and precipitation. Further subsections compare REMO simulations forced by ECHAM5 with one REMO simulation driven by ERA15 reanalyses and investigate the impacts of initial conditions of different REMO ensemble members on seasonal trends. The final subsection determines the signal-to-noise ratio of the presented seasonal trends by means of a one-way analysis of variance.

4.1.1 Annual cycle

First, the annual cycles of E-OBS, CRU, REMO and ECHAM5 temperature and precipitation of the present-day time period 1961-1990 are computed from climatological monthly means of all 12 months. The annual cycle is exemplarily compared for two selected regions in the western and eastern Mediterranean, i.e. south-eastern Spain and central Turkey, and the monthly means of E-OBS, CRU and REMO are averaged over 4×4 0.5° grid boxes to cover larger representative areas. If more than eight of 16 E-OBS grid boxes feature missing values, the 4×4 grid box average is declared as missing value. For ECHAM5, only the corresponding 1.875° grid box is analysed.

Thus, Fig. 4.1 depicts the annual cycles of temperature and precipitation in both selected regions for E-OBS, CRU, REMO and ECHAM5 in 1961-1990. For temperature, the annual cycles of both regions yield temperature maxima in summer and minima in winter with higher annual amplitude over continental Turkey due to lower winter temperatures compared to the rather maritime Spanish region. E-OBS and CRU match mostly very well and REMO yields quite good agreement with the observations over all months except for slight overestimations over Turkey in winter. ECHAM5 shows stronger disagreement to observations than REMO revealing higher temperatures over Spain in all months and higher and lower temperatures over Turkey in summer and winter, respectively (Fig. 4.1, left). For precipitation, the annual cycles of both regions depict summer dryness and winter rainfall but Turkey shows a higher annual amplitude due to stronger winter precipitation. The differences between E-OBS and CRU are larger than for temperature, especially over Turkey revealing strong discrepancies in winter. REMO yields rather good agreement to observations over both regions in summer but overestimates observed values over Spain in winter. Over Turkey, REMO overestimates CRU and underestimates E-OBS winter values thus, lying in the uncertainty range spread by the two observational datasets. ECHAM5 shows smaller values than both REMO and observations

in spring and summer. In winter, ECHAM5 depicts similar rainfall to REMO over Spain and strongly overestimates all datasets over Turkey (Fig. 4.1, right). Thus, both regions feature the typical Mediterranean annual cycle with warm, dry summers and cool, wet winters. REMO captures quite well the observed annual cycles for temperature and precipitation in both regions but shows discrepancies for winter rainfall where even observational datasets reveal strong uncertainties. ECHAM5 yields larger disagreement to observations than REMO in both regions and nearly all months.

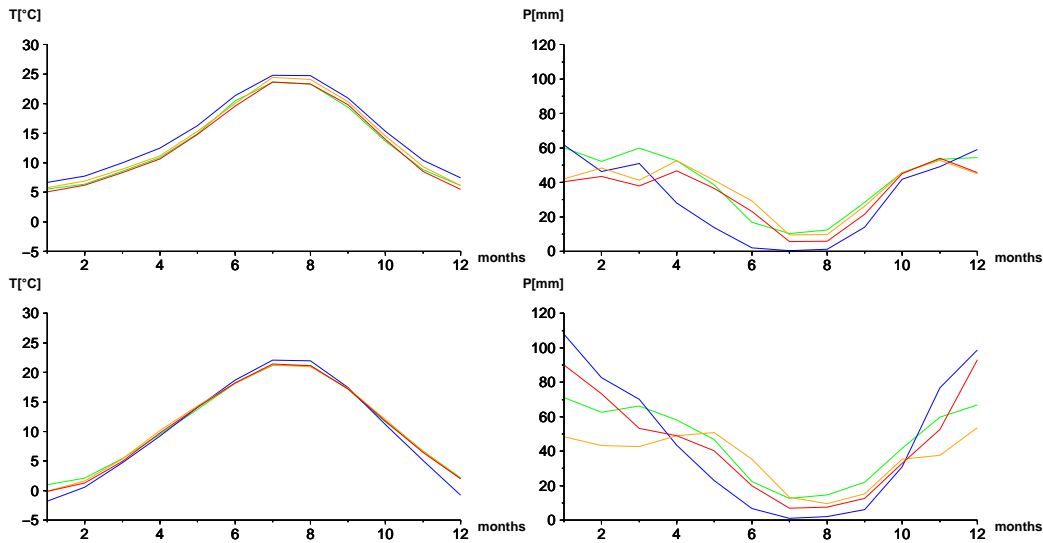


Figure 4.1: Annual cycle of temperature (left) and precipitation (right) over south-eastern Spain (top) and central Turkey (bottom) from E-OBS (red), CRU (orange), REMO (green) and ECHAM5 (blue) in 1961-1990.

4.1.2 Climate means

In this subsection, the seasonal climatological means of REMO and ECHAM5 are validated with those of E-OBS and CRU observations in the present-day time period 1961-1990. In this study, only the winter and summer means are shown and compared because they represent the extreme seasons of the year revealing maximum and minimum temperature and precipitation values in annual cycle (see subsection 4.1.1) and are thus, most appropriate for the investigation of extreme events denoting the focus of this study. The means of the transitional seasons spring and autumn mostly lie in between the corresponding winter and summer results.

Fig. 4.2 shows the winter and summer temperature means of E-OBS, REMO and ECHAM5 in 1961-1990. CRU temperature and precipitation means are not shown because they are basically consistent with E-OBS results. Generally, a very good agreement between simulated and observed temperature means can be stated in both

seasons with strong north-south temperature gradient revealing minima of -14°C over eastern Turkey and the Caucasus region in winter and maxima of 36°C over north-western Africa and the Middle East in summer. In winter, REMO agrees well with E-OBS and CRU over the whole area with some underestimations over Africa compared to CRU. ECHAM5 overestimates temperatures over Italy and eastern Turkey due to coarse resolution of mountain topography and shows even smaller temperature means than REMO over northern Africa and Middle East yielding a stronger disagreement to CRU observations (Fig. 4.2, left). In summer, REMO agrees well with E-OBS but shows some minor overestimations of temperature means over the Atlas mountains and south-eastern Turkey. But CRU observations also feature slightly higher values than E-OBS over these regions revealing uncertainties in observational datasets. ECHAM5 further overestimates observed temperatures over the Balkans and Atlas mountains and yields lower temperatures over northern Africa (Fig. 4.2, right). Generally, the validation of temperature means in 1961-1990 yields good agreement between REMO and both observational datasets in seasonal and spatial distribution. ECHAM5 overestimates observed temperature means over mountains, e.g. eastern Turkey in winter and the Atlas mountains in summer, due to coarse resolution of topography and yields some cooler temperatures than REMO over northern Africa probably pointing at missing small-scale processes, such as regional wind patterns. This leads to a stronger disagreement of ECHAM5 with E-OBS and CRU observations.

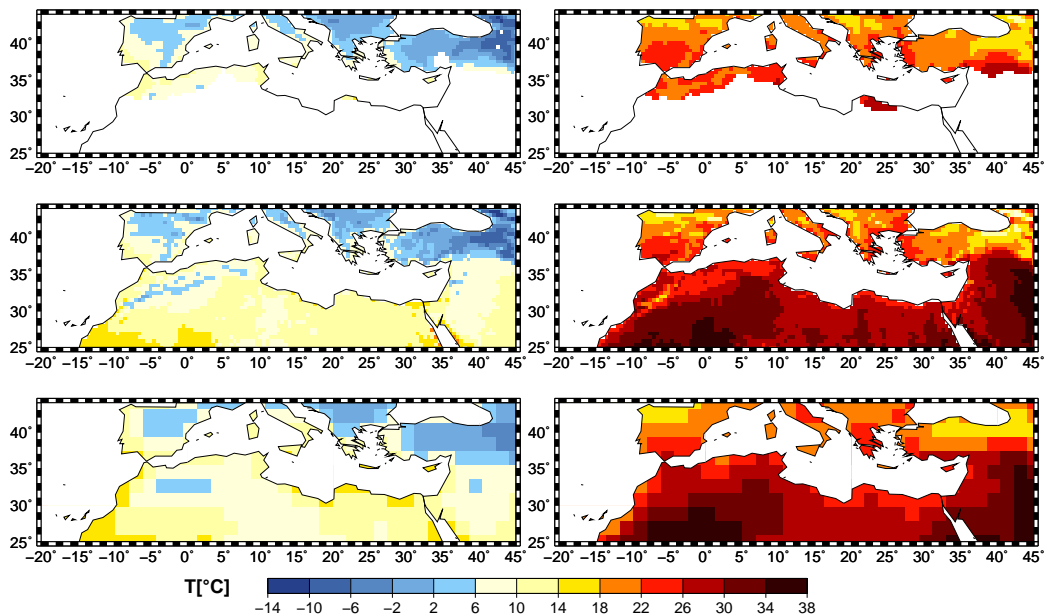


Figure 4.2: Validation of climatological winter (left) and summer (right) temperature means of REMO (middle) and ECHAM5 (bottom) with corresponding E-OBS means (top) during 1961-1990.

Fig. 4.3 displays the corresponding climatological precipitation means of E-OBS, REMO and ECHAM5 in 1961-1990. Generally, E-OBS and CRU observations reveal a north-south gradient of precipitation with maxima of 800mm over Galicia in winter and minima of less than 10mm over northern Africa, Near and Middle East in summer. In winter, REMO slightly overestimates E-OBS over the region of maximum precipitation at the western coasts of southern Europe, further over central Spain and Bulgaria and yields several discrepancies over the eastern Mediterranean: underestimations over the Near East and western Turkey and overestimations over eastern Turkey. But the latter differences can be stated as well for CRU compared to E-OBS describing several uncertainties in observed precipitation over the eastern Mediterranean perhaps due to lacking station data. Furthermore, REMO slightly underestimates rainfall over Africa and overestimates precipitation over the Middle East compared to CRU observations. ECHAM5 yields similar rainfall patterns to REMO but less topographic details with less precipitation over mountain ranges. Furthermore, ECHAM5 shows less rainfall than E-OBS and REMO over Morocco, Italy and the Middle East but better agreement to E-OBS over central Turkey (Fig. 4.3, left). In summer, REMO slightly underestimates E-OBS and CRU precipitation over Italy and the Balkans and overestimates E-OBS over Turkey and the Atlas mountains where CRU data as well yields higher values. Further overestimations can be stated over north-eastern Africa compared to CRU and over the northern Balkans and the Caucasus region probably caused by artificial rainfall due to boundary effects of the REMO model grid. ECHAM5 rainfall is smaller than all other datasets nearly over the whole Mediterranean area and shows less agreement with observations than REMO (Fig. 4.3, right). Thus, REMO agrees basically well with observations but slightly overestimates maximum precipitation regions over the northern Mediterranean in winter, especially over western coastlines and mountain ranges, probably due to the inclusion of windward and lee effects in simulations compared to the smoothed rainfall maxima of spatially interpolated E-OBS observations or due to deficiencies in regional climate modelling. Strongest discrepancies between REMO and E-OBS can be found over the Atlas mountains and the eastern Mediterranean but exactly over these regions the differences between E-OBS and CRU observational datasets are also highest. ECHAM5 yields mostly less topographic details and less rainfall than REMO, especially in summer, usually degrading agreement with observations.

Generally, dynamical downscaling from ECHAM5 on 1.875° to REMO on 0.5° resolution yields several improvements of regional climate modelling: the high spatial resolution of REMO enhances the representation of small-scale topographic details of

temperature and precipitation in context of the strong orography and large land-sea contrast in the Mediterranean area. Furthermore, REMO reaches warmer African and cooler mountain temperatures than ECHAM5 both improving the validation with observations. Concerning precipitation, REMO presents higher means than ECHAM5 over the whole area in summer and over Middle East and mountain ranges and western coastlines of the northern Mediterranean in winter, sometimes even overestimating observational values.

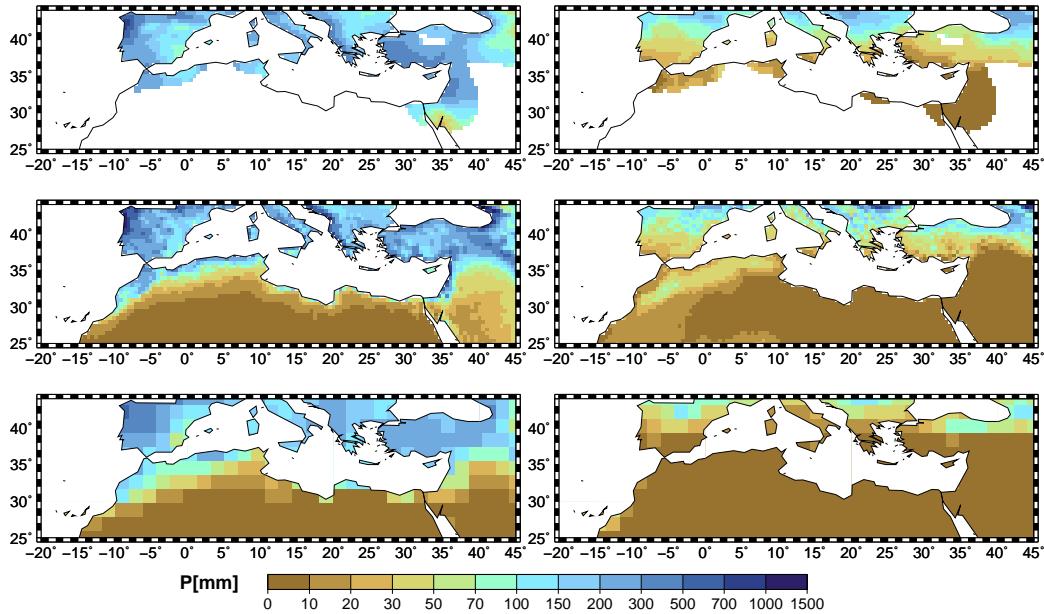


Figure 4.3: Validation of climatological winter (left) and summer (right) precipitation means of REMO (middle) and ECHAM5 (bottom) with corresponding E-OBS means (top) during 1961-1990.

4.1.3 Validation tests

For validation of REMO temperature and precipitation in the Mediterranean area with E-OBS data, two statistical tests are applied to prove if the sample means and variances of REMO ensemble mean and E-OBS originate from the same populations for a certain grid box and season in the present-day time period 1961-1990. The precondition of both statistical tests, i.e. independent normal distributed samples, is successfully proved in subsection 4.1.4 for most REMO and E-OBS grid boxes and seasons except for summer precipitation over some African and Arabian regions. A further precondition of the sample mean test requires no significant differences in sample variances which is verified by the sample variance test for many Mediterranean grid boxes (see below). The variances of seasonal E-OBS and REMO means in 1961-1990 are basically consistent in spatial and seasonal distribution except for

some regional discrepancies, especially for summer temperature, but are not shown or explicitly discussed here. For REMO ensemble means, the variances are computed by squaring the average standard deviation of the corresponding ensemble members because the variability of different ensemble members is balanced in building the ensemble mean.

Fig. 4.4 depicts the results of the validation tests for temperature and precipitation means and variances of E-OBS and REMO in 1961-1990. For temperature, many grid boxes in winter and summer yield equal populations for E-OBS and REMO variances except over eastern Turkey in winter and over the central Mediterranean in summer. The validation results are more mixed for temperature means revealing many grid boxes with significantly large differences between observed and simulated sample means pointing at differing populations of E-OBS and REMO, especially over Italy in winter and over the Atlas mountains and eastern Turkey in summer (Fig. 4.4, first and second row). Concerning precipitation, the validation results of summer are rather similar for sample means and variances yielding mostly equal populations for E-OBS and REMO samples except over the Near East and Turkey. Validation results for winter precipitation are basically consistent to summer results but slightly worse for precipitation means revealing many grid boxes with large differences between observed and simulated rainfall, especially over the eastern Mediterranean (Fig. 4.4, third and fourth row.).

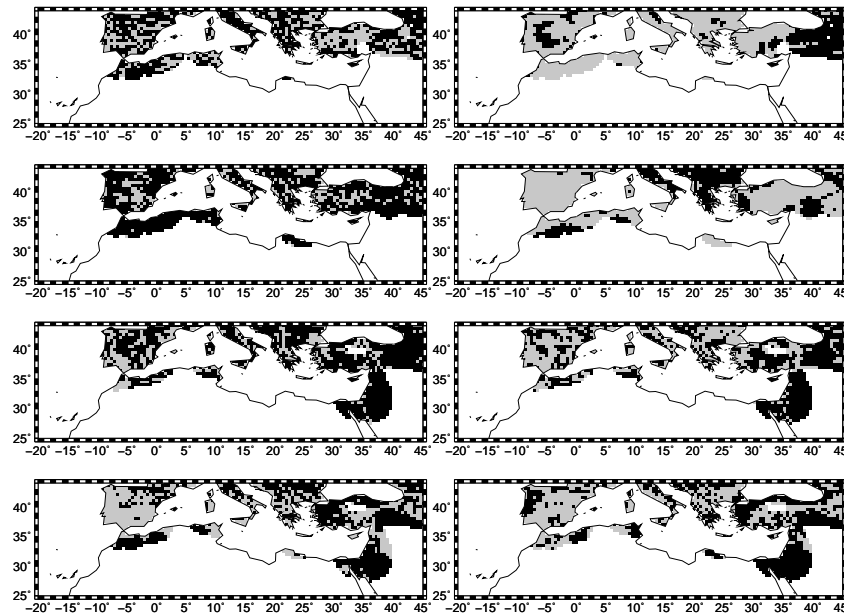


Figure 4.4: Results of the validation tests for winter and summer temperature (first and second row) and winter and summer precipitation (third and fourth row) from REMO ensemble mean with E-OBS in 1961-1990: corresponding sample means (left) and variances (right) originate from equal (grey) or different populations (black).

Thus, the REMO ensemble mean yields mostly good validation results with E-OBS data concerning temperature and precipitation variances denoting rather good representations of observed climate variability except for some eastern Mediterranean areas. But worse validation results are stated for the seasonal means, especially concerning summer temperature and winter precipitation, pointing at relatively large disagreements of small-scale details between observed and simulated means despite the good agreement of large-scale spatial and seasonal patterns determined in subsection 4.1.2. Generally, the validation results for temperature and precipitation means and variances are strongest over the Iberian Peninsula and weakest over the eastern Mediterranean.

4.1.4 Climate trends

This subsection presents seasonal temperature and precipitation trends of REMO, ECHAM5, E-OBS and CRU which are built using linear regression for the present-day time period 1961-1990 and applying a two-tailed test of the corresponding regression coefficients at a significance level of 5%. The preconditions of the linear regression, i.e. normal distribution of original data and trend residuals and absence of autocorrelation in trend residuals, are exemplarily proved for E-OBS, CRU, REMO and ECHAM5 temperature and precipitation data in the present-day time period 1961-1990. The Kolmogorov-Smirnov test at a significance level of 5% yields mostly good agreement of the empirical distributions of both data samples and trend residuals with the Normal distribution, especially for the residuals. But several precipitation grid boxes over the Sahara in winter and over northern Africa, Near and Middle East in summer are not normally distributed, probably due to small numbers of rain days. For ECHAM5, this region extends over the whole southern Mediterranean in summer due to a strongly reduced number of rain days (cf. subsection 6.1.1). Furthermore, REMO shows some grid boxes over the Middle East that are not normally distributed for summer temperature. For E-OBS, most of these grid boxes have already been omitted due to missing data completeness tests (see section 3.1). But for all other datasets, these regions are not removed but the interpretation of linear regression trends is performed with caution. The analysis of autocorrelation in trend residuals yields no limitations for linear regression due to only small maximum step sizes with significant values of the autocorrelation function: on average 0-1 years of autocorrelation over the whole Mediterranean area with only some single grid boxes reaching maxima of 2-4 years.

The following results of the validation of seasonal REMO temperature and precipitation trends with corresponding E-OBS trends in 1961-1990 have been submitted

for publication to the International Journal of Climatology and the description is partly extracted from this manuscript (PAXIAN et al., 2011). The main question is if REMO forced by ECHAM5 in a model-into-model-approach with the only real boundary condition observed CO₂ emissions shows at all some predictability concerning temperature and precipitation trends in 1961-1990 in the Mediterranean which is strongly controlled by mid-latitude circulation variability (cf. chapter 1). In this study, the seasonal ECHAM5 trends are additionally presented to evaluate probable added values by regional dynamical downscaling from ECHAM5 on 1.875° to REMO on 0.5° resolution and CRU trends are further discussed to include the uncertainty arising from differing observational datasets. As for the climatological means only the winter and summer results are depicted and discussed in this study although some specific trend patterns are found in the transitional seasons spring and autumn.

Thus, Fig. 4.5 depicts the seasonal temperature trends of E-OBS, REMO and ECHAM5 for 1961-1990. In winter, a very strong and significant E-OBS cooling pattern is obvious over Turkey reaching values of up to -4°C and warming patterns over southern Europe partly significant over Spain. CRU shows similar present-day trends but slightly smaller cooling over Turkey which extends further south to Middle East and northern Africa. REMO reproduces a slight cooling pattern over Turkey with values of up to -1°C not reaching significance and shows negligible trends over the western Mediterranean. ECHAM5 depicts equal temperature trends to REMO but reaches stronger warming patterns over north-western Africa revealing stronger disagreement to cooling trends of CRU over the Sahara (Fig. 4.5, left). Concerning summer, we can see strong and significant E-OBS warming trends over Spain, the Atlas Mountains and eastern Turkey and some cooling trends over western Turkey which are mostly not significant. The CRU observations yield extended warming over Spain and north-western Africa but smaller trends over the Atlas mountains and no summer warming at all over eastern Turkey. The corresponding REMO trends capture the warming over Spain and to a lower extent that over the Atlas mountains and north-western Africa. But the simulated warming patterns over Italy, the Balkans and Turkey do not reach significance. ECHAM5 yields stronger warming patterns over north-western Africa with slightly higher agreement to CRU observations than REMO (Fig. 4.5, right). Thus, REMO is basically able to capture the observed cooling pattern over Turkey in winter and the observed warming pattern over the western Mediterranean in summer but with much lower intensity. Further differences between simulated and observed present-day trends in 1961-1990 concerning spatial patterns and intensities of change prevail over southern Europe

in winter and Turkey in summer. But over Turkey and the Atlas mountains differing E-OBS and CRU observational datasets reveal several uncertainties of observed trends. ECHAM5 shows equal temperature trends to REMO but stronger warming over north-western Africa (PAXIAN et al., 2011).

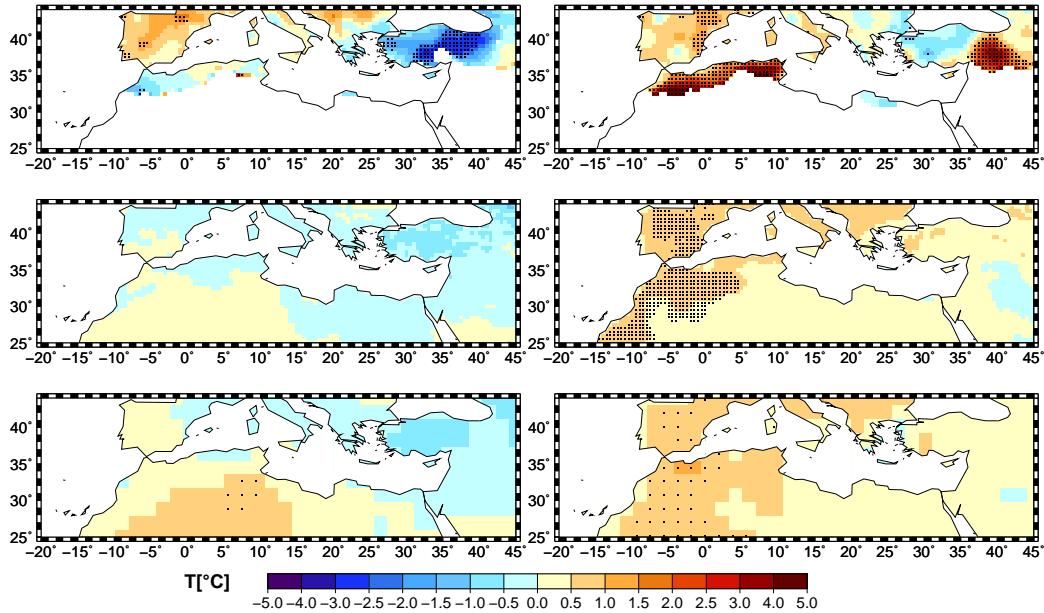


Figure 4.5: Validation of winter (left) and summer (right) temperature trends of REMO (middle) and ECHAM5 (bottom) with corresponding E-OBS trends (top) during 1961-1990, applying a significance level of 5% (dots).

The corresponding seasonal precipitation trends of E-OBS, REMO and ECHAM5 are presented in Fig. 4.6. In winter, E-OBS shows strong and significant drying patterns of up to -300 mm over the whole northern Mediterranean region, especially over the western Iberian Peninsula, Morocco, Greece and western Turkey, and some small wetting patterns over the Near East. The CRU observations reveal equal patterns but smaller drying intensities and no wetting over the Near East. REMO mostly reproduces these drying patterns but without significance and with less intensity reaching a maximum of -200mm over Portugal. Some wetting trends are prominent over eastern and northern Spain and the Atlas mountains and some drying over the Near East in contrast to E-OBS. Significant drying trends can only be found over the Middle East. ECHAM5 yields similar patterns of change to REMO but slightly smaller trend intensities (Fig. 4.6, left). Summer precipitation shows a mixed pattern of small trends hardly reaching any significance in all datasets. Some small drying tendencies can be stated in E-OBS and CRU over the Atlas mountains, the Balkans and eastern Turkey and wetting over southern Turkey. REMO mostly reproduces these small trends with some disagreements over northern Spain and Turkey. The strong drying over the northern Balkans and the Caucasus re-

gion in REMO again probably points at artificial boundary effects of the model grid. ECHAM5 yields similar results to REMO but decreased drying over the Atlas mountains (Fig. 4.6, right). Thus, both models basically reproduce the observed patterns of precipitation change but strongly underestimate observed winter drying of E-OBS over the whole Mediterranean. The agreement with the smaller CRU drying trends is higher but still not sufficient. The higher REMO resolution yields more fine scale structures and stronger drying than ECHAM5 and thus, slightly better accordance to observed trends (PAXIAN et al., 2011).

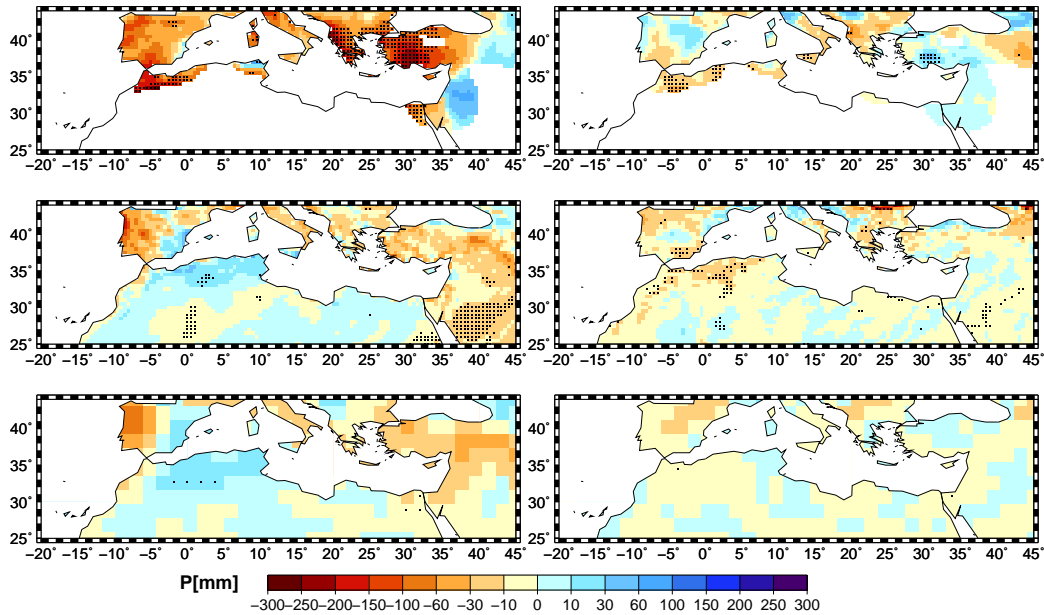


Figure 4.6: Validation of winter (left) and summer (right) precipitation trends of REMO (middle) and ECHAM5 (bottom) with corresponding E-OBS trends (top) during 1961-1990, applying a significance level of 5% (dots).

Generally, this model-into-model-approach REMO forced by ECHAM5 is able to capture some observed temperature and precipitation trends in 1961-1990 but several discrepancies can be stated, especially in winter. This leads to the conclusion that the only real boundary condition CO_2 emissions does not clearly prevail over other drivers influencing temperature and precipitation in the Mediterranean area, e.g. mid-latitude circulation, tropical climate dynamics or ocean-atmosphere interactions. The observations show several trend patterns that are related to a strong observed NAO increase in 1961-1990 (cf. chapter 1), i.e. cooling over Turkey and drying over the whole Mediterranean area in winter, which are not completely captured in REMO. Thus, several discrepancies between observed and simulated trend patterns might be explained due to differences in mid-latitude large-scale circulation, especially in winter. Therefore, impacts of mid-latitude circulation on present-day and long-term temperature and precipitation trends are further investigated in chap-

ter 5 (PAXIAN et al., 2011).

4.1.5 Comparison with ERA15-forced REMO simulation

Generally, the simulations of REMO version 5.7 driven by ECHAM5 are most appropriate for comparing future and present-day simulations or investigating dynamical downscaling compared to the driving ECHAM5 because in the given model-into-model-approach only observed GHG emissions are included as real boundary conditions. But these observed boundary conditions alone are often not sufficient to explain and reproduce present-day observed temperature and precipitation variability because other drivers, e.g. simulated mid-latitude circulation variability, are often not in phase with the observed ones (see chapter 5). Thus, for general validation of the REMO model with CRU and E-OBS observations in the present-day time period, usually simulations forced by reanalysis data are applied, e.g. the given REMO 5.0 simulation driven by ERA15 reanalyses, because they contain all observed boundary forcings necessary for reproducing observed temperature and precipitation variability.

Thus, the seasonal means and trends of the single REMO 5.0 simulation driven by ERA15 reanalyses in 1980-2000 are compared to corresponding E-OBS and REMO 5.7 results (Fig. 4.7) in order to validate the REMO model driven by observed boundary conditions and evaluate the differences between REMO 5.7 simulations driven by ECHAM5 and observations in 1961-1990 already discussed before. For seasonal temperature means, a general good agreement of both REMO 5.0 and 5.7 simulations with observations can be stated but both simulated means are slightly smaller than observed ones over the Atlas mountains in winter and slightly higher over the Atlas mountains and Near East in summer. Thus, REMO 5.0 yields no improvement of REMO 5.7 validation results for temperature means. Furthermore, the present-day trend patterns of REMO 5.0 fit quite well with observed trends in 1980-2000 revealing extended warming with maximum over Spain and Italy and minimum over Turkey in winter and strong and significant warming over the northern Mediterranean with maximum over the Balkans and Turkey in summer. But trend intensities and significance are smaller in REMO 5.0. Instead, REMO 5.7 shows reverse trend maxima and minima in winter and significant warming over the Iberian Peninsula and the eastern Mediterranean in summer not fitting well with observed trends (Fig. 4.7, first and second row).

For precipitation, REMO 5.0 yields much smaller climatological means than REMO 5.7 over the northern Mediterranean and the Middle East and some higher means over north-western Africa in winter. In summer, REMO 5.0 shows higher values over

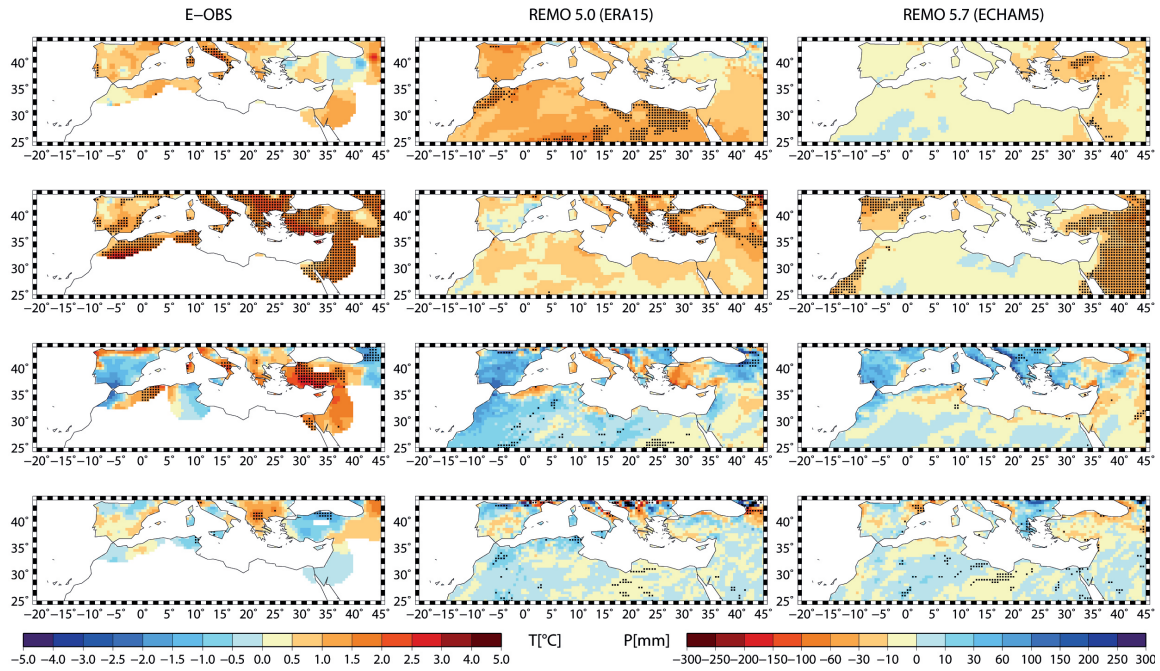


Figure 4.7: Validation of winter and summer temperature (first and second row) and winter and summer precipitation trends (third and fourth row) of a REMO 5.0 simulation driven by ERA15 reanalyses (middle) and REMO 5.7 ensemble mean forced by ECHAM5 (right) during 1980-2000 with corresponding E-OBS trends (left), applying a significance level of 5% (dots).

the Atlas mountains and the Balkans and smaller values over Africa. The agreement to observations strongly increases for REMO 5.0 over the northern Mediterranean in winter but some differences over Turkey and Near East in winter and overestimations over the Atlas mountains and the Balkans in summer remain. Furthermore, the precipitation trends of REMO 5.0 in 1980-2000 often show similar trend patterns to observations featuring drying over the central Atlas mountains, Italy, Greece and western Turkey and wetting over Spain and eastern Turkey in winter and further drying over southern Spain, Greece and eastern Turkey in summer. Some difference can be stated over northern Spain, Bulgaria, central Turkey and Near East but accordance is much higher than for REMO 5.7 simulations yielding strong wetting patterns over the northern Mediterranean in winter and over the Balkans in summer (Fig. 4.7, third and fourth row). Additionally, REMO 5.0 yields similarly good validation results for annual cycles of temperature and precipitation to REMO 5.7 but much stronger agreement to observations for winter rainfall (cf. subsection 4.1.1).

Generally, REMO 5.0 yields stronger agreement to observations than REMO 5.7, especially for precipitation means and present-day trends, due to similar boundary conditions to observations. Thus, the REMO model is generally able to reproduce observed present-day temperature and precipitation means and trends in the

Mediterranean area during 1980-2000 if forced by observed boundary conditions but differing simulated boundary conditions from ECHAM5 might cause differences, especially in present-day trends.

4.1.6 Impact of initial conditions on climate trends

In this subsection the impact of differing initial conditions in different REMO ensemble members on present-day validation results is analysed to further evaluate the stated differences between observations and simulations in the present-day time period 1961-1990, especially concerning seasonal trends. Climatological means, variances and validation tests yield mostly rather small differences between different REMO ensemble members and are thus, not shown here but strong differences can be stated in seasonal trends. Thus, Fig. 4.8 presents the temperature and precipitation trends of different REMO ensemble members in 1961-1990.

In winter, the REMO ensemble mean is only slightly able to capture the strong observed cooling over Turkey and drying over the whole area, i.e. probably the signals of a strongly positive NAO in observations, and the observed warming over the western Mediterranean is not reproduced (cf. Fig. 4.5, left and Fig. 4.6, left). The second ensemble member shows quite good agreement with E-OBS and CRU observations featuring strong trend patterns related to a positive NAO and slight warming over Spain. The third ensemble member yields as well slight signals of a positive NAO but with maximum drying trends over the Iberian Peninsula and no warming trend over southern Europe. In contrast to that, the first ensemble member even describes winter warming over Turkey and mostly wetting over southern Europe and the Atlas mountains, i.e. signals of a negative NAO (Fig. 4.8, left and middle).

For summer, the observed warming over the western Mediterranean is partly reproduced in the REMO ensemble mean but the slight cooling and strong warming trends over Turkey are not captured (cf. Fig. 4.5, right). The first and second ensemble members reproduce the strength of the western Mediterranean warming pattern but the spatial pattern is partly shifted towards Spain and Italy and towards north-western Africa, respectively. The third ensemble member yields only slight warming trends over the western Mediterranean. The dipole change pattern over Turkey is not captured by any of the ensemble members (Fig. 4.8, right). Finally, summer precipitation shows only small and mostly not significant trends and is thus, not analysed here (cf. Fig. 4.6, right).

Generally, high impacts of initial conditions on seasonal temperature and precipitation trends of REMO ensemble members in 1961-1990 can be identified revealing strongly differing trend patterns, e.g. two ensemble members mostly reproduce the

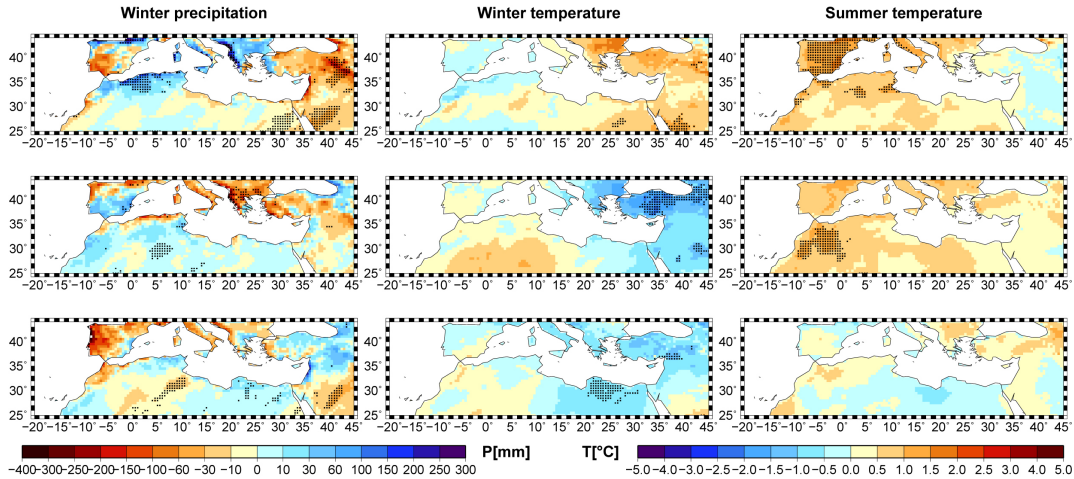


Figure 4.8: Seasonal trends of the first (top), second (middle) and third (bottom) REMO ensemble member for winter precipitation (left) and winter (middle) and summer temperature (right) during 1961-1990, applying a significance level of 5% (dots).

observed winter trends related to a positive NAO and one member even features signals of a negative winter NAO. Consequently, the resulting REMO ensemble mean reveals winter temperature and precipitation trend patterns of a slightly positive NAO underestimating the strong present-day trends of E-OBS and CRU observations. These impacts of initial conditions and mid-latitude circulation variability on present-day trends are investigated in more detail in the following chapter 5.

4.1.7 One-way Analysis of Variance

The final subsection applies one-way analyses of variance to evaluate the signal-to-noise ratios of the simulated seasonal temperature and precipitation trends of the REMO and ECHAM5 model ensembles in the present-day time period. The one-way analyses of variance are performed for three ensemble members of REMO and ECHAM5 in 1961-1990 to estimate the proportion of total temperature and precipitation variance accounted for by an external boundary forcing, e.g. increasing GHG concentrations, common to all ensemble members in context of internal model variability (Fig. 4.9). Furthermore, the one-way analysis of variance is performed for the 10-year running means of REMO temperature and precipitation in order to amplify the GHG signal on the interdecadal time scale by smoothing interannual variations.

Winter temperature reveals GHG signals of 20-30% over Spain and western Turkey and significance over northern Spain for REMO and only some significant signals of 30% over northern-eastern Africa with different spatial pattern for REMO running

means. ECHAM5 yields similar intensities and spatial structures to REMO but slightly stronger signals over northern Africa and smaller signals over Turkey (Fig. 4.9, left). REMO summer temperature yields significant GHG signals of up to 20-30% over Italy, the Balkans and Turkey mostly increasing for running means to maximum values of 30-50% over Bulgaria, northern Spain and several parts of northern Africa with slightly changed spatial pattern. ECHAM5 shows equal results but higher values than REMO over the Atlas mountains and smaller values over Middle East (Fig. 4.9, middle). For precipitation, the GHG signal of REMO reaches 30-40% over the Atlas mountains and Libya in winter. The running means of REMO yield higher local signals of 40-50% over Libya and the Middle East and ECHAM5 shows equal signals over the Atlas mountains but much smaller signals than REMO over Libya (Fig. 4.9, right). Summer precipitation is not shown because only small local hotspots of GHG signals spread over the whole Mediterranean area can be stated reaching values of 30% for REMO and ECHAM5 and 40-50% for REMO running means.

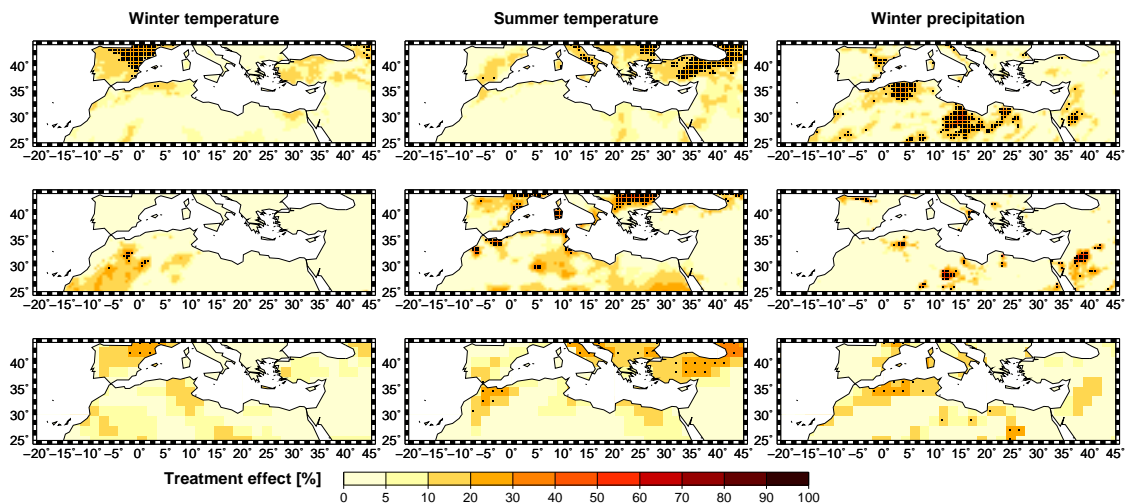


Figure 4.9: Results of one-way analysis of variance for three ensemble members of REMO (top), REMO applying 10-year running means (middle) and ECHAM5 (bottom) in 1961-1990: fraction of external treatment effect [%] for winter (left) and summer temperature (middle) and winter precipitation (right), applying a significance level of 5% (dots).

Generally, the common GHG signal of different REMO ensemble members in present-day temperature and precipitation variability of 1961-1990 is rather weak and constrained to smaller areas reaching maximum values of 20-40% over Spain and Turkey for winter and summer temperature, respectively, and over the Atlas mountains and Libya for winter precipitation. But for many areas and seasons most variance on the interannual time scale is still explained by internal variability, i.e. discrepancies in temperature and precipitation variance between different ensemble

members due to differing initial conditions, e.g. the strongly different NAO signals in winter temperature over Turkey and in winter precipitation over southern Europe (cf. subsection 4.1.6). ECHAM5 yields only minor differences to REMO signals in spatial pattern and intensity. But 10-year REMO running means reveal increased GHG signals due to smoothed interannual variations and slightly changed spatial patterns pointing at partly different impacts of initial conditions on interannual and interdecadal time scales.

4.2 Dynamical downscaling of long-term climate

In this section, the results of the analysis of Mediterranean temperature and precipitation means and trends in the long-term period 1961-2050 are presented. This time period is chosen for long-term analysis of trends and variance in order to allow the simulated GHG signal to emerge from interdecadal variability. Future projections for the different A1b and B1 emission scenarios are compared and dynamical downscaling from ECHAM5 to REMO simulations is investigated. The following subsections present the annual cycles of both temperature and precipitation for the future time period 2021-2050 compared to 1961-1990 and the seasonal trends for the long-term period 1961-2050. Furthermore, one-way and two-way analyses of variance are applied to investigate the signal-to-noise ratios of the long-term temperature and precipitation trends separately for the A1b and B1 emission scenarios and to determine the future change signal common to both scenarios, respectively.

4.2.1 Annual cycle

In this section, the annual cycles of temperature and precipitation in the two selected western and eastern Mediterranean regions, i.e. south-eastern Spain and central Turkey, are computed for the A1b and B1 emission scenarios of REMO and ECHAM5 ensemble means in the future time period 2021-2050 and compared to those of the present-day time period 1961-1990 (Fig. 4.10). For temperature, the future annual cycle of REMO shows in both regions temperature increases over all seasons compared to 1961-1990, especially in summer, with slightly stronger warming in the A1b emission scenario than in B1. ECHAM5 shows equal A1b and B1 warming patterns to REMO. The relationship between REMO and ECHAM5 annual cycles in 1961-1990 revealing higher ECHAM5 temperatures over Spain and higher and lower values over Turkey in summer and winter, respectively, further remains in 2021-2050 (Fig. 4.10, left). For precipitation, strong decreases of rainfall are prominent in the future annual cycles of REMO for nearly all months of spring,

summer and autumn in both regions slightly higher for A1b than for B1 compared to 1961-1990. In winter, the A1b scenario produces rather drying patterns except for some wetting over Turkey in December. Instead, the B1 scenario shows wetting over Turkey in the whole winter and over Spain in January. The drying and wetting patterns of ECHAM5 are mostly similar to those of REMO except for some higher drying in B1 than A1b in March and April over Spain and no wetting over Turkey in January and February in B1. ECHAM5 yields lower future rainfall than REMO over both regions in summer and higher values over Turkey in winter in 2021-2050 (Fig. 4.10, right). This difference between REMO and ECHAM5 rainfall is consistent to present-day annual cycles in 1961-1990. Thus, the annual cycle of temperature yields strong future warming over the whole year, especially in summer in the A1b emission scenario. The annual cycle of precipitation shows future drying in nearly all months, particularly in A1b, with some wetting patterns in winter in B1. Thus, future warming and drying is projected for nearly all seasons with stronger intensity in A1b than B1 but for winter the kind of precipitation change seems to depend on the selected emission scenario. ECHAM5 reveals mostly similar temperature and precipitation change patterns to REMO but present-day systematic differences between ECHAM5 and REMO annual cycles seem to remain in future time periods.

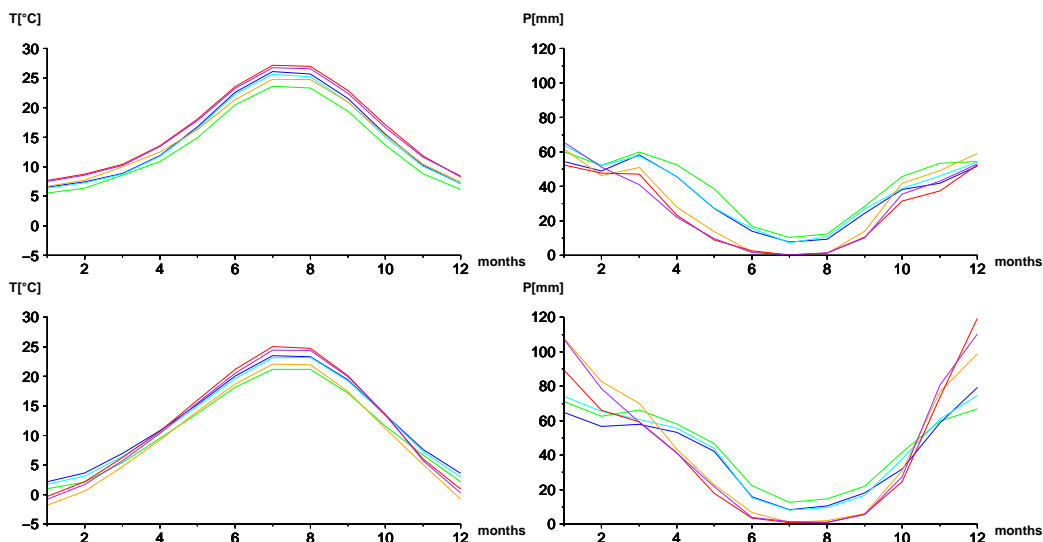


Figure 4.10: Annual cycle of temperature (left) and precipitation (right) over south-eastern Spain (top) and central Turkey (bottom) for REMO (green) and ECHAM5 (orange) in 1961-1990 and REMO for A1b (blue) and B1 (cyan) emission scenarios and ECHAM5 for A1b (red) and B1 (purple) in 2021-2050.

4.2.2 Climate trends

Fig. 4.11 depicts the long-term seasonal temperature trends for the A1b and B1 emission scenarios of the REMO ensemble mean and for the A1b scenario of ECHAM5 in the long-term period 1961-2050. Generally, REMO yields a strong and significant warming over the whole Mediterranean in all seasons and scenarios. The temperature increase in the A1b emission scenario reaches 1-3°C in winter with maxima over eastern Turkey and 2-4°C in summer with highest values over the Atlas mountains, southern Europe and Turkey (Fig. 4.11, top). The B1 emission scenario shows equal spatial patterns of change but smaller warming intensities of 0.5-2°C in winter and 1.5-3°C in summer (Fig. 4.11, middle). ECHAM5 produces a similar significant warming pattern over the whole area but 0.5-1°C stronger temperature trends over Africa, Near and Middle East in both seasons and scenarios (Fig. 4.11, bottom). Thus, a strong and significant future warming can be stated over the whole Mediterranean area, especially in summer. The A1b emission scenario yields stronger warming than the B1 scenario revealing larger temperature changes with higher GHG forcing and ECHAM5 shows stronger temperature increases than REMO over the southern Mediterranean probably due to regional-scale cooling mechanisms in REMO, e.g. impacts of local wind systems or land use changes.

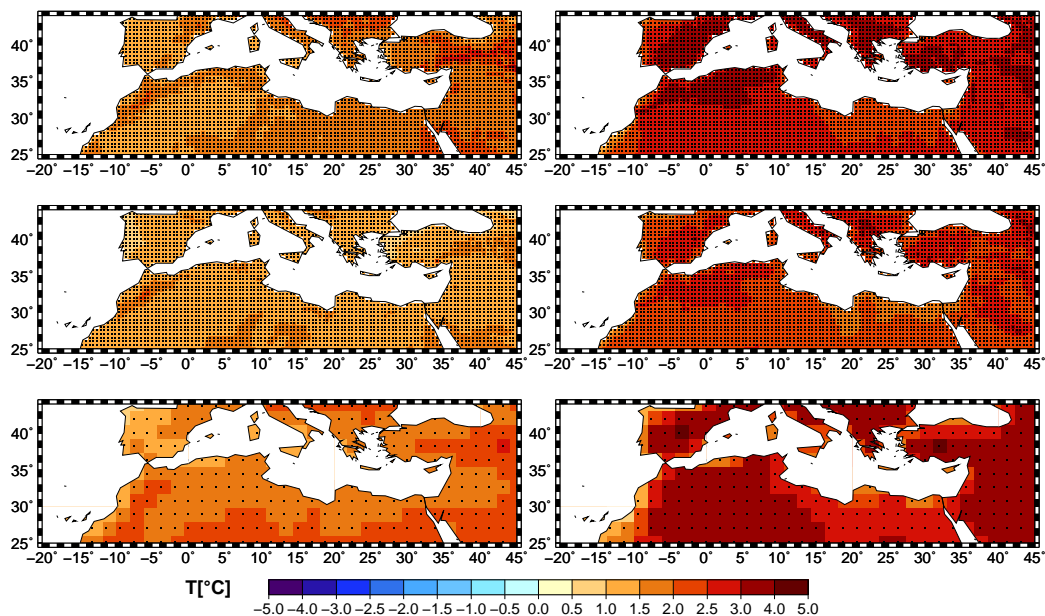


Figure 4.11: Comparison of winter (left) and summer (right) temperature trends of REMO during 1961-2050 for the A1b (top) and B1 emission scenarios (middle) with corresponding ECHAM5 trends for A1b (bottom), applying a significance level of 5% (dots).

Furthermore, the corresponding precipitation trends of REMO and ECHAM5 in the long-term period 1961-2050 are shown in Fig. 4.12. In winter, REMO produces

rather strong and significant drying patterns over the Atlas mountains, north-eastern Africa, the Near and Middle East and southern Turkey with some maxima reaching -200mm. Further strong but not significant drying trends can be found in most of southern Europe. Wetting patterns up to +200mm are prominent over the western Balkans, northern Turkey and the Caucasus region. In summer, strong and significant drying patterns of up to -100mm can be stated over the Atlas mountains, southern Europe and Turkey (Fig. 4.12, top). The B1 scenario shows slightly smaller drying trends over the northern and southern Mediterranean in summer and winter, respectively, and stronger wetting patterns over the Iberian Peninsula, the western Balkans, Turkey and the Caucasus region in winter. Significance of wetting trends is only reached over the eastern regions but the difference between the emission scenarios over the Iberian Peninsula is rather strong (Fig. 4.12, middle). ECHAM5 yields an equal spatial distribution of precipitation change but smaller intensities over the Atlas mountains, southern Europe and Turkey in summer and over the Middle East and northern Turkey in winter and less topographic details in winter, e.g. concerning the mountain ranges over the Balkans and Turkey (Fig. 4.12, bottom). The strong wetting pattern over Spain in B1 is hardly prominent in ECHAM5 (not shown). Generally, future precipitation change reveals strong drying trends over southern Europe and Turkey in summer moving towards northern Africa and Arabia in winter, especially in A1b, allowing winter wetting patterns

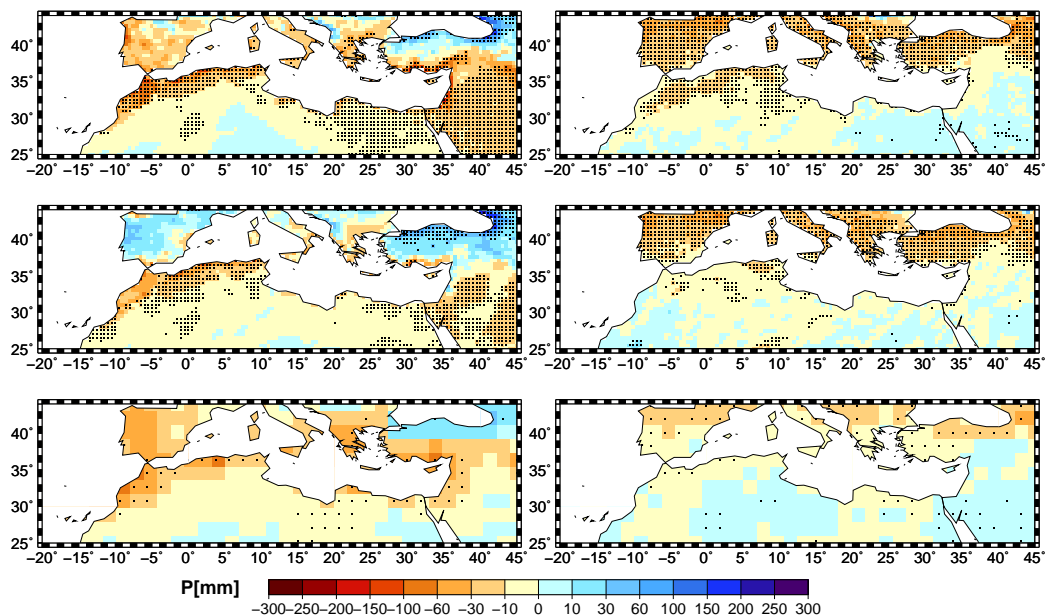


Figure 4.12: Comparison of winter (left) and summer (right) precipitation trends of REMO during 1961-2050 for the A1b (top) and B1 emission scenarios (middle) with corresponding ECHAM5 trends for A1b (bottom), applying a significance level of 5% (dots).

over southern Europe and Turkey, particularly in B1. Future drying is larger in A1b than in B1 due to stronger GHG impacts and the related stronger northerly shift of North Atlantic storm tracks. But the larger winter wetting over the northern Mediterranean in B1 contradicts to this assumption of larger rainfall changes with higher GHG forcing and might probably result from local thermodynamic effects of a warmer atmosphere, especially represented in REMO, exceeding the impacts of slightly decreasing storm tracks. Furthermore, REMO shows higher rainfall change intensities and improved small-scale topographic details of precipitation change patterns, e.g. over mountains ranges or coastlines, compared to ECHAM5.

4.2.3 One-way Analysis of Variance

The results of one-way analyses of variance present the signal-to-noise ratios of the long-term temperature and precipitation trends of REMO and ECHAM5 in 1961-2050 separately for each A1b and B1 emission scenario. Fig. 4.13 depicts the external treatment effects from one-way analyses of variance for REMO temperature for the A1b and B1 emission scenarios in 1961-2050 and for 10-year REMO running means for A1b. Both seasons yield strong and significant GHG signals over the whole Mediterranean emerging to 40-50% over north-eastern Africa and Middle East in winter and 60-70% over Morocco and Middle East in summer for the A1b emission scenario of REMO (Fig. 4.13, top). The B1 scenario presents a rather similar spatial distribution but 10-20% smaller signals in both seasons even revealing weak and not significant GHG signals over the Balkans and Turkey in winter (Fig. 4.13, middle). The 10-year running means of REMO reach much higher GHG signals exceeding 80% and 90% over the southern Mediterranean in winter and summer in A1b, respectively. The spatial pattern equals that of original REMO data (Fig. 4.13, bottom). The ECHAM5 results are not shown but reach slightly higher GHG signals than REMO, especially over the southern Mediterranean in winter. Thus, the GHG signals for temperature in 1961-2050 are strong and significant over the whole area, especially for the A1b scenario over the southern Mediterranean in summer, agreeing well with long-term temperature trends (see subsection 4.2.2). But areas of highest GHG signals in the southern Mediterranean do not necessarily match areas of strongest long-term trends in the northern Mediterranean due to larger impacts of initial conditions over the northern than southern areas. Highest values are reached for REMO running means due to smoothed interannual variations. ECHAM5 yields partly higher GHG signals than REMO agreeing with slightly stronger temperature trends.

Furthermore, Fig. 4.14 shows the corresponding external treatment effects from

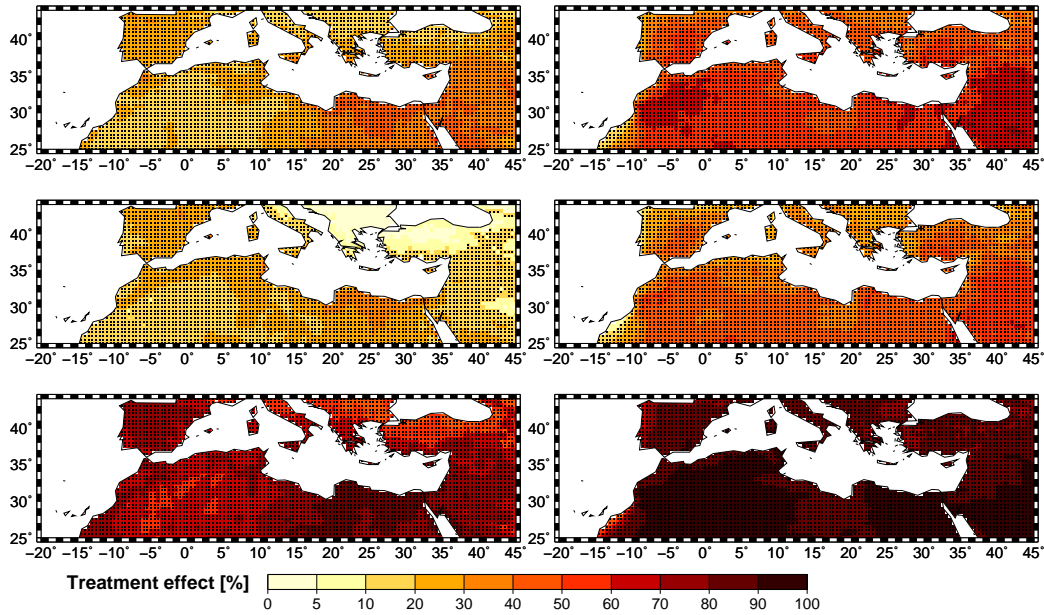


Figure 4.13: Results of one-way analysis of variance for three ensemble members of REMO for the A1b (top) and B1 emission scenarios (middle) and REMO applying 10-year running means for A1b (bottom) in 1961-2050: fraction of external treatment effect [%] for temperature in winter (left) and summer (right), applying a significance level of 5% (dots).

one-way analysis of variance for REMO precipitation in 1961-2050. REMO reaches only small but significant, local GHG signals of up to 20-30% over north-eastern Africa and the Middle East in winter and over northern Spain in summer in the A1b scenario (Fig. 4.14, top). The B1 scenario shows rather equal results for summer but the signals are shifted towards north-western Africa and Spain in winter (Fig. 4.14, middle). The 10-year running means yield increased signals of up to 40-60% over north-eastern Africa and the Middle East in winter and over southern Europe in summer in A1b (Fig. 4.14, bottom). ECHAM5 results yield small signals of 10-20% with partly different spatial distributions to REMO. Generally, GHG signals for precipitation are smaller than for temperature and more locally distributed due to strong impacts of internal variability. But areas of highest signals mostly fit quite well with areas of highest precipitation trends for both REMO and ECHAM5, i.e. over the northern Mediterranean in summer and over the southern Mediterranean in winter (see subsection 4.2.2). Differences in the spatial distribution of winter signals between the A1b and B1 emission scenarios agree mostly well with corresponding winter rainfall trend differences. The agreement with precipitation trends is even higher for REMO running means yielding highest GHG signals due to reduced small-scale variability. ECHAM5 reveals partly different spatial signal patterns than REMO probably pointing at differing impacts of initial conditions on REMO and ECHAM5 precipitation.

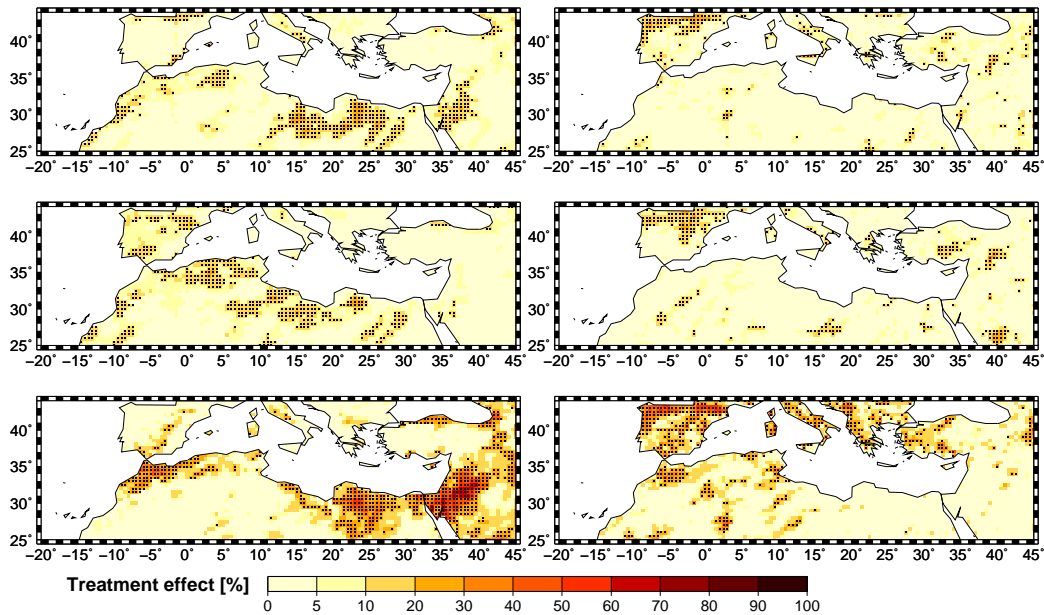


Figure 4.14: Results of one-way analysis of variance for three ensemble members of REMO for the A1b (top) and B1 emission scenarios (middle) and REMO applying 10-year running means for A1b (bottom) in 1961-2050: fraction of external treatment effect [%] for precipitation in winter (left) and summer (right), applying a significance level of 5% (dots).

4.2.4 Two-way Analysis of Variance

Finally, the results of the two-way analysis of variance for temperature of REMO, ECHAM5 and REMO applying 10-year running means in the long-term time period 1961-2050 are discussed (Fig. 4.15). The external treatment effect describes the GHG signal common to both A1b and B1 emission scenarios. For both seasons, the common GHG signals of REMO lie in between the one-way analysis of variance signals for the two emission scenarios with maximum values of 50% over north-eastern Africa in winter and 70% over Morocco and the Middle East in summer (Fig. 4.15, top). Adequately to the one-way analysis of variance results, the 10-year running means of REMO reach much higher common GHG signals exceeding even values of 80-90% (not shown), and ECHAM5 yields slightly higher signals than REMO, especially in winter (Fig. 4.15, middle).

The agreement between the external treatment effects of the one-way and two-way analyses of variance is so strong because the differences between the A1b and B1 emission scenarios are rather small in simulating Mediterranean temperature in 1961-2050. The scenarios are equal for the present-day time period 1961-2000 and yield similar spatial patterns of future temperature change with slightly different intensities in 2001-2050. Thus, the block and interaction effects of the two-way analysis of variance, i.e. the time independent and dependent impacts of the differ-

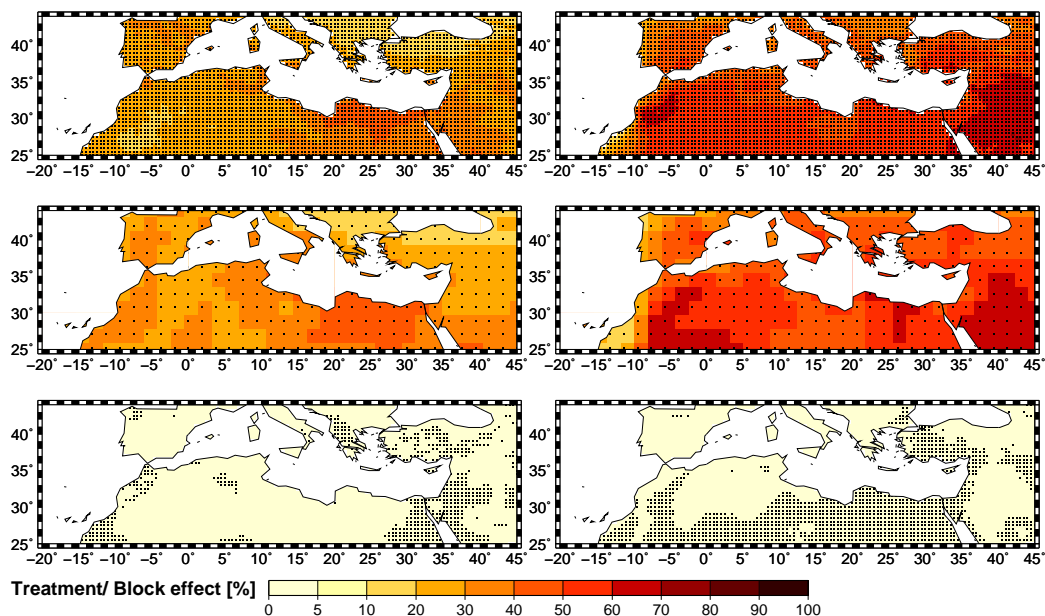


Figure 4.15: Results of two-way analysis of variance in 1961-2050: fraction of external treatment effect [%] for three ensemble members of REMO (top) and ECHAM5 (middle) and fraction of block effect [%] for REMO applying 10-year running means (bottom) for temperature in winter (left) and summer (right), applying a significance level of 5% (dots).

ent emission scenarios, are smaller than 5% over the whole Mediterranean reaching hardly any significance for REMO and ECHAM5 and are not shown here. For the REMO running means, the size of both effects remains small but the significance increases over the eastern Mediterranean in winter and over the southern Mediterranean in summer, especially for the block effect, due to the reduction of interannual variations (Fig. 4.15, bottom). Sensitivity tests show that two-way analyses of variance for 2001-2050 yield higher block and interaction effects with smaller common GHG signals due to increased differences between A1b and B1 emission scenarios in shorter future time periods. Generally, the common GHG signals of both A1b and B1 emission scenarios for temperature in 1961-2050 are strong and significant over the whole Mediterranean area and lie in between the single GHG signals of these scenarios from one-way analysis of variance. Furthermore, both block and interaction effects are very small and mostly not significant except for some significance for REMO running means denoting only slight differences between the A1b and B1 emission scenarios in projecting GHG signals for Mediterranean temperature.

Fig. 4.16 depicts the corresponding results of the two-way analysis of variance for precipitation in 1961-2050. The common GHG signal of both A1b and B1 emission scenarios of REMO reaches significance over nearly the whole area and maxima of 20-40% over the southern and northern Mediterranean in winter and summer, respectively (Fig. 4.16, top). The 10-year running means yield equal spatial pat-

terns with increased GHG signals of up to 50-60% but less significance (not shown). ECHAM5 shows slightly smaller signals of similar spatial distribution (Fig. 4.16, middle). Thus, the common GHG signals of the two-way analysis of variance reveal similar maxima to the single A1b and B1 signals of the one-way analyses of variance but are more extended over large Mediterranean regions with increased significance. But this amplification of GHG signals should be interpreted with caution probably denoting a statistical artefact which results from doubling ensemble simulations of small rainfall trends from two rather similar future emission scenarios.

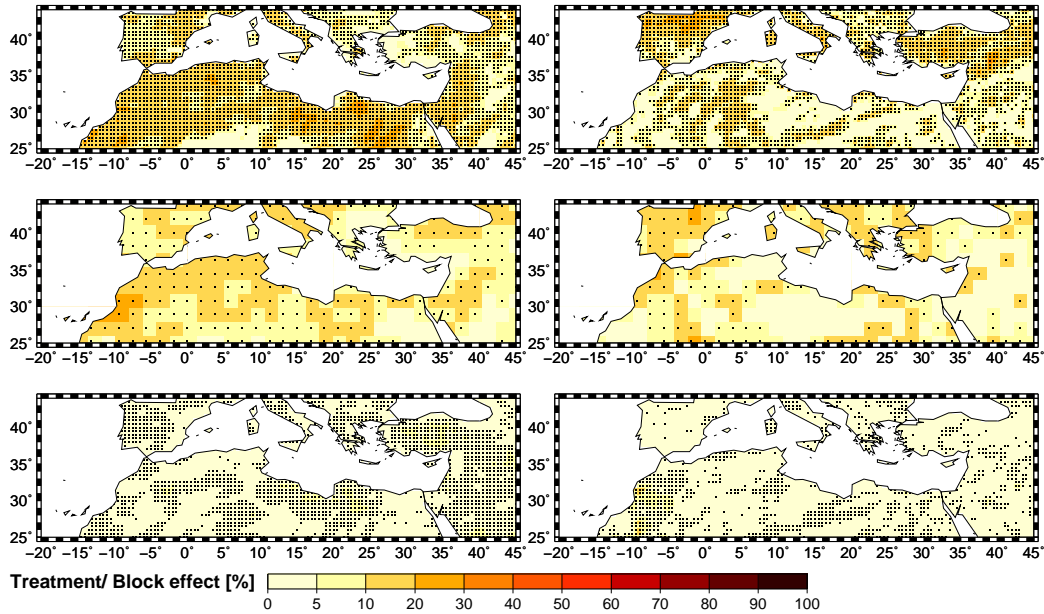


Figure 4.16: Results of two-way analysis of variance in 1961-2050: fraction of external treatment effect [%] for three ensemble members of REMO (top) and ECHAM5 (middle) and fraction of block effect [%] for REMO applying 10-year running means (bottom) for precipitation in winter (left) and summer (right), applying a significance level of 5% (dots).

As for temperature, the block and interaction effects of REMO and ECHAM5 are mostly not significant and smaller than 5% over the whole area. But the significance of both effects strengthens for REMO running means, especially for the block effect. Furthermore, the variance accounted for by the block effect increases to 10-20% over Libya and central Turkey in winter and over Morocco in summer for REMO running means denoting regions of different long-term precipitation means in A1b and B1 emission scenarios (Fig. 4.16, bottom) and that by the interaction effect increases to 20-30% over the Iberian Peninsula in winter identifying regions of different long-term precipitation trends (not shown). Thus, the common GHG signal of both emission scenarios for precipitation is weaker than for temperature but reaches 20-40% and expanded significance over the southern and northern Mediterranean in winter and summer, respectively, agreeing well with regions of strongest precipitation trends in

1961-2050 (see subsection 4.2.2). ECHAM5 yields slightly smaller GHG signals than REMO matching with smaller precipitation trends. Block and interaction effects are mostly small and not significant but several time independent and dependent impacts of the different A1b and B1 emission scenarios can be stated for the running means of REMO due to smoothed interannual variability denoting differences in long-term precipitation means and trends, respectively.

5 Impact of mid-latitude circulation on temperature and precipitation

The previous chapter reveals good agreement between E-OBS and REMO climatological means of temperature and precipitation but discrepancies between observed and simulated present-day trends for 1961-1990. Thus, it seems that the only real boundary condition CO_2 in this model-into-model-approach does not clearly prevail over other drivers influencing temperature and precipitation in the Mediterranean area. Like many former studies have shown (see chapter 1) one of the main drivers in the Mediterranean area is the mid-latitude circulation variability, especially in winter. In this chapter, the impacts of mid-latitude circulation dynamics on Mediterranean temperature and precipitation variability are analysed, and differences between observed and simulated large-scale modes of variation are investigated to understand and evaluate the discrepancies between observed and simulated trends in 1961-1990. Furthermore, the influences of large-scale circulation and residual circulation-unrelated drivers, e.g. CO_2 , are separated. The question is analysed if the predictability of a RCM driven by a GCM with the only real boundary condition CO_2 increases after removal of the impact of mid-latitude circulation variability on temperature and precipitation. Finally, the impact of mid-latitude circulation dynamics on temperature and precipitation variability is investigated for the long-term period 1961-2050 in order to reveal how the influences of present-day modes of variation evolve in future time periods compared to those of circulation-unrelated drivers, e.g. GHGs. This long-term period is chosen here in accordance to the results of trend analysis to allow the simulated GHG signal to emerge from interdecadal variability. The following sections present the corresponding results for the present-day and long-term time periods 1961-1990 and 1961-2050.

5.1 Mid-latitude circulation in present-day climate

S-mode PCA is applied to seasonal NCEP and ECHAM5 sea level pressure anomalies over the geographical area extending from 70° W to 50° E and from 20° N to 70° N in 1961-1990 and the leading ten PCs are used to represent the most important observed and simulated modes of variation of large-scale mid-latitude circulation dynamics. For better comparison, the ECHAM5 ensemble mean data have been interpolated to the 2.5° NCEP resolution. The modes of variation from ECHAM5 are calculated separately and not projected onto those of NCEP to reach comparable patterns because we aim at comparing the impacts of mid-latitude circulation and residual circulation-unrelated drivers, e.g. GHGs, that are inherent in each dataset. Furthermore, a cross-validated stepwise multiple regression between seasonal E-OBS or REMO temperature and precipitation and large-scale NCEP or ECHAM5 modes of variation is performed for 1961-1990, respectively, to determine the impact of mid-latitude circulation dynamics on Mediterranean temperature and precipitation variability. Finally, the original temperature and precipitation trends are separated into circulation-related and circulation-unrelated trends and compared between models and observations. The following subsections describe the corresponding results of PCA, multiple regression and trend separation for observations and models and some further analysis on the dependence of simulated circulation dynamics on initial conditions. These results have been submitted for publication in the *International Journal of Climatology*. Thus, the description closely follows this manuscript (PAXIAN et al., 2011).

5.1.1 Observed and simulated mid-latitude circulation variability

This subsection describes the validation of the simulated mid-latitude circulation variability of the winter and summer seasons in 1961-1990 with observations, i.e. the leading ten PCs of ECHAM5 and NCEP seasonal sea level pressures are compared with each other. According to literature (BARNSTON and LIVEZEY, 1987; TRIGO et al., 2006b; NOAA-CPC, 2010) the most important large-scale modes of northern Hemisphere atmospheric circulation impacting on the Mediterranean climate are the NAO, the EA, the EA/WR (EU2) and the SCAND patterns (EU1). Fig. 5.1 shows the eigenvector loadings (left) derived from NCEP and the PC time series (right) of both NCEP and ECHAM5 of those PCs which are identified by the statistical model as the most influential large-scale modes of variation for Mediterranean temperature and precipitation (see subsection 5.1.2). Corresponding

ECHAM5 eigenvector loadings are not shown because they are basically consistent with those of NCEP reanalyses. In general, ECHAM5 is characterized by leading PCs with lower variability in both eigenvector loadings and PC time series than those from NCEP because the ensemble mean of three different runs is analysed. But the PCs of individual runs show similarly strong variability to observations (cf. Fig. 5.7, PAXIAN et al. (2011)).

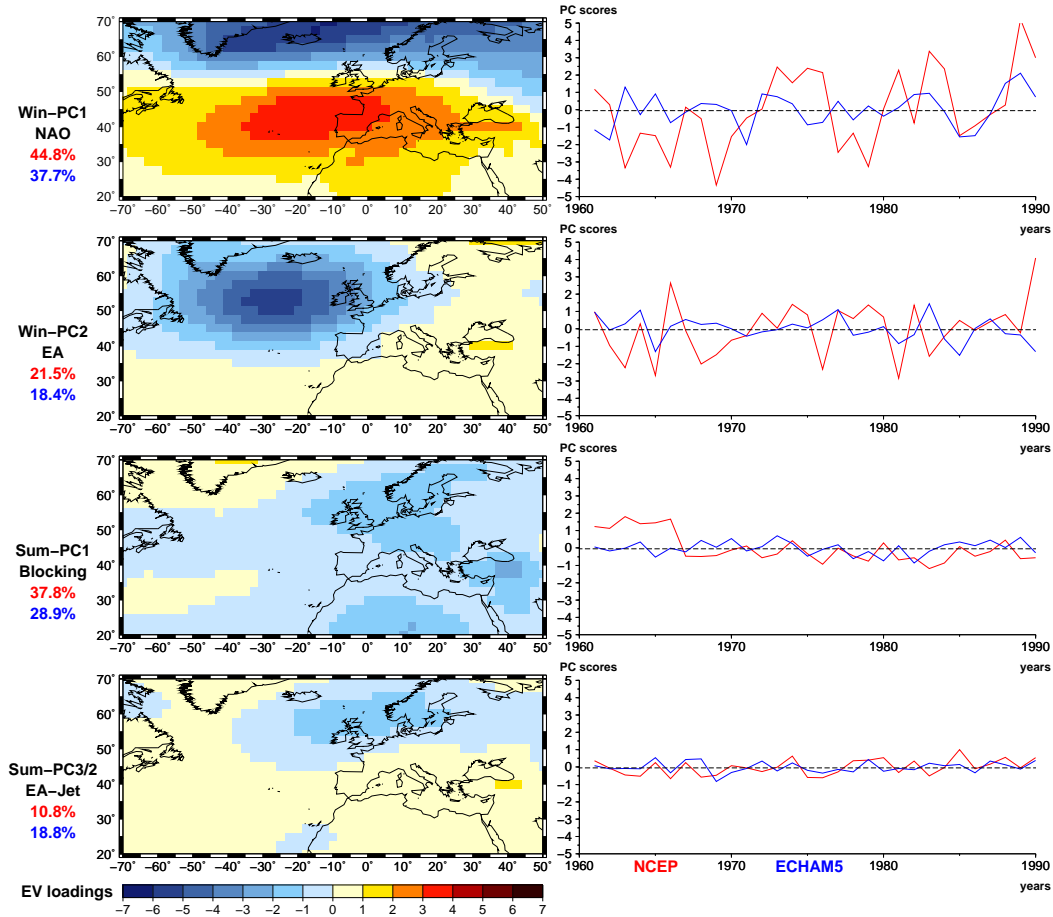


Figure 5.1: Mid-latitude large-scale modes of variation during 1961-1990: Eigenvector (EV) loadings derived from NCEP with explained variances [%] for NCEP (red) and ECHAM5 (blue) (left) and PC time series of NCEP (red) and ECHAM5 (blue) (right) of those PCs with highest impact (mostly first and second PCs) on winter and summer Mediterranean temperature and precipitation. Sum-PC3/2 signifies the third PC of NCEP and the second PC of ECHAM5 in summer (see text for further explanation).

The leading winter modes of variation of both model and observations show high variability and fit well with those from literature. The winter PCs of NCEP describe a strengthening NAO in the first PC and a recently increasing EA pattern in the second PC (Fig. 5.1, first and second row). The third and fourth PCs have been identified as the SCAND and EA/WR patterns showing no recent trend and a rather weakening tendency, respectively. These four modes of variation explain

44.8%, 21.5%, 10.1% and 9.0% of the total variance of the NCEP sea level pressure anomalies. The identification of these modes is confirmed by correlations of the resulting NCEP PC time series to the corresponding seasonal means of the monthly teleconnection indices from NOAA-CPC (2010) yielding coefficients of 0.89 (NAO), 0.83 (EA), 0.64 (SCAND) and 0.70 (EAWR). The ECHAM5 winter circulation is characterized by the same four leading modes of variation but reveals different temporal evolutions showing only a slight NAO increase and an EA pattern decrease (Fig. 5.1, first and second row, right). The SCAND and EA/WR patterns yield no trend and a slightly decreasing tendency, respectively. The variances accounted for by these modes yield 37.7%, 18.4%, 15.2% and 7.8% agreeing well with observations. The spatial configuration of the ECHAM5 modes of variation is also quite similar to the observed one but the centre of action of the EA pattern lies further east over Great Britain and the SCAND pattern centre over Spain is more intensive compared to the corresponding NCEP patterns. ECHAM5 PC time series are not correlated with those of NOAA-CPC (2010) for pattern identification because the simulated modes of variation are mostly not in phase with observations. The residual modes explain less amounts of total variance, are more difficult to interpret due to mixed structures of eigenvector loadings and are thus, not discussed here (PAXIAN et al., 2011).

The leading PCs of mid-latitude summer circulation are characterized by lower variability in both eigenvector loadings and PC time series. In NCEP summer circulation, the first PC shows wide-spread low pressure extending over whole Europe, Turkey and northern Africa that can be interpreted as some kind of blocking pattern with recently weakening intensity (Fig. 5.1, third row). But interpretation is difficult because there are also some similarities to the Subtropical Zonal (SZ) pattern of BARNSTON and LIVEZEY (1987) and the correlation to the NOAA-CPC (2010) teleconnection indices yields a correlation coefficient of -0.40 to the NAO. The second PC describes a recently decreasing summer NAO pattern, and the third PC in Fig. 5.1 (forth row) represents a slightly increasing EA-Jet pattern (DÜNKELOH and JACOBET, 2003; NOAA-CPC, 2010); this can be confirmed by correlation coefficients of 0.76 and 0.62 to the corresponding NOAA-CPC (2010) teleconnection indices, respectively. These modes of variation account for 37.8%, 18.0% and 10.8% of total sea level pressure variance. The first summer PC of ECHAM5 resembles the first NCEP PC but shows less variability of low pressures in the eigenvector loadings, especially over North Africa and Turkey, and slightly more variability of high pressures over Greenland. Thus, according to NCEP this ECHAM5 pattern is interpreted as a slight blocking pattern as well. Furthermore, we can see the EA-Jet

pattern in the second PC centred further north-east over the Scandinavian Peninsula than in NCEP and a slight summer version of the EA pattern in the third PC. The NAO and SZ patterns with distinct centres over the northern Atlantic and North Africa, respectively, can hardly be found in ECHAM5. All simulated summer PC time series show only negligible recent trends, and explained variances of the mentioned patterns reach values of 28.9%, 18.8% and 13.8% (Fig. 5.1, third and fourth row, right). Further modes of variation yield less spatial structures and temporal variability and are rather difficult to interpret. Generally, we can state rather similar spatial patterns but strong differences in temporal evolutions when comparing major modes of variation of simulated and observed mid-latitude circulation variability in the Mediterranean area in winter and summer of 1961-1990 (PAXIAN et al., 2011).

5.1.2 Impact of mid-latitude circulation on climate

Having identified differences in temporal evolution between simulated and observed mid-latitude circulation dynamics this section determines the kind and strength of the impact of mid-latitude circulation variability on Mediterranean temperature and precipitation. Fig. 5.2 presents the results of the cross-validated stepwise multiple regression between regional E-OBS or REMO temperature and large-scale NCEP or ECHAM5 modes of variation for 1961-1990, respectively. For observed winter temperature, the maximum variance accounted for by all predictors of the statistical model reaches 70-80% over Spain and the Atlas Mountains and 30-50% over the eastern Mediterranean area. The first predictors are the EA pattern in the western Mediterranean and the NAO over Turkey yielding robustness values of over 0.9 and strong positive and negative correlations to winter temperature, respectively. Further influence can be stated by the EA/WR pattern over Bulgaria and northern Greece and by the NAO as second predictor over the Atlas mountains reaching slightly lower robustness values (Fig. 5.2, first row). The simulated winter temperature shows similar multiple regression results to observations but an overlapping influence of the EA pattern and the NAO over Turkey as first and second predictors and no impact of the EA/WR pattern over the eastern Balkans. The region of maximum explained variances of 70-80% is shifted further east towards the central Mediterranean (Fig. 5.2, second row, PAXIAN et al. (2011)).

In summer, most observed temperature variance (60-70%) is explained by the fifth PC of NCEP (interpreted as summer version of SCAND) over the Iberian Peninsula. Further influences are obvious by the EA-Jet over Italy and the Atlas Mountains and by the blocking pattern over the Balkans and western Turkey reaching maximum explained variances of 30-50%. All these major patterns yield robustness values over

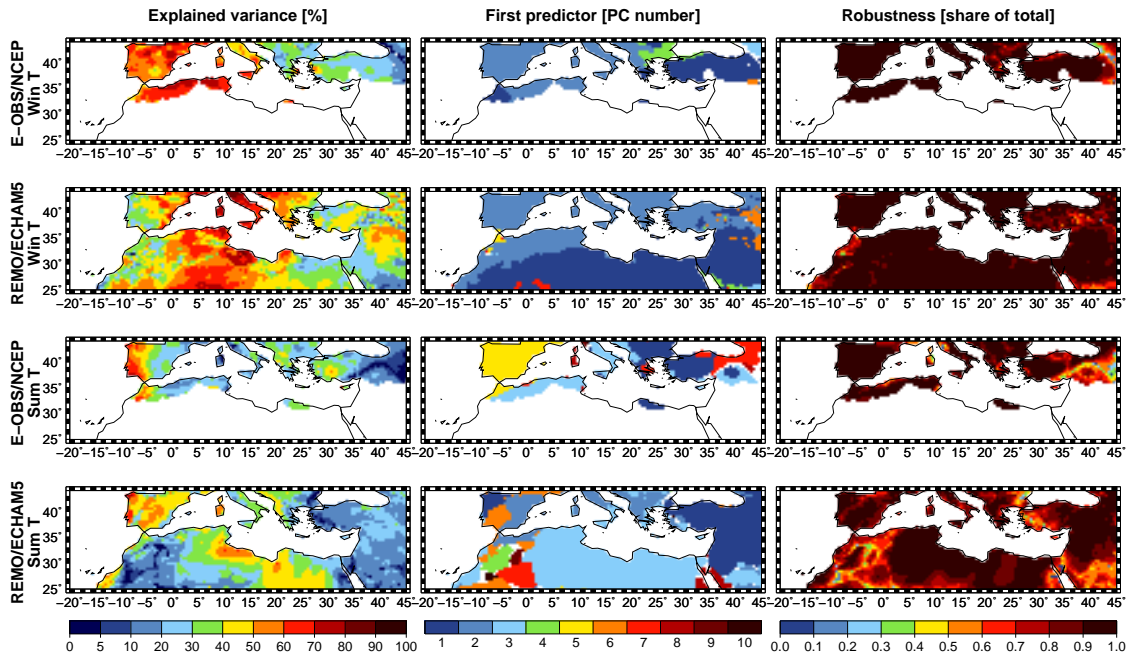


Figure 5.2: Results of cross-validated stepwise multiple regression based on E-OBS or REMO predictands and NCEP or ECHAM5 predictors for winter and summer temperature in 1961-1990: temperature variance explained by all circulation predictors selected by the statistical model (left), PC number of first circulation predictor (middle) and its robustness over 1,000 iterations (right).

90% except for eastern Turkey with only 50-70% (Fig. 5.2, third row). The simulated summer temperature shows correlations to the EA-Jet over southern Europe, to the slight blocking pattern over Galicia, Turkey and the Middle East and to the summer EA pattern over northern Africa yielding maximum explained variances by all predictors of 50-60% over the Iberian Peninsula and Libya. Most patterns reach robustness values over 80%, other regions like western Turkey, Saudi-Arabia and north-western Africa of only 50-60% (Fig. 5.2, fourth row). Generally, the multiple regression results for temperature reveal rather good agreement between observed and simulated major circulation predictors, e.g. the NAO and EA patterns in winter and the EA-Jet and blocking patterns in summer, featuring homogeneous and strong correlations between Mediterranean temperature and mid-latitude circulation, especially over the western and central areas in winter (PAXIAN et al., 2011).

Fig. 5.3 depicts the corresponding multiple regression results for precipitation in 1961-1990. For observed winter precipitation, maximum variance explained by all predictors reaches up to 70-80% over western Turkey and the Iberian and Balkan Peninsulas. The NAO is identified as the first predictor over southern Europe and some Turkish regions and there is some further influence over Turkey by the EA and SCAND patterns. All these patterns yield strong negative correlations to winter

precipitation and the robustness values mostly exceed 0.9. In eastern Turkey and the Near East we further find impacts of several less important modes of variation with robustness values reaching only 0.5-0.8. The NAO is also identified as second predictor over whole western Turkey likewise as the EA pattern over the Iberian Peninsula revealing negative and positive correlations to precipitation, respectively (Fig. 5.3, first row). Concerning simulated winter precipitation, the spatial pattern is more heterogeneous including influences of several PCs of higher order. The NAO impact is constrained to the Iberian Peninsula and the western coasts of Italy, the Balkans and Turkey. Further influences of the EA pattern over the Iberian Peninsula, of the SCAND pattern over southern Europe and north-western Africa and of the EA/WR pattern over the Middle East and western Sahara can be identified. These major patterns mostly reveal robustness values over 80%, and maximum explained variance reaches 70-80% over the Iberian Peninsula (Fig. 5.3, second row, PAXIAN et al. (2011)).

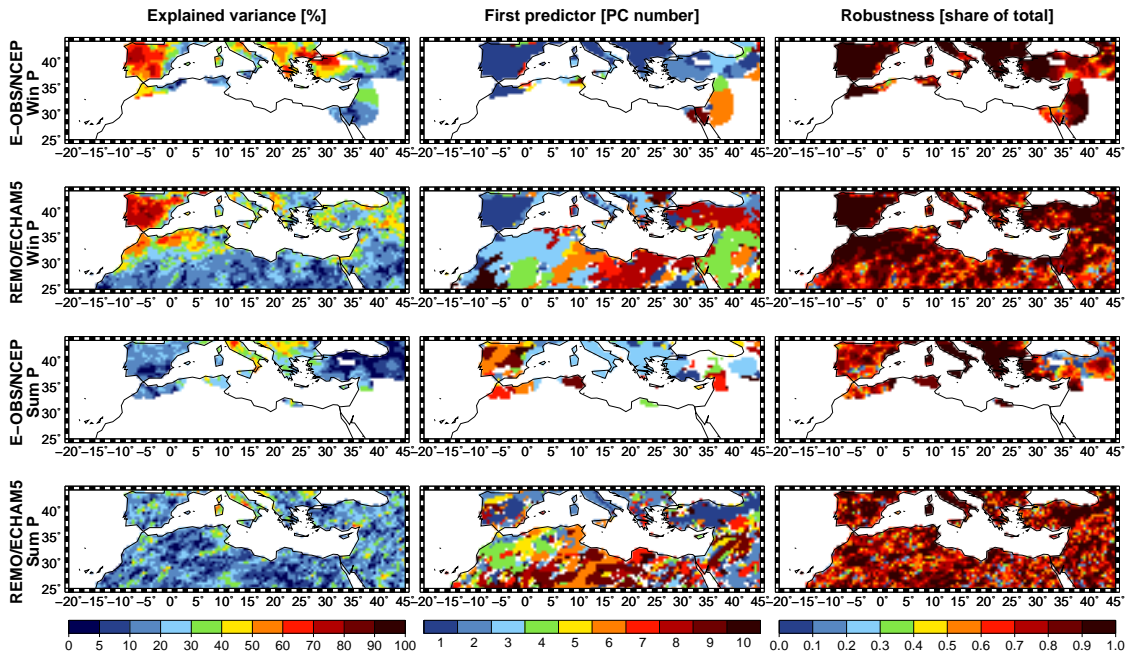


Figure 5.3: Results of cross-validated stepwise multiple regression based on E-OBS or REMO predictands and NCEP or ECHAM5 predictors for winter and summer precipitation in 1961-1990: precipitation variance explained by all circulation predictors selected by the statistical model (left), PC number of first circulation predictor (middle) and its robustness over 1,000 iterations (right).

During summer, correlation between large-scale modes of variation and Mediterranean precipitation is generally much lower. Concerning observations, strongest impacts occur by the EA-Jet pattern over Italy, the Balkans and Turkey reaching maximum explained variances of 40-50% and robustness values over 90%. Smaller influences can be stated by the blocking pattern over southern Turkey and by sev-

eral less important modes of variation over the Iberian Peninsula where robustness falls to 60-80% and variance accounted for to 10-30%. Over central Turkey and the Caucasus region no single circulation predictor can be found with robustness values higher than 50% denoting areas without any robust relationship between summer rainfall and mid-latitude circulation variability (Fig. 5.3, third row). For simulated summer precipitation, the geographical pattern is very heterogeneous with slight impacts of many PCs of higher order. There is a major influence of the EA-Jet pattern over southern Europe as well and further impacts of the blocking pattern over Spain and Turkey. But these patterns only account for 10-50% of total summer variance and show robustness values over 60% (Fig. 5.3, fourth row). Thus, the multiple regression results for precipitation are more heterogeneous than for temperature but still confirm the strong influence of large-scale circulation on the western and central Mediterranean area in winter. Some agreement between observed and simulated major circulation predictors can be stated, especially for the NAO in winter and the EA-Jet in summer. Though, it is weaker than for temperature due to the more heterogeneous influence pattern and the smaller impact of mid-latitude circulation on precipitation in many Mediterranean regions, especially in summer (PAXIAN et al., 2011).

5.1.3 Circulation-related and -unrelated climate trends

This section highlights the separation of the original temperature and precipitation trends of E-OBS and REMO into the circulation-related parts determined by multiple regression with mid-latitude circulation variability and the circulation-unrelated parts denoting the impacts of further influencing factors, e.g. GHGs. One major aim is to investigate the impacts of mid-latitude modes of variation on Mediterranean temperature and precipitation trends and to determine differences between observations and models to evaluate the discrepancies between simulated and observed trends in 1961-1990. Another aim is to analyse whether the prevailing model-into-model-approach shows higher predictability of Mediterranean temperature and precipitation in 1961-1990 when using observed CO_2 emissions as only real boundary condition after removal of the impact of mid-latitude circulation variability which strongly differs between model and observations (PAXIAN et al., 2011).

Fig. 5.4 compares the circulation-related and circulation-unrelated trends of REMO and E-OBS winter and summer temperatures for 1961-1990. For winter temperature, the E-OBS circulation part shows a very strong and significant cooling trend over Turkey and a partly significant warming trend over Spain and Italy which can be explained by an intense strengthening of the NAO and EA patterns,

respectively. The resulting circulation-unrelated part holds a relatively weak and not significant cooling trend over Turkey and only few trends over the western and central Mediterranean (Fig. 5.4, first row). The corresponding circulation part of REMO contains cooling trends over southern Europe due to a decreasing EA pattern and a significant cooling over Turkey and north-western Africa due to both increasing NAO and decreasing EA patterns. The circulation-unrelated part yields some significant warming patterns over northern Italy, the Balkans and north-western Africa (Fig. 5.4, second row). Thus, strong impacts of the NAO and EA patterns on winter temperature trends can be seen but differing observed and simulated temporal evolutions of these modes of variation induce differing circulation-related trends in E-OBS and REMO. But the circulation-unrelated observed and simulated temperature trends match each other better than the original trends (Fig. 4.5). However, some differences still remain over Turkey, Italy and the Atlas mountains. These minor discrepancies may be related to modes of variation neglected in the predictor setting, to differences in other factors contributing to interdecadal model variability, e.g. oceanic forcing, or to other boundary conditions or mechanisms (PAXIAN et al., 2011).

Concerning summer, the E-OBS circulation part holds strong and significant cooling trends over the Balkans and western Turkey and warming trends over south-eastern Turkey caused by a decreasing blocking pattern. A strong and significant warming trend over the Atlas mountains can be explained by an increasing EA-Jet pattern. The resulting circulation-unrelated part shows no cooling trend over Turkey any more and a decrease of western Mediterranean warming trends (Fig. 5.4, third row) in comparison to original data trends (Fig. 4.5). For REMO, hardly any impact of atmospheric circulation is detected and the circulation-unrelated trends (Fig. 5.4, fourth row) closely resemble the original data trends (Fig. 4.5). Thus, REMO does not reproduce the strong circulation-related trends of E-OBS due to impacts of the blocking and EA-Jet patterns. But the agreement of summer temperature trends strongly improves over the Atlas Mountains, the Balkans and western Turkey after removing impacts of mid-latitude circulation. Nevertheless, differences in intensity remain over Spain, the Atlas Mountains and eastern Turkey which can perhaps be explained by uncertainties and low density of high mountain station measurements. Different observational datasets differ over mountainous areas, e.g. the CRU observations do not show the strong E-OBS warming trend over eastern Turkey during 1961-1990 (cf. subsection 4.1.4, PAXIAN et al. (2011)).

The corresponding circulation-related and circulation-unrelated trends of REMO and E-OBS precipitation are presented in Fig. 5.5. In winter, the circulation part

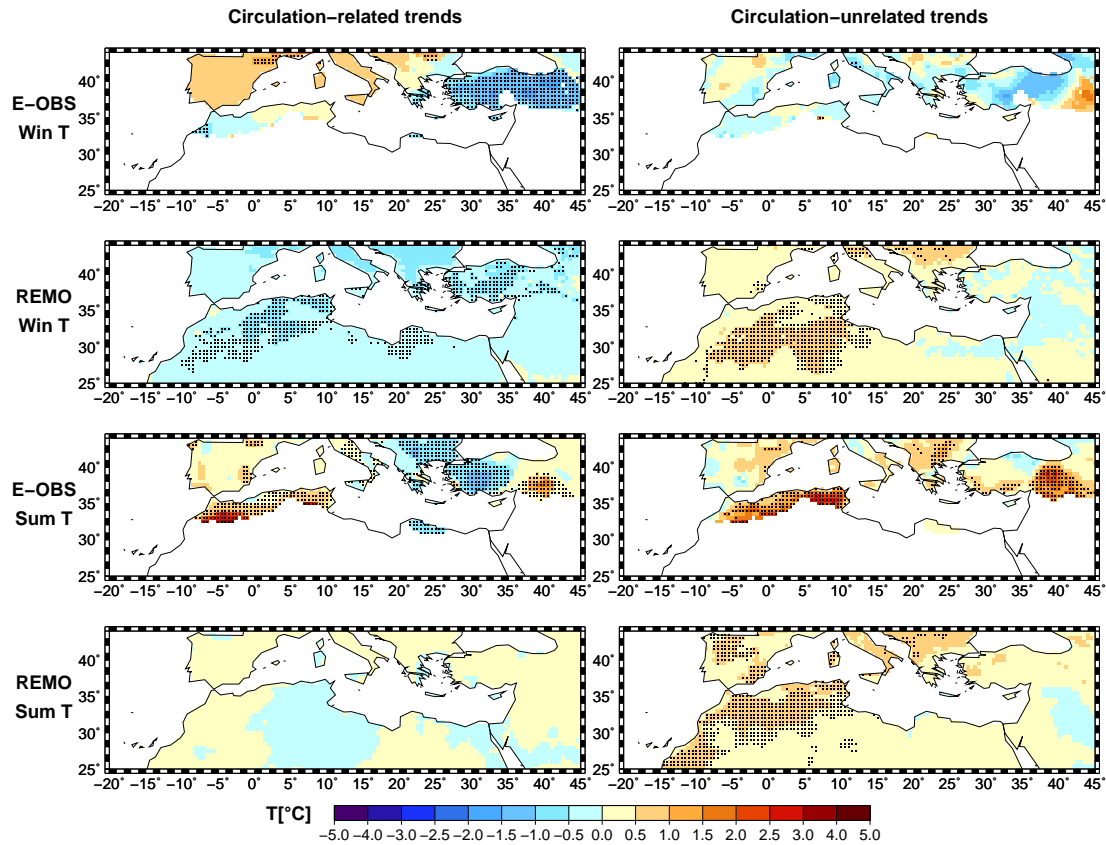


Figure 5.4: Comparison of circulation-related (left) and circulation-unrelated (right) winter and summer temperature trends during 1961-1990 between REMO and E-OBS after separation of influences by mid-latitude circulation variability, applying a significance level of 5% (dots).

of E-OBS holds strong and significant drying trends over whole southern Europe and Turkey due to a strong increase of the NAO and a combined increase of the NAO and EA patterns, respectively. The circulation-unrelated part yields only some small and not significant drying patterns over Greece and Turkey and several small wetting patterns over southern Europe (Fig. 5.5, first row). The circulation part of REMO shows a partly significant drying pattern constrained to the Iberian Peninsula due to both an increasing NAO and a decreasing EA pattern. The circulation-unrelated part shows smaller drying trends than the original data (Fig. 4.6) even yielding wetter conditions over the Iberian Peninsula, especially over Galicia (Fig. 5.5, second row). Thus, REMO reveals less and smaller circulation-related drying trends than E-OBS due to differing temporal evolutions of observed and simulated NAO and EA patterns. Nevertheless, agreement of winter precipitation trends can be strongly enhanced over southern Europe and Turkey by removing the impacts of mid-latitude circulation (PAXIAN et al., 2011).

Concerning summer, the circulation part of E-OBS shows only some weak but significant drying tendencies over Italy, Greece, western and eastern Turkey due to

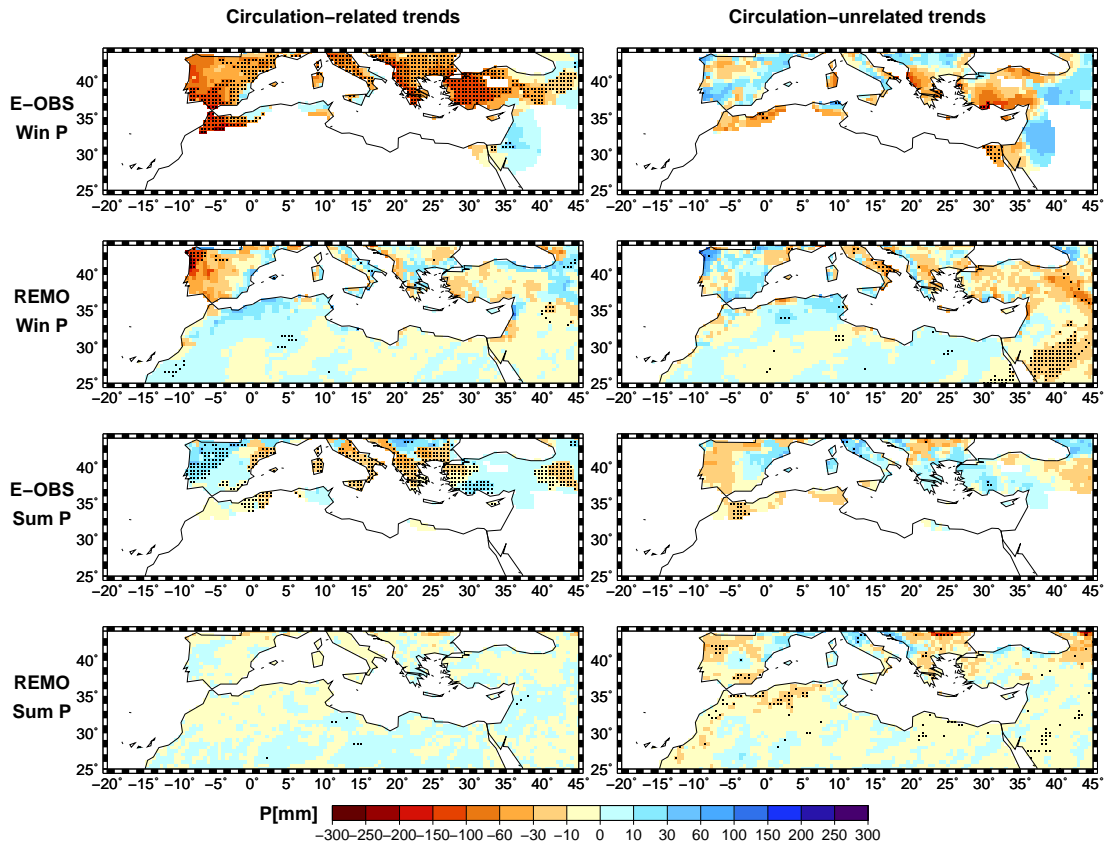


Figure 5.5: Comparison of circulation-related (left) and circulation-unrelated (right) winter and summer precipitation trends during 1961-1990 between REMO and E-OBS after separation of influences by mid-latitude circulation variability, applying a significance level of 5% (dots).

an increasing EA-Jet pattern and wetting tendencies over southern Turkey due to a decreasing blocking pattern. Further slight trends over the western Mediterranean are caused by PCs of higher order. The resulting circulation-unrelated part hardly shows any significant trend and strongly resembles original data trends with some differences over Italy and Greece (Fig. 4.6). Some E-OBS grid boxes in Egypt and Near East are omitted in multiple regression because they reveal less precipitation values greater than zero than the number of bootstrap years (Fig. 5.5, third row). For simulated summer precipitation, nearly no impact of mid-latitude circulation is prominent in the circulation-related part and the circulation-unrelated part (Fig. 5.5, fourth row) strongly equals the original data trends (Fig. 4.6). Consequently, only some small impacts of mid-latitude circulation can be stated for E-OBS summer precipitation but none for REMO. Thus, removing circulation-related parts of variability hardly shows any influence on summer precipitation trends (PAXIAN et al., 2011).

Thus, physical correlation between major mid-latitude circulation dynamics and Mediterranean temperature or precipitation variability agrees rather well between

models and observations. But mostly REMO does not reproduce the observed strong circulation-related trends due to differing temporal evolutions of mid-latitude modes of variation in ECHAM5 and NCEP. However, in most Mediterranean regions the predictability of this model-into-model-approach increases after removal of the impact of mid-latitude circulation variability. Areas with high agreement of circulation-unrelated trends, e.g. most of southern Europe in summer, indicate where the predictability of seasonal temperature and precipitation using observed CO_2 emissions reaches sufficiency if the impact of mid-latitude circulation variability is disregarded, i.e. observed changes in the background state of regional climate due to increasing atmospheric GHG concentrations are captured by REMO. Areas with strong disagreement between circulation-unrelated trends, e.g. eastern Turkey and the Near East, identify Mediterranean regions where temperature and precipitation variability is influenced as well by further factors, e.g. tropical climate dynamics or ocean-atmosphere interactions, and thus, the predictability using observed CO_2 emissions remains low. Additionally, disagreeing circulation-unrelated trends might indicate deficiencies or uncertainties in model performance or observational data, e.g. over mountainous areas. For instance, similar investigations of CRU observations reveal smaller intensities of winter drying over the whole Mediterranean, winter cooling over Turkey and summer warming over the Atlas Mountains and eastern Turkey in original trends and circulation-unrelated trends of 1961-1990 (cf. subsection 4.1.4) in contrast to the presented E-OBS results (PAXIAN et al., 2011).

As for climatological means the spring and autumn results are not depicted because the impacts of mid-latitude circulation variability on Mediterranean temperature and precipitation generally lie in between the winter and summer results concerning the maximum explained variances in multiple regression analysis. The agreement of spring and autumn temperature and precipitation trends between model and observations and thus, the predictability of this model-into-model-approach can as well be enhanced by removing the influences of mid-latitude circulation variability, i.e. mainly strong E-OBS cooling and drying trends due to impacts of the NAO and SCAND patterns. But this is not valid for spring temperature: The circulation-unrelated spring temperature trends of observations and model data fit a bit worse than the small and mostly not significant original data trends due to a cooling influence of an increasing SCAND pattern in southern Europe in E-OBS whose removal leads to a significant warming pattern in the circulation-unrelated part which is not reproduced in REMO. This situation is depicted in Fig. 5.6 and shows that a significant temperature or precipitation trend in the circulation-related part can counterbalance a significant equal-sized trend of opposite sign in the circulation-

unrelated part so that the original data does not reveal any significant trend at all. This example generally proves that the removal of the impact of mid-latitude circulation variability, i.e. the circulation-related part, from the original temperature and precipitation trends does not necessarily reduce the signal-to-noise-ratio but is able to reveal significant trends in the circulation-unrelated part that have been masked before by opposite trends forced by large-scale circulation (PAXIAN et al., 2011).

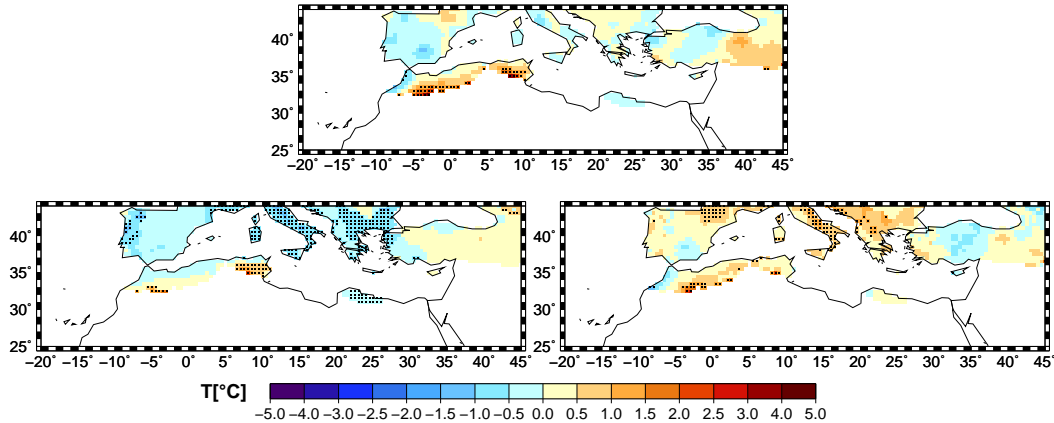


Figure 5.6: Comparison between original (top), circulation-related (left) and circulation-unrelated (right) spring temperature trends of E-OBS during 1961-1990 after separation of influences by mid-latitude circulation variability, applying a significance level of 5% (dots).

Finally, in order to compare the influences of large-scale circulation variability with those of smaller regional modes of variation the single impact of the winter NAO on Mediterranean temperature and precipitation variability in present-day times is compared to that of the regional winter MO pattern expressed by the Mediterranean Oscillation Index (MOI, CONTE et al. (1989)), i.e. the standardised 500hPa geopotential difference between Algiers and Cairo. The correlations of the NAO index determined as first PC of NCEP and ECHAM5 to E-OBS and REMO temperature or precipitation are built and compared to those of the station-based MOI derived from KLIWEX-MED cooperation and the simulated MOI for corresponding REMO station grid box values, respectively. Then, the same trend separation into circulation-related and circulation-unrelated trends is performed as for the multiple regression analysis. Mostly the MO yields higher correlation values to Mediterranean temperature and precipitation variability than the NAO probably due to the more regional focus but observed circulation-related trends are much lower due to a smaller observed MO increase in present-day times compared to the NAO. Simulated MO and circulation-related trends are as weak as for the simulated NAO. Thus, the observed impacts of the regional MO on Mediterranean temperature and precipitation variability are smaller than those of the large-scale NAO pattern

due to the strong observed NAO increase and the agreement of present-day E-OBS and REMO temperature and precipitation trends is less improved in removing the impacts of the regional MO pattern.

5.1.4 Dependence of simulated circulation variability on initial conditions

In the previous chapter 4 a strong impact of initial conditions on REMO temperature and precipitation trends in the Mediterranean area is identified. Thus, in order to further evaluate the differences between simulated and observed mid-latitude circulation variability the impact of initial conditions on simulated circulation dynamics is estimated for the three ECHAM5 ensemble members relying on different initial condition sets. Fig. 5.7 shows exemplarily the temporal evolution and variability of the first winter PC, identified as NAO pattern, of the three ECHAM5 ensemble members, compared to that of the corresponding ensemble mean and NCEP. The PC time series of the different ensemble members show high variability comparable to the observed NAO and strong differences to each other and to the ensemble mean in temporal evolution: Two ECHAM5 ensemble members yield a positive NAO trend and one member reveals a negative trend resulting in a slight NAO increase in the corresponding ensemble mean. Thus, the linear regression lines of all simulated NAO time series for 1961-90 yield a great range of regression coefficients between +0.05 and -0.01 but none of them reaches the high regression coefficient of +0.11 of the observed NAO. Consequently, a strong impact of initial conditions on simulated circulation variability can be stated (PAXIAN et al., 2011).

In order to further quantify the impact of initial conditions on mid-latitude circulation dynamics a one-way analysis of variance (cf. section 3.3) is performed for all seasonal modes of variation of the three ECHAM5 ensemble members in 1961-1990. But the sequence and spatial structures of the leading ten PCs partly differ for different ensemble members. To keep the comparability of all patterns over different members the sea level pressure data of the ensemble members is projected onto the seasonal modes of variation of the ECHAM5 ensemble mean determined before (cf. section 3.4). Thus, resulting spatial patterns are identical but projected PC time series strongly differ for different ECHAM5 ensemble members. The one-way analysis of variance between the projected PC time series of the three ensemble members estimates the fractions of internal and external variability within the ECHAM5 model ensemble for each PC in each season of 1961-1990 separately. Fig. 5.8 depicts exemplarily the results for PC1 to PC4 in all seasons. The total variance accounted for by internal variability due to differing initial conditions exceeds 80% for each PC

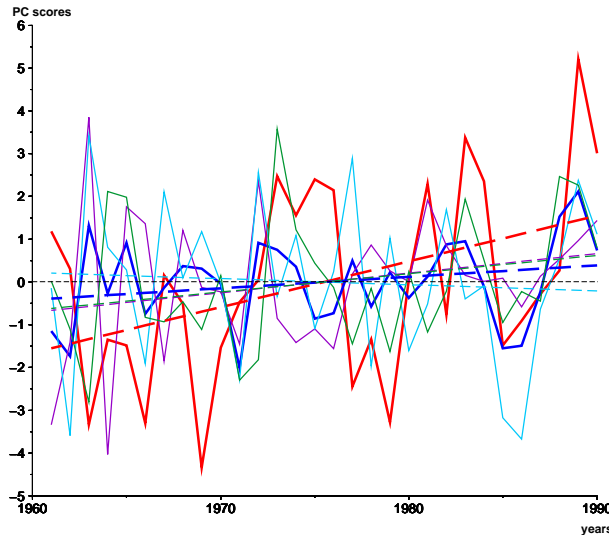


Figure 5.7: Comparison of PC time series of the first winter PC during 1961-1990 (identified as NAO) and corresponding linear trend lines between ECHAM5 ensemble mean (blue), its ensemble members (purple, light blue and green) and NCEP (red).

in each season. The maximum explained variance due to an external CO_2 forcing common to all ECHAM5 ensemble members is about 18% for the second winter PC and the tenth spring PC (not shown) marginally reaching significance. For several PCs and seasons, the fraction of external variability even remains zero, e.g. the first spring PC (PAXIAN et al., 2011).

In order to test whether the strong present-day impact of initial conditions on simulated circulation dynamics decreases in future time periods with increasing CO_2 emissions the ECHAM5 ensemble member data of the whole time period 1961-2050 applying the A1b emission scenario is projected onto the modes of variation of the ECHAM5 ensemble mean of 1961-1990 (cf. section 3.4). The one-way analysis of variance is adequately applied to all 30-year time windows from 1961-1990 to 2021-2050. Fig. 5.8 shows maximum explained variances of 25-28% due to the external treatment effect but significance is only reached for some PCs and seasons over few consecutive years, e.g. the first and second winter PCs. On the other hand, the first spring PC yields zero values over the whole time period. In most cases like for the first winter and summer PCs the analysis reveals strong decadal variations of the treatment effect with only slight long-term trends. Only in some cases the fraction of external variability strongly increases reaching significance, e.g. for the second summer PC, indicating a possible enhancement of predictability based on CO_2 in future time periods. But other cases even reveal intensive decreases of the treatment effect, e.g. for the second winter PC. Sensitivity tests yield similar results even for longer time periods until 2100 and larger time windows of 50 to 80 years

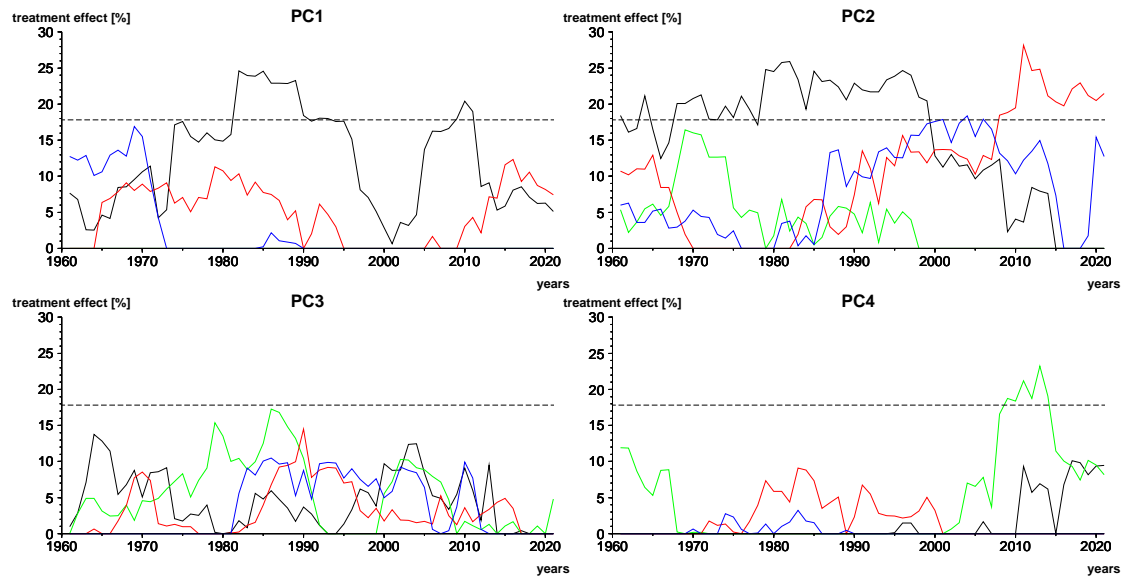


Figure 5.8: Results of one-way analysis of variance for the projected PC time series of three ECHAM5 ensemble members for all 30-year time windows moving from 1961-1990 to 2021-2050 applying the A1b scenario (x-axis denotes first years of corresponding time windows, dashed line identifies significance level): fraction of external treatment effect [%] for different modes of variation identified by PC1 (upper left), PC2 (upper right), PC3 (lower left) and PC4 (lower right) in winter (black), spring (green), summer (red) and autumn (blue).

causing rather smoothed variations of the treatment effect. It can be concluded that initial conditions have a strong impact on simulated circulation variability in present-day times which even remains high in future time periods with increasing GHG emissions. Thus, differing initial conditions between observations and models are supposed to induce the mentioned strong differences in temporal evolutions of observed and simulated modes of variation causing the discussed discrepancies in present-day temperature and precipitation trends. One might conclude that 30-year trends generally suffer from strong impacts of interdecadal variability and thus, only reveal low predictability based on CO_2 because the considered time scale is shorter than that one affected by GHG forcing (PAXIAN et al., 2011).

5.2 Mid-latitude circulation in long-term climate

The predictability of the given model-into-model-approach for Mediterranean temperature and precipitation trends in 1961-1990 is found to be quite low in several regions due to strong discrepancies in temporal evolutions of observed and simulated mid-latitude modes of variation probably due to differing initial conditions. This impact of initial conditions on mid-latitude circulation variability even remains high

in future time periods. But on the other hand, the impact of mid-latitude circulation on temperature and precipitation variability probably decreases due to increasing influences of GHGs in long-term and future time periods. Thus, even if the predictability of the given model-into-model-approach can not be evaluated in future time periods due to missing observations, the question arises how the present-day impacts of mid-latitude circulation dynamics on Mediterranean temperature and precipitation variability change compared to those of residual circulation-unrelated drivers, e.g. GHGs. Probably some careful considerations on the predictability of the given model-into-model approach in future time periods can be deduced. Thus, the same analysis steps than for the present-day time period 1961-1990 are performed for the long-term time period 1961-2050. In the following, the corresponding results of PCA, multiple regression and trend separation for the long-term period are presented and compared to the corresponding results of the present-day time period.

5.2.1 Simulated mid-latitude circulation variability

In order to analyse the future evolution of the simulated mid-latitude modes of variation of 1961-1990 the ECHAM5 sea level pressure data of 1961-2050 applying A1b and B1 emission scenarios are projected onto the ECHAM5 modes in 1961-1990. This projection further avoids that long-term sea level pressure trends dominate the first PC because the strong trend variability blocks out modes of variation with real physical meaning. Thus, spatial patterns of eigenvector loadings and present-day temporal evolutions of projected PC time series are similar to the modes of variation of 1961-1990. The future PC time series reveal approximately equal variabilities to present-day times but strongly differing temporal evolutions for the A1b and B1 emission scenarios, e.g. the slightly strengthening winter NAO pattern of the present-day time period further increases in A1b for 2001-2050 but shows decadal oscillations for B1 with two maxima in 2015 and 2035 and one minimum around 2030. Further long-term trends of modes of variation influencing Mediterranean temperature and precipitation variability are not discussed here but mentioned in the following subsections.

5.2.2 Impact of mid-latitude circulation on climate

The cross-validated stepwise multiple regression is adequately performed between REMO temperature or precipitation and large-scale ECHAM5 modes of variation in 1961-2050 for both A1b and B1 emission scenarios applying 1,000 iterations and 18

random bootstrap years for cross validation. Fig. 5.9 presents the first circulation predictors and variances accounted for by all predictors of the statistical model for winter and summer temperature and precipitation for both emission scenarios. Explained variances of B1 are not shown because they are rather similar to A1b.

For winter temperature, the strong present-day impact of the EA pattern over southern Europe remains in both future scenarios but further extends over northern Africa in A1b blocking out the present-day NAO impacts. In the B1 emission scenario, the influences of the EA pattern over the western Mediterranean are replaced by those of the EA/WR pattern. The maximum explained variance over the central Mediterranean strongly decreases to 40-60% (Fig. 5.9, first row). But circulation influences strongly change for summer temperature. The present-day major impacts of the EA-Jet and blocking patterns disappear except for some influences of the blocking pattern as second predictor over the western Iberian Peninsula. The impact of the summer EA pattern is shifted further north in B1 and to the second predictor in A1b. Instead, strong impacts can be stated by the sixth PC over the whole Mediterranean area in A1b and over the western Mediterranean with additional influences of the fourth PC, identified as summer EA/WR pattern, over the southern and eastern Mediterranean in B1. The sixth PC is rather difficult to interpret showing only small variabilities of sea level pressure with negative values over northern Europe and the northern Atlantic and positive pressure values extending over southern and eastern Europe, northern Africa and the subtropical Atlantic but reveals a clearly negative trend in 1961-2050. The maximum explained variances remain 40-60% for A1b extending over large Mediterranean regions but strongly decrease to 30-50% for B1 (Fig. 5.9, second row).

Concerning winter precipitation, the future impact of the NAO pattern further extends over southern Europe and north-western Africa for both A1b and B1 emission scenarios. The heterogeneous present-day impact pattern of higher order PCs remains in the southern and eastern Mediterranean with reduced influences of the SCAND and EA/WR patterns. The maximum explained variance only slightly decreases in both scenarios (Fig. 5.9, third row). For summer precipitation, the impact of circulation variability further weakens yielding maximum explained variances of only 20-30% mainly over southern Europe and Turkey. The spatial impact pattern remains heterogeneous with mostly decreasing influences of the EA-Jet and blocking patterns as well as increasing impacts of the summer versions of the EA and EA/WR patterns and of several higher order PCs in both scenarios (Fig. 5.9, fourth row).

Generally, the impacts of the most important present-day modes of variation on

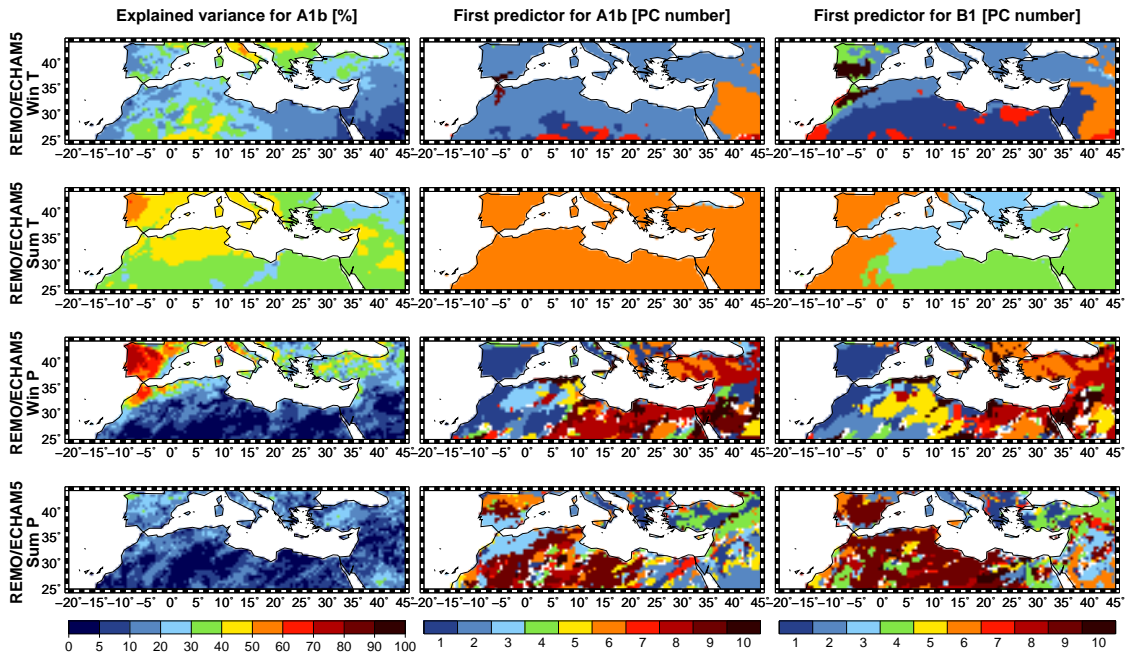


Figure 5.9: Results of cross-validated stepwise multiple regression based on REMO predictands and ECHAM5 predictors for winter and summer temperature and precipitation in 1961-2050: temperature and precipitation variance explained by all circulation predictors selected by the statistical model for the A1b emission scenario (left) and PC number of first circulation predictor for the A1b (middle) and B1 (right) emission scenarios.

Mediterranean temperature and precipitation in winter remain in 1961-2050, i.e. the EA pattern over the central Mediterranean for temperature and the NAO over the western Mediterranean for precipitation. But in summer several changes of influencing modes of variation can be stated, especially for temperature. This might be explained by generally less robust impacts of mid-latitude circulation in summer or by high correlations of strongly increasing summer temperatures to modes with equal strong trends, e.g. the clearly decreasing sixth PC, but probably without real physical relationship. Furthermore, the explained variances of all predictors of the statistical model mostly decrease in 1961-2050, except for summer temperature in A1b, denoting smaller impacts of mid-latitude circulation dynamics on Mediterranean temperature and precipitation variability. This might be due to stronger impacts of GHG or other influencing circulation-unrelated factors in long-term and future time periods.

5.2.3 Circulation-related and -unrelated climate trends

Finally, Fig. 5.10 displays the circulation-related and circulation-unrelated trends of winter and summer temperature and precipitation in 1961-2050 for the A1b emission scenario of REMO. For winter temperature, the circulation-related part re-

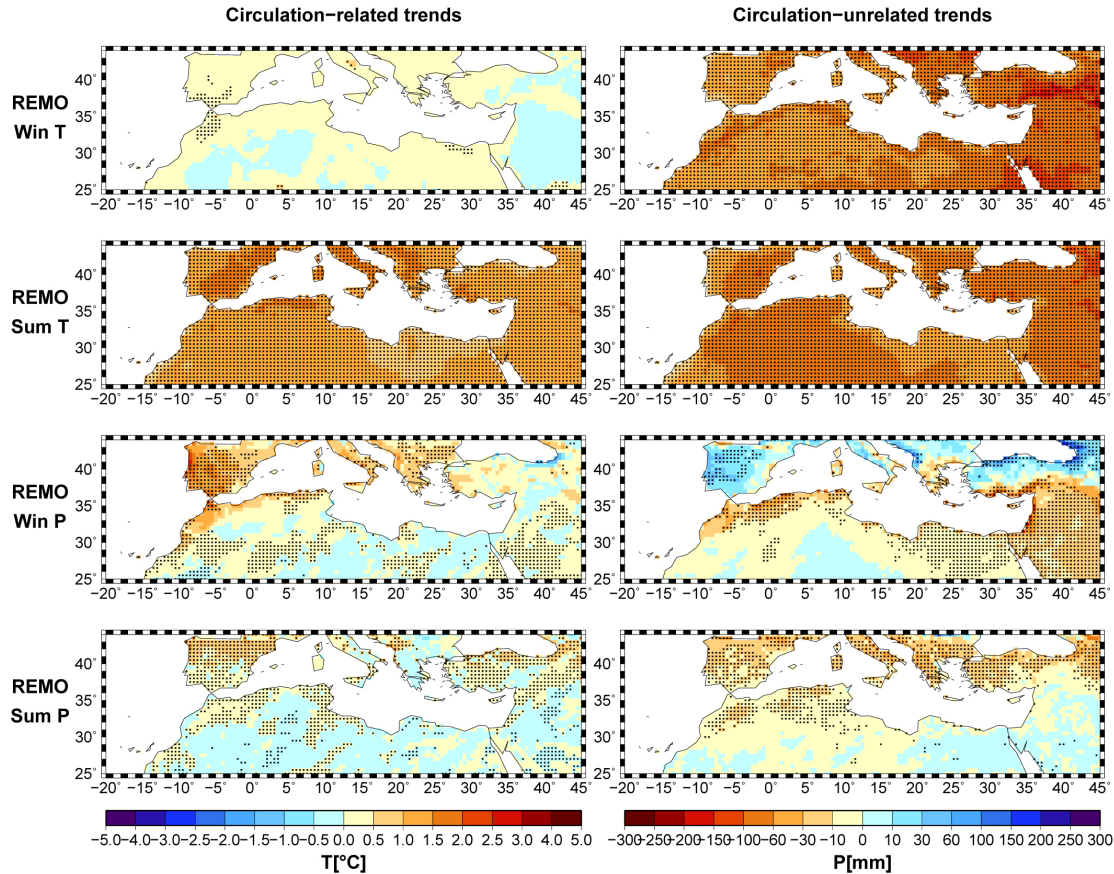


Figure 5.10: Comparison of circulation-related (left) and circulation-unrelated (right) winter and summer temperature and precipitation trends of the A1b emission scenario of REMO during 1961-2050 after separation of influences by mid-latitude circulation variability, applying a significance level of 5% (dots).

reveals hardly any significant trend mainly due to lacking long-term trends of the most influencing EA pattern (Fig. 5.10, first row), and the circulation-unrelated trends strongly resemble the strong warming trends of the original data (Fig. 4.11). Concerning summer, the circulation-related part holds strong and significant warming trends over the whole Mediterranean area due to a weakening of the sixth PC and a strengthening EA pattern as second predictor. Thus, there might be an artificially enhanced contribution to circulation-related trends due to the probably non-physical link between summer temperature and the sixth PC. The circulation-unrelated trends reveal slightly stronger warming patterns over the whole area (Fig. 5.10, second row) but smaller than the original data trends (Fig. 4.11). The B1 scenario yields rather similar results to A1b in winter but much smaller circulation-related trends in summer and thus, higher resulting circulation-unrelated trends.

For winter precipitation, an increasing NAO pattern causes significant drying

trends over southern Europe, north-western Africa and parts of Middle East in the circulation-related part. The resulting circulation-unrelated part yields similar drying and wetting tendencies over the eastern Mediterranean compared to original data (Fig. 4.12) but decreased drying patterns over the Atlas mountains and increased wetting patterns over southern Europe (Fig. 5.10, third row). In summer, a strengthening EA pattern and weakening of the sixth PC over the western Mediterranean and an increasing EA/WR pattern over the eastern Mediterranean induce small but significant drying trends in the circulation-related part. Thus, the northern Mediterranean drying patterns in the resulting circulation-unrelated part are slightly decreased (Fig. 5.10, fourth row) in comparison to the original data (Fig. 4.12). The B1 scenario shows equal spatial patterns but smaller trend intensities than A1b, except for the circulation-unrelated part in winter revealing strong and significant wetting patterns over the Iberian Peninsula, the western Balkans and northern Turkey exceeding also original B1 data trends (Fig. 4.12).

Generally, the kind of mid-latitude circulation impacts on Mediterranean temperature and precipitation often alters in 1961-2050 compared to 1961-1990 due to changing influencing modes of variation, e.g. in summer, or changing long-term trends of modes, e.g. the EA pattern for winter temperature. But the winter drying patterns over southern Europe due to an increasing NAO remain in the long-term period, especially in the A1b scenario. However, the strength of circulation impacts mostly weakens in 1961-2050 like decreasing explained variances have shown in the previous subsection. On the other hand, the circulation-unrelated trends become stronger and more significant than in 1961-1990 revealing intensive warming patterns over the whole Mediterranean strongly exceeding circulation-related temperature trends, except for summer temperature in A1b with only slight exceedance, and drying patterns over the northern and southern Mediterranean in summer and winter, respectively. In winter, the circulation-unrelated trends further yield extended wetting patterns over southern Europe and Turkey, especially in the B1 scenario, that partly counterbalance the drying trends due to an increasing NAO pattern. Thus, decreasing impacts of mid-latitude circulation and increasing influences of residual circulation-unrelated drivers, e.g. GHGs, might probably point at an increased predictability of the given model-into-model approach for Mediterranean temperature and precipitation trends in the long-term time period 1961-2050.

6 Quantile-based precipitation extreme indices

Having analysed Mediterranean mean temperature and precipitation in present-day and future time periods the following three chapters describe different approaches of investigating temperature and precipitation extremes in the Mediterranean area from daily datasets. The first approach determines seasonal extreme indices based on empirical quantiles. The focus is laid on precipitation because a KLIWEX-MED cooperation is performed aiming at comparing dynamical and statistical downscaling techniques for precipitation extremes (see chapter 9, HERTIG et al. (2012)). Thus, several quantile-based extreme indices are applied describing both frequency and intensity of extreme precipitation events: R95N [days], SDII95p [mm], R95AM [mm] and R95T [%]. Furthermore, CDD [days] is regarded for analysis of dry periods. Thereby, different rain day definitions have been applied for precipitation indices and CDD: all days with rainfall exceeding the 0.1mm and 1mm thresholds, respectively. The analysis is performed for E-OBS, REMO and ECHAM5 data according to previous chapters. Monthly CRU data are not further considered for extreme value analysis due to lacking daily resolution. For both models, the first ensemble member is applied instead of the ensemble mean due to reasons of comparability with the statistical downscaling of the KLIWEX-MED cooperation which is performed with the first ECHAM5 ensemble member. The following sections describe the results of quantile-based precipitation extreme indices and CDD for the present-day and future time periods 1961-1990 and 2021-2050.

6.1 Validation and dynamical downscaling of present-day climate

This section compares the quantile-based precipitation extremes of E-OBS, REMO and ECHAM5 for winter and summer in the present-day time period 1961-1990 in order to validate the skill of the climate models in simulating precipitation extremes and to find possible added values of dynamical downscaling from ECHAM5

to REMO. First, the number of rain days is presented being considerably important for the definition of precipitation extremes. Then, the present-day results for CDD and precipitation extreme indices are compared. Finally, some further investigations on scale effects and subscale processes in dynamical downscaling are made.

6.1.1 Number of precipitation days

The quantile-based precipitation extreme indices and consecutive dry days for E-OBS, REMO and ECHAM5 are based on two different thresholds of rain days, i.e. rainfall exceeding 0.1mm and 1mm, respectively. In order to increase the understanding of differing rainfall extremes between these different datasets the number of rain days following both definitions is estimated per season averaged over the present-day period 1961-1990.

Fig. 6.1 presents the number of rain days following different thresholds for E-OBS, REMO and ECHAM5 in 1961-1990. Generally, the number of rain days follows quite closely the spatial distribution of seasonal precipitation sums featuring more rain days in winter over the northern Mediterranean than in summer over the southern Mediterranean. For the lower 0.1mm threshold, E-OBS reaches 20-60 rain days over Europe and Turkey in winter and less than 10 rain days over Africa and Near East in summer. In winter, both models mostly overestimate observed rain days except over the Near East yielding maxima of up to 70-80 rain days over Galicia and eastern Turkey (Fig. 6.1, left). In summer, REMO mostly overestimates observed rain days, especially over the Atlas mountains and Turkey. ECHAM5 shows smaller values than REMO over Africa yielding more agreement with E-OBS over the southern Mediterranean but stronger differences over the northern rim of the Mediterranean area (Fig. 6.1, middle). For the higher 1mm threshold, the spatial distribution of E-OBS rain days remains but the number of rain days decreases, especially over the northern Mediterranean in winter. The winter results are not shown because they are rather similar to those of the smaller threshold yielding smaller overestimations of both models compared to observed rain days which mainly occur over Spain, northern Turkey and the western Balkans. Simulated rain days over the Near East are still less than observed ones. In summer, REMO yields slightly more rain days than E-OBS, especially over the Atlas mountains and Turkey, but ECHAM5 strongly underestimates E-OBS and REMO over the whole Mediterranean area (Fig. 6.1, right). Consequently, both models simulate generally more rain days than E-OBS in winter, especially for the lower 0.1mm threshold. In summer, REMO rather overestimates observed rain days and ECHAM5 strongly underestimates E-OBS rain days for the higher 1mm threshold.

These differences between simulated and observed numbers of rain days can be partly explained by the problem of comparing model and observational rainfall datasets on different spatial scales: area-averaged REMO and E-OBS grid boxes yield more rain days with less intensity than original local station data due to the area-averaging to coarser grid resolution. But the E-OBS values are closer to original stations because they result from statistical interpolation of station values thus, conserving parts of the original station statistical properties. Instead, the simulated values of REMO are directly calculated on a coarser model grid not knowing about the fine scale station information behind it therefore, resulting in higher numbers of rain days compared to E-OBS. Such differences mainly prevail in summer due to deficiencies in simulating local convection processes. But winter differences are equally high due to higher total numbers of rain days. This problem of comparing simulated and observed datasets on different spatial scales can be solved by applying a weather generator to daily REMO data which produces virtual station time series with similar statistical properties to original stations (see chapter 8). ECHAM5 yields similar overestimations of observed rain days to REMO in winter but strongly underestimates E-OBS in summer over the whole area. These underestimations cannot be explained by this problem of comparison but probably the coarse grid ECHAM5 model generally fails in simulating summer convective rainfall events producing as well much smaller summer rainfall totals compared to observations (cf. Fig. 4.3).

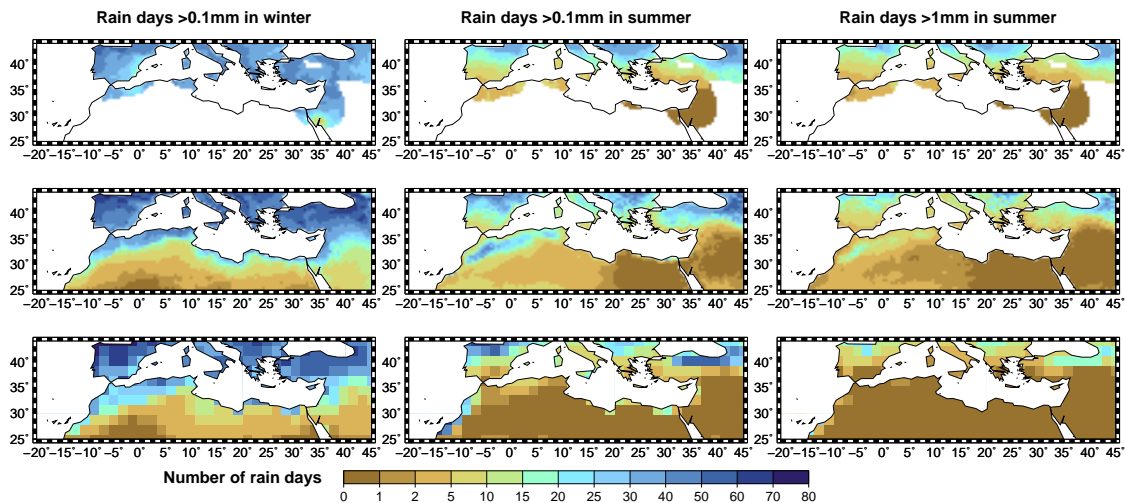


Figure 6.1: Validation of the number of rain days from REMO (middle) and ECHAM5 (bottom) with E-OBS rain days (top) for rainfall threshold 0.1mm in winter (left) and summer (middle) and for rainfall threshold 1mm in summer (right) in 1961-1990.

6.1.2 Maximum number of consecutive dry days

The maximum number of consecutive dry days of E-OBS, REMO and ECHAM5 in 1961-1990 is depicted in Fig. 6.2. Generally, the spatial distribution of CDD is inverse to that of seasonal precipitation totals reaching maximum values over the southern Mediterranean in summer and minimum values over southern Europe and Turkey in winter. Thus, E-OBS reaches 5-20 and 10-80 consecutive dry days over the northern Mediterranean in winter and summer, respectively, and even exceeds 90 days over the Near East in summer indicating an entirely dry summer character of this region. In winter, there is a quite good agreement between both models and observations with some underestimations of CDD over the Iberian Peninsula and Turkey and some overestimations over the Near East due to increased and decreased numbers of rain days, respectively (Fig. 6.2, left). In summer, REMO underestimates observed CDD over the Atlas mountains, southern Spain and Turkey and yields some small overestimations over the northern rim of the area. ECHAM5 strongly overestimates the CDD values of both E-OBS and REMO over the whole Mediterranean area. Several ECHAM5 and E-OBS grid boxes over the southern Mediterranean in summer are removed because no single rain day occurs in that season in 1961-1990 (Fig. 6.2, right). Thus, in winter model performance is rather good with smaller CDD differences to observations over the Iberian Peninsula, Turkey and the Near East but in summer strong underestimations and overestimations of ob-

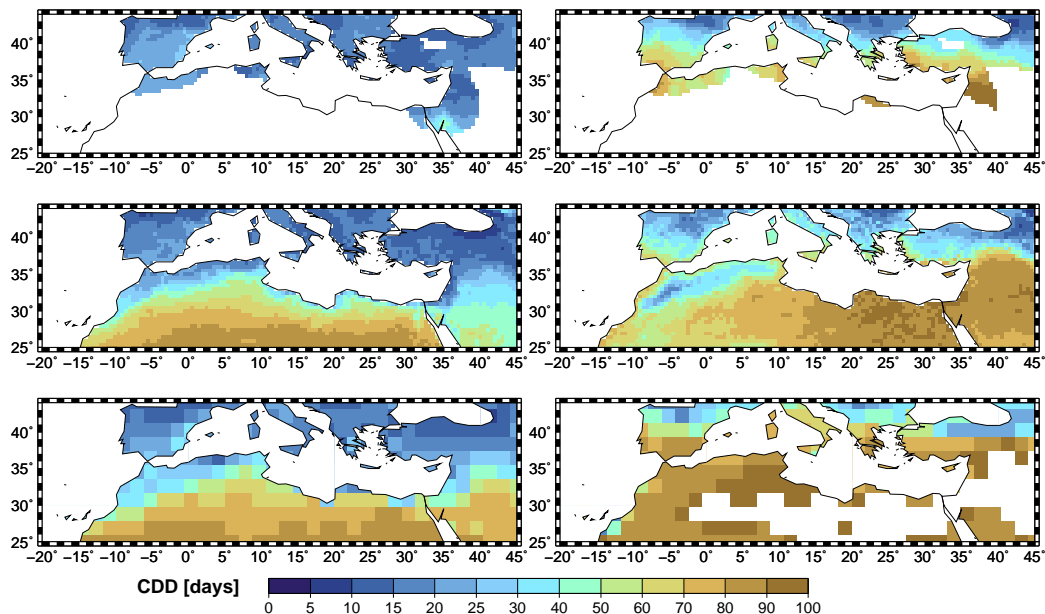


Figure 6.2: Validation of the maximum number of consecutive dry days (CDD) from REMO (middle) and ECHAM5 (bottom) with CDD of E-OBS (top) for winter (left) and summer (right) in 1961-1990.

served CDD in REMO and ECHAM5 can be stated, respectively. The comparison of simulated and observed CDD closely follows the corresponding discrepancies in number of rain days for the higher 1mm threshold of the previous subsection. But CDD is a very sensitive variable because small differences in numbers of rain days can cause huge differences in CDD, especially over dry regions in the summer season when only small numbers of rain days prevail.

6.1.3 Precipitation extreme indices

In the following, several quantile-based precipitation extreme indices are presented. The 95% quantile of daily precipitation upon which the following indices are based is not further described here because it reveals rather similar patterns to the seasonal rainfall totals (Fig. 4.3) with maximum values over the western coasts and mountain ranges of the northern Mediterranean area (cf. HERTIG et al. (2012)).

The frequency of extreme rainfall events is described by the number of rain days exceeding the 95% quantile R95N of E-OBS, REMO and ECHAM5 in 1961-1990 (Fig. 6.3). R95N presents approximately 5% of the number of rain days per season with minimum rainfall amount of 0.1mm (cf. Fig. 6.1) taking into account small differences between the reference quantiles determined by the bootstrap technique following ZHANG et al. (2005) and the quantiles over the whole present-day time period. Thus, observed R95N yields 1-3.5 extreme rainfall days in winter and 0.5-2.5 days in summer featuring a similar spatial distribution to the number of rain days. In winter, overestimations of observed R95N by 0.5-1 days can be stated in both models over southern Europe and Turkey with some underestimations over the Near East (Fig. 6.3, left). In summer, the agreement between models and observations is higher but some overestimations of observed R95N over northern Spain and Turkey can be seen for both models, especially for ECHAM5 (Fig. 6.3, right). Many grid boxes over Africa and Arabia are removed due to missing values in both seasons, even some over southern Europe and Turkey in summer. Consequently, both models tend to overestimate the observed frequency of extreme rainfall events over many parts of the northern Mediterranean due to increased numbers of simulated rain days, especially in winter. But the frequency of extreme precipitation over the southern Mediterranean area can not be investigated due to small numbers of rain days.

Furthermore, the intensity of extreme rainfall events is determined by the simple daily intensity index SDII95p of those rain days exceeding the 95% quantile depicted in Fig. 6.4 for E-OBS, REMO and ECHAM5 in 1961-1990. The SDII95p of E-OBS features values of 5-20mm over southern Europe and Turkey in summer and 5-40mm in winter reaching maxima of 50mm over Galicia. In winter, ECHAM5

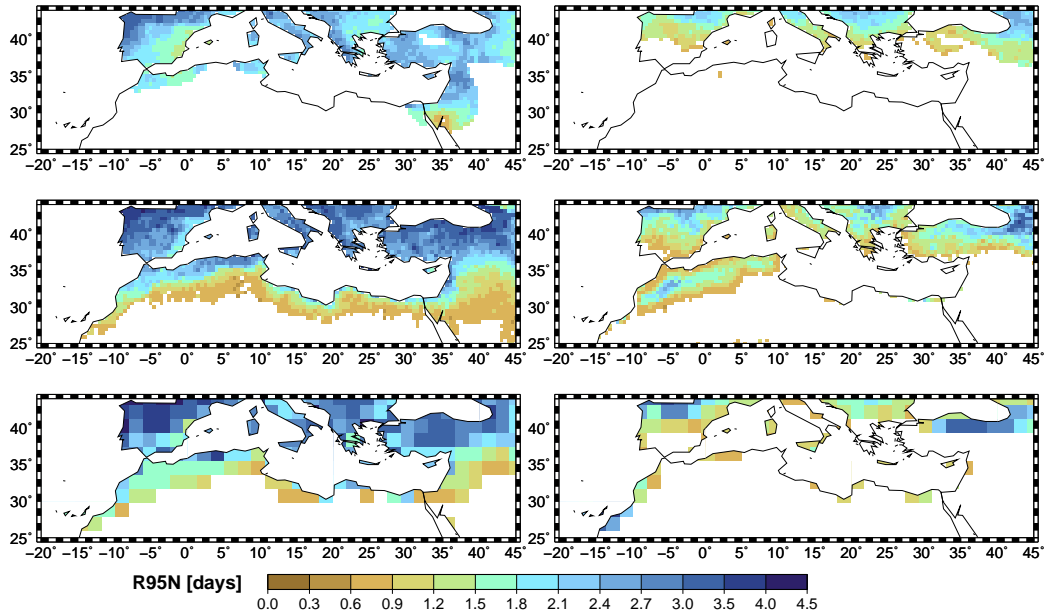


Figure 6.3: Validation of the number of rain days exceeding the 95% quantile (R95N) from REMO (middle) and ECHAM5 (bottom) with R95N of E-OBS (top) for winter (left) and summer (right) in 1961-1990.

mostly fits quite well with observations but underestimates observed intensities over the maximum rainfall regions at the western coasts and mountain ranges of the northern Mediterranean. REMO mostly overestimates observed SDII95p, especially strong over the maximum rainfall regions, e.g. over Galicia, the western Balkans, southern Turkey and coastal Israel. Over the Near East observations show generally far higher intensities probably due to uncertainties of spatial interpolation in areas of low station density (Fig. 6.4, left). In summer, agreement is higher with REMO and ECHAM5 only slightly overestimating and underestimating observed intensities, respectively. The strong REMO intensities over the northern Balkans and the Caucasus region probably result from REMO model frame effects (Fig. 6.4, right).

Thus, accordance between observed and simulated intensities is better in summer than in winter probably because of smaller summer rainfall totals. ECHAM5 rainfall intensities are generally smaller than those of E-OBS and REMO probably due to shortcomings of coarse grid GCMs in simulating intensities of small-scale precipitation extreme events. The high-resolution model REMO features higher extreme rainfall intensities but strongly overestimates observed intensities over the western coasts and mountain ranges of the northern Mediterranean in winter according to the seasonal rainfall totals (subsection 4.1.2). This probably results from the inclusion of windward and lee effects in simulations or points at model deficiencies in simulating rainfall intensities. But spatial interpolation of gridded E-OBS data is known to smooth extreme rainfall intensities compared to local stations (HAY-

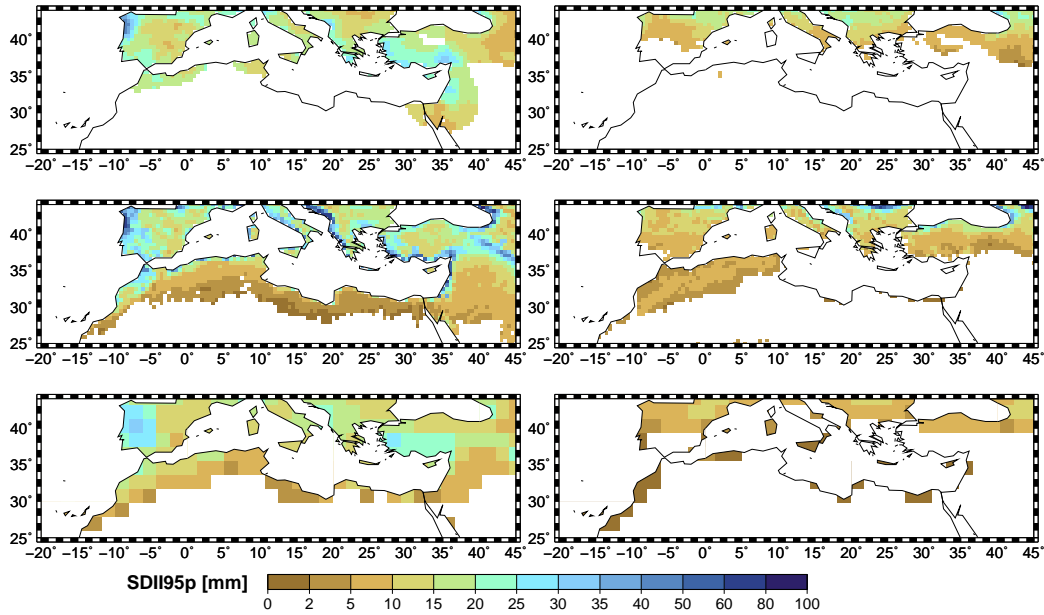


Figure 6.4: Validation of the simple daily intensity index of rain days exceeding the 95% quantile (SDII95p) from REMO (middle) and ECHAM5 (bottom) with SDII95p of E-OBS (top) for winter (left) and summer (right) in 1961-1990.

LOCK et al., 2008) and interpolation uncertainty rises in areas of low station density, e.g. over mountains. It is rather difficult to evaluate the difference between higher REMO and smaller E-OBS intensities. Thus, the weather generator of chapter 8 presents the direct comparison of extreme precipitation values from original station data and virtual stations produced from daily REMO data.

The total rainfall amount of all days exceeding the 95% quantile (R95AM) in 1961-1990 can be determined by multiplying the number of extreme rainfall days R95N with the average daily intensity SDII95p. In winter, REMO strongly overestimates observed R95AM due to both increased frequency and intensity over the whole area, especially at the western coasts and over mountain ranges of the northern Mediterranean. The overestimations of ECHAM5 are quite smaller featuring increased frequencies but slightly decreased intensities. In summer, agreement is better with REMO and ECHAM5 only slightly overestimating and underestimating observed extreme rainfall amounts, respectively, due to stronger agreement of summer frequencies and intensities between models and observations. Finally, the share of extreme rainfall amount in total rainfall amount (R95T) is estimated for E-OBS, REMO and ECHAM5 in 1961-1990. E-OBS reaches a mixed R95T picture of 15-25% over the whole area in both winter and summer reaching partly higher values in summer due to increased convective rainfall extremes and decreased precipitation totals. Both models yield higher R95T values of 20-35% in both winter and summer mostly due to higher amounts of extreme rainfall except for ECHAM5

in summer showing stronger underestimations for rainfall totals than for rainfall extremes compared to observations.

6.1.4 Scale effects and subscale processes

This subsection aims at separating the effect of dynamical downscaling from ECHAM5 to REMO into the scale effect of increased model grid resolution and the impact of subscale processes inherent to RCM physics. In the previous subsections the rainfall extremes of REMO on 0.5° are directly compared to those of ECHAM5 on the coarse grid resolution 1.875° in order to find added values of dynamical downscaling. But comparisons on different spatial scales are difficult because maximum rainfall intensities on larger spatial units are always smaller than those on smaller spatial scales because of less amount of available energy for precipitation formation. Due to this scale effect increasing the model resolution always leads to higher precipitation intensities (cf. HENSE and FRIEDERICHS (2006); PAETH and DIEDERICH (2010)). Thus, if the RCM REMO is interpolated to the coarser 1.875° grid of the GCM ECHAM5, this scale effect is removed and the impacts of the subscale processes inherent to REMO physics are prominent allowing for the separation of the two dynamical downscaling effects.

Therefore, the daily REMO data on 0.5° is linearly interpolated to 2° grid resolution applying both land and sea grid boxes in order to approximately fit the ECHAM5 1.875° resolution. Due to this interpolation process few REMO grid box rows in the west and south of the model grid area are removed. For the aggregated 2.0° REMO data, the rainfall extreme indices R95N and SDII95p are exemplarily computed for 1961-1990 (Fig. 6.5). The REMO 2.0° results are compared to those of REMO 0.5° and ECHAM5 1.875° in order to determine the scale effect and subscale processes of dynamical downscaling, respectively. REMO 2.0° yields mostly higher R95N values than both REMO 0.5° and ECHAM5 1.875° in winter and summer, especially over the northern Mediterranean (Fig. 6.5, left). Thus, the dynamical downscaling of R95N from ECHAM5 1.875° to REMO 0.5° can be separated into two effects: the subscale processes of REMO 2.0° compared to ECHAM5 1.875° cause a strong increase of the frequencies of extreme rainfall days and the scale effect from REMO 2.0° to REMO 0.5° yields decreasing frequencies. For SDII95p, REMO 2.0° lies mostly higher than ECHAM5 1.875° but lower than REMO 0.5° results for both winter and summer (Fig. 6.5, right). Thus, both the subscale processes of REMO 2.0° compared to ECHAM5 1.875° and the scale effect from REMO 2.0° to REMO 0.5° produce increasing intensities of extreme rainfall.

Therefore, the dynamical downscaling from ECHAM5 1.875° to REMO 0.5° is

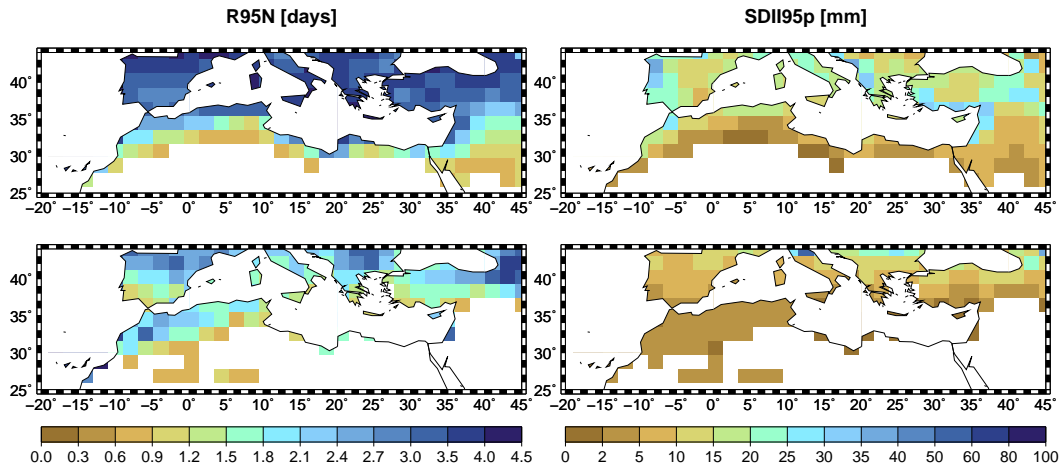


Figure 6.5: Number (R95N, left) and simple daily intensity index (SDII95p, right) of rain days exceeding the 95% quantile of REMO linearly interpolated to 2.0° resolution for winter (top) and summer (bottom) in 1961-1990.

separated into two effects: the scale effect of increased REMO resolution produces decreased frequencies and increased intensities of extreme rainfall in reducing the area-averaging effect of coarse grid model datasets. But this scale effect is overlaid by subscale processes, e.g. concerning small-scale convection or clouds, which are real added values of REMO RCM physics and tend to increase both frequency and intensity of extreme rainfall events in this study. Generally, removing the scale effect decreases and increases the agreement between REMO and ECHAM5 for frequency and intensity of rainfall extremes, respectively. One has to keep in mind that comparisons of datasets on different spatial resolutions always contain such impacts of the scale effect.

6.2 Dynamical downscaling of future climate

Finally, the considered precipitation extremes CDD, R95N, SDII95p, R95AM and R95T are computed for the future time period 2021-2050 and the future changes compared to the present-day time period 1961-1990 are calculated. The corresponding results are presented for the A1b and B1 emission scenarios of both REMO and ECHAM5 models in order to reveal probable added values of dynamical downscaling. Thus, the following subsections describe the future changes of precipitation days, CDD and of the quantile-based precipitation extreme indices.

6.2.1 Number of precipitation days

The future change in the number of rain days for both rainfall thresholds 0.1mm and 1mm in 2021-2050 compared to 1961-1990 is computed for the A1b and B1 emission scenarios of REMO and ECHAM5. Fig. 6.6 presents the changes in rain days for the smaller rainfall threshold. In winter, the number of rain days yields strong and significant decreases of up to seven rain days over the southern and eastern Mediterranean featuring further small decreases and increases over southern Europe and northern Turkey in the A1b scenario of REMO, respectively. The B1 scenario depicts smaller decreases over the Middle East than A1b but higher decreases over the Atlas mountains and stronger increases over Spain, the Balkans, Turkey and the Caucasus region of up to five rain days not reaching significance. ECHAM5 yields smaller decreases over the Middle East and stronger decreases and smaller increases over southern Europe compared to REMO (Fig. 6.6, left). In summer, strong and significant future decreases of the number of rain days are found over the whole northern Mediterranean with maxima of nine rain days over northern Spain in the A1b scenario of REMO. The B1 scenario produces equal spatial patterns of change with less intensity than A1b except over Greece and ECHAM5 yields smaller changes over Italy, Greece and the Atlas mountains compared to REMO (Fig. 6.6, right). The results for the higher 1mm rainfall threshold are not shown because the

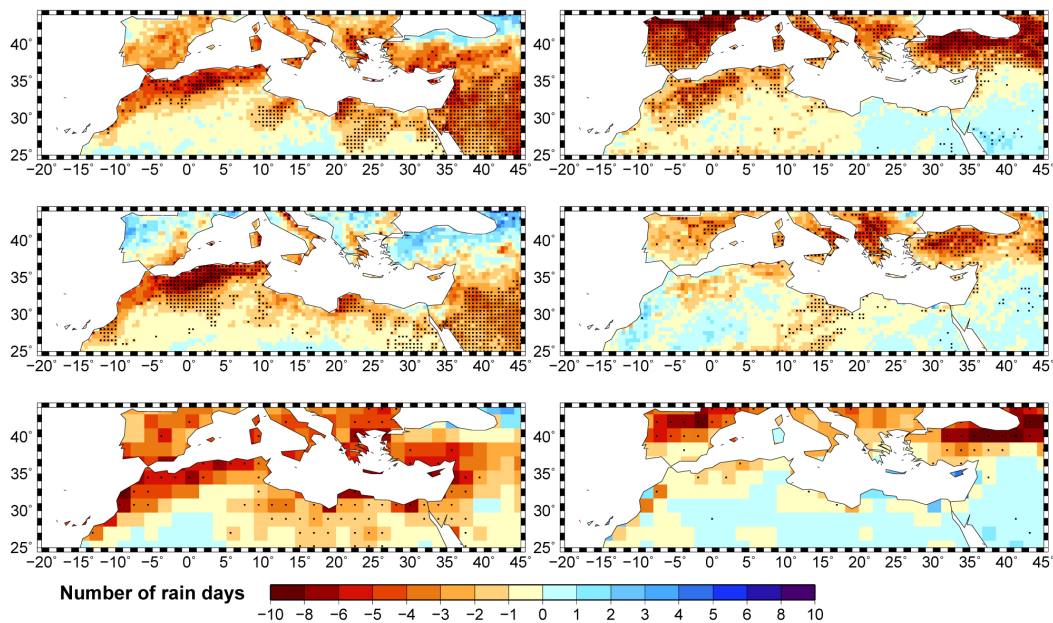


Figure 6.6: Change in the number of rain days of REMO for the A1b (top) and B1 emission scenarios (middle) and ECHAM5 for A1b (bottom) for the rainfall threshold 0.1mm during winter (left) and summer (right) in 2021-2050 compared to 1961-1990, applying a significance level of 5% (dots).

change patterns are similar to the lower threshold but yield generally smaller changes due to less rain days exceeding the higher threshold except for stronger increases over the northern Mediterranean in winter for B1. Thus, future changes of the number of rain days show equal patterns to long-term trends of seasonal precipitation totals featuring strong and significant decreases over the southern and northern Mediterranean in winter and summer, respectively, with some slight increases over the northern Mediterranean in winter not reaching significance. The B1 scenario yields smaller decreasing and stronger increasing patterns than A1b and ECHAM5 mostly smaller changes than REMO.

6.2.2 Maximum number of consecutive dry days

Fig. 6.7 depicts the change in the maximum number of consecutive dry days for A1b and B1 emission scenarios of REMO and ECHAM5 in 2021-2050 compared to 1961-1990. The A1b scenario of REMO shows strong and significant CDD increases of up to 20 days over Egypt and Arabia in winter and over Spain and Turkey in summer with several smaller and mostly not significant increasing and decreasing patterns over the northern Mediterranean in winter and the southern Mediterranean in summer (Fig. 6.7, top). The B1 scenario shows generally smaller changes of CDD than A1b but stronger decreasing CDD patterns over southern Europe and Turkey in winter (Fig. 6.7, middle). The CDD change of ECHAM5 yields mostly similar

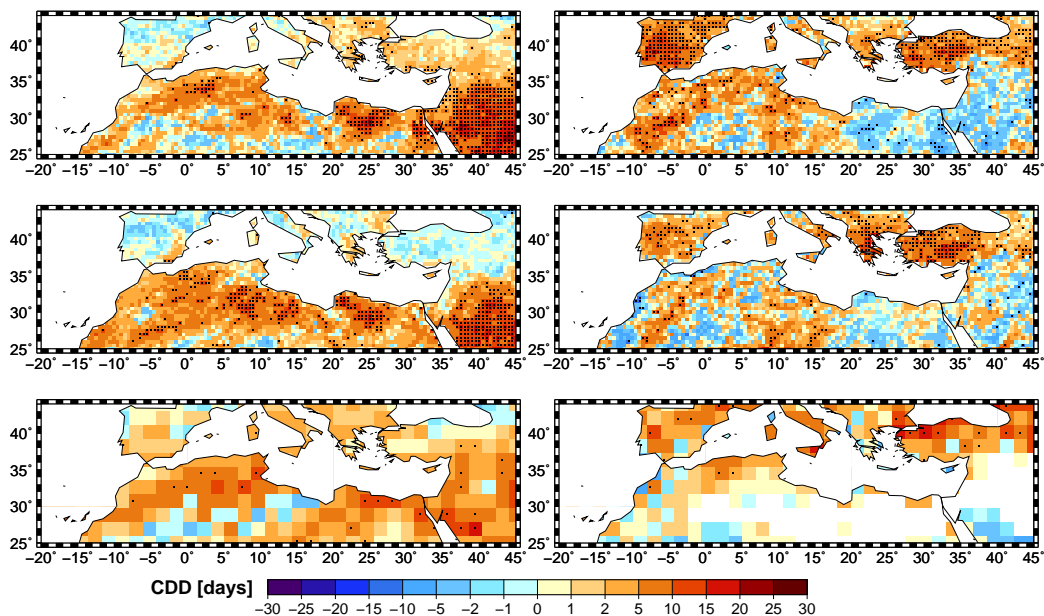


Figure 6.7: Change in the maximum number of consecutive dry days (CDD) of REMO for the A1b (top) and B1 emission scenarios (middle) and ECHAM5 for A1b (bottom) during winter (left) and summer (right) in 2021-2050 compared to 1961-1990, applying a significance level of 5% (dots).

spatial patterns to REMO but smaller amounts of change (Fig. 6.7, bottom). Thus, the CDD change is strongly consistent with the future changes in numbers of rain days revealing increasing lengths of dry periods in regions and seasons of decreasing numbers of rain days and vice versa.

6.2.3 Precipitation extreme indices

This subsection investigates the possible future changes of the quantile-based precipitation extreme indices R95N, SDII95p, R95AM and R95T. Fig. 6.8 depicts the future change of the number of rain days exceeding the 95% quantile (R95N) for the A1b and B1 emission scenarios of REMO and ECHAM5 in 2021-2050 compared to 1961-1990. The R95N change in the A1b scenario of REMO shows several significant decreases over the southern Mediterranean and strong increases over Spain and Turkey in winter only partly reaching significance. In summer, strong and significant decreases can be stated for the whole northern Mediterranean (Fig. 6.8, top). The B1 scenario reveals mostly smaller R95N decreases of less significance than A1b in both seasons, stronger R95N increases of higher significance over the northern Mediterranean in winter and some small R95N increases over the western Mediterranean in summer (Fig. 6.8, middle). ECHAM5 features equal R95N change results to REMO with mostly smaller amounts of change and less significance (Fig. 6.8, bottom). Thus, the future R95N change agrees mostly well with the future change in number of rain days with decreasing numbers of extreme rain days matching with decreasing total numbers of rain days and vice versa. But considerable discrepancies can be stated over Spain and Turkey for both models in winter, especially for the A1b scenario: decreasing total numbers of rain days but increasing numbers of extreme rain days implying a strong increase of the relative frequency of extreme events. Instead, in B1 both total numbers of rain days and extreme rain days increase over these regions.

Furthermore, Fig. 6.9 displays the future change of SDII95p for REMO and ECHAM5 in 2021-2050 compared to 1961-1990. In winter, the A1b scenario of REMO shows increases of extreme rainfall intensities over Spain, the western Balkans and Turkey and decreases over the southern Mediterranean revealing only little significance but small-scale maximum intensity changes over mountain ranges, e.g. the western Atlas mountains, Balkans and Caucasus region and southern and eastern Turkey. In summer, mostly significant decreases can be found over the northern Mediterranean with maxima over northern Turkey and some increases over the Balkans (Fig. 6.9, top). Both the B1 scenario and ECHAM5 yield equal spatial patterns but mostly smaller intensity changes with less significance compared to A1b

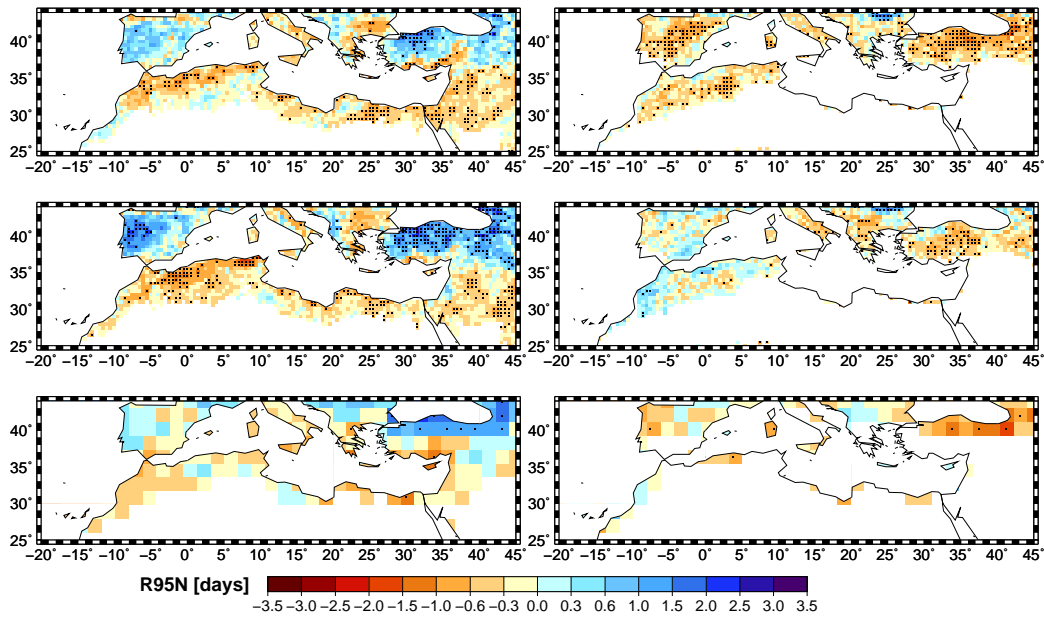


Figure 6.8: Change in the number of rain days exceeding the 95% quantile (R95N) of REMO for the A1b (top) and B1 emission scenarios (middle) and ECHAM5 for A1b (bottom) during winter (left) and summer (right) in 2021-2050 compared to 1961-1990, applying a significance level of 5% (dots).

and REMO, respectively. Furthermore, the coarse ECHAM5 grid resolution is not able to reveal detailed topographic structures of maximum rainfall intensity changes such as REMO (Fig. 6.9, middle and bottom). Overall, the change of extreme rainfall intensity (SDII95p) follows approximately that of extreme rainfall frequency (R95N) revealing decreasing extreme intensities over Spain, the Atlas mountains and Turkey in summer and over the southern Mediterranean area in winter and increasing intensities over the Iberian Peninsula and Turkey in winter. However, the future SDII95p change yields increasing intensities over the Balkans in summer and small-scale maximum rainfall intensity changes over mountain ranges. REMO features considerably more topographic details of small scale intensity changes than the coarse ECHAM5 grid revealing some added value of regional climate modelling.

The change of total extreme rainfall amount (R95AM) in 2021-2050 compared to 1961-1990 is a combination of the changes in frequency and intensity of extreme rainfall days. Generally, the future change patterns are similar for frequency and intensity of extreme precipitation but rainfall intensity yields more small-scale topographic maximum change patterns over mountain ranges. In winter, strong R95AM increases are found over the northern Mediterranean in the A1b scenario of REMO, especially over Portugal, the western Balkans and northern Turkey, and decreases can be stated mainly over the southern Mediterranean, particularly over the Atlas mountains, Greece and southern Turkey. But significance is only reached over

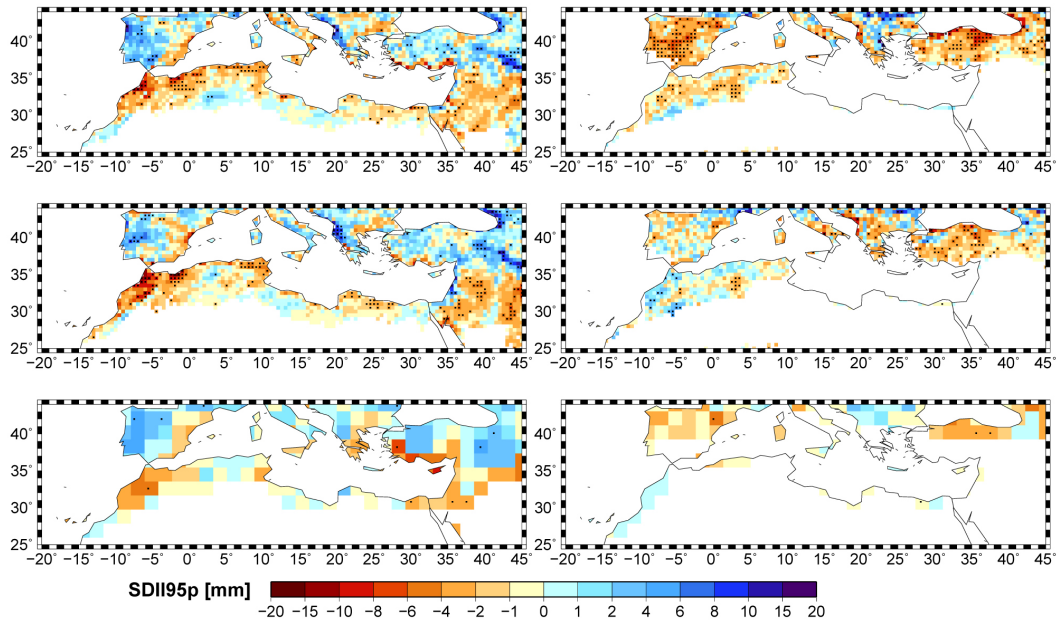


Figure 6.9: Change in the simple daily intensity index of rain days exceeding the 95% quantile (SDII95p) of REMO for the A1b (top) and B1 emission scenarios (middle) and ECHAM5 for A1b (bottom) during winter (left) and summer (right) in 2021-2050 compared to 1961-1990, applying a significance level of 5% (dots).

the Atlas mountains and Turkey. In summer, strong and significant decreases prevail over Spain, the Atlas mountains and northern Turkey. ECHAM5 reveals equal spatial patterns of change but with less intensity and the B1 scenario features less R95AM decreases in summer and stronger increases in winter. Finally, the future change of the share of extreme rainfall amount in total rainfall amount (R95T) reaches maximum values of up to 10-15% and mostly quite similar change patterns to R95AM except for some increases of R95T over the Balkans in summer. Thus, the change in extreme rainfall amounts is mostly more important for determining the future R95T change than that of seasonal precipitation totals.

7 Temperature and precipitation extremes from a Generalized Pareto Distribution

A further method for calculating temperature and precipitation extremes is matching a statistical extreme value distribution to the given datasets. In this study, a Generalized Pareto Distribution is fitted to the daily temperature and precipitation data of E-OBS, REMO and ECHAM5 in the present-day time period 1961-1990 for each natural season and model run separately. Temperature and precipitation return values are built for the return times 5, 10, 15, 20, 25 and 30 years. For both models, the GPD results are averaged over all ensemble members to reach the ensemble mean results. Furthermore, the return values of aggregated temperature and precipitation datasets over 5, 11, 21 and 31 days are calculated in order to investigate longer-term wet or warm periods, serving as indicator for heat waves. Thus, the performance of the models in calculating temperature and precipitation extremes for the present-day time period can be validated with observed extremes, and systematic differences between the models can be investigated in order to find possible added values of dynamical downscaling. Finally, also temperature and precipitation extremes of the future time period 2021-2050 for the A1b and B1 emission scenarios of both models are computed. The first section presents the validation and dynamical downscaling results for the present-day time period 1961-1990 and the second section describes the simulated temperature and precipitation extremes for the future time period 2021-2050.

7.1 Validation and dynamical downscaling of present-day climate

The uncertainty of the following GPD results strongly depends on the data sample sizes, i.e. the numbers of extreme days exceeding the quantile threshold which are applied for GPD fitting. The temperature data samples of E-OBS, REMO and

ECHAM5 show more than 270 extreme days per GPD fit averaged over all quantile thresholds and model runs. The precipitation sample is much smaller because only rain days with precipitation amounts higher than 0.1mm are considered. This threshold for rain days is chosen because the higher threshold of 1mm yields similar GPD results but excludes more southern Mediterranean grid boxes from GPD analysis. The REMO precipitation sample reaches less than 40 and 90 extreme days over the southern Mediterranean in summer and winter, respectively, and maximum values of over 200 extreme days over Galicia and the Caucasus region in winter. ECHAM5 shows less extreme days than REMO in summer due to smaller numbers of rain days and E-OBS in both winter and summer featuring less than 10 extreme days on average over northern Africa and the Near East in summer (cf. subsection 6.1.1). But the precipitation sample size strongly increases with higher aggregation levels reaching numbers of extreme days over southern Europe comparable to those for temperature but remains low over northern Africa. Thus, small data samples prevail mainly for precipitation, especially for E-OBS and ECHAM5, over the southern Mediterranean and in summer. GPD fitting may be difficult or even impossible in these cases because small data samples worsen the GPD fit to empirical data and increase the spread between parametric bootstraps. Both uncertainties are regarded in the following subsections in performing Kolmogorov-Smirnov tests and computing variation coefficients of the GPD return values, respectively.

The first subsection presents the E-OBS, REMO and ECHAM5 GPD return values of the present-day time period 1961-1990 for a return time of 20 years and an aggregation level of one day (1d-20a-RTVs) for both temperature and precipitation and the uncertainties of the corresponding GPD fits. The 1d-20a-RTV is chosen as standard return value of this study describing a return time of medium length within the given range of considered return times and the analysis of daily temperature and precipitation extremes without aggregation in contrast to longer-term extreme periods of higher aggregation levels. Furthermore, some closer evaluation of dynamical downscaling from ECHAM5 to REMO for the temperature and precipitation 1d-20a-RTV is performed, the corresponding GPD parameters are discussed and finally, the GPD return values for different return times and aggregation levels are described.

7.1.1 GPD fit and uncertainty

First, the GPD return values and corresponding variation coefficients of daily REMO temperature are validated and compared with those of E-OBS and ECHAM5 for 1961-1990 (Fig. 7.1), respectively. Generally, the seasonal 1d-20a-RTVs show a

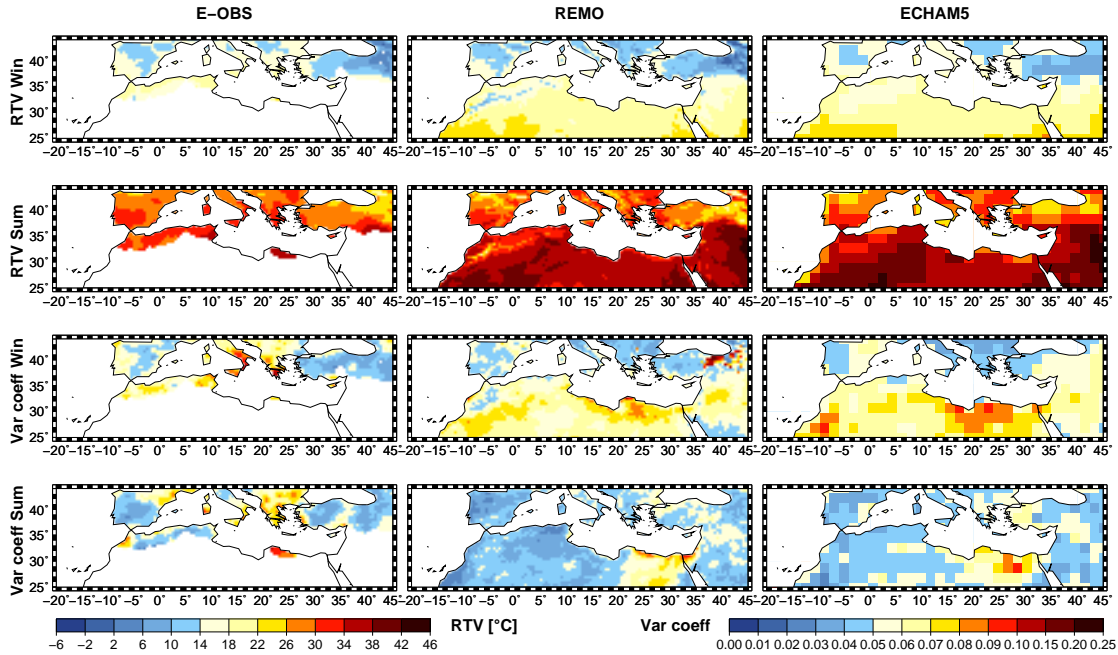


Figure 7.1: Validation of GPD 1d-20a-RTVs from REMO (middle) and ECHAM5 (right) for winter and summer temperature with E-OBS return values (left) and corresponding variation coefficients in 1961-1990.

similar geographical distribution to the seasonal temperature means (cf. Fig. 4.5) with maximum values over Africa and Arabia in summer and minimum values over eastern Turkey in winter and a general good agreement between E-OBS, REMO and ECHAM5. In winter, REMO yields more topographic details than both E-OBS and ECHAM5 over the Atlas mountains, Italy, the Balkans and eastern Turkey and slightly underestimates the observed extremes over the Balkans and Italy denoting areas of highest uncertainty in E-OBS (see below). ECHAM5 shows as well underestimations of observed extremes over the Balkans but further reveals overestimations over the mountains of eastern Turkey and higher values over the Atlas mountains compared to REMO due to coarse grid resolution (Fig. 7.1, first row). In summer, REMO shows several detailed small-scale structures with decreased temperature extremes over the Iberian, Balkan and Turkish mountains which might probably point at improvements compared to the coarse ECHAM5 grid and the spatial interpolation of E-OBS. ECHAM5 yields similar underestimations of observed extremes over northern Spain and northern Turkey but further overestimations over the Atlas mountains (Fig. 7.1, second row). Both E-OBS and REMO rainfall extremes are approximately 4-10°C and 6-12°C higher than the corresponding seasonal temperature means in summer and winter, respectively. ECHAM5 yields even 2°C stronger extremes compared to seasonal means.

The variation coefficients of the presented GPD estimates are higher in winter than

in summer and yield maximum values of 10-15% over eastern Turkey and northern Africa in REMO and ECHAM5 and over Italy and Greece in E-OBS. Generally, the variation coefficients are highest for E-OBS and ECHAM5 and lowest for REMO according to the different sample sizes (Fig. 7.1, third and fourth row). The high REMO variation coefficients over eastern Turkey for winter temperature are not prominent in ECHAM5 or E-OBS and disappear with higher aggregation levels. Thus, single daily REMO data values such as especially cold winter days in mountainous Turkish regions probably cause a strong spread of parametric bootstraps. But generally, the relative standard error of the parametric bootstrap sampling is quite small due to large temperature data samples. Furthermore, the Kolmogorov-Smirnov tests of the GPD fits for a significance level of 10% are positive over all Mediterranean grid boxes indicating a very good agreement between theoretical GPD fits and empirical sample data. Thus, the 1d-20a-RTVs of temperature are similarly distributed to seasonal temperature means, and the agreement of temperature extremes between both models and observations is rather good. But REMO yields more topographic details over mountainous areas in comparison to the spatial interpolation of E-OBS and the coarse ECHAM5 grid probably improving the extreme results of both datasets. The variation coefficients and Kolmogorov-Smirnov tests yield rather small uncertainties for the GPD analysis of temperature extremes.

The corresponding GPD return values and variation coefficients for daily REMO, E-OBS and ECHAM5 precipitation in 1961-1990 are presented in Fig. 7.2. The spatial patterns of the seasonal 1d-20a-RTVs equal those of the corresponding seasonal precipitation totals (cf. Fig. 4.6) yielding maximum values over southern Europe in winter and minimum values over northern Africa in both summer and winter. But the 1d-20a-RTVs of REMO mostly overestimate E-OBS extremes over the northern Mediterranean in both seasons, especially over the maximum precipitation regions over western coasts and mountain ranges in winter, and underestimate the observed extremes over the Near East in winter. ECHAM5 mostly rather underestimates observed precipitation extremes, especially over the maximum rainfall regions and the Near East in winter and over many parts of the northern Mediterranean in summer (Fig. 7.2, first and second row). The 1d-20a-RTVs exceed the seasonal totals (related to one day) by up to 50mm in summer and 50-100mm in winter with REMO reaching higher magnitudes of extremes compared to seasonal totals than E-OBS and ECHAM5 in winter.

The variation coefficients present relative uncertainties of the GPD return values between 6-10% over southern Europe and Turkey in winter and 30-80% over northern Africa in both seasons with maximum in summer and are higher for REMO than

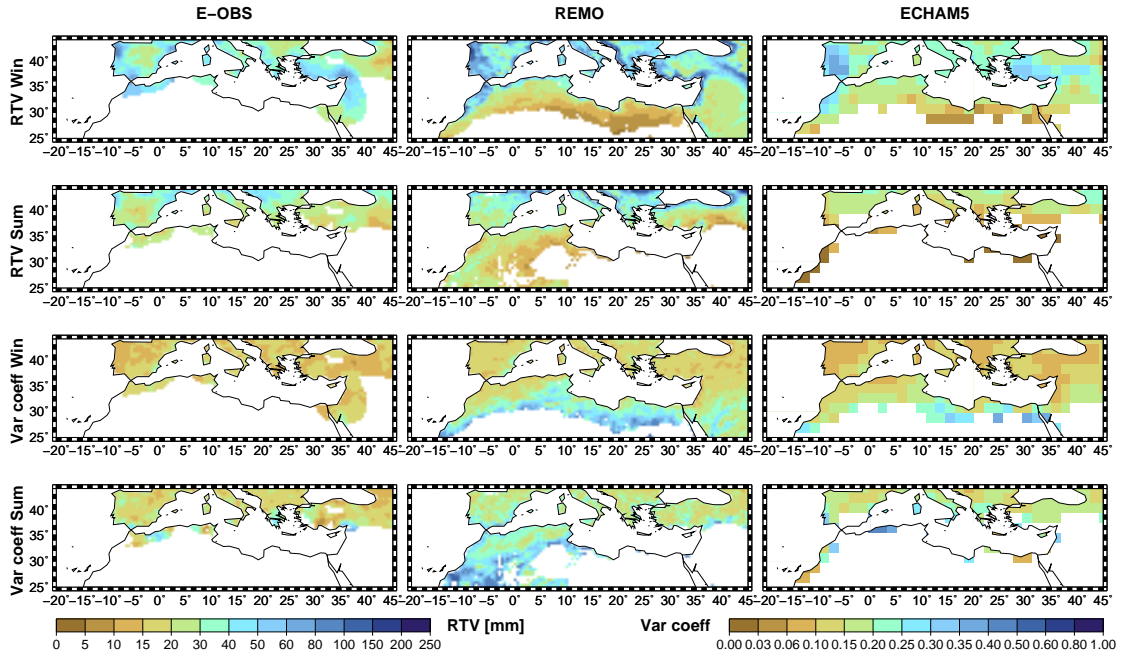


Figure 7.2: Validation of GPD 1d-20a-RTVs from REMO (middle) and ECHAM5 (right) for winter and summer precipitation with E-OBS return values (left) and corresponding variation coefficients in 1961-1990.

for E-OBS and ECHAM5 due to larger return values and standard errors in REMO (Fig. 7.2, third and fourth row). These relative spreads between different parametric bootstraps are far higher than those for temperature because of much smaller precipitation sample sizes over the southern Mediterranean in summer. There are many grid boxes in the southern and eastern Mediterranean, especially for E-OBS and ECHAM5 in summer, for which the GPD analysis cannot be performed due to small data samples. The Kolmogorov-Smirnov test is mostly positive for all resulting grid boxes identifying successful GPD fits to empirical data. Thus, the spatial patterns of 1d-20a-RTVs for precipitation equal those of the seasonal rainfall totals. The spatial and seasonal distributions of simulated and observed extreme rainfall agree generally well but REMO overestimates observed rainfall extremes, especially over the maximum rainfall regions in winter, and ECHAM5 rather underestimates observed values in winter and summer. Consequently, REMO succeeds in increasing the low rainfall extremes of the coarse grid ECHAM5 model but even tends to overestimate observed extremes. These results are rather similar to those of the seasonal precipitation totals and the quantile-based extreme indices and discussions of the corresponding results have already been given in these chapters (cf. subsections 4.1.2 and 6.1.3). Furthermore, the uncertainties of the GPD fit for daily precipitation data are much higher than those for temperature due to smaller rainfall data samples, especially over the southern Mediterranean in summer.

Generally, the presented GPD 1d-20a-RTVs of E-OBS, REMO and ECHAM5 temperature and precipitation for 1961-1990 fit quite well with corresponding empirical quantiles denoting good performance of the theoretical GPD fits to empirical sample data. Fig. 7.3 presents the differences between GPD 1d-20a-RTVs and corresponding empirical quantiles for 1961-1990 exemplarily for the best and worst validation results for both temperature and precipitation extremes. The GPD 1d-20a-RTVs of ECHAM5 summer temperature and winter precipitation show high agreement with empirical quantiles reaching maximum differences of 0.2-0.5 °C and 2-10mm only (Fig. 7.3, bottom). In contrast, the 1d-20a-RTVs of E-OBS winter temperature and REMO summer precipitation yield relatively high disagreements with empirical quantiles of up to 2°C over southern Italy and the Balkan Peninsula and 20-25 mm over the north-western Africa mostly denoting regions of small data samples or high variation coefficients (Fig. 7.3, top). However, sensitivity tests performed for REMO show that the differences between GPD return values and empirical quantiles remain mostly smaller than 1.645 times the GPD standard error for both temperature and precipitation even for higher return times, i.e. the empirical quantiles lie within the 90% confidence intervals of the GPD return values defined by the GPD standard error over parametric bootstraps. Thus, the deviations of fitted GPD return values from empirical quantiles are well described by the method of parametric bootstrap sampling and by the resulting variation coefficients.

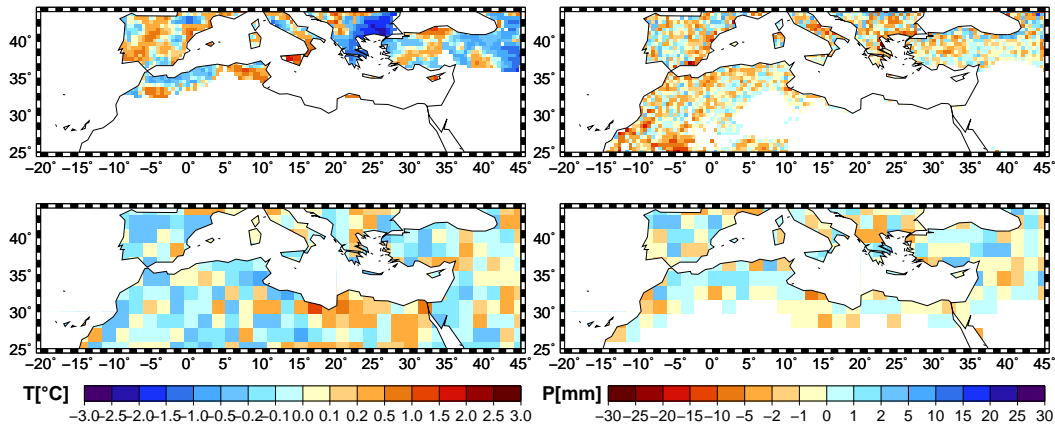


Figure 7.3: Differences between GPD 1d-20a-RTVs and empirical quantiles of ECHAM5 summer and E-OBS winter temperature (lower and upper left) and ECHAM5 winter and REMO summer precipitation (lower and upper right) for 1961-1990.

7.1.2 Evaluation of dynamical downscaling

In order to perform a detailed evaluation of dynamical downscaling for temperature and precipitation extremes both REMO and E-OBS summer and winter GPD 1d-

20a-RTVs for 1961-1990 are interpolated to the 1.875° resolution of ECHAM5 by Inverse Distance Weighting (IDW). This simple interpolation method averages for every new grid box the four nearest old grid boxes in weighting them with the inverse of the corresponding geographical distance to the new grid box applying the cosine rule for sides from spherical trigonometry for the grid box mean coordinates on the globe. The new grid box is set to missing value if any of the four nearest old grid boxes is defined as missing value. The IDW interpolation is applied for temperature and precipitation instead of the quadratic spline interpolation used for sea level pressure in this study (section 3.4) because the latter produces unrealistic negative precipitation values over dry areas if the rainfall gradients of neighbouring grid boxes are strong. However, one has to keep in mind that the IDW interpolation slightly tends to smooth temperature and precipitation extremes.

After interpolation the difference of GPD 1d-20a-RTVs between REMO and E-OBS is compared to that between ECHAM5 and E-OBS on 1.875° (Fig. 7.4). For temperature, REMO mostly underestimates the E-OBS 1d-20a-RTVs, especially in

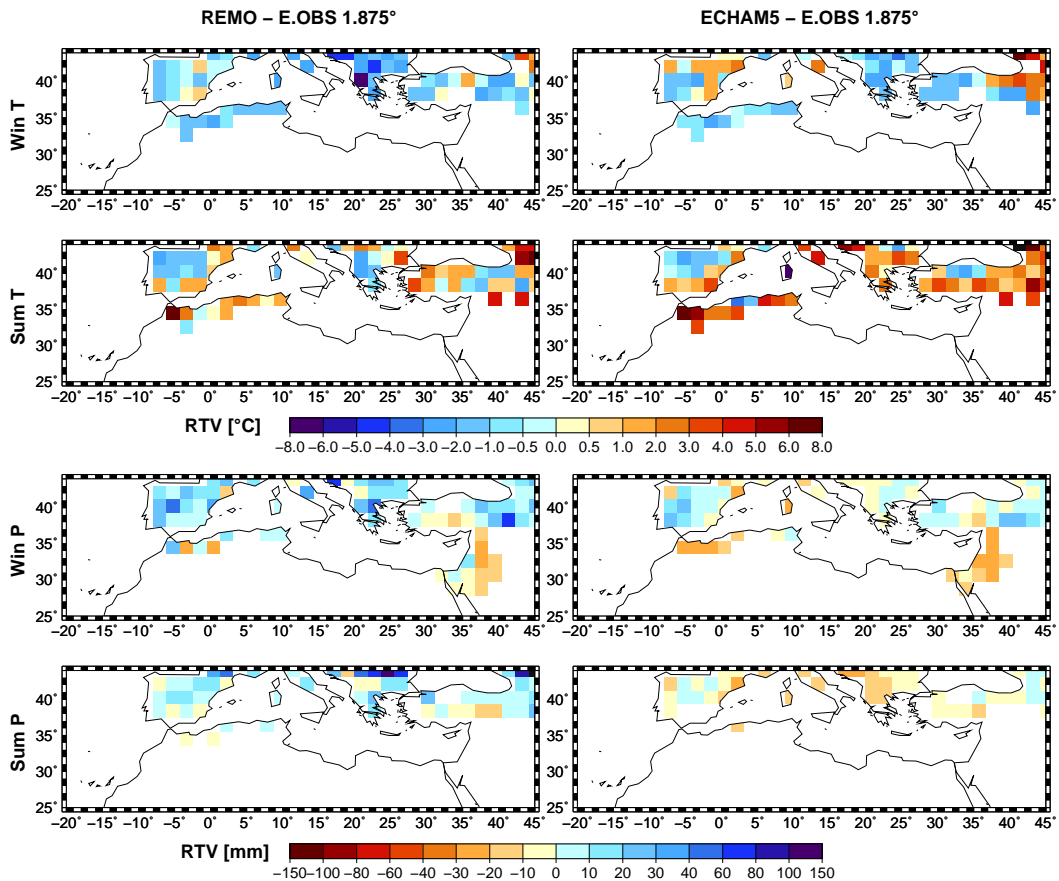


Figure 7.4: Difference of GPD 1d-20a-RTVs between REMO and E-OBS (left) and between ECHAM5 and E-OBS (right) on 1.875° for temperature and precipitation in winter and summer of 1961-1990.

winter and over mountain ranges in summer, but shows some overestimations in summer. ECHAM5 yields usually higher values than E-OBS in summer and a mixed pattern of higher and smaller values in winter. Generally, REMO agrees slightly better with E-OBS than ECHAM5 over Spain and Turkey in winter and over the Atlas mountains in summer. Only the Balkans in winter show higher disagreements of REMO with E-OBS (Fig. 7.4, first and second row). For precipitation, there is a rather good accordance of the 1d-20a-RTVs between ECHAM5 and E-OBS in both seasons except some underestimations of ECHAM5 over the Atlas mountains and Near East in winter and over the northern Mediterranean in summer. REMO produces generally too high rainfall extremes over the northern Mediterranean, especially in winter, and some underestimations over the Near East in winter similar to ECHAM5 (Fig. 7.4, third and fourth row).

Thus, dynamical downscaling from ECHAM5 to REMO improves the high-resolution representation of warm temperature extremes over mountainous regions of the Mediterranean area denoting an added value of regional climate modelling but generally worsens the agreement of rainfall extremes with E-OBS over the northern Mediterranean in winter due to overestimated precipitation extremes in REMO. Further discussions and explanations on the precipitation topic can be found in the chapters on seasonal precipitation totals and quantile-based extreme indices (cf. subsections 4.1.2 and 6.1.3). The weather generator of the following chapter 8 produces local virtual rainfall stations from gridded REMO data and performs a direct comparison to original rainfall stations at the local scale avoiding the discussed impacts of statistical interpolation or area-averaging in gridded E-OBS and REMO datasets.

7.1.3 GPD parameters

Fig. 7.5 depicts the GPD parameters for daily E-OBS, REMO and ECHAM5 temperature without aggregation for the present-day time period 1961-1990. Due to similar patterns in both winter and summer only summer results are shown here. The first GPD parameter presents the distribution mean revealing equal spatial patterns to the 1d-20a-RTV and approximately similar differences between models and observations already discussed in subsection 7.1.1 (Fig. 7.5, left). The second parameter points at the dispersion of the distribution and reaches highest values over the Iberian Peninsula, Tunisia and Libya. Even if several differences between observed and simulated values can be stated the spatial distribution agrees rather well (Fig. 7.5, middle). Finally, the third parameter yields exclusively positive values over the whole Mediterranean area denoting long-tailed distributions for all

datasets. REMO and ECHAM5 match quite well with observed values except some slight overestimations over the Balkans (Fig. 7.5, right). But in winter accordance of the third parameter is slightly worse due to some discrepancies over the Balkans in E-OBS and eastern Turkey in REMO denoting regions of high variation coefficients and thus, high uncertainty of the GPD fit. Consequently, a rather good agreement in the general spatial distribution of GPD parameters can be stated for E-OBS, REMO and ECHAM5 temperature.

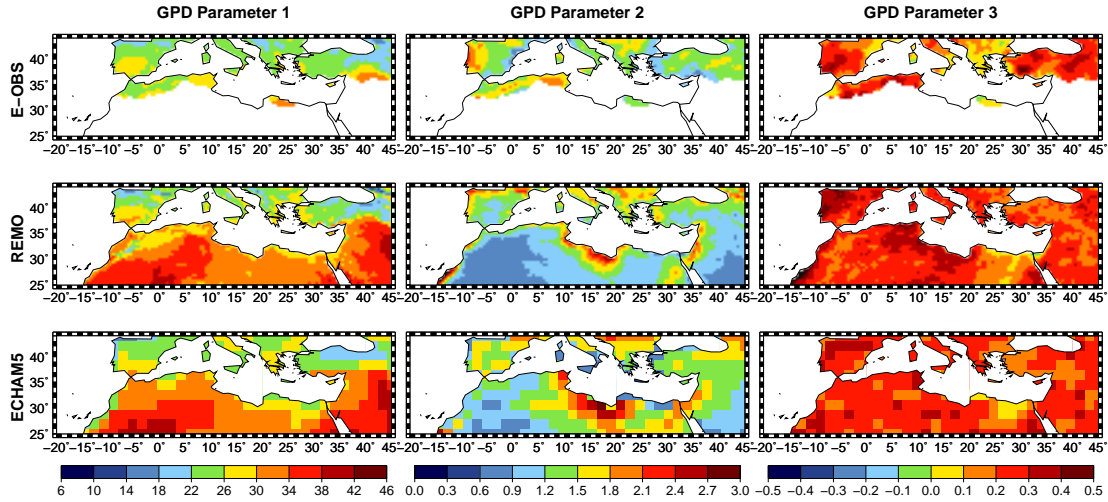


Figure 7.5: Validation of the first (left), second (middle) and third GPD parameter (right) from REMO (middle) and ECHAM5 (bottom) summer temperature without aggregation with E-OBS parameters (top) in 1961-1990.

Corresponding GPD parameters for daily winter precipitation are shown in Fig. 7.6. Summer precipitation results are not depicted revealing mostly similar patterns to winter. The first GPD parameter shows approximately the same spatial distribution than the 1d-20a-RTV (see subsection 7.1.1) with maximum values over western coasts and mountain ranges of the northern Mediterranean. Both models reproduce the general spatial distribution of observations but REMO overestimates and ECHAM5 rather underestimates observed values over these maximum regions (Fig. 7.6, left). The second parameter yields quite equal patterns to the first parameter revealing strongest GPD dispersions over regions with highest GPD means and similar differences between models and observations (Fig. 7.6, middle). Finally, stronger disagreements can be stated for the third parameter reaching mostly positive values in E-OBS and ECHAM5 but negative values in REMO, especially strong over northern Africa, indicating long-tailed and short-tailed distributions, respectively. But several negative values can also be detected for E-OBS, especially over eastern Spain, agreeing well with REMO. However, ECHAM5 seems to match the observed third GPD parameter better than REMO although ECHAM5 underestimates the

observed maximum parameter values (Fig. 7.6, right). For higher aggregation levels, the third GPD parameter of REMO changes as well to positive signs. Thus, both REMO and ECHAM5 mostly reproduce the general spatial distribution of observed GPD parameters but yield overestimations and underestimations for the first and second GPD parameters like for the 1d-20a-RTVs, and rather long-tailed distributions can be stated for E-OBS and ECHAM5 in contrast to short-tailed distributions for REMO in the third GPD parameter. This discrepancy of gridded REMO data can be strongly improved by the application of the dynamical-statistical weather generator resulting in high agreement with observational rainfall stations (see chapter 8).

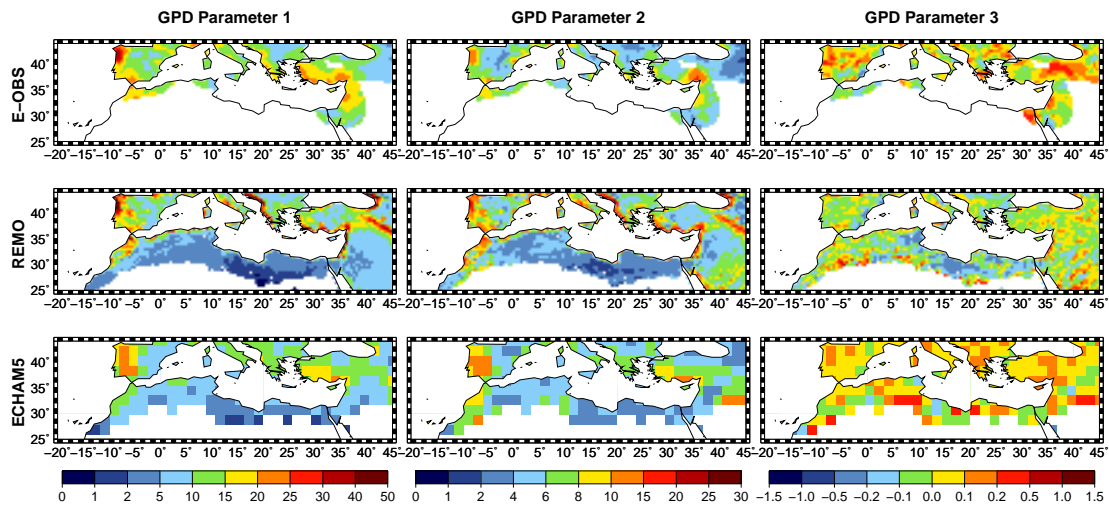


Figure 7.6: Validation of the first (left), second (middle) and third GPD parameter (right) from REMO (middle) and ECHAM5 (bottom) winter precipitation without aggregation with E-OBS parameters (top) in 1961-1990.

7.1.4 GPD return values of different return times and aggregation levels

In order to have a closer look at the impact of different return times and aggregation levels on GPD return values for temperature and precipitation several exemplary Mediterranean regions are investigated in more detail similar to those chosen for the analysis of the seasonal cycle (see subsection 4.1.1). The GPD return values of the regions are averaged from 4x4 REMO and E-OBS grid boxes to fit approximately one ECHAM5 grid box. If more than eight grid boxes are declared as missing values, the resulting area-averaged REMO and E-OBS grid box is removed.

Fig. 7.7 depicts the GPD 1d-RTVs of E-OBS, REMO and ECHAM5 temperature for different return times and the corresponding GPD 20a-RTVs for different aggregation levels in 1961-1990 for two selected regions and seasons. For both central

Turkey in winter and Morocco in summer, the 1d-RTVs slightly increase with higher return times describing more rare extreme events (Fig. 7.7, top) and the 20a-RTVs decrease with higher aggregation levels due to the averaging procedure in temperature aggregation (Fig. 7.7, bottom). This holds for all selected regions and for both models and observations. Furthermore, over all return times and aggregation levels REMO fits quite better to E-OBS than ECHAM5 which strongly underestimates and overestimates observed values over central Turkey in winter and Morocco in summer, respectively. This detailed analysis at regional scale strongly confirms the previous validation and dynamical downscaling results for temperature over mountainous areas. Generally, for all selected regions and datasets the temperature return values increase with increasing return times denoting higher temperature magnitudes for more rare extreme events and decrease for increasing aggregation levels revealing smaller temperature extremes for longer-term warm periods averaged over several days, indicating heat waves.

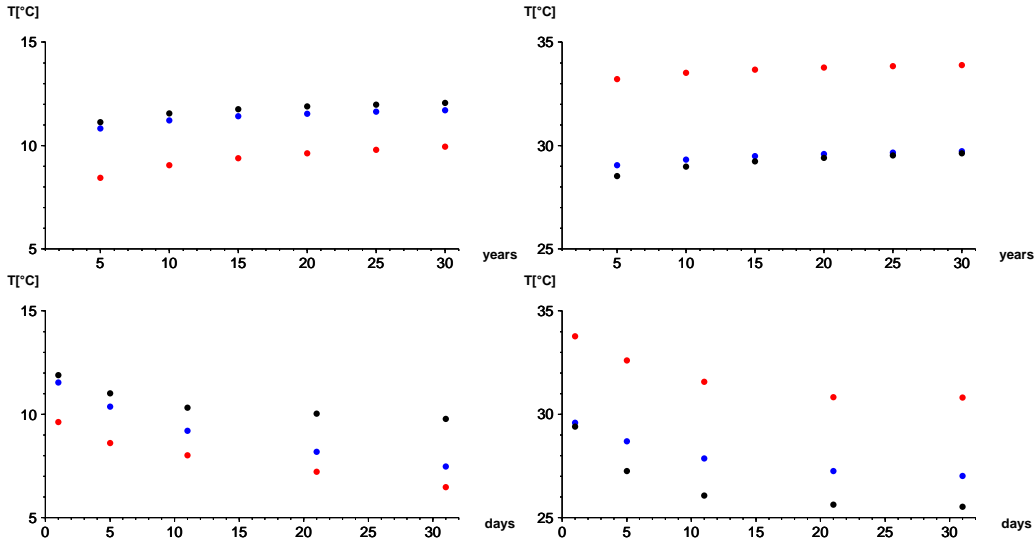


Figure 7.7: GPD 1d-RTVs of E-OBS (black), REMO (blue) and ECHAM5 temperature (red) for different return times (top) and corresponding GPD 20a-RTVs for different aggregation levels (bottom) for central Turkey in winter (left) and Morocco in summer (right) in 1961-1990.

The corresponding GPD 1d-RTVs for different return times and GPD 20a-RTVs for different aggregation levels for precipitation are shown in Fig. 7.8 for two selected regions and seasons. In Spain for both winter and summer seasons the GPD 1d-RTVs and GPD 20a-RTVs increase with higher return times of more rare rainfall extremes and with larger aggregation levels due to the adding procedure of precipitation aggregation (Fig. 7.8, top and bottom). This can be stated in all considered regions and datasets. Both ECHAM5 and REMO overestimate E-OBS return values but the agreement between ECHAM5 and E-OBS is higher than that between REMO

and E-OBS, especially in summer when ECHAM5 rainfall extremes are nearly identical to those of E-OBS except for higher aggregation levels. Once more this regional analysis confirms the previous validation and dynamical downscaling results for precipitation. On the one side, with higher aggregation levels the sample size of precipitation data strongly increases leading to lower variation coefficients of 2-20% over the whole area, and more southern Mediterranean grid boxes are appropriate for the GPD fit. But on the other side, the number of negative Kolmogorov-Smirnov tests due to lower critical values for larger sample sizes increases also mainly in the southern Mediterranean. Generally, the precipitation return values increase with both increasing return times and aggregation levels describing higher precipitation sums for more rare extreme events as well as for longer-term wet periods aggregated over several days in all selected regions, seasons and datasets.

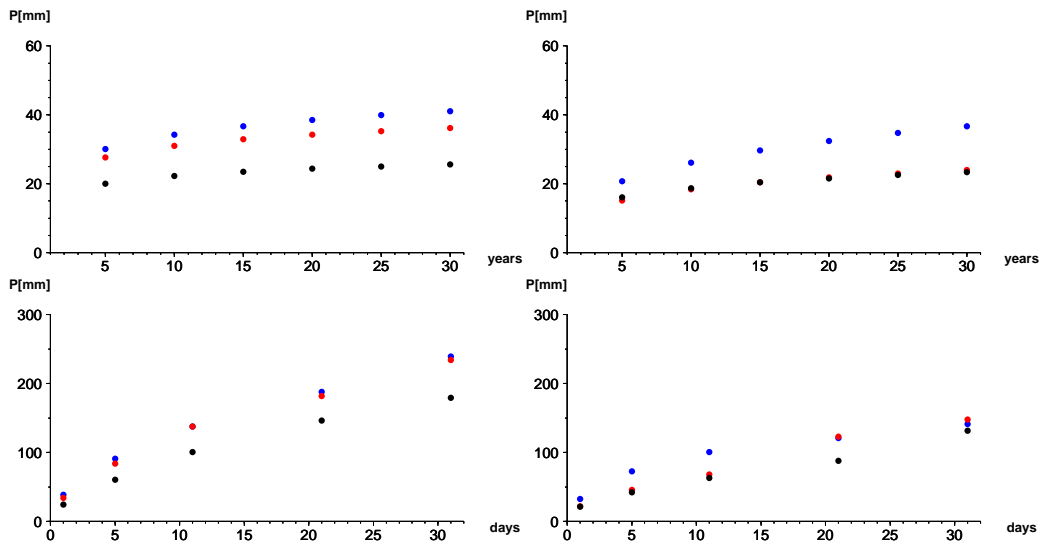


Figure 7.8: GPD 1d-RTVs of E-OBS (black), REMO (blue) and ECHAM5 precipitation (red) for different return times (top) and corresponding GPD 20a-RTVs for different aggregation levels (bottom) for Spain in winter (left) and summer (right) in 1961-1990.

7.2 Dynamical downscaling of future climate

After the validation of the present-day GPD return values of both REMO and ECHAM5 with the observed extremes of E-OBS in 1961-1990 the corresponding temperature and precipitation return values of the future time period 2021-2050 are computed for the A1b and B1 emission scenarios. The future changes compared to the present-day time period 1961-1990 are calculated and the dynamical downscaling from ECHAM5 to REMO is investigated for temperature and precipitation extremes. The following subsections describe the resulting future GPD 1d-20a-RTV changes

for temperature and precipitation with corresponding uncertainties of the GPD fits, the future changes of the GPD parameters and the return value changes for different return times and aggregation levels.

7.2.1 GPD fit and uncertainty

Fig. 7.9 displays the GPD 1d-20a-RTV change of REMO and ECHAM5 temperature in 2021-2050 compared to 1961-1990. In summer, REMO shows significant 1d-20a-RTV increases of 1.5-3°C over the whole Mediterranean with maxima of 4°C over the Iberian Peninsula and eastern Turkey for the A1b scenario. In winter, 1d-20a-RTV increases prevail as well but significance and intensity of change are smaller yielding highest change values over north-eastern Africa (Fig. 7.9, top). The B1 scenario yields equal spatial patterns of change but with slightly smaller intensities and less significance (Fig. 7.9, middle). ECHAM5 reveals stronger 1d-20a-RTV increases than REMO over the whole Mediterranean area in both seasons, especially over northern Africa and the Middle East (Fig. 7.9, bottom). The change of 1d-20a-RTVs shows similar spatial patterns but slightly smaller change intensities compared to the seasonal mean temperature trends in 1961-2050 (see subsection 4.2.2) except for a stronger increase of temperature extremes over northern Africa and the Near East in winter for both models.

The temperature data sample sizes remain large in the future time period. Thus,

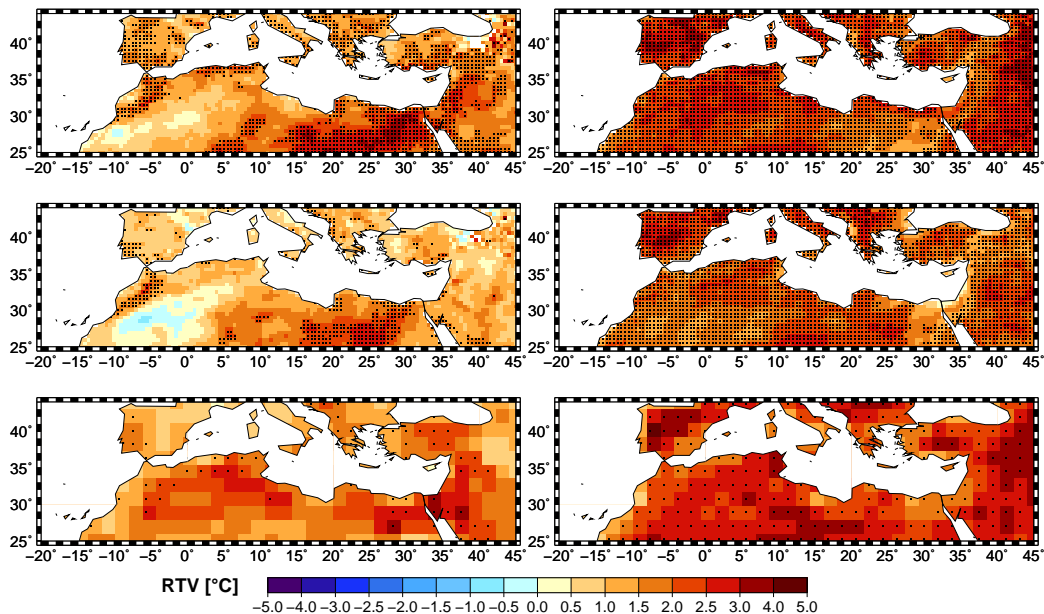


Figure 7.9: GPD 1d-20a-RTV change of REMO temperature for the A1b (top) and B1 emission scenarios (middle) and ECHAM5 temperature for A1b (bottom) during winter (left) and summer (right) in 2021-2050 compared to 1961-1990, applying a significance level of 5% (dots).

the Kolmogorov-Smirnov test results are mostly unchanged, the agreement with empirical quantiles only slightly worsens and the variation coefficients yield only small changes. But the REMO winter temperature over eastern Turkey depicts some problems in GPD fitting probably due to single extremely cold winter days because several grid boxes are deleted due to negative Kolmogorov-Smirnov tests and the variation coefficients depict various small-scale changes pointing at uncertain GPD fits and strongly differing parametric bootstraps. Generally, the future temperature extremes strongly increase over the whole Mediterranean area, especially in summer for the A1b emission scenario, with equal spatial distribution but mostly slightly smaller change intensities than the seasonal mean temperature trends in 1961-2050. ECHAM5 yields stronger increases than REMO, especially over the southern Mediterranean, agreeing well with seasonal mean temperature trends.

The GPD 1d-20a-RTV change of REMO and ECHAM5 precipitation for 2021-2050 compared to 1961-1990 is depicted in Fig. 7.10. The A1b emission scenario of REMO yields maximum changes in daily rainfall extremes of up to 30-50mm revealing decreasing patterns over the southern Mediterranean in winter and over the Iberian Peninsula and Turkey in summer and increasing patterns over the northern Mediterranean in winter and over the Balkans in summer (Fig. 7.10, top). The B1 scenario displays rather similar spatial change patterns and intensities to A1b with only some small differences (Fig. 7.10, middle). ECHAM5 yields equal change patterns to REMO as well but only very small change intensities of up to 10mm (Fig. 7.10, bottom). All presented changes do not reach significance over the whole area mainly due to small precipitation data samples causing high standard errors of the parametric bootstrap sampling. In comparison to the trends of the seasonal rainfall totals in 1961-2050 (see subsection 4.2.2) the regions with increases in rainfall extremes are larger than those with increases in seasonal totals. Thus, several regions can be identified in REMO with decreasing rainfall totals but increasing precipitation extremes, e.g. the Iberian Peninsula, southern Turkey and the Near East in winter and the Balkans in summer. Furthermore, smaller differences between A1b and B1 emission scenarios are stated for GPD rainfall extremes than for seasonal rainfall totals.

Due to slightly smaller data samples in the future time period the variation coefficient mostly increases, the agreement with empirical quantiles is slightly worse and slightly less grid boxes in the southern Mediterranean are appropriate for GPD analysis. Thus, the precipitation extremes of the future time period 2021-2050 mostly increase and decrease over the northern and southern Mediterranean in winter, respectively, and mostly decrease over the northern Mediterranean in summer except

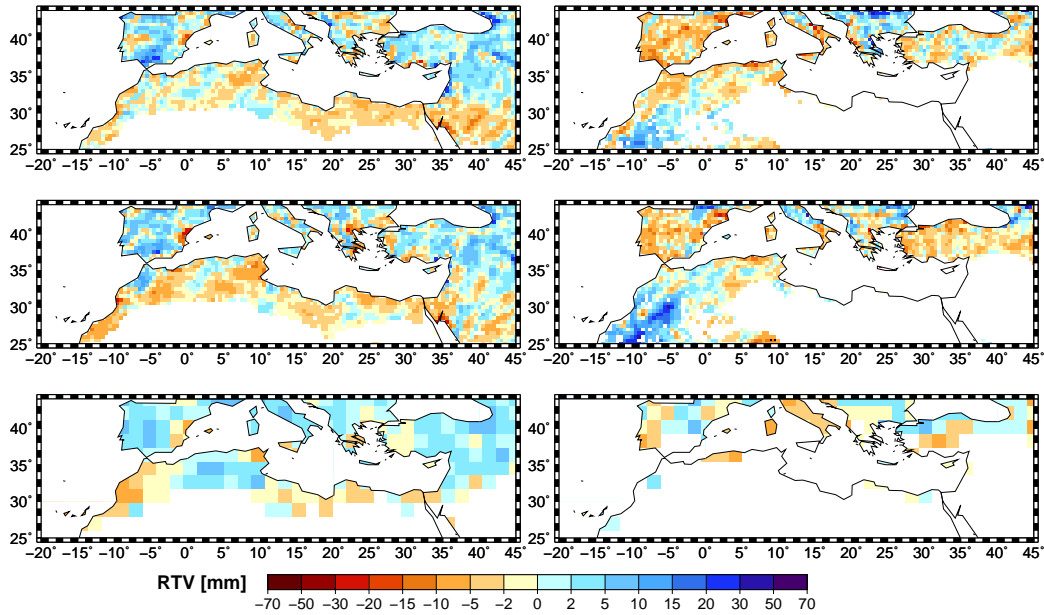


Figure 7.10: GPD 1d-20a-RTV change of REMO precipitation for the A1b (top) and B1 emission scenarios (middle) and ECHAM5 precipitation for A1b (bottom) during winter (left) and summer (right) in 2021-2050 compared to 1961-1990, applying a significance level of 5% (dots).

for some increases over the Balkans. But all these changes do not reach significance. The regions of increasing precipitation extremes are more expanded over southern Europe and Turkey in winter and over the Balkans in summer than the regions of increasing seasonal rainfall totals in 1961-2050 revealing several Mediterranean regions with decreasing rainfall totals but increasing precipitation extremes. Furthermore, ECHAM5 yields smaller changes of precipitation extremes than REMO.

7.2.2 GPD parameters

The change of GPD parameters of daily REMO and ECHAM5 summer temperature without aggregation for 2021-2050 related to 1961-1990 for the A1b emission scenario is depicted in Fig. 7.11 (first and second row). Winter results are not depicted here showing rather similar change patterns to summer but smaller increases of the first GPD parameter. The first parameter reaches strong increases over the whole Mediterranean area in summer larger for ECHAM5 than for REMO and similar to the 1d-20a-RTV change. Smaller increases prevail for the second GPD parameter over the whole area reaching slightly higher values for REMO than for ECHAM5. The third parameter yields a mixed spatial change pattern of both small increases and decreases with strong agreement between REMO and ECHAM5. Thus, strongest future change of GPD parameters can be found for the distribution mean with some smaller increases of the GPD dispersion and mixed changes of the

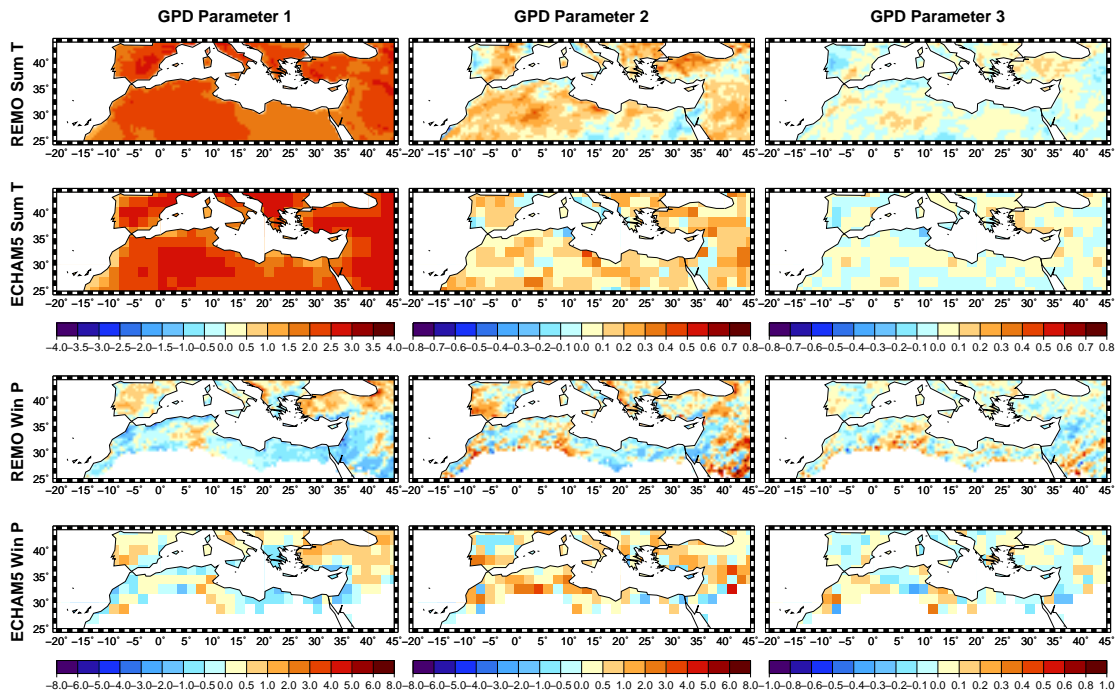


Figure 7.11: Change of the first (left), second (middle) and third GPD parameter (right) for the A1b emission scenario of REMO and ECHAM5 summer temperature and winter precipitation for 2021-2050 compared to 1961-1990.

GPD shape parameter. This probably points at a linear displacement of the GPD to higher temperature extremes without major future changes in the GPD shape.

The corresponding change of the GPD parameters for daily winter precipitation without aggregation is displayed in Fig. 7.11 (third and fourth row). Summer shows similar patterns to winter but strong decreases in the first GPD parameter over southern Europe larger for REMO than for ECHAM5 and is not shown here. In winter, the change of the first GPD parameter shows similar change patterns to the 1d-20a-RTV change with strong increases and decreases over the northern and southern Mediterranean, respectively, but several differences can be stated for REMO over Tunisia, the Balkans and Middle East. The change patterns of the second and third GPD parameters are strongly mixed with slightly dominating increasing tendencies. ECHAM5 shows generally similar spatial change patterns to REMO but less small-scale structures and slightly smaller changes for all parameters. Thus, future changes of GPD parameters for daily precipitation clearly prevail in the location parameter revealing both increases and decreases depending on the considered Mediterranean region and season. But these changes of the distribution mean are strongly overlaid by various changes in the second and third GPD parameter having major influences on the future shape of the GPD.

7.2.3 GPD return values of different return times and aggregation levels

The regional impacts of different return times and aggregation levels on future GPD return value changes are investigated for the same Mediterranean regions as in the present-day time period. Fig. 7.12 presents the GPD 1d-RTV changes of REMO and ECHAM5 temperature and precipitation for the A1b and B1 emission scenarios for different return times in 2021-2050 compared to 1961-1990 and the corresponding GPD 20a-RTV changes for different aggregation levels. The temperature return values are shown for Israel and the Balkans in winter and the precipitation return values for Spain in summer and winter. For winter temperature over Israel, the 1d-RTV change clearly increases with higher return times and for winter temperature over the Balkans, the 20a-RTV change is more disturbed but increases also slightly with higher aggregation levels (Fig. 7.12, left). This result is confirmed in several other selected regions but some regions yield rather constant or even decreasing return value changes with increasing return times or aggregation levels. In those regions shown, the A1b scenario causes higher 1d-RTV and 20a-RTV changes than the B1 scenario being consistent over many other regions. Furthermore, winter precipitation over Spain yields increasing 1d-RTV changes with higher return times except for the B1 scenario of ECHAM5, and summer precipitation over Spain results in increasing 20a-RTV changes of negative signs with higher aggregation levels, espe-

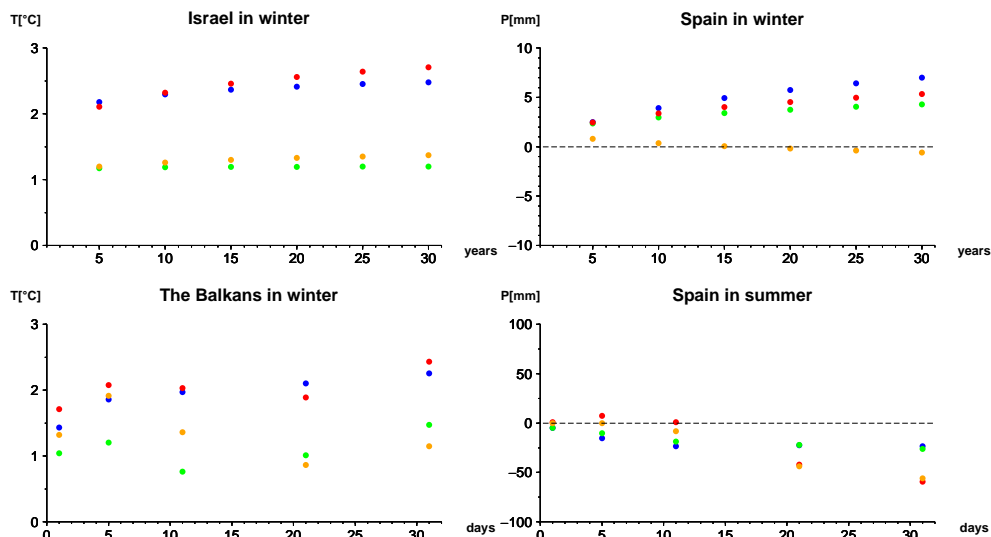


Figure 7.12: GPD 1d-RTV change of temperature (left) and precipitation (right) from REMO for the A1b (blue) and B1 emission scenarios (green) and from ECHAM5 for A1b (red) and B1 (orange) for different return times (top) and corresponding GPD 20a-RTV change for different aggregation levels (bottom) in 2021-2050 compared to 1961-1990 for several selected Mediterranean regions and seasons.

cially for ECHAM5 at the highest aggregation levels (Fig. 7.12, right). This increase of absolute return value changes with increasing return times and aggregation levels is consistent over most regions and seasons analysed.

Consequently, in many regions and seasons the absolute future change of temperature and precipitation extremes increases with higher return times and aggregation levels when more rare extreme events and longer-term heat waves or wet periods aggregated over several days are regarded, respectively. Thereby, the geographical pattern of future changes remains constant for different return times but alters for different aggregation levels. Significance of future change mostly decreases with higher return times due to higher variation coefficients and thus, larger spread between different parametric bootstraps at the upper tails of the fitted GPD. For higher aggregation levels, significance increases and even reaches few significant changes of precipitation extremes probably indicating that the increasing GHG concentrations of future simulations impact stronger on temperature and rainfall extremes on the monthly scale than on the daily scale.

8 Precipitation extremes from a weather generator

The final results chapter describes precipitation extremes constructed by a dynamical-statistical weather generator (PAETH and DIEDERICH, 2010) considering orographic impacts of windward and lee effects, a stochastic term describing the spatial spread within a model grid box and a PDF matching of simulated to observed distributions. This method presents the final step in computing and analysing extreme values because the virtual stations derived from gridded REMO model data are directly compared with original stations at the local scale to avoid erroneous impacts of statistical interpolation or area-averaging in gridded observational and simulated datasets (cf. subsections 4.1.2, 6.1.3 and 7.1.2). This analysis is solely performed for rainfall and not for temperature because precipitation strongly varies on different temporal and spatial scales. Furthermore, simulated area-averaged rainfall is known to strongly overestimate the number of rain days and underestimate daily mean and extreme intensities (ZOLINA et al., 2004; PAETH and DIEDERICH, 2010) and gridded E-OBS data is found to smooth extreme rainfall intensities compared to local stations due to spatial interpolation (HAYLOCK et al., 2008). Thus, in the first section the performance of the weather generator is investigated and the resulting virtual precipitation stations are validated with original stations in present-day climate. Thereby, the extended present-day time period 1960-2000 is applied to increase the data sample size for the application of the weather generator. Then, precipitation extremes from virtual and original station data are constructed by means of a GPD fit similar to the previous chapter for the present-day time period 1961-1990 for validation and compared to former gridded rainfall extremes from REMO, ECHAM5 and E-OBS data. The final subsection presents the precipitation extremes of virtual station data for the future time period 2021-2050 for both A1b and B1 emission scenarios with some further comparisons to gridded future REMO and ECHAM5 rainfall extremes.

8.1 Validation of the weather generator in present-day climate

The dynamical-statistical weather generator constructs relationships between area-averaged grid box precipitation and local rainfall station values using several Mediterranean precipitation stations, gridded ERA40 horizontal wind fields on 0.5° resolution and orographic gradients for original stations and model grid boxes from SRTM elevation data for the extended present-day time period 1960-2000. These relationships are applied to gridded 0.5° REMO rainfall and wind data for 1961-2050 to derive virtual rainfall stations at the local scale, separately for each REMO model ensemble member. Thus, this section describes the input data and general performance of the weather generator and validates the resulting virtual station data with original rainfall stations during 1960-2000. The first subsection presents the observed and simulated rainfall and horizontal wind field input data from original stations, ERA40 and REMO and the elevation values and orographic gradients for both stations and REMO grid boxes. The second subsection describes the relationships between original station rainfall, observed horizontal winds and orographic gradients denoting the orographic term of the weather generator. The two final subsections validate the resulting virtual rainfall stations from gridded REMO model output with original station data during the extended present-day time period 1960-2000 concerning the distribution of daily rainfall and several precipitation characteristics, i.e. number of rainless days and daily rainfall intensity and variability.

8.1.1 Precipitation, wind and orography input data

From all 330 given original precipitation stations of the Mediterranean area 102 stations remain after tests for homogeneity and completeness (cf. subsection 2.1.1). Due to the calculation of orographic gradients for REMO grid boxes over three grid box elevation values (cf. chapter 3.8) four original stations lying in the ultimate northern row of the REMO model domain ($\geq 44.75^\circ$ N) are sorted out as well as two stations lying further north outside the REMO grid. Three Turkish stations are removed because of more than 65% missing values in the station time series. Thus, 93 Mediterranean rainfall stations remain for the application of the weather generator during the extended present-day time period 1960-2000 revealing high station density over the Iberian Peninsula and the Near East and several stations over the central Mediterranean area but only two stations over northern Africa (cf. Fig. 8.1). Nearly all stations contain rainfall data over all years of the considered time period. Those two stations starting a bit later and seven stations ending earlier

are kept for analysis with slightly smaller sample sizes. If missing values occur, all station precipitation statistics applied in this study are calculated from all days with rainfall data and extrapolated to the whole number of days per year.

Fig. 8.1 presents the precipitation, wind and orography input data from original stations and REMO grid boxes for the application of the weather generator in 1960-2000. The REMO precipitation and wind input data is exemplarily depicted for the first ensemble member because all three ensemble members yield rather similar results. The average annual precipitation sum for original stations and REMO is shown in Fig. 8.1 (upper left). Generally, a good agreement between observed and simulated spatial rainfall distributions can be stated with maximum and minimum values over the western coasts and mountain ranges of the northern Mediterranean and over the Sahara desert, respectively. But REMO tends to slightly overestimate annual rainfall sums in some Mediterranean regions in comparison to original stations according well with the overestimations of REMO rainfall compared to gridded E-OBS values presented and discussed in subsection 4.1.2.

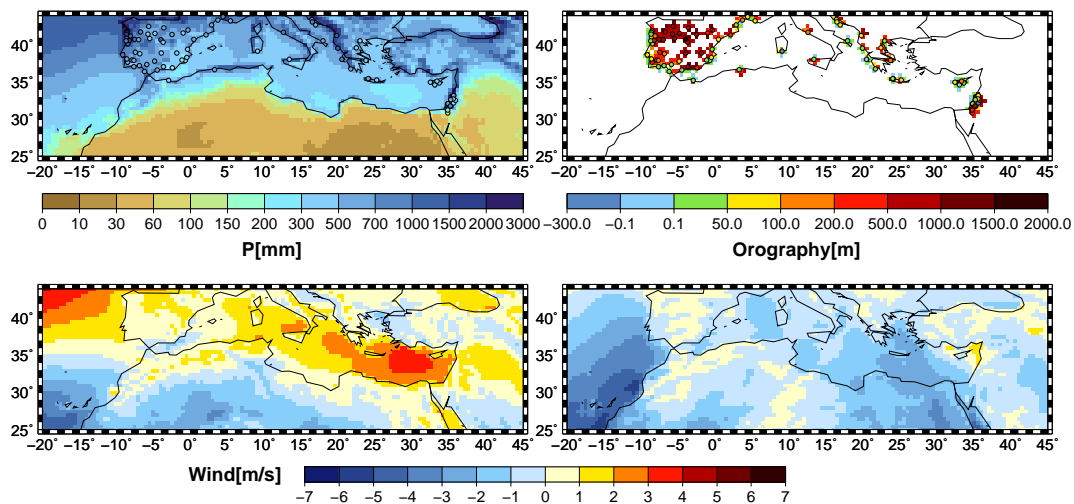


Figure 8.1: Input data of original stations and the first REMO ensemble member for the application of the weather generator in 1960-2000: average annual precipitation sum of stations (dots) and REMO (upper left), average annual zonal and meridional 10m wind fields of REMO (lower left and right) and elevation values of stations (dots) and REMO grid boxes derived from SRTM elevation data (upper right).

Furthermore, Fig. 8.1 (lower left and right) depicts the average annual zonal and meridional 10m wind fields of REMO revealing general patterns of north-westerly and north-easterly winds in the northern and southern Mediterranean, respectively. Maximum westerly winds can be stated over the northern Atlantic ocean and the eastern Mediterranean sea and maximum northerly winds over the subtropical Atlantic ocean and north-eastern Africa. The agreement with corresponding ERA40

horizontal wind fields interpolated to the 0.5° REMO grid is very strong with some higher wind intensities in REMO and thus, not depicted here. During the performance of the weather generator the REMO land water mask is not applied for rainfall and wind input data because 15 original stations on the Mediterranean coastline lie on REMO ocean grid boxes due to truncation errors of the land water mask.

Finally, station and REMO grid box elevation values are derived from 90m SRTM elevation maps to construct corresponding orographic gradients in zonal and meridional direction because the difference between station and grid box orographic gradients is essential for the calculation of the orographic term of the weather generator. Fig. 8.1 (upper right) displays the elevation values of all given original stations and corresponding REMO grid boxes as well as the elevation values of all REMO grid boxes necessary for the calculation of the orographic gradients of REMO. The original stations exactly depict the orographic features of the Mediterranean area at 90m SRTM grid resolution including the diverse elevation values of coastlines, islands and mountain ranges, even the Jordan valley below sea level in the Near East. The maximum and minimum station elevation values are 1,947m (Navacerrada, Spain) and -261m (Deir, Israel). The REMO grid box elevation values agree generally well with stations in spatial distribution but are strongly smoothed featuring maximum and minimum heights of 1,149m (Granada, Spain) and 3m (Torrevieja, Spain). This smoothing of elevation values changes coastlines and removes topographic details like mountain peaks or valleys, e.g. the Jordan valley is not clearly reproduced. Maximum differences in elevation values between stations and REMO can be found over regions revealing such small-scale topographic details: 876m (Amiandos, Cyprus) and -403m (Deir, Israel). But other stations fit quite well with REMO yielding slight differences in elevation values of only 2m (Tavira, Spain). Concerning the orographic gradients in zonal and meridional direction, the strongest station values can be found over mountainous areas like Spain (Navacerrada, $+23\text{m}/100\text{m}$) or Israel (Kefar, $-35\text{m}/100\text{m}$). But many stations yield smaller gradients, e.g. three stations lying directly on the shore feature elevation values and orographic gradients of nearly zero. The orographic gradients of REMO are strongly reduced to values between $+1\text{m}/100\text{m}$ and $-1\text{m}/100\text{m}$ due to smoothed area-averaged elevation values, and often the orographic gradient signs change compared to stations. Strongest differences to stations can be found over such mountainous areas (Navacerrada $+23\text{m}/100\text{m}$, Kefar $-36\text{m}/100\text{m}$) and strongest agreement on the Mediterranean coastlines. Thus, the REMO grid box means strongly smooth the original station elevation values and orographic gradients revealing largest differences over small-scale mountainous areas.

8.1.2 Orographic term

For the application of the orographic term of the dynamical-statistical weather generator, the existence of multiple original stations per REMO grid box is essential because the orographic term is based on the rainfall anomaly of a certain station from the corresponding grid box mean which is computed from several stations within that grid box. PAETH and DIEDERICH (2010) use a minimum threshold of 13 stations per grid box because their test area Benin is very small ($7^\circ \times 4^\circ$ in latitude and longitude direction) and available station density is very high (131 rainfall stations in total). Unfortunately, the given station data base of this study containing only 93 Mediterranean precipitation stations is too small to carry out a comprehensive analysis for the large Mediterranean area. Most REMO grid boxes with original stations are single-station grid boxes. Only six multi-station REMO grid boxes are available over the whole Mediterranean area: four in Galicia, Crete, Cyprus and Israel with two stations per grid box each and two in Israel with five stations per grid box each (cf. Fig. 8.1). Thus, the threshold for the application of the orographic term is set to two stations per REMO grid box, and only 18 stations in six multi-station REMO grid boxes allow the calculation of the orographic term and the corresponding stochastic part determining the spatial rainfall spread within a model grid box. The Mediterranean area is further too large to transfer the orographic or stochastic relationships defined for these stations to the whole area. Hence, for all other original stations in single-station grid boxes only PDF matching can be computed but no orographic term or stochastic part.

For all 18 stations in multi-station grid boxes, the station orographic gradient anomalies respective to the corresponding elevation grid box means and the horizontal ERA40 wind fields are combined to the orographic wind-ward or lee effects per station which are correlated to the corresponding station rainfall anomalies. This correlation reaches maximum values of 0.35 (Kebutzat, Israel) and -0.22 (Jerusalem, Israel) and several stations with absolute correlations higher than 0.20 slightly exceeding corresponding results of PAETH and DIEDERICH (2010) over Benin. Nearly all correlation coefficients reach significance which is proved via two-sided t-test on a significance level of 5% following SCHÖNWIESE (2006). If horizontal wind fields are regarded separately, zonal wind shows higher correlation to precipitation than meridional wind. The corresponding linear regression coefficients yield values between +0.45 and -0.96, and the statistical properties of the residual of the linear regression which are later applied for the calculation of the stochastic part reveal zero mean values and standard deviations of 2.9-9.2mm depending on the selected station. The negative orographic correlations do not seem physically correct mean-

ing that higher orographic gradient anomalies in wind-ward and lee situations are related to smaller and higher precipitation anomalies, respectively, and not vice versa like for positive correlation coefficients. No geographical pattern of stations with negative correlations is obvious, and data sampling errors can be excluded with 1,374-4,655 data points, i.e. days, used in any correlation. Furthermore, negative correlations are present over all tested orographic distances from five to 201 SRTM elevation grid boxes. Thus, we assume that negative correlations between orographic gradients and precipitation result either from the small number of stations per grid box distorting the computation of realistic rainfall grid box means or from wrong given geographical coordinates of the original stations. Several major station location deficiencies have already been corrected but small local errors are rather difficult to correct. Thus, the orographic term yields maximum absolute correlations between orographic wind-ward or lee effects and station precipitation anomalies of 0.20-0.35 but reveals several stations with negative correlation coefficients probably due to small numbers of stations per grid box or erroneous station location coordinates.

8.1.3 Precipitation distribution of virtual station data

Two versions of the weather generator have been applied: a full version including orographic and stochastic terms and PDF matching for those 18 stations in multi-station REMO grid boxes and a PDF matching version without orographic and stochastic parts for all Mediterranean stations. Thus, the impact of the orographic and stochastic terms can be evaluated for 18 stations. During the Mediterranean dry season the number of rain days and thus, the quality of PDF matching is strongly reduced. Due to the PDF matching threshold a large amount of stations and REMO grid boxes cannot be PDF matched at all during summer months and both weather generator versions cannot be performed, especially over the eastern Mediterranean area where on average 3.5 months per original station lack enough rainfall data for PDF matching.

After applying the orographic term, the stochastic part and the PDF matching for both weather generator versions, i.e. the full version and PDF matching only, the daily rainfall distributions of the resulting virtual station data and REMO are validated with original stations for January and July in 1960-2000 in comparing the Gamma (Γ) distribution functions fitted to all data below the 80% quantile (Fig. 8.2). Exemplarily the results of the first REMO ensemble member are presented. In January, REMO works quite well in reproducing the daily station rainfall distributions because winter rainfall rather originates from large-scale frontal systems which are well simulated by RCMs. Many stations are in good agreement with

REMO and both weather generator versions (Fig. 8.2, upper left). Nevertheless, at several stations the typical discrepancies between area-averaged model and local station rainfall data can be stated: REMO produces too many precipitation events of low intensity and too little rainfall extremes. But both weather generator versions clearly overcome this problem and show similar daily distribution functions to original station data (Fig. 8.2, upper middle and right).

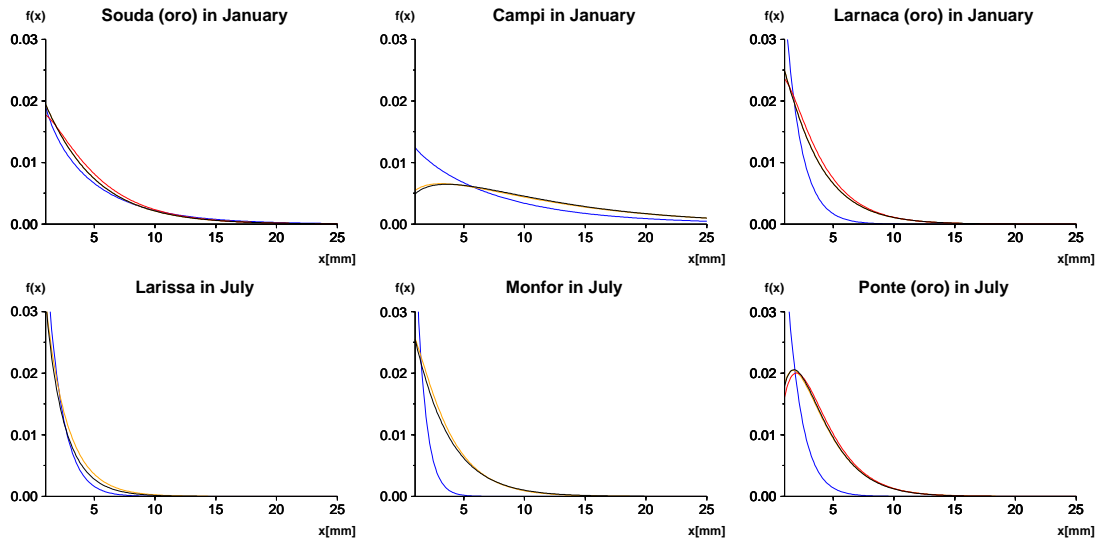


Figure 8.2: Validation of Gamma (Γ) distributions of daily rainfall from the first REMO ensemble member (blue), PDF matching (orange) and full weather generator (red) with original station distributions (black) for Souda (Greece), Campi (Portugal) and Larnaca (Cyprus) in January and Larissa (Greece), Monfor and Ponte (Portugal) in July of 1960-2000. (oro) identifies stations with orographic term.

In July, the share of local convective rainfall events which are more difficult to simulate by RCMs increases and only few stations are obvious where REMO already agrees with observed rainfall distributions (Fig. 8.2, lower left). At most stations there are strong deviations between simulated REMO and observed rainfall distributions denoting the typical differences between area-averaged and local rainfall data which can be solved by the application of both weather generator versions in all cases (Fig. 8.2, lower middle and right). Generally, the daily rainfall distributions of the PDF matching and original stations are often identical and the full weather generator only slightly deviates from these distributions revealing only small impacts of the orographic term and the stochastic part. The results are quite similar for the second and third REMO ensemble member. Sensitivity tests show that the improvement of the daily rainfall distribution due to the weather generator works even better for the REMO ensemble mean featuring the statistical properties of a strongly averaged precipitation dataset with even more low intensity rainfall events and less extremes than the REMO ensemble members. Thus, area-averaged REMO

rainfall yields several discrepancies to the daily rainfall distribution of local stations, especially in summer. But the weather generator is strongly able to reduce the number of rainfall events with less intensity and increase the amount of precipitation extremes of virtual station data compared to REMO, mainly due to PDF matching, resulting in strong agreement of original and virtual stations in daily rainfall distribution. The orographic term and the stochastic part show hardly any impact.

8.1.4 Precipitation characteristics of virtual station data

In order to further validate the performance of both weather generator versions in the extended present-day time period 1960-2000 several precipitation characteristics of the original stations, REMO output, the full weather generator and the PDF matching are compared. First, the whole area is separated into three sectors identifying the western (Iberian Peninsula), central (Italy and the Balkans) and eastern Mediterranean area (Cyprus and Israel) and the accumulated mean annual precipitation sums of all stations or corresponding grid boxes in each sector are analysed. The results of the first REMO ensemble member are exemplarily discussed. In the western sector the REMO rainfall total of 907mm is strongly reduced to 705mm for both weather generator versions exactly agreeing with 706mm for original station data. In the central sector the reduction of the REMO rainfall sum of 984mm to 729mm for both weather generator versions is slightly too strong underestimating the original station total of 739mm. Finally, in the eastern sector the PDF matching reduces the REMO precipitation total of 577mm to 508mm lying again slightly below the original station sum of 517mm. But the full weather generator total of 455mm strongly underestimates the original station rainfall sum. This underestimation is robust over all ensemble members but disappears if the REMO ensemble mean is regarded. Thus, the weather generator is quite successful in adjusting the higher annual rainfall totals of REMO to the lower original station sums. But this reduction is slightly overestimated by PDF matching. The orographic term and the stochastic part of the full weather generator reveal hardly any impact over the western and central Mediterranean area probably due to only two stations appropriate for the full version in each sector. But the full weather generator strongly underestimates original station totals over the eastern Mediterranean which might probably be explained by a stronger reduction tendency in the orographic term due to increased orographic lee effects of selected stations in 1960-2000. Furthermore, the uncertainty of the weather generator is generally highest over the eastern Mediterranean area where the rainfall data sample sizes are small due to large numbers of rainless days.

Then, further precipitation characteristics of both weather generator versions and

the first REMO ensemble member are validated with original stations for January and July of 1960-2000: the percentage of rainless days with rainfall smaller than 0.1mm and the average daily rainfall intensity and variability (Fig. 8.3). For this analysis, several stations around the whole Mediterranean area with successful PDF matching and if possible high orographic correlations are selected exemplarily: Ponte, Aguiar (Portugal), Zamora (Spain), Corfu, Larissa, Chania (Greece), Irbid and Kebutzat (Israel) for January and Extremo, Ponte, Aguiar (Portugal), Zamora (Spain), Corfu, Larissa (Greece), Lastovo (Croatia) and Thessaloniki (Greece) in July. Generally, REMO shows a smaller number of rainless days than original stations over the western and central Mediterranean in January and better agreement over the eastern Mediterranean. In July when the number of rainless days increases, this discrepancy between REMO and original stations becomes smaller. Eastern Mediterranean stations can not be investigated in summer because nearly 100% of rainless days does not allow PDF matching for both weather generator versions. In both January and July, the PDF matching perfectly adjusts the number of rainless days from REMO to the corresponding original station values. The orographic and stochastic terms of the full weather generator reveal only minor impacts but overestimate original station values for Kebutzat in Israel and several further eastern Mediterranean stations not depicted here (Fig. 8.3, left). This agrees well with the decreased annual precipitation sums of the full weather generator over the eastern Mediterranean area described before.

Daily rainfall intensities and variabilities show quite similar patterns and mostly higher values in winter than in summer. In July, REMO underestimates both variables in comparison to the original stations at nearly every location. In January, both overestimations and underestimations occur. But PDF matching is again able to match the REMO output to the original stations in most cases and the orographic and stochastic terms of the full weather generator yield only small impacts (Fig. 8.3, middle and right). The second and third REMO ensemble members show rather similar results. Instead, REMO ensemble mean values feature much larger differences to original stations and the weather generator achieves much better improvements: clear increase of number of rainless days and of daily rainfall intensity and variability in both January and July. Furthermore, the overestimation of rainless days over the eastern Mediterranean by the orographic term is reduced in accordance to the results of the annual precipitation totals described before. Thus, REMO reveals more rain days than original stations, especially in winter, and less rainfall intensity and variability in summer. In winter, both overestimations and underestimations of the daily station intensity and variability can be stated. The PDF matching reduces the

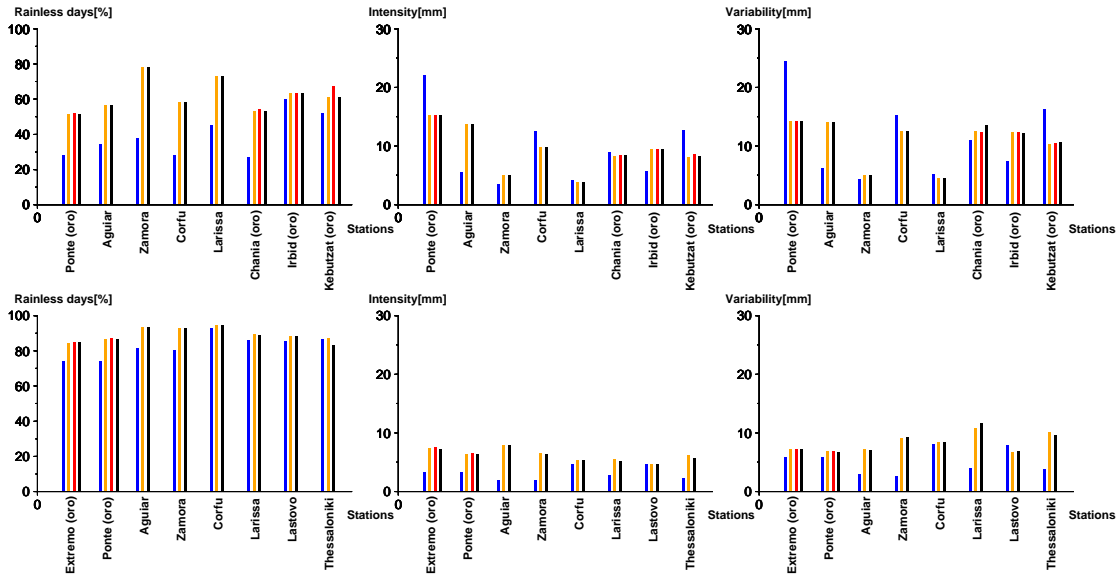


Figure 8.3: Validation of characteristics of daily rainfall from the first REMO ensemble member (blue), PDF matching (orange) and full weather generator (red) with original station characteristics (black) for several Mediterranean stations in January (top) and July (bottom) of 1960-2000: fraction of rainless days (left) and daily precipitation intensity (middle) and variability (right). (oro) identifies stations with orographic term.

number of simulated rain days, increases rainfall intensity and variability in summer and matches both variables to original stations in winter resulting in strong agreement between virtual and original stations confirming the changes in daily rainfall distributions of subsection 8.1.3. The orographic term and the stochastic part of the full weather generator reveal only small impacts but overestimate the numbers of rainless days of original stations over the eastern Mediterranean agreeing well with decreased annual precipitation sums highlighted before.

8.2 Precipitation extremes of present-day climate

After having successfully validated the performance of the weather generator in 1960-2000 the orographic term, the stochastic part and the PDF matching of both weather generator versions, i.e. the full weather generator and the PDF matching only, are applied to the rainfall and horizontal wind time series of all three REMO ensemble members for the whole time period 1961-2050 applying A1b and B1 emission scenarios and corresponding virtual station time series are constructed. The correction of outliers described in the methods chapter (see section 3.8) works successfully, and the maximum daily rainfall values of present-day virtual stations lie in the same range than those of original stations and future virtual stations only slightly higher. In this section, the GPD fit of the previous chapter is applied to

build precipitation extremes of the original and virtual station data for both weather generator versions during the present-day time period 1961-1990. The following subsections describe the validation of the resulting GPD return values and parameters for both weather generator versions with original stations and further comparisons with corresponding gridded REMO, ECHAM5 and E-OBS values determined in the previous chapter for the whole Mediterranean area and in more detail for several selected stations.

8.2.1 GPD return values and parameters

The GPD is applied for all 93 original and virtual stations for both versions of the weather generator. Generally, the GPD analysis is more uncertain for virtual and original stations than for area-averaged REMO and E-OBS data because the sample of extreme precipitation days for GPD analysis is smaller. Furthermore, if a virtual station is not PDF matched in a certain month of the present-day time period 1961-1990, the corresponding three-month season is removed in GPD analysis for both present-day and future time periods. For higher aggregation levels of 21 or 31 days, a season is also deleted if a neighbouring month outside the season is not PDF matched. If the adjustment of the number of rain days of a virtual station to the corresponding original station in a certain month is not stationary from the present-day to the future time period, the corresponding three-month season is removed from GPD analysis for the future time period only (cf. section 3.8).

However, in winter the rainfall extremes of nearly all original and virtual stations can be calculated. The full weather generator results are available for Galicia, Cyprus and Israel but the GPD results of Crete are removed due to negative Kolmogorov-Smirnov tests. In summer, many original and virtual stations are deleted in southern Spain, Greece, Cyprus and Israel due to large numbers of rainless days, the corrections mentioned before or negative Kolmogorov-Smirnov tests in GPD analysis. Only Galicia shows results for the full weather generator. Generally, all stations with negative Kolmogorov-Smirnov tests in GPD analysis denoting uncertain GPD fits to the empirical data are depicted with white dots in the following plots. Those stations which are not PDF matched due to low numbers of rain days are not shown at all because the weather generator can not be performed.

Thus, the GPD results for virtual stations of both full weather generator and PDF matching are validated with original station results and comparisons are done with former gridded rainfall extremes from REMO, ECHAM5 and E-OBS in 1961-1990 (Fig. 8.4). Generally, there is a quite good agreement of the 1d-20a-RTVs between virtual and station data with slightly higher virtual station extremes but hardly any

impact of the orographic and stochastic terms of the full weather generator which is thus, not depicted here. Maximum values can be found over Portugal, southern and eastern Spain, western Greece and Israel in winter and minimum values are obvious over Portugal, southern Spain and southern Italy in summer and central Spain in winter (Fig. 8.4, top and middle). The 1d-20a-RTVs of virtual and original stations are higher than the corresponding REMO and E-OBS rainfall extremes (cf. Fig. 7.2), respectively. The good accordance of virtual and original station extremes is achieved by balancing the overestimated REMO rainfall extremes compared to E-OBS in winter, mainly due to higher original station winter values than E-OBS.

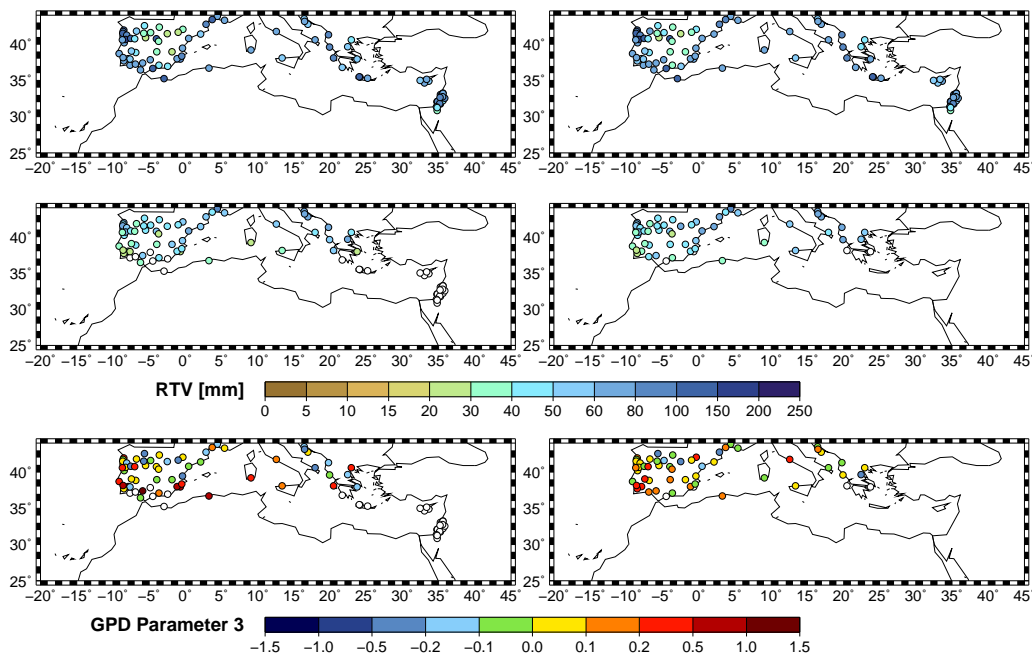


Figure 8.4: Validation of GPD 1d-20a-RTVs for PDF matching (right) with original station return values (left) for winter (top) and summer (middle) precipitation and corresponding third GPD parameters in summer (bottom) in 1961-1990.

A rather good agreement of present-day GPD return values with empirical quantiles can be stated for both virtual and original stations but higher GPD standard errors than for REMO and E-OBS are seen probably due to higher GPD return values. The first and second GPD parameters of virtual and original stations fit quite well with each other and are larger than the corresponding REMO and E-OBS parameters due to higher station return values as well. The third GPD parameter yields a mixed picture of positive and negative values in winter and summer for both virtual and original stations agreeing much better with each other (Fig. 8.4, bottom) than the mostly negative REMO parameters with the rather positive E-OBS parameters (cf. Fig. 7.6, right). For most GPD parameters, the impact of orographic and stochastic parts is rather small. Thus, the 1d-20a-RTVs of original

and virtual station rainfall show rather equal spatial patterns but mostly higher values than E-OBS and REMO precipitation extremes, respectively, and a very good agreement with each other, mainly due to higher original station values in winter compared to E-OBS. Furthermore, the third GPD parameter yields higher agreement for original and virtual stations than for E-OBS and REMO. These improvements are mainly due to PDF matching because the orographic and stochastic parts of the full weather generator reveal only minor impacts.

8.2.2 GPD return values of selected stations

This section performs a closer comparison of virtual and original station rainfall extremes with corresponding single grid box values of REMO and E-OBS on 0.5° and ECHAM5 on 1.875° resolution and some further analyses of return values for different return times and aggregation levels. Thus, several exemplary virtual stations with successful PDF matching, strong present-day performance of the weather generator and if possible large orographic correlation are selected over the Mediterranean area: Extremo, Monfor (Portugal), Thessaloniki (Greece), Jerusalem and Beer-Sheva (Israel) in winter and Extremo, Monfor (Portugal), Thessaloniki (Greece), Ponte and Aguiar (Portugal) in summer. The 1d-20a-RTVs of these selected original and virtual stations and of the corresponding E-OBS, REMO and ECHAM5 grid boxes for winter and summer precipitation in 1961-1990 are depicted in Fig. 8.5 (upper left and right). The full weather generator and PDF matching agree very well with each other and with original stations sometimes even revealing identical return values, e.g. for Ponte in summer. The accordance between virtual and original station data is stronger than that between REMO and original stations as well as between REMO and E-OBS. ECHAM5 is always smaller than REMO with mostly less agreement to stations but more and less agreement to E-OBS in winter and summer, respectively. Thus, REMO shows rather good validation results in contrast to ECHAM5 in summer while in winter REMO is often closer to stations and ECHAM5 to E-OBS. But strongest agreement is found between original and virtual station data for both weather generator versions.

Fig. 8.5 (lower left and right) depicts the 1d-RTVs for several return times and the 20a-RTVs for several aggregation levels exemplarily for Extremo in Portugal for summer and winter precipitation in 1961-1990, respectively. Like in the previous chapter the 1d-RTVs and 20a-RTVs increase with both increasing return times and aggregation levels for all datasets in all seasons and for all selected stations. Validation results remain more or less similar for different return times and smaller aggregation levels. But with higher aggregation levels the relationships between

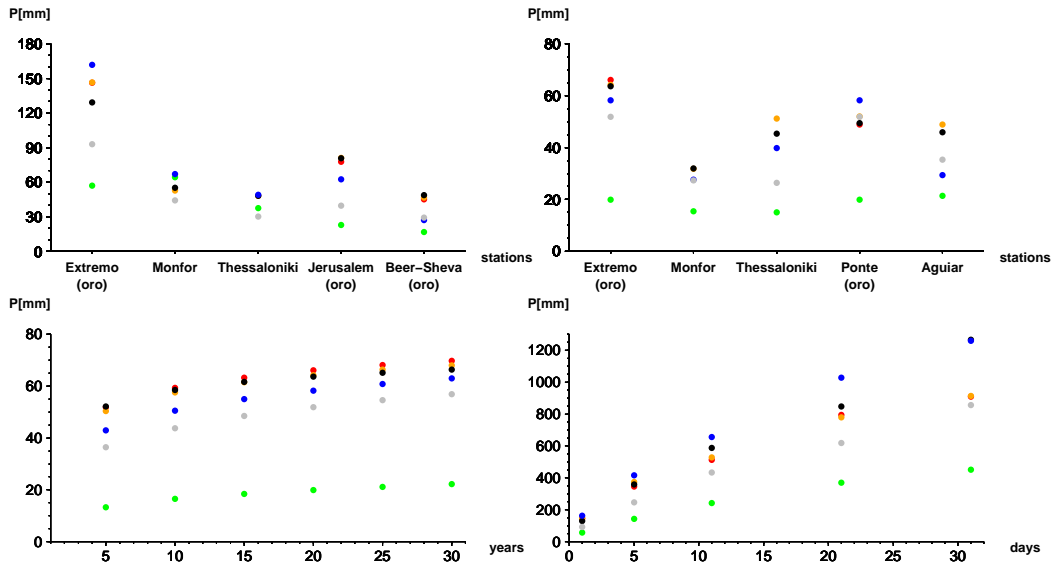


Figure 8.5: GPD return values for precipitation from original stations (black), PDF matching (orange), full weather generator (red), E-OBS (grey), REMO (blue) and ECHAM5 (green) in 1961-1990: 1d-20a-RTVs for selected Mediterranean stations in winter (upper left) and summer (upper right), 1d-RTVs for several return times for Extremo (Portugal, oro) in summer (lower left) and 20a-RTVs for several aggregation levels for Extremo (Portugal, oro) in winter (lower right). (oro) identifies stations with orographic term.

different datasets strongly change probably due to the change of the precipitation regime from daily to monthly scale and no distinct change pattern can be stated over all seasons and selected stations. Thus, the agreement in 1d-20a-RTVs for precipitation between original and virtual stations is strongly higher than that between E-OBS and REMO or ECHAM5 for all selected stations and seasons revealing only small differences between PDF matching and full weather generator. Furthermore, the return values of original and virtual stations increase with both increasing return times and aggregation levels agreeing well with the results of the previous chapter.

8.3 Precipitation extremes of future climate

In this section, the GPD fit of the previous chapter is applied to construct precipitation extremes of virtual station data for both PDF matching and full weather generator in the future time period 2021-2050 for the A1b and B1 emission scenarios, and the future changes compared to the present-day time period 1961-1990 are computed. Thus, the first subsection compares the future changes of GPD return values and parameters from both weather generator versions with those of gridded REMO data from the previous GPD chapter for the whole Mediterranean area. The second subsection gives a closer analysis of future changes of precipitation extremes

for several selected Mediterranean stations compared to both corresponding REMO and ECHAM5 grid box values.

8.3.1 GPD return values and parameters

In comparison to the present-day time period some further virtual stations in southern Spain and Greece are removed in GPD analysis of the future time period because of negative Kolmogorov-Smirnov tests and the removal of virtual stations due to lacking PDF matching or during the adjustment of the number of rain days. Fig. 8.6 presents the 1d-20a-RTV change for precipitation from PDF matching in 2021-2050 compared to 1961-1990 for both A1b and B1 emission scenarios and the corresponding results from the full weather generator for A1b. In winter, a clear increasing pattern of 1d-20a-RTVs is obvious for the A1b scenario of the PDF matching over the whole Mediterranean area, especially over the Iberian Peninsula, with few decreasing patterns over Italy and Greece. In summer, mostly decreases of 1d-20a-RTVs can be seen over the Iberian Peninsula and several increases over the central Mediterranean (Fig. 8.6, top). The B1 scenario shows similar spatial patterns to A1b with only small differences and several stations with slightly reduced change intensities (Fig. 8.6, middle). The orographic and stochastic parts of the full weather generator yield generally only slight differences to PDF matching, e.g. turn the sign of the small 1d-20a-RTV change over Galicia in summer (Fig. 8.6, bottom). But all described 1d-20a-RTV changes do not reach significance for any season, scenario or weather generator version.

In comparison to REMO (cf. Fig. 7.10) the 1d-20a-RTV changes of virtual stations yield slightly stronger change intensities, especially in winter, but rather equal spatial change patterns except for more increases in summer, especially over Spain. The first and second GPD parameters of virtual stations yield rather similar changes to 1d-20a-RTVs but a decrease of the first parameter over Israel in A1b is obvious. The third GPD parameter shows a mixed pattern of positive and negative changes in both winter and summer. Generally, the future change of 1d-20a-RTVs for virtual station rainfall reveals strong increases of precipitation extremes over nearly the whole area in winter and decreases over most of the Iberian Peninsula and increases over Italy and Greece in summer. Only small differences can be stated between PDF matching and full weather generator and between A1b and B1 emission scenarios. Furthermore, the virtual stations yield stronger increases in winter and less decreases in summer compared to gridded REMO rainfall extremes.

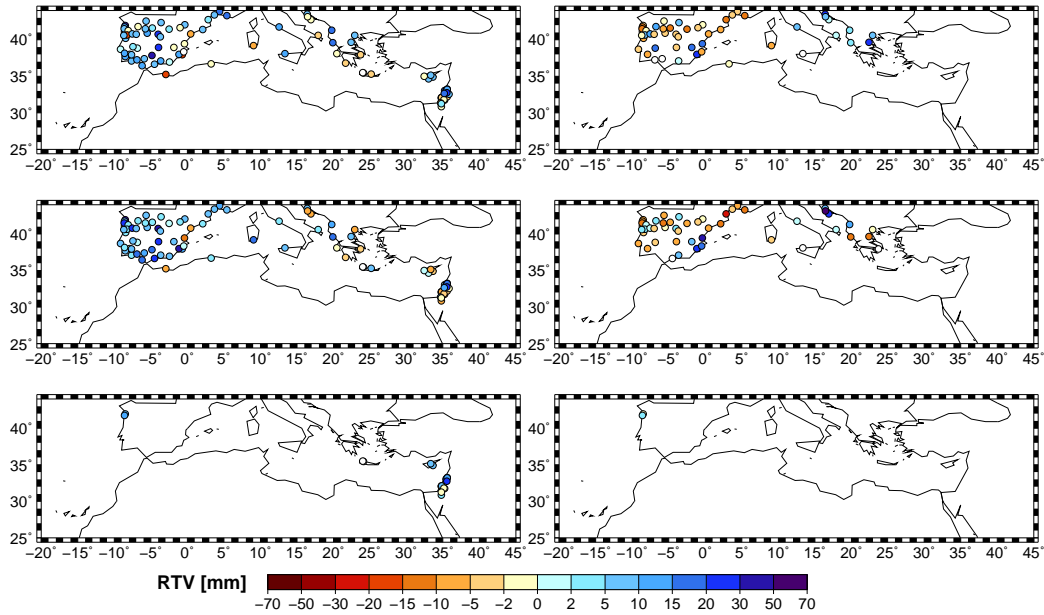


Figure 8.6: GPD 1d-20a-RTV change for precipitation from PDF matching in 2021-2050 compared to 1961-1990 applying A1b (top) and B1 emission scenarios (middle) and from the full weather generator for A1b (bottom) in winter (left) and summer (right).

8.3.2 GPD return values of selected stations

For a closer comparison of the future changes of GPD precipitation extremes in 2021-2050 compared to 1961-1990 between PDF matching, full weather generator, REMO and ECHAM5 for both A1b and B1 emission scenarios and for the investigation of return values for different return times and aggregation levels, the same exemplary virtual stations are analysed than for the present-day time period (cf. subsection 8.2.2). Generally, the different downscaling methods, models and scenarios yield a multitude of various future GPD return values spanning the uncertainty range of future changes in rainfall extremes for each station and season which can hardly be interpreted. For several stations, the band of possible future changes in precipitation extremes rather agrees in direction of change but for many stations the relatively large spread of different downscaling methods, models and scenarios does not allow any certain statement on future change of rainfall extremes.

Thus, Fig. 8.7 shows exemplarily the future GPD 1d-RTV change in 2021-2050 compared to 1961-1990 for several return times for the two stations Extremo (Portugal) and Thessaloniki (Greece) in winter. For Extremo, the band of possible future changes clearly points at an increase of future rainfall extremes but the intensity of change strongly depends on the chosen downscaling method, model and scenario. The PDF matching strongly exceeds the estimates of the full weather generator, REMO and ECHAM5 for both emission scenarios (Fig. 8.7, left). But for Thessa-

loniki, the uncertainty range of possible future changes contains both positive and negative changes of precipitation extremes with strongest future increases and decreases estimated by the PDF matching for A1b and REMO for B1, respectively. Thus, no clear pattern of future change in rainfall extremes can be stated (Fig. 8.7, right). But both stations agree in increasing absolute future change intensities with increasing return times. For many stations, seasons, models and downscaling methods, the absolute future change of precipitation extremes increases with both higher return times and aggregation levels but in several cases remains constant or even decreases. Thus, the closer comparison of future changes in precipitation extremes reveals a relatively large spread between PDF matching, full weather generator, REMO and ECHAM5 and between the two emission scenarios for many stations and seasons. Only some selected stations reveal a clear picture of the direction of future change. Furthermore, the absolute future change of rainfall extremes increases with both increasing return times and aggregation levels for many stations, seasons, models and downscaling methods consistent with the corresponding results of the previous GPD chapter.

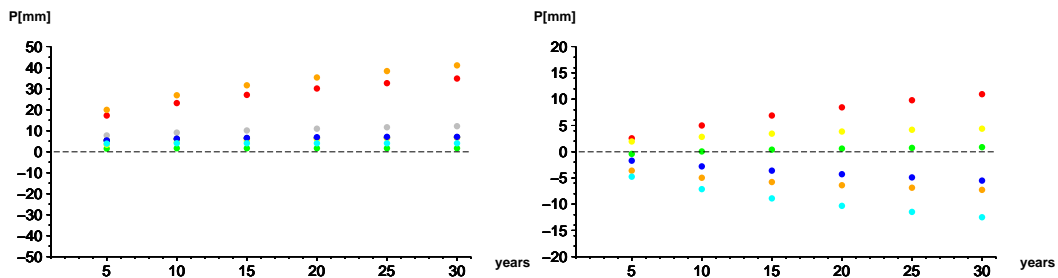


Figure 8.7: GPD 1d-RTV change for winter precipitation from PDF matching (red/orange), full weather generator (black/gray), REMO (blue/cyan) and ECHAM5 (green/yellow) for different return times in 2021-2050 compared to 1961-1990 applying A1b/ B1 emission scenarios for Extremo (Portugal, left) and Thessaloniki (Greece, right) with and without orographic term, respectively.

9 Synthesis

This synthesis gives a summary of the major findings of this study following the sequence of the results chapters 4, 5, 6, 7 and 8. Furthermore, these results are discussed in the context of state-of-the-art research work in order to evaluate the contribution of this study to the understanding of the future climate change of temperature and precipitation means and extremes in the Mediterranean area revealing several new, confirming but also contradictory findings with respect to recent scientific publications. Finally, some main conclusions for the Mediterranean climate are drawn from the major findings of this study and a short outlook describes the uncertainties and shortcomings of the prevailing study and presents which main aspects require further research work. Thus, the first section contains the summary and discussion and the second section presents the conclusions and outlook.

9.1 Summary and Discussion

The first results **chapter 4** presents the analysis of Mediterranean temperature and precipitation means and trends in 1961-1990. Seasonal temperature means reveal good agreement between REMO and observations in seasonal and spatial distribution. For precipitation, REMO agrees basically well with observations but depicts several differences over the eastern areas and slightly overestimates maximum rainfall regions in winter probably due to included windward and lee effects in REMO compared to smoothed rainfall maxima of interpolated E-OBS data or RCM deficiencies. Dynamical downscaling from ECHAM5 (1.875°) to REMO (0.5°) reveals an enhanced representation of small-scale topographic details, larger temperatures over northern Africa, cooler mountain temperatures and higher rainfall over the whole area in summer and over the maximum rainfall regions in winter. Thus, dynamical downscaling mostly improves validation with E-OBS except for winter rainfall. Concerning present-day temperature trends, REMO basically captures the observed winter cooling over Turkey and summer warming over the western Mediterranean but with lower intensity and reveals discrepancies over southern Europe in winter and Turkey in summer. ECHAM5 shows stronger warming over north-western Africa

than REMO. For precipitation, both models basically reproduce the observed trend patterns but strongly underestimate winter drying over the whole area. REMO yields more fine-scale structures and stronger drying than ECHAM5 and slightly better accordance to observations. Therefore, this model-into-model-approach is not able to capture all observed temperature and precipitation trends, especially in winter, leading to the conclusion that the only real boundary condition CO_2 emissions does not clearly prevail over other Mediterranean drivers. But REMO is found to reproduce observed trends if forced by observed boundary conditions of the ERA15 reanalyses. Finally, one-way analyses of variance evaluate the signal-to-noise ratios of simulated seasonal temperature and precipitation trends revealing rather weak GHG signals with maxima of 20-40% because most variance is explained by internal variability due to differing initial conditions of different ensemble members. But GHG signals increase for 10-year REMO running means due to smoothed interannual variations.

Concerning future times, the long-term seasonal temperature trends of 1961-2050 reveal strong and significant warming patterns over the whole Mediterranean, especially in summer for the A1b scenario. REMO yields smaller warming than ECHAM5 over the southern Mediterranean. Long-term precipitation trends depict strong drying patterns over the northern Mediterranean in summer moving towards northern Africa and Arabia in winter, especially in A1b, and winter wetting patterns over southern Europe and Turkey, particularly in B1. REMO shows stronger rainfall changes and improved small-scale topographic details compared to ECHAM5. Concerning signal-to-noise ratios of long-term trends, one-way analysis of variance reveals strong and significant GHG signals over the whole area for temperature with maxima of 60-70% over the southern areas in summer. The GHG signals for rainfall are smaller and more locally distributed reaching maxima of 20-30% over the southern and northern areas in winter and summer, respectively. REMO running means reach 20-30% higher GHG signals for both variables. Finally, two-way analyses of variance determine the future change signals common to both emission scenarios and reveal similar GHG signals to the one-way analyses of variance for temperature and similar maxima with more extended significance for precipitation. This is due to minor differences between the A1b and B1 scenarios in the long-term period denoted by mostly small and not significant block and interaction effects except for some impacts of differing emission scenarios for REMO running means, especially for rainfall.

The findings of this study agree very well with former validation and dynamical downscaling studies over the Mediterranean area. They confirm systematic

warm and dry biases of GCMs over mountain ranges compared to observations due to smoothed orography in coarse GCM grids and corresponding improvements by high-resolution RCMs featuring an enhanced representation of small-scale details of the complex Mediterranean orography and land-sea contrast (JACOB et al., 2007; GIORGI and LIONELLO, 2008; GIORGI and COPPOLA, 2009). Furthermore, this study agrees with GIORGI and LIONELLO (2008) who reveal that global GCM simulations generally reproduce observed Mediterranean warming and summer drying patterns but do not capture the strong present-day winter drying probably due to the insufficient ability of GCMs to reproduce the observed interdecadal variability of large-scale atmospheric modes (OSBORN, 2004). This deficiency is further passed by driving GCMs to nested RCMs in model-into-model-approaches (GIORGI et al., 2004a; GIORGI and LIONELLO, 2008). But PAETH and HENSE (2005) find in accordance with this study that REMO is able to capture both observed trends and large-scale circulation if forced by observed boundary conditions. Concerning long-term temperature and precipitation trends, the present study strongly confirms previous European and international cooperation studies of GCM and RCM ensembles agreeing on future Mediterranean warming and drying (CHRISTENSEN et al., 2007; CHRISTENSEN and CHRISTENSEN, 2007; GIORGI and LIONELLO, 2008; GIORGI and COPPOLA, 2009; GOODESS et al., 2009). But this study reveals some larger drying maxima in winter than in summer and winter wetting over the northern Mediterranean expands further south in both A1b and B1 scenarios. The dynamical downscaling results of this study further confirm the increased representation of small-scale orographic and coastline features in future temperature and rainfall changes with high-resolution RCMs stated by GIORGI and LIONELLO (2008) and GIORGI and COPPOLA (2009). Concerning signal-to-noise ratios of long-term trends, this study is consistent with PAETH and HENSE (2002) who apply one-way analysis of variance to four coupled GCM simulations in 1880-2049 and find strong GHG signals of 70-80% for Mediterranean temperature but small signals of 10-20% for precipitation due to dominating internal variability. They state as well increasing GHG signals for running means and longer-term and future time periods.

The **chapter 5** analyses the impact of mid-latitude circulation on Mediterranean temperature and precipitation in 1961-1990. The major NCEP and ECHAM5 modes of variation defined by s-mode PCA are identified as the NAO, EA, SCAND and EA/WR patterns in winter and the EA-Jet and blocking patterns in summer. Observed and simulated modes reveal mostly similar spatial patterns but strong differences in temporal evolutions. Cross-validated stepwise multiple regressions to E-OBS and REMO temperature and precipitation yield strong correlations with max-

imum explained variances of 70-80% over the western and central Mediterranean in winter. The separation of REMO and E-OBS temperature and precipitation trends reveals differing circulation-related trends due to different temporal evolutions of large-scale modes of variation: In winter, E-OBS shows stronger cooling over Turkey and stronger drying over the northern Mediterranean than REMO due to a stronger NAO increase, and opposite temperature trends over southern Europe are caused by opposite trends of the EA pattern. In summer, E-OBS reveals stronger cooling over the Balkans and western Turkey and stronger warming over the Atlas Mountains due to a more decreasing blocking pattern and a more increasing EA-Jet, respectively, but hardly any influence of circulation on rainfall. However, improved agreement of observed and simulated circulation-unrelated trends in most regions reveals that the predictability of this model-into-model-approach with only real boundary condition CO_2 emissions mostly increases after removing impacts of mid-latitude circulation. But strong disagreements in circulation-unrelated trends remain over eastern Turkey and the Near East probably identifying further drivers not considered in this study, e.g. tropical climate dynamics, or uncertain mountain observations. Finally, one-way analyses of variance for mid-latitude modes of variation of different ECHAM5 ensemble members reveal strong impacts of initial conditions on simulated circulation variability. Thus, differing observed and simulated initial conditions are supposed to induce the strong differences in temporal evolutions of the identified modes of variation which cause differing present-day temperature and precipitation trends. This probably indicates that 30-year trends generally reveal rather low model predictability based on CO_2 due to strong inter-decadal variability because the time scale is shorter than that one affected by GHG forcing (cf. PAXIAN et al. (2011)).

During 1961-2050 the impacts of major present-day modes of variation remain in winter, i.e. the EA pattern for temperature and the NAO for rainfall, but several changes are found in summer because of less robust impacts of mid-latitude circulation. The multiple regression reveals mostly decreased explained variances denoting smaller impacts of mid-latitude circulation probably due to stronger GHG impacts in long-term and future time periods. The trend separation shows often changing circulation-related temperature and precipitation trends but winter drying over southern Europe due to an increasing NAO remains, especially in A1b. The circulation-unrelated trends become stronger and more significant mostly exceeding circulation-related trends: intensive warming over the whole area, summer and winter drying over the northern and southern Mediterranean, respectively, and extended winter wetting over the northern areas, especially in B1, which partly counterbal-

ances the NAO-induced drying. Thus, decreasing impacts of mid-latitude circulation and increasing influences of circulation-unrelated drivers, e.g. GHG, probably point at an increased predictability of the given model-into-model approach in 1961-2050 but this assumption cannot be evaluated with observations.

On the one hand, these findings confirm the observed impacts of mid-latitude circulation dynamics on Mediterranean temperature and precipitation variability known from literature, e.g. the influences of the NAO on eastern Mediterranean temperature (BEN-GAI et al., 2001; XOPLAKI, 2002) and northern Mediterranean rainfall (ULBRICH et al., 1999; GOODESS and JONES, 2002; TÜRKES and ERLAT, 2005) and the impacts of the EA pattern on western Mediterranean temperature (SÁENZ et al., 2001) in winter. Several former studies have already related the recent strong Mediterranean drying to the strong positive phase of the NAO in the 1980s and 1990s (HURRELL, 1995; QUADRELLI et al., 2001; XOPLAKI et al., 2004; JACOBET et al., 2007). Concerning summer, the most influencing circulation modes for Mediterranean temperature and rainfall are found to be the EA-Jet and blocking conditions over whole Europe in accordance to several former studies (DÜNKELOH and JACOBET, 2003; XOPLAKI et al., 2003; CASSOU et al., 2005; CARRIL et al., 2008). On the other hand, this study agrees with OSBORN (2004) highlighting the inability of many GCMs to capture the present-day multidecadal trends of large-scale circulation and with GIORGI and LIONELLO (2008) relating an insufficient GCM representation of the recent strong NAO increase to the GCM deficiency to simulate the observed strong Mediterranean winter drying. VAN ULDEN and VAN OLDENBORGH (2006) find as well impacts of simulated large-scale circulation biases compared to observations on rainfall and temperature biases over central Europe which probably leads to limited model predictability of future European climate change, particularly for precipitation. For future times, several studies already projected positive winter NAO trends with increasing atmospheric GHG concentrations (ULBRICH and CHRISTOPH, 1999; COPPOLA et al., 2005; STEPHENSON et al., 2006) further enhancing Mediterranean winter drying (CHRISTENSEN et al., 2007) which agrees with the findings of this study. Furthermore, increased predictability of GHG related climate change due to decreased impacts of circulation in long-term and future time periods is partly confirmed by several studies: STEPHENSON et al. (2006) reveal decreasing impacts of future NAO changes on Mediterranean temperature variability with increasing GHG concentrations but rather constant future impacts on rainfall variability. GIORGI and BI (2009) find as well increasing GCM predictability of GHG-forced rainfall signals over the Mediterranean compared to internal multi-decadal variability in future times. PAETH and HENSE (2002) re-

veal increasing GHG signals of Mediterranean temperature and precipitation for longer-term and future time periods.

The **chapter 6** determines seasonal quantile-based rainfall extreme indices and the CDD index in 1961-1990. The spatial distribution of rain days and rainfall extremes is rather consistent with seasonal totals but SDII95p reveals more small-scale maxima over mountains and the CDD distribution is exactly vice-versa. Both models simulate more rain days than E-OBS except over the Near East, especially in winter due to higher absolute values, but ECHAM5 strongly underestimates observed rain days for the 1mm threshold in summer. Overestimated numbers of rain days are typical for area-averaged model rainfall simulated on coarse model grids compared to E-OBS data interpolated from local stations which reveal less rain days of higher intensity than simulations. Concerning CDD, strong underestimations and overestimations of observations are stated for REMO and ECHAM5 in summer, respectively, but rather good model performance in winter. For R95N, both models reveal overestimations of observed frequencies over southern Europe and Turkey and some underestimations over the Near East in winter and larger agreement with E-OBS in summer, especially REMO. Both CDD and R95N biases strongly relate to rain day biases. Concerning SDII95p, REMO mostly overestimates E-OBS, especially over the maximum rainfall regions in winter, probably due to windward and lee effects in REMO compared to interpolated E-OBS data or RCM deficiencies. ECHAM5 rather underestimates observed intensities over these regions revealing shortcomings of coarse grid GCMs in simulating small-scale rainfall extremes, particularly in winter. Consequently, both models overestimate observed R95AM in winter, especially REMO over the maximum rainfall regions, but only slight overestimations and underestimations can be stated for REMO and ECHAM5 in summer, respectively. Observed R95T is overestimated by both models in both seasons mostly due to higher amounts of extreme rainfall. Finally, the dynamical downscaling of rainfall extremes from ECHAM5 to REMO can be separated into two effects: the scale effect of improved resolution reduces the area-averaging effects of the coarse ECHAM5 grid in decreasing frequencies and increasing intensities of extreme rainfall. The subscale processes of REMO model physics denote real added values of dynamical downscaling and increase both frequency and intensity of ECHAM5 extremes in this study but sometimes increase the differences to E-OBS extremes.

Furthermore, future changes in numbers of rain days in 2021-2050 compared to 1961-1990 reveal equal spatial change patterns to long-term trends of seasonal precipitation totals. The B1 scenario yields smaller decreasing and stronger increasing

patterns than A1b and ECHAM5 mostly smaller changes than REMO. Future CDD and R95N changes are mostly consistent with these change patterns and reveal increasing lengths of dry periods and decreasing numbers of extreme rain days in regions and seasons of decreasing numbers of rain days and vice versa. But R95N increases are more expanded than increases of rainfall totals in both models revealing decreasing numbers of rain days but increasing numbers of extreme rain days over Spain and Turkey in winter, especially in A1b. Future SDII95p changes follow those of R95N but yield increasing summer intensities over the Balkans and more small-scale topographic details of maximum intensity changes for REMO than for ECHAM5. Finally, future changes of R95AM and R95T are rather similar to changes in frequency and intensity of rainfall extremes.

Concerning dynamical downscaling of rainfall extremes, several studies highlight deficiencies of coarse-grid GCMs in reproducing realistic fine-scale structures of rainfall extremes and improved representations in high-resolution RCMs (CHRISTENSEN and CHRISTENSEN, 2003; FREI et al., 2006; GAO et al., 2006). But SEMMLER and JACOB (2004) and BENISTON et al. (2007) still state underestimated RCM extreme rainfall intensities over mountains due to smoothed topography and ZOLINA et al. (2004) describe overestimated numbers of rain days and underestimated extreme intensities in area-averaged model simulations compared to local stations. This study partly confirms these findings because REMO enhances the representation of small-scale topographic features of rainfall extremes but tends to overestimate E-OBS extremes and the scale effect of REMO improves the area-averaging effects of the coarse ECHAM5 grid but subscale processes partly worsen the agreement with E-OBS. Possibly the agreement of extreme intensities is higher if local stations instead of interpolated E-OBS data are considered. In KLIWEX-MED cooperation, regional and statistical downscaling approaches of winter rainfall extremes are compared concluding that both methods improve coarse-grid ECHAM5 extremes: dynamical downscaling simulates more realistic intensities but overestimates frequencies and statistical downscaling produces more realistic frequencies but underestimates intensities compared to local stations (HERTIG et al., 2012).

In terms of future changes of dry periods, this study strongly confirms former GCM and RCM studies agreeing on decreasing numbers of rain days (FREI et al., 2006) and increasing durations of dry spells or droughts over the Mediterranean area (VOSS et al., 2002; TEBALDI et al., 2006; BENISTON et al., 2007) but decreasing maximum dry spell lengths over the north-western areas in winter (GAO et al., 2006). However, recent GCM and RCM studies are rather controversial in simulating future changes of Mediterranean heavy rainfall intensities and frequencies

probably due to the multitude of different statistical methods, models or time scales applied: In winter, the mixed heavy rainfall trends over the northern Mediterranean found in this study lie in between the generally decreasing patterns of PAETH and HENSE (2005), FREI et al. (2006) and BENISTON et al. (2007) and rather increasing patterns of GAO et al. (2006) and GOUBANOVA and LI (2007) over southern Europe. The decreasing winter trends over the southern Mediterranean agree well with GAO et al. (2006) over north-western Africa. In summer, the prevailing negative heavy rainfall patterns of this study generally confirm decreasing trends over southern Europe in BENISTON et al. (2007) and GOUBANOVA and LI (2007) and over the eastern Mediterranean in CHRISTENSEN and CHRISTENSEN (2003) but contradict to rather increasing trends over the western and eastern Mediterranean in CHRISTENSEN and CHRISTENSEN (2003) and PAETH and HENSE (2005), respectively. But this study strongly confirms the general identification of more expanded areas of increasing rainfall extremes than increasing totals (GAO et al., 2006) indicating Mediterranean regions with decreasing totals but increasing extremes in both winter and summer (CHRISTENSEN and CHRISTENSEN, 2003; SEMMLER and JACOB, 2004; GAO et al., 2006; GOUBANOVA and LI, 2007). This points at a broadening of the daily rainfall distribution function (PAL et al., 2004; GAO et al., 2006). In KLIWEX-MED cooperation, statistical downscaling rather agrees with REMO in simulating mainly decreasing extreme rainfall frequencies with some increases over southern Europe in winter but rather disagrees with REMO in projecting strongly heterogeneous change patterns for winter extreme intensities (HERTIG et al., 2012). Finally, this study finds that high-resolution RCMs are generally able to produce small-scale topographic structures in future extreme rainfall changes in accordance to GAO et al. (2006).

The **chapter 7** applies the GPD function for estimating Mediterranean temperature and precipitation extremes in 1961-1990. The GPD 1d-20a-RTVs of temperature are similarly distributed to seasonal temperature means with rather good agreement between models and observations. But REMO yields more small-scale details and decreased temperature extremes over mountains probably improving both interpolated E-OBS and coarse grid ECHAM5 data. Maximum variation coefficients of 10-15% show rather small GPD uncertainties due to large data samples. The GPD parameters of E-OBS, REMO and ECHAM5 reveal a rather good agreement in spatial distribution. The first parameter equals the spatial pattern of the 1d-20a-RTV and the third parameter denotes long-tailed distributions. For precipitation, the geographical distribution of the 1d-20a-RTVs resembles that of seasonal rainfall totals. Both models basically agree with E-OBS but REMO overestimates observed rain-

fall extremes, especially over the maximum rainfall regions in winter, and ECHAM5 rather underestimates observed extremes in both seasons in accordance to seasonal totals and quantile-based extremes. Maximum variation coefficients of 30-80% reveal larger GPD uncertainties due to smaller sample sizes, especially over northern Africa in summer. Both REMO and ECHAM5 mostly reproduce the geographical patterns of observed GPD parameters but yield similar overestimations and underestimations for the first and second parameters than for the 1d-20a-RTV and rather long-tailed distributions can be stated for E-OBS and ECHAM5 in contrast to short-tailed distributions for REMO. Consequently, dynamical downscaling from ECHAM5 to REMO reveals small-scale topographic details of temperature extremes and larger winter rainfall extremes over the northern areas partly worsening agreement to E-OBS extremes. Finally, both temperature and rainfall return values are found to increase with larger return times denoting higher magnitudes for more rare extremes. For larger aggregation levels, temperature return values decrease identifying smaller magnitudes of longer-term heat waves compared to daily extremes and precipitation return values increase indicating higher extreme rainfall sums for wet periods aggregated over several days.

Furthermore, the future change of the 1d-20a-RTVs for REMO temperature in 2021-2050 compared to 1961-1990 depicts strong and mostly significant increases over the whole area, especially in summer in A1b, with similar spatial patterns but mostly slightly smaller increases than the long-term temperature trends of 1961-2050. ECHAM5 yields stronger increases than REMO over the southern Mediterranean. Future changes of GPD parameters for temperature reveal strong increases in distribution mean, smaller increases in dispersion and mixed changes in the shape parameter probably pointing at a linear GPD displacement to higher values without major changes in shape. For precipitation, the future change of the 1d-20a-RTVs reveals similar change patterns to the long-term precipitation trends but more expanded regions of increasing rainfall extremes over southern Europe and Turkey in winter and over the Balkans in summer identifying regions with decreasing totals but increasing extremes. Both A1b and B1 scenarios display rather similar results, and ECHAM5 yields smaller changes than REMO. But changes do not reach significance due to small sample sizes causing large GPD standard errors. The GPD parameters reveal strongest future change in location with similar change patterns to the 1d-20a-RTV but overlaid by various changes in the second and third parameters strongly influencing the future shape of the GPD. Finally, the absolute future changes of both temperature and rainfall extremes increase with higher return times and aggregation levels in many regions and seasons.

Several validation studies find rather good agreement of present-day GCM and RCM simulations of Mediterranean temperature extremes and heat waves with observations but larger biases and inter-model spreads occur compared to mean temperatures (MEEHL and TEBALDI, 2004; CLARK et al., 2006; DIFFENBAUGH et al., 2007; KJELLSTRÖM et al., 2007). However, no improvements of dynamical downscaling from global to regional scale are explicitly highlighted. The future increase of temperature extremes over the whole Mediterranean found in this study is strongly consistent with previous studies concerning extreme indices of daily minimum and maximum temperatures (CLARK et al., 2006; DIFFENBAUGH et al., 2007; KJELLSTRÖM et al., 2007), GPD return values of daily temperature (PAETH and HENSE, 2005) and statistical downscaling of the 5th and 95th percentile of winter minimum and summer maximum temperature, respectively (HERTIG et al., 2010). This study finds slightly smaller increases of temperature extremes than temperature means in contrast to GOUBANOVA and LI (2007) projecting that future changes in extremes of minimum and maximum temperatures strongly and slightly exceed future mean changes, respectively. But PAETH and HENSE (2005) suggest both widening and narrowing of the shape of daily temperature distributions for different Mediterranean regions until 2020. Furthermore, several studies project increasing intensities of heat waves in the Mediterranean area, especially in summer (MEEHL and TEBALDI, 2004; CLARK et al., 2006; BENISTON et al., 2007; FISCHER and SCHÄR, 2010) agreeing well with increasing temperature extremes aggregated over several days stated in this study. Concerning precipitation extremes, dynamical downscaling results for present-day GPD return values are rather consistent with quantile-based estimates already discussed before. The future changes in GPD rainfall extremes as well basically agree with future R95N and SDII95p changes but reveal smaller differences between A1b and B1 scenarios and more expanded regions of increasing rainfall extremes over southern Europe in winter. Thus, the comparison to previous studies reveals similar results to quantile-based extreme indices but more agreement with those works projecting increasing winter rainfall extremes over southern Europe. The relative consistency of changes in precipitation extremes for larger GPD return times with smaller GPD return times or percentile estimates found in this study is confirmed by similar conclusions of TRENBERTH et al. (2007) for present-day observations. Concerning GPD parameters, major impacts of the location parameter on future changes in extreme temperatures and combined impacts of all three parameters on future changes in rainfall extremes found in this study are generally confirmed by GOUBANOVA and LI (2007) and KHARIN and ZWIERS (2005) for GEV fits over the Mediterranean area and on global scale, respectively.

Finally, the **chapter 8** constructs virtual rainfall stations from gridded REMO data in applying a dynamical-statistical weather generator considering orographic and stochastic terms and PDF matching. Due to the small given station data base two weather generator versions are applied: a PDF matching for all 93 stations and a full weather generator for those 18 stations in multi-station REMO grid boxes required for the estimation of orographic and stochastic terms. The orographic term yields maximum absolute correlation coefficients between orographic wind-ward or lee effects and station rainfall anomalies of 0.20-0.35 but reveals several stations with unrealistic negative correlations probably due to low station density or erroneous location coordinates. The PDF matching can not be performed for many stations in summer due to small numbers of rain days, especially over the eastern areas. During the expanded validation period 1960-2000, the distribution of daily rainfall reveals typical discrepancies between area-averaged REMO and local station data: REMO produces too many low-intensity precipitation events and too little rainfall extremes, especially in summer. REMO reveals further higher annual rainfall totals, smaller numbers of rainless days, especially in winter, less daily rainfall intensity and variability in summer and both overestimations and underestimations of intensity and variability in winter compared to original stations. However, the PDF matching is very successful in adjusting REMO rainfall to original stations resulting in strong agreement of virtual and original stations in all investigated precipitation characteristics. But virtual stations slightly underestimate annual rainfall totals of original stations. Generally, the orographic and stochastic terms of the full weather generator yield hardly any impact.

Then, rainfall extremes of original and virtual stations for both weather generator versions are built via GPD fits. The 1d-20a-RTVs of original and virtual station rainfall in 1961-1990 reveal mostly higher values than gridded E-OBS and REMO precipitation extremes, respectively. The agreement between virtual and original stations is larger than between E-OBS and REMO or ECHAM5 for all stations and seasons. The third GPD parameter yields as well higher agreement, and the return values of virtual and original stations increase with both higher return times and aggregation levels. These improvements are mainly due to PDF matching because the orographic and stochastic parts reveal only minor impacts. Furthermore, future changes of the 1d-20a-RTVs for virtual station rainfall of 2021-2050 compared to 1961-1990 reveal slightly stronger changes, especially in winter, and less decreases in summer, particularly over Spain, compared to gridded REMO extremes and only small differences between both emission scenarios and both weather generator versions. The absolute future change of rainfall extremes increases with both higher

return times and aggregation levels for many virtual stations and seasons. In accordance to this study, several works reveal differences in statistical rainfall properties between area-averaged model output and local stations, e.g. in the probability density function of daily rainfall (ZOLINA et al., 2004; PAETH and DIEDERICH, 2010). The dynamical-statistical weather generator of this study has been applied in Benin by PAETH and DIEDERICH (2010): They report as well strong improvements of gridded model output in all considered rainfall characteristics, i.e. less weak rain days and higher daily extreme intensities in daily distribution functions and increased numbers of rainless days, rainfall intensity and variability in July, and large agreement of resulting virtual and original stations. PAETH and DIEDERICH (2010) find these improvements mainly reached by PDF matching because orographic effects of the weather generator are rather small due to small orographic variance in Benin. Over the Mediterranean, the orographic variance is much stronger but small station densities do not permit appropriate calculation of orographic effects for all stations and the impacts of PDF matching as well exceed those of orographic effects in this study. However, the correlation between orographic wind-ward or lee effects and station rainfall anomalies of this study reaches slightly higher values than PAETH and DIEDERICH (2010). Further studies have applied orographic or physical downscaling approaches (FUNK et al., 2003; SALATHE, 2005) or stochastic weather models producing random local weather events (WILKS, 1999) to area-averaged model output in order to construct appropriate rainfall input data for local applications or impact research. Concerning rainfall extremes, this study confirms that both interpolated E-OBS observations and area-averaged model output underestimate extreme rainfall intensities of local stations (ZOLINA et al., 2004; HAYLOCK et al., 2008) and that the virtual stations of the weather generator are able to capture such large station extreme intensities (PAETH and DIEDERICH, 2010). Several further studies reveal good performance of stochastic weather generators compared to observations concerning extreme events: yearly maxima and 10- and 20-year GEV return values of daily rainfall at 20 global sites including the Mediterranean area (SEMENOV, 2008), extreme 10-day winter rainfall maxima over the Meuse river catchment in Belgium and France (LEANDER et al., 2005) and daily temperature extremes over western and central Europe (KYSLEY and DUBROVSKY, 2005). Finally, SEMENOV and BARROW (1997) have already concluded that local stochastic weather generators improve the large discrepancies of GCM and RCM simulations in reproducing observed weather statistics in order to construct local climate change scenarios.

9.2 Conclusions and Outlook

The two main topics of this study are the analysis of dynamical downscaling of present-day and future temperature and precipitation over the Mediterranean area from global to regional scale and the comprehensive investigation of Mediterranean temperature and precipitation extremes including the comparison of a broad spectrum of different statistical methods of extreme value analysis for rainfall extremes. The preceding summary and discussion of the major findings of this study reveal that they generally confirm recent research work on means and extremes of Mediterranean temperature and precipitation but several new aspects are found and some clarification is given concerning the strongly controversial topic of rainfall extremes. The major conclusions for the simulation of present-day and future Mediterranean temperature and precipitation which can be drawn from the findings of this study are presented in the following paragraphs:

First, this study reveals several added values of dynamical downscaling from the global GCM ECHAM5 on 1.875° to the RCM REMO on 0.5° : Generally, the high spatial resolution of REMO strongly improves the representation of small-scale processes and regional details associated with the strong orography and large land-sea contrast in the Mediterranean area. Concerning temperature, REMO reaches larger means over northern Africa and smaller means and extremes with enhanced topographic details over mountain peaks mostly improving validation with observations. For precipitation, REMO produces fine-scale structures over coastal regions and mountain ranges and yields generally higher means and extremes in both seasons, especially over the maximum rainfall regions in winter, but sometimes overestimates observations. Improved REMO resolution further reduces the area-averaging effects of the coarse ECHAM5 grid by decreasing frequencies and increasing intensities of extreme rainfall but subscale processes of REMO partly worsen the agreement with E-OBS extremes. Concerning future changes, REMO reveals smaller changes in temperature means and extremes over the southern Mediterranean than ECHAM5 and generally larger changes in rainfall means and extremes with improved topographic details, especially for extreme intensities. Thus, REMO strongly improves the representation of temperature and precipitation means and extremes over the Mediterranean area compared to ECHAM5 and highlights the need for high-resolution regional climate modelling in regions of large orographic gradients and land-sea contrast, especially concerning small-scale rainfall extremes related to local processes or feedbacks. But REMO overestimates rainfall means and extremes of gridded E-OBS observations probably due to smoothing effects in interpolated E-OBS data or deficiencies of regional climate modelling. Hence, validation of climate model data

is often difficult to evaluate because strong differences may result from various data construction methods, e.g. spatial interpolation in E-OBS versus coarse-grid model simulation, or different resolutions may imply different scale effects, e.g. differing extreme rainfall frequencies and intensities between REMO and ECHAM5.

Furthermore, this study reveals that ECHAM5 produces similar spatial patterns of major mid-latitude circulation modes to observations but strongly differing present-day temporal evolutions probably induced by differing initial conditions. These discrepancies between simulated and observed modes of variation cause strongly differing circulation-related temperature and precipitation trends, especially in winter, but improved agreement can mostly be stated for circulation-unrelated trends. Thus, the only real boundary condition CO_2 emissions of the given model-into-model-approach does not clearly prevail over other Mediterranean drivers in 1961-1990. However, model predictability concerning present-day trends mostly increases after removing the impacts of mid-latitude circulation. For the long-term period, mostly decreasing impacts of mid-latitude circulation on Mediterranean temperature and precipitation variability and increasing influences of circulation-unrelated drivers, e.g. GHG, are found probably pointing at improved model predictability. Consequently, the low model predictability based on real CO_2 emissions concerning Mediterranean temperature and precipitation trends in 1961-1990 does not necessarily indicate insufficient model performance in simulating GHG related climate change. It can also be related to unknown initial conditions and interdecadal model variability, such as mid-latitude circulation, differing from observations and masking background GHG related climate change trends. This is supported by the fact that REMO is able to reproduce observed trends if driven by observed boundary conditions. But the problem of the unknown initial state of a climate model simulation is generally very difficult to handle, e.g. by model ensemble approaches, and mostly causes out-of-phase relationships between observations and models at time scales below the predictive time scale from a given climate forcing. Probably 30-year trends generally reveal rather low model predictability based on CO_2 and strong influences of interdecadal variability because the time scale is shorter than the predictive time scale of GHG forcing. Thus, model predictability based on radiative forcing may be generally raised in regarding longer-term and future time scales with increasing GHG impacts like this study indicates or in considering additional real boundary conditions, e.g. aerosols, land cover changes, sea surface temperatures or soil and vegetation processes, already intended in recent projects on decadal climate forecasting (cf. PAXIAN et al. (2011)).

The future projections for Mediterranean temperature means and extremes of

this study are strongly consistent with previous GCM or RCM studies applying both percentile estimates and extreme value distributions. Long-term temperature trends reveal strong and significant future warming patterns over the whole Mediterranean, especially in summer for the A1b scenario, and the corresponding signal-to-noise ratios depict strong and significant GHG signals exceeding impacts of natural variability. Future changes of temperature extremes show similar strong increases over the whole area to mean temperature trends. Furthermore, increasing intensities of longer-term temperature extremes aggregated over several days, indicating heat waves, are stated and some evidence is found that temperature extremes of higher return times reveal larger changes than those of lower return times. Thus, the projected strong warming patterns and increasing daily temperature extremes and heat wave intensities in future time periods are expected to highly impact on the Mediterranean ecology, economy and society, e.g. affecting forest fires, tourist destinations and human health, in a region which is already very vulnerable to climate variability due to dense population and strong dependence on limited natural resources. Therefore, robust information on regional or local climate change in Mediterranean temperature means and extreme events and corresponding uncertainties, like provided by this study, are strongly needed.

Furthermore, future projections of Mediterranean rainfall depict strong summer drying over the northern parts and winter drying over the southern parts, especially in A1b, with some winter wetting patterns over the northern areas, particularly in B1, mostly agreeing with previous studies. The signal-to-noise ratios show small and local GHG signals with strong impacts of internal variability. Future changes in consecutive dry days and heavy rainfall are mostly consistent with trends of seasonal precipitation totals but several regions with decreasing totals and increasing extremes are identified indicating a possible broadening of the future rainfall distribution function. Furthermore, this study finds some indication for increasing absolute future changes of rainfall extremes with higher return times in many regions and seasons. Previous GCM and RCM studies strongly agree in simulating future increases of Mediterranean dry periods consistent to this study but are controversial in projecting future heavy rainfall changes probably due to different statistical methods, models or time scales applied and the large uncertainties inherent to such assessments. This study reveals strong agreement in future heavy rainfall projections based on quantiles and GPD functions and lies in between the uncertainty range given by previous works. The projected future changes in the Mediterranean water cycle are probably associated with large ecologic and socio-economic impacts, e.g. floods, droughts, crop failures and water shortages, highlighting as well the need

for robust regional or local climate change estimates over the Mediterranean area. This especially holds for the highly uncertain topic of local heavy rainfall events, the identification of hot spot regions with increased risks of both floods and droughts and the political scope of action given by the strong differences between emission scenarios in future winter rainfall projections.

Finally, this study applies a dynamical-statistical weather generator including orographic and stochastic terms and PDF matching to derive local virtual precipitation stations from gridded REMO data. These virtual stations overcome typical discrepancies of area-averaged model output in simulating statistical rainfall properties compared to local stations, e.g. overestimated numbers of low-intensity rainfall events, and are able to capture the large station extreme intensities underestimated by both gridded REMO and interpolated E-OBS data. Future changes of virtual station rainfall extremes feature local climate change information and reveal slightly stronger increases in winter and less decreases in summer than gridded REMO extremes. The improvements of the weather generator are mainly reached by PDF matching in this study because the orographic effects can only be calculated for some Mediterranean grid boxes due to the small available station density. Therefore, the weather generator strongly improves the representation of rainfall and rainfall extremes over the Mediterranean area in constructing local virtual stations from area-averaged model output and features the final step in downscaling of climate variability and extremes from regional to local scale. The weather generator is particularly required for climate variables of small-scale spatial variability like precipitation and regions of strong topographic gradients and land-sea contrasts like the Mediterranean area. The resulting local information on rainfall means and extremes is applied for areas without appropriate station coverage in present-day times and serves as local climate change projection and input data for climate impact research studies in future times, e.g. concerning river discharge, soil erosion or agriculture (WILKS, 1999; BUSCHE et al., 2005; LEANDER et al., 2005; SALATHE, 2005).

The following outlook describes the main uncertainties of this study, proposes possible improvements for these shortcomings and presents major aspects of the simulation of Mediterranean temperature and precipitation which require further research work. Concerning the available database of this study, the prevailing REMO ensemble simulations driven by ECHAM5/MPI-OM applying both future GHG emission and land degradation scenarios are highly appropriate for analysing the present-day and future Mediterranean climate variability but several further improvements might be performed: The only major deficiency of the prevailing REMO simulations features the location of the Mediterranean area outside the centre but near

the northern border of the model domain probably causing boundary effects, e.g. artificial rainfall, which results from the fact that the simulations have been originally constructed with focus on western Africa. Generally, improved RCM resolution enhances the representation of many climatic features, especially small-scale rainfall and rainfall extremes, over regions with large orography and land-sea contrasts like the Mediterranean area and can be exemplarily achieved by multiple model nesting (GAO et al., 2006). The RCM performance may be further enhanced by improving sub-grid scale parameterisations, like convection or clouds, and by developing and implementing past and future scenarios of realistic boundary conditions, like GHGs, aerosols, sea surface temperatures or land cover changes, probably increasing model predictability, e.g. concerning present-day temperature and rainfall trends. Additionally, the prevailing approach to nest an atmospheric RCM into a global coupled atmosphere-ocean GCM may be further improved by applying a coupled atmosphere-ocean RCM coupling atmospheric and oceanic components directly at the regional scale to investigate the impacts of a fully interactive ocean (ARTALE et al., 2010). Finally, large multi-model ensembles of different GCMs and RCMs may be used to capture the uncertainties of Mediterranean climate projections concerning model formulation, future emission scenarios and internal climate variability related to unknown initial conditions (DEQUE et al., 2007). Concerning observational data, the prevailing station database of 93 stations over the whole Mediterranean area is far too small to allow an appropriate calculation of the orographic and stochastic terms of the weather generator requiring several stations per REMO grid box. Thus, further Mediterranean stations need to be recovered but station collection from national meteorological services is often laborious, restricted and not free of charge.

Furthermore, this study applies various statistical methods thereby advancing several basic method components, especially concerning the multiple regression (modification of predictor selection), the GPD function fits (averaging of return values over all thresholds and bootstraps, measurements of uncertainty) and the weather generator (calculation of orographic and stochastic terms per station). The applied statistical methods are generally very robust due to comprehensive quantification of uncertainties but several shortcomings may need some further improvements: The PCA reveals some difficulties in the distinct identification of mid-latitude circulation patterns which might probably be eased by rotating principal components but first rotation attempts did not succeed to adequately represent the observed winter NAO pattern. The major deficiency of all statistical methods of extreme value analysis features the sensitivity of extreme values to sampling errors in small

data samples. This is most striking for the estimation of rainfall extremes during the dry Mediterranean summer season and strongly increases the uncertainties of quantile calculation, parameter estimation in GPD fitting and PDF matching in the weather generator. Several measures are applied to quantify such uncertainties, e.g. bootstrap sampling, but more confident extreme value estimates would generally be achieved in investigating longer-term time series of both observations and simulations. Similar uncertainties of small data samples are found in multiple regression between large-scale circulation dynamics and summer precipitation variability. Furthermore, quantile-based rainfall extreme indices are estimated from the first REMO ensemble member due to reasons of comparability with the statistical downscaling in KLIWEX-MED cooperation and may reveal more robust results in averaging the extreme value estimates from all three REMO ensemble members adequately to GPD function fits. Concerning GPD return values, the uncertainties of choosing appropriate thresholds and return times for extreme value analysis are adequately treated in this study but the sporadic occurrence of Mediterranean summer precipitation causes systematic errors in fitting GPD functions to aggregated rainfall over several days. Finally, the weather generator suffers from several uncertainties: the assumed temporal stationarity of the orographic term, stochastic part, PDF matching and adjustment of numbers of rain days which are transferred from present-day to future time periods, the assumption of ergodicity in the stochastic part and unrealistic negative correlations between station rainfall and orography. The performance of the weather generator may be further improved by including cross-validation to avoid strong dependences between virtual stations and corresponding original stations in present-day times.

The prevailing study mostly confirms previous works and finds several new aspects on the simulation of present-day and future Mediterranean temperature and precipitation, especially concerning dynamical downscaling of extremes and the controversial topic of precipitation extremes, but several topics might require some further research work: The analysis of impacts of mid-latitude circulation dynamics on Mediterranean temperature and precipitation variability may be extended by influences of tropical climate dynamics, like ENSO or monsoons, to reach a more comprehensive understanding of the underlying mechanisms. Furthermore, the indication of this study that model predictability based on observed CO_2 emissions increases and impacts of large-scale circulation decrease at longer time scales may be validated with observations in long-term present-day periods. Additional works may further deepen the analysis of Mediterranean extreme events performed in this study, e.g. concerning quantile-based temperature extreme indices, GEV return values of

daily temperature and precipitation and longer-term extremes such as heat waves, wet periods and dry spells or droughts. But the major topic should be to further understand and quantify the uncertainties in future projections of Mediterranean heavy rainfall events from previous studies due to differing statistical methods, climate models and time scales applied. This study has performed some important steps in this direction but further efforts are needed to clarify the future picture of Mediterranean rainfall extremes. For a better understanding of the mechanisms of changes in extreme events, analyses of variance may be applied to determine the signal-to-noise ratios of estimated changes and impacts of large-scale circulation dynamics on the variability of extreme events may be investigated. Further works might analyse the impacts of subscale processes in RCMs on the variability of extremes which overlay the scale effect of improved resolution like this study shows. Concerning the weather generator, further improvements of local virtual stations might be reached by inclusion of additional deterministic factors influencing the transfer functions between local and gridded rainfall, e.g. the station distance to the sea. Finally, climate impact studies should be advanced to estimate the magnitude of ecologic and socio-economic impacts of future climate change in temperature and precipitation means and extremes over the Mediterranean area.

Thus, this study is consistent with several previous works in projecting strong future warming and drying over the whole Mediterranean, increasing heat wave intensities and drought lengths and rather decreasing intensities and frequencies of heavy rainfall events except for increases over some northern parts in winter. Thereby, several regions with decreasing rainfall totals but increasing extremes are identified. The large magnitude of projected changes in this climate change hot spot (GIORGI, 2006) is expected to strongly impact on the Mediterranean ecology (biodiversity, forest fires, soil erosion), economy (agriculture, tourist destinations, hydroelectricity production) and society (human health, water shortages, floods) clearly continuing present-day trends. But the Mediterranean countries are densely populated and urbanised and strongly dependent on limited natural resources, particularly water, and partly reveal limited financial and technical capacities for adaptation, especially the south-eastern countries. Consequently, the high exposure to climate change impacts and the low capacity for adaptation lead to a strong vulnerability of the Mediterranean area to future climate change. This highlights the need for developing adequate regional and local climate change projections, especially concerning extreme events, which are delivered to political decision-makers and local stakeholders of the Mediterranean area to enforce adequate measures for the mitigation and adaptation to climate change. Thus, various climate studies have already been performed con-

tributing to develop a comprehensive picture of the future Mediterranean climate. This study presents as well several new aspects of the simulation of Mediterranean climate variability, mainly on the topics of dynamical downscaling from global to regional scale and analysis of temperature and precipitation extreme events. But still plenty of research work needs to be done to meet essential requirements and clarify major uncertainties of future Mediterranean climate projections, e.g. high-resolution RCM multi-model ensembles to derive local climate change information or improved methods of extreme value analysis to determine robust estimates of future rainfall extremes.

Bibliography

- ALPERT, P., 2002: The paradoxical increase of Mediterranean extreme daily rainfall in spite of decrease in total values. – *Geophysical Research Letters* **29**(11), 1–4.
- ALPERT, P., M. BALDI, R. ILANI, S. KRICHAK, C. PRICE, X. RODÓ, H. SAARONI, B. ZIV, P. KISHCHA, J. BARKAN, A. MARIOTTI, E. XOPLAKI, 2006: Chapter 2 Relations between climate variability in the Mediterranean region and the tropics: ENSO, South Asian and African monsoons, hurricanes and Saharan dust. – In: P. LIONELLO, P. MALANOTTE-RIZZOLI, and R. BOSCOLO (Eds.), *Mediterranean Climate Variability, Developments in Earth and Environmental Sciences 4*, Elsevier, Amsterdam, 149–177.
- ARRHENIUS, S., 1926: *Erde und Weltall* – Akademische Verlagsgesellschaft m.b.h., Leipzig, 342.
- ARTALE, V., S. CALMANTI, P. MALANOTTE-RIZZOLI, G. PISACANE, V. RUPOLO, M. TSIMPLIS, 2006: Chapter 5 The Atlantic and Mediterranean Sea as connected systems. – In: P. LIONELLO, P. MALANOTTE-RIZZOLI, and R. BOSCOLO (Eds.), *Mediterranean Climate Variability, Developments in Earth and Environmental Sciences 4*, Elsevier, Amsterdam, 283–323.
- ARTALE, V., S. CALMANTI, A. CARILLO, A. DELL’AQUILA, M. HERRMANN, G. PISACANE, P. M. RUTI, G. SANNINO, M. V. STRUGLIA, F. GIORGI, X. BI, J. S. PAL, S. RAUSCHER, 2010: An atmosphere-ocean regional climate model for the Mediterranean area: assessment of a present climate simulation. – *Climate Dynamics* **35**(5), 721–740.
- AUGUST, D., M. GEIGER, 2008: Drought in the Mediterranean. Recent developments. WWF Germany. http://www.wwf.de/fileadmin/fm-wwf/pdf_neu/WWF_Studie_Drought_in_th_Mediterranean.pdf, last accessed on 10.01.12.
- BAHRENBERG, G., E. GIESE, J. NIPPER, 1999: *Statistische Methoden in der Geographie, Band 1 Univariate und bivariate Statistik* – Teubner Studienbuecher der Geographie, Stuttgart, Leipzig, 236.

- BARNSTON, A., R. LIVEZEY, 1987: Classification, seasonality and persistence of low-frequency atmospheric circulation patterns. – *Monthly Weather Review* **115**(6), 1083–1126.
- BARREDO, J. I., 2009: Normalised flood losses in Europe: 1970-2006. – *Natural Hazards and Earth System Sciences* **9**, 97–104.
- BEGERT, M., E. ZENKLUSEN, C. HÄBERLI, C. APPENZELLER, L. KLOK, 2008: An automated procedure to detect discontinuities; performance assessment and application to a large European climate data set. – *Meteorologische Zeitschrift* **17**(5), 663–672.
- BEN-GAI, T., A. BITAN, A. MANES, P. ALPERT, Y. KUSHNIR, 2001: Temperature and surface pressure anomalies in Israel and the North Atlantic Oscillation. – *Theoretical and Applied Climatology* **69**, 171–177.
- BENISTON, M., D. B. STEPHENSON, O. B. CHRISTENSEN, C. A. T. FERRO, C. FREI, S. GOYETTE, K. HALSNAES, T. HOLT, K. JYLHÄ, B. KOFFI, J. PALUTIKOF, R. SCHÖLL, T. SEMMLER, K. WOTH, 2007: Future extreme events in European climate: an exploration of regional climate model projections. – *Climatic Change* **81**(S1), 71–95.
- BORTZ, J., C. SCHUSTER, 2010: *Statistik für Human- und Sozialwissenschaftler* – Springer, Berlin, 655.
- BRUNET, M., P. D. JONES, E. AGUILAR, A. MOBERG, D. LISTER, A. WALTHER, 2007: Long-term changes in extreme temperatures and precipitation in Spain. – *Contributions to Science* **3**(3), 331–342.
- BRUNETTI, M., M. MAUGERI, T. NANNI, 2002: Atmospheric circulation and precipitation in Italy for the last 50 years. – *International Journal of Climatology* **22**(12), 1455–1471.
- BUDYKO, M. I., A. B. RONO, A. L. YANNSHIN, 1987: *History of the Earth's Atmosphere* – Springer, Berlin, Heidelberg, New York, London, Paris, Tokyo, 139.
- BUSCHE, H., C. HIEPE, B. DIEKKRÜGER, 2005: Modelling the effects of changes in landuse and precipitation on hydrological and erosive processes in a sub-humid African catchment. – *Proceedings of 3rd international SWAT Conference* **25**, 434–443.

- CARRIL, A. F., S. GUALDI, A. CHERCHI, A. NAVARRA, 2008: Heatwaves in Europe: areas of homogeneous variability and links with the regional to large-scale atmospheric and SSTs anomalies. – *Climate Dynamics* **30**(1), 77–98.
- CASSOU, C., L. TERRAY, A. S. PHILLIPS, 2005: Tropical Atlantic Influence on European Heat Waves. – *Journal of Climate* **18**(15), 2805–2811.
- CHANGNON, S. D., 2003: Measures of Economic Impacts of Weather Extremes. – *Bulletin of the American Meteorological Society* **84**(9), 1231–1235.
- CHRISTENSEN, J., B. HEWITSON, A. BUSUIOC, A. CHEN, X. GAO, I. HELD, R. JONES, R. K. KOLLI, W.-T. KWON, R. LAPRISE, V. MAGAÑA RUEDA, L. MEARNS, C. G. MENÉNDEZ, J. RÄISÄNEN, A. RINKE, A. SARR, P. WHETTON, 2007: Regional Climate Projections. – In: S. SOLOMON, D. QIN, M. MANNING, Z. CHEN, M. MARQUIS, K. AVERYT, M. TIGNOR, and H. MILLER (Eds.), *Climate Change 2007: The Physical Science Basis. Contribution of Working Group I to the Fourth Assessment Report of the Intergovernmental Panel on Climate Change*, Cambridge University Press, Cambridge, New York.
- CHRISTENSEN, J. H., O. B. CHRISTENSEN, 2003: Severe summertime flooding in Europe. – *Nature* **421**(February), 805–806.
- CHRISTENSEN, J. H., O. B. CHRISTENSEN, 2007: A summary of the PRUDENCE model projections of changes in European climate by the end of this century. – *Climate Change (Prudence Special Issue)* **81**, 7–30.
- CHRISTENSEN, J. H., F. BOBERG, O. B. CHRISTENSEN, P. LUCAS-PICHER, 2008: On the need for bias correction of regional climate change projections of temperature and precipitation. – *Geophysical Research Letters* **35**(20).
- CHRISTOPH, M., P. SPETH, M. BOLLIG, J. BURKHARDT, B. DIEKKRÜGER, G. MENZ, M. RÖSSLER, W. SCHUG, 2004: Effizienter und tragfähiger Umgang mit Süßwasser anhand zweier Beispiele in Nordwest- bzw. Westafrika. – In: J. LOZAN, K. GRASS L, P. HUPFER, L. MENZEL, and C. SCHÖNWIESE (Eds.), *Warnsignal Klima: Genug Wasser für alle? Wissenschaftliche Auswertungen*, Hamburg, 282–286.
- CLARK, R. T., S. J. BROWN, J. M. MURPHY, 2006: Modeling Northern Hemisphere Summer Heat Extreme Changes and Their Uncertainties Using a Physics Ensemble of Climate Sensitivity Experiments. – *Journal of Climate* **19**, 4418–4435.

- COLES, S., 2001: An introduction to statistical modeling of extreme values – Springer Verlag, Berlin, 208.
- CONTE, M., A. GIUFFRIDA, S. TEDESCO, 1989: The Mediterranean Oscillation: impact on precipitation and hydrology in Italy. – In: Proceedings of the conference on climate and water, 1:121–137, Helsinki. Publications of the Academy of Finland.
- COPPOLA, E., F. KUCHARSKI, F. GIORGI, F. MOLTENI, 2005: Bimodality of the North Atlantic Oscillation in simulations with greenhouse gas forcing. – Geophysical Research Letters **32**(23), 2–5.
- CUBASCH, U., D. KASANG, 2000: Anthropogener Klimawandel – Klett-Perthes, Gotha, Stuttgart, 128.
- CULLEN, H. M., P. B. DEMENOCAL, 2000: North Atlantic influence on Tigris-Euphrates streamflow. – International Journal of Climatology **20**(8), 853–863.
- DEL RÍO, S., L. HERRERO, R. FRAILE, A. PENAS, 2010: Spatial distribution of recent rainfall trends in Spain (1961-2006). – International Journal of Climatology **31**(5), 656–667.
- DELLA-MARTA, P. M., H. WANNER, 2006: A Method of Homogenizing the Extremes and Mean of Daily Temperature Measurements. – Journal of Climate **19**, 4179–4197.
- DELLA-MARTA, P. M., M. R. HAYLOCK, J. LUTERBACHER, H. WANNER, 2007: Doubled length of western European summer heat waves since 1880. – Journal of Geophysical Research **112**(D15), 1–12.
- DEQUE, M., S. SOMOT, 2008: Analysis of heavy precipitation for France using high resolution ALADIN RCM simulations. – Időjaras Quaterly Journal of the Hungarian Meteorological Service **112**(3-4), 179–190.
- DEQUE, M., D. ROWELL, D. LÜTHI, F. GIORGI, J. CHRISTENSEN, B. ROCKEL, D. JACOB, E. KJELLSTRÖM, M. DE CASTRO, B. VAN DEN HURK, 2007: An intercomparison of regional climate simulations for Europe: assessing uncertainties in model projections. – Climatic Change **81**(S1), 53–70.
- DIFFENBAUGH, N. S., J. S. PAL, F. GIORGI, X. GAO, 2007: Heat stress intensification in the Mediterranean climate change hotspot. – Geophysical Research Letters **34**(11), 1–6.

- DUDA, R. O., P. E. HART, D. G. STORK, 2001: Pattern Classification (2nd ed.) – Wiley, New York, 680.
- DÜNKELOH, A., J. JACOBET, 2003: Circulation dynamics of Mediterranean precipitation variability 1948-98. – *International Journal of Climatology* **23**(15), 1843–1866.
- DUNN, P. K., 2004: Occurrence and quantity of precipitation can be modelled simultaneously. – *International Journal of Climatology* **24**(10), 1231–1239.
- EARTH SYSTEM RESEARCH LABORATORY, 2011: NCEP/NCAR Reanalysis 1: Summary. <http://www.esrl.noaa.gov/psd/data/gridded/data.ncep.reanalysis.html>, last accessed on 05.08.2011.
- ECA&D, 2009: E-OBS gridded dataset. European Climate Assessment & Dataset. <http://eca.knmi.nl/download/ensembles/download.php>, last accessed on 17.08.2009.
- ECA&D, 2011: FAQ. European Climate Assessment & Dataset. <http://eca.knmi.nl/FAQ/index.php>, last accessed on 04.08.2011.
- ECMWF, 2011: ERA40 daily fields. European Centre for Medium-Range Weather Forecasts. http://data-portal.ecmwf.int/data/d/era40_daily/, last accessed on 20.12.2011.
- EFTHYMIADIS, D., C. M. GOODESS, P. D. JONES, 2011: Trends in Mediterranean gridded temperature extremes and large-scale circulation influences. – *Natural Hazards and Earth System Science* **11**(8), 2199–2214.
- ELGUINDI, N., S. SOMOT, M. DÉQUÉ, W. LUDWIG, 2009: Climate change evolution of the hydrological balance of the Mediterranean, Black and Caspian Seas: impact of climate model resolution. – *Climate Dynamics* **36**(1-2), 205–228.
- ENDLICHER, W., 2000: Der Mittelmeerraum. – In: W. WEISCHET and W. ENDLICHER (Eds.), *Regionale Klimatologie. Band 2. Die Alte Welt: Europa, Afrika, Asien*, Teubner, Stuttgart, 625.
- ENSEMBLES, 2011: ENSEMBLES Project overview. <http://www.ensembles-eu.org/>, last accessed on 03.08.2011.
- ERMOLD, W., M. STEELE, 2005: Polar science center Hydrographic Climatology (PHC). <http://psc.apl.washington.edu/Climatology.html>, last accessed on 15.07.2011.

- ERRICO, R. M., D. J. STENSRUD, K. D. RAEDER, 2001: Estimation of the error distributions of precipitation produced by convective parametrization schemes. – *Quarterly Journal of the Royal Meteorological Society* **127**, 2495–2512.
- FARR, T. G., P. A. ROSEN, E. CARO, R. CRIPPEN, R. DUREN, S. HENSLEY, M. KOBRICK, M. PALLER, E. RODRIGUEZ, L. ROTH, D. SEAL, S. SHAFFER, J. SHIMADA, J. UMLAND, 2007: The Shuttle Radar Topography Mission. – *Reviews of Geophysics* **45**(RG2004).
- FEDDEMA, J. J., S. FREIRE, 2001: Soil degradation, global warming and climate impacts. – *Climate Research* **17**, 209–216.
- FERNANDEZ, S., ENGREF, 2007: L'eau virtuelle dans les pays Mediteraneens: un indicateur pour contribuer a l'analyse des questions de gestion et de repartition de l'eau en situation de penurie. Rapport d'etude regionale du Plan Bleu. http://www.planbleu.org/publications/eau_virtuelle_FR.pdf, last accessed on 03.02.2011.
- FISCHER, E. M., C. SCHÄR, 2009: Future changes in daily summer temperature variability: driving processes and role for temperature extremes. – *Climate Dynamics* **33**(7-8), 917–935.
- FISCHER, E. M., C. SCHÄR, 2010: Consistent geographical patterns of changes in high-impact European heatwaves. – *Nature Geoscience* **3**(6), 398–403.
- FISCHER, E. M., S. I. SENEVIRATNE, D. LÜTHI, C. SCHÄR, 2007: Contribution of land-atmosphere coupling to recent European summer heat waves. – *Geophysical Research Letters* **34**(6), 1–6.
- FLOHN, H., 1985: Das Problem der Klimaänderungen in Vergangenheit und Zukunft – Wissenschaftliche Buchgesellschaft, Darmstadt, 228.
- FOWLER, H. J., C. G. KILSBY, 2003: Implications of changes in seasonal and annual extreme rainfall. – *Geophysical Research Letters* **30**(13), 1999–2002.
- FREI, C., R. SCHÖLL, S. FUKUTOME, J. SCHMIDLI, P. L. VIDALE, 2006: Future change of precipitation extremes in Europe: Intercomparison of scenarios from regional climate models. – *Journal of Geophysical Research* **111**(D6).
- FUNK, C., J. MICHAELSEN, J. VERDIN, G. ARTAN, G. HUSAK, G. SENAY, H. GADAIN, T. MAGADAZIRE, 2003: The collaborative historical African rainfall model: description and evaluation. – *International Journal of Climatology* **23**(1), 47–66.

- GAERTNER, M. A., O. B. CHRISTENSEN, J. A. PREGO, J. POLCHER, C. GALLARDO, M. CASTRO, 2001: The impact of deforestation on the hydrological cycle in the western Mediterranean: an ensemble study with two regional climate models. – *Climate Dynamics* **17**(11), 857–873.
- GAERTNER, M. A., D. JACOB, V. GIL, M. DOMÍNGUEZ, E. PADORNO, E. SÁNCHEZ, M. CASTRO, 2007: Tropical cyclones over the Mediterranean Sea in climate change simulations. – *Geophysical Research Letters* **34**(14), 1–5.
- GALLEGO, M. C., J. A. GARCIA, J. M. VAQUERO, V. L. MATEOS, 2006: Changes in frequency and intensity of daily precipitation over the Iberian Peninsula. – *J. Geophys. Res.* **111**(D24), D24105.
- GAO, X., J. S. PAL, F. GIORGI, 2006: Projected changes in mean and extreme precipitation over the Mediterranean region from a high resolution double nested RCM simulation. – *Geophysical Research Letters* **33**(3), 2–5.
- GARCÍA, J. A., M. C. GALLEGO, A. SERRANO, J. M. VAQUERO, 2007: Trends in Block-Seasonal Extreme Rainfall over the Iberian Peninsula in the Second Half of the Twentieth Century. – *Journal of Climate* **20**(1), 113.
- GARCÍA-HERRERA, R., E. HERNÁNDEZ, D. BARRIOPEDRO, D. PAREDES, R. M. TRIGO, I. F. TRIGO, M. A. MENDES, 2007: The Outstanding 2004/05 Drought in the Iberian Peninsula: Associated Atmospheric Circulation. – *Journal of Hydrometeorology* **8**(3), 483–498.
- GARCÍA-HERRERA, R., J. DÍAZ, R. M. TRIGO, J. LUTERBACHER, E. M. FISCHER, 2010: A Review of the European Summer Heat Wave of 2003. – *Critical Reviews in Environmental Science and Technology* **40**(4), 267–306.
- GIBSON, R., P. KALLBERG, S. UPPALA, A. HERNANDEZ, A. NOMURA, E. SERRANO, 1997: ERA description. Reanalysis Project Report Series No. 1. European Centre for Medium-Range Weather Forecasts (ECMWF).
- GIORGI, F., 2002: Variability and trends of sub-continental scale surface climate in the twentieth century. Part I: observations. – *Climate Dynamics* **18**(8), 675–691.
- GIORGI, F., 2006: Climate change hot-spots. – *Geophysical Research Letters* **33**(8), 1–4.
- GIORGI, F., X. BI, 2009: Time of emergence (TOE) of GHG-forced precipitation change hot-spots. – *Geophysical Research Letters* **36**(L06709), 1–6.

- GIORGI, F., E. COPPOLA, 2009: Projections of twenty-first century climate over Europe. – *The European Physical Journal Conferences* **1**, 29–46.
- GIORGI, F., P. LIONELLO, 2008: Climate change projections for the Mediterranean region. – *Global and Planetary Change* **63**(2-3), 90–104.
- GIORGI, F., X. BI, J. PAL, 2004a: Mean, interannual variability and trends in a regional climate change experiment over Europe. I. Present-day climate (1961–1990). – *Climate Dynamics* **22**(6-7), 733–756.
- GIORGI, F., X. BI, J. PAL, 2004b: Mean, interannual variability and trends in a regional climate change experiment over Europe. II: climate change scenarios (2071–2100). – *Climate Dynamics* **23**(7-8), 839–858.
- GLAHN, H., D. LOWRY, 1972: The Use of Model Output Statistics (MOS) in Objective Weather Forecasting.. – *Journal of Applied Meteorology* **11**, 1203–1211.
- GLOWA, 2011: Welcome to GLOWA (Global Change and the Hydrological Cycle) Jordan River. <http://www.glowa-jordan-river.de/>, last accessed on 04.08.2011.
- GOLDBERG, V., C. BERNHOFER, 2000: Ein Konzept zur Regionalisierung des Klimas komplexer Mittelgebirgslandschaften, veranschaulicht am Beispiel des Ostertgebirges. – *Erdkunde* **54**(3), 263–270.
- GOODESS, C. M., P. D. JONES, 2002: Links between circulation and changes in the characteristics of Iberian rainfall. – *International Journal of Climatology* **22**(13), 1593–1615.
- GOODESS, C. M., D. JACOB, M. DEQUE, J. M. GUTTIERREZ, R. HUTH, E. KENDON, G. C. LECKEBUSCH, P. LORENZ, V. PAVAN, 2009: Downscaling methods, data and tools for input to impact assessments. – In: P. VAN DER LINDEN and J. F. B. MITCHELL (Eds.), *Summary of research and results from the ENSEMBLES project*, Met Office Hadley Centre, UK, 59–78.
- GOODMAN, A., 2008: Spain suffers worst drought. CNN Madrid. http://articles.cnn.com/2008-04-18/world/spain.drought_1_drinking-water-reservoir-levels-water-demand, last accessed on 10.01.2012.
- GOUBANOVA, K., L. LI, 2007: Extremes in temperature and precipitation around the Mediterranean basin in an ensemble of future climate scenario simulations. – *Global and Planetary Change* **57**(1-2), 27–42.

- HAGEMANN, S., M. BOTZET, L. DÜMENIL, B. MACHENHAUER, 1999: Derivation of global GCM boundary conditions from 1 km land use satellite data. MPI Report No. 289. Max Planck Institute for Meteorology, Hamburg.
- HANSEN, J. A., K. A. EMANUEL, 2003: Forecast 4D-Var: Exploiting Model Output Statistics. – *Quarterly Journal of the Royal Meteorological Society* **129**(589), 1255–1267.
- HATZAKI, M., H. A. FLOCAS, D. N. ASIMAKOPOULOS, P. MAHERAS, 2007: The eastern Mediterranean teleconnection pattern: identification and definition. – *International Journal of Climatology* **27**(6), 727–737.
- HAYLOCK, M., 2005: STARDEX. Statistical and Regional dynamical Downscaling of Extremes for European regions. <http://www.cru.uea.ac.uk/projects/stardex/>, last accessed on 10.01.2012.
- HAYLOCK, M. R., N. HOFSTRA, A. M. G. KLEIN TANK, E. J. KLOK, P. D. JONES, M. NEW, 2008: A European daily high-resolution gridded data set of surface temperature and precipitation for 1950-2006. – *Journal of Geophysical Research* **113**(D20).
- HENSE, A., P. FRIEDERICHS, 2006: Wind and Precipitation Extremes in the Earth's Atmosphere. – In: S. ALBEVERIO, V. JENTSCH, and H. KANTZ (Eds.), *Extreme events in nature and society*, Springer, Berlin, 352.
- HERTIG, E., J. JACOBET, 2008a: Assessments of Mediterranean precipitation changes for the 21st century using statistical downscaling techniques. – *International Journal of Climatology* **28**(8), 1025–1045.
- HERTIG, E., J. JACOBET, 2008b: Downscaling future climate change: Temperature scenarios for the Mediterranean area. – *Global and Planetary Change* **63**(2-3), 127–131.
- HERTIG, E., S. SEUBERT, J. JACOBET, 2010: Temperature extremes in the Mediterranean area: trends in the past and assessments for the future. – *Natural Hazards and Earth System Science* **10**(10), 2039–2050.
- HERTIG, E., A. PAXIAN, G. VOGT, S. SEUBERT, H. PAETH, J. JACOBET, 2012: Statistical and dynamical downscaling assessments of precipitation extremes in the Mediterranean area. – *Meteorologische Zeitschrift* **21**, in print.
- HOFF, H., 2008: CIRCE Research Line 7 - Climate Vulnerability of Mediterranean Ecosystems. CIRCE EU Project.

- HOFSTRA, N., M. HAYLOCK, M. NEW, P. JONES, 2009: Testing E-OBS European high-resolution gridded data set of daily precipitation and surface temperature. – *J. Geophys. Res* **114**, 1–33.
- HOFSTRA, N., M. NEW, C. MCSWEENEY, 2010: The influence of interpolation and station network density on the distributions and trends of climate variables in gridded daily data. – *Climate Dynamics* **35**(5), 841–858.
- HOSKING, J., 1990: L-moments: analysis and estimation of distributions using linear combinations of order statistics. – *Journal of the Royal Statistical Society. Series B (Methodological)* **52**(1), 105–124.
- HURRELL, J., 1995: Decadal trends in the North Atlantic Oscillation: regional temperatures and precipitation. – *Science* **269**, 676–679.
- IAASTD, 2008: Summary for Decision Makers of the Central and West Asia and North Africa (CWANA) Report. International Assessment of Agricultural Knowledge, Science and Technology for Development, Washington.
- IPCC, 2011: Organization. Intergovernmental Panel on Climate Change. <http://www.ipcc.ch/organization/organization.shtml>, last accessed on 10.01.2012.
- JACOB, D., 2001: A note to the simulation of the annual and inter-annual variability of the water budget over the Baltic Sea drainage basin. – *Meteorology and Atmospheric Physics* **77**(1-4), 61–73.
- JACOB, D., 2011: REMO - Model Characteristics. <http://www.remo-rcm.de/REMO-Model-Characteristics.1268.0.html>, last accessed on 12.07.2011.
- JACOB, D., B. J. J. M. VAN DEN HURK, U. ANDRAE, G. ELGERED, C. FORTELIUS, L. P. GRAHAM, S. D. JACKSON, U. KARSTENS, C. KÖPKEN, R. LINDAU, R. PODZUN, B. ROCKEL, F. RUBEL, B. H. SASS, R. N. B. SMITH, X. YANG, 2001: A comprehensive model inter-comparison study investigating the water budget during the BALTEX-PIDCAP period. – *Meteorology and Atmospheric Physics* **77**(1-4), 19–43.
- JACOB, D., L. BÄRRING, O. B. CHRISTENSEN, J. H. CHRISTENSEN, M. CASTRO, M. DÉQUÉ, F. GIORGI, S. HAGEMANN, M. HIRSCHI, R. JONES, E. KJELLSTRÖM, G. LENDERINK, B. ROCKEL, E. SÁNCHEZ, C. SCHÄR, S. I. SENEVI-RATNE, S. SOMOT, A. ULDEN, B. HURK, 2007: An inter-comparison of regional climate models for Europe: model performance in present-day climate. – *Climatic Change* **81**(S1), 31–52.

- JACOBET, J., 1994: Atmosphärische Zirkulationsänderungen bei anthropogen verstärktem Treibhauseffekt – jahreszeitliche Analysen in den Außertropen beider Hemisphären auf der Basis von Ausgabedaten globaler Klimamodellsimulationen (Projektbericht). – Würzburger Geographische Manuskripte **34**, 101.
- JACOBET, J., 2000: Rezente Klimaentwicklung im Mittelmeerraum. – Petermanns Geographische Mitteilungen **144**(6), 22–33.
- JACOBET, J., A. DÜNKELOH, 2005: The Eastern Mediterranean Transient in Relation to Atmospheric Circulation Dynamics. – Hydrogeologie and Umwelt **33**, 1–8.
- JACOBET, J., C. BECK, A. PHILIPP, 1998: Annual to decadal variability in climate in Europe - objectives and results of the German contribution to the European climate research project ADVICE. – Würzburger Geographische Manuskripte **43**, 163.
- JACOBET, J., P. JÖNSSON, L. BÄRRING, C. BECK, M. EKSTRÖM, 2001: Zonal indices for Europe 1780-1995 and running correlations with temperature. – Climatic Change **48**, 219–241.
- JACOBET, J., A. DÜNKELOH, E. HERTIG, 2007: Mediterranean Rainfall Changes and their Causes. – In: J. LOZAN, H. GRASSL, P. HUPFER, L. MENZEL, and C. SCHÖNWIESE (Eds.), *Global Change: Enough Water for all?*, Hamburg, 195–199.
- JUNGCLAUS, J. H., N. KEENLYSIDE, M. BOTZET, H. HAAK, J.-J. LUO, M. LATIF, J. MAROTZKE, U. MIKOLAJEWICZ, E. ROECKNER, 2006: Ocean Circulation and Tropical Variability in the Coupled Model ECHAM5/MPI-OM. – Journal of Climate **19**(16), 3952–3972.
- KALNAY, E., M. KANAMITSU, R. KISTLER, W. COLLINS, D. DEAVEN, L. GANDIN, M. IREDELL, S. SAHA, G. WHITE, J. WOOLLEN, 1996: The NCEP/NCAR 40-year reanalysis project. – Bulletin of the American Meteorological Society **77**(3), 437–471.
- KANG, I.-S., J.-Y. LEE, C.-K. PARK, 2004: Potential Predictability of Summer Mean Precipitation in a Dynamical Seasonal Prediction System with Systematic Error Correction. – Journal of Climate **17**(4), 834–844.
- KHARIN, V., F. ZWIERS, 2005: Estimating Extremes in Transient Climate Change Simulations. – Journal of Climate **18**, 1156–1173.

- KHARIN, V. V., F. W. ZWIERS, 2000: Changes in the Extremes in an Ensemble of Transient Climate Simulations with a Coupled Atmosphere-Ocean GCM. – *Journal of Climate* **13**(21), 3760–3788.
- KIOUTSIOUKIS, I., D. MELAS, C. ZEREFOS, 2010: Statistical assessment of changes in climate extremes over Greece (1955–2002). – *International Journal of Climatology* **30**(11), 1723–1737.
- KISTLER, R., W. COLLINS, S. SAHA, G. WHITE, J. WOOLLEN, E. KALNAY, M. CHELLIAH, W. EBISUZAKI, M. KANAMITSU, V. KOUSKY, H. VAN DEN DOOL, R. JENNE, M. FIORINO, 2001: The NCEP–NCAR 50–Year Reanalysis: Monthly Means CD–ROM and Documentation. – *Bulletin of the American Meteorological Society* **82**(2), 247–267.
- KJELLSTRÖM, E., L. BÄRRING, D. JACOB, R. JONES, G. LENDERINK, C. SCHÄR, 2007: Modelling daily temperature extremes: recent climate and future changes over Europe. – *Climatic Change* **81**(S1), 249–265.
- KLEIN TANK, A. M. G., G. P. KÖNNEN, 2003: Trends in Indices of Daily Temperature and Precipitation Extremes in Europe, 1946–99. – *Journal of Climate* **16**(22), 3665.
- KLEIN TANK, A. M. G., J. B. WIJNGAARD, G. P. KÖNNEN, R. BÖHM, G. DEMARÉE, A. GOCHEVA, M. MILETA, S. PASHIARDIS, L. HEJKRLIK, C. KERN-HANSEN, R. HEINO, P. BESSEMOULIN, G. MÜLLER-WESTERMEIER, M. TZANAKOU, S. SZALAI, T. PÁLSDÓTTIR, D. FITZGERALD, S. RUBIN, M. CAPALDO, M. MAUGERI, A. LEITASS, A. BUKANTIS, R. ABERFELD, A. F. V. VAN ENGELEN, E. FORLAND, M. MIETUS, F. COELHO, C. MARES, V. RAZUVAEV, E. NIEPLOVA, T. CEGNAR, J. ANTONIO LÓPEZ, B. DAHLSTRÖM, A. MOBERG, W. KIRCHHOFER, A. CEYLAN, O. PACHALIUK, L. V. ALEXANDER, P. PETROVIC, 2002: Daily dataset of 20th-century surface air temperature and precipitation series for the European Climate Assessment. – *International Journal of Climatology* **22**(12), 1441–1453.
- KLOK, E. J., A. M. G. KLEIN TANK, 2008: Updated and extended European dataset of daily climate observations. – *International Journal of Climatology* **29**(8), 1182–1191.
- KÖPPEN, W., 1936: Das geographische System der Klimate. – In: W. KÖPPEN and R. GEIGER (Eds.), *Handbuch der Klimatologie* 3, Gebrueder Borntraeger, Berlin, 46.

- KOSTOPOULOU, E., P. D. JONES, 2005: Assessment of climate extremes in the Eastern Mediterranean. – *Meteorology and Atmospheric Physics* **89**(1-4), 69–85.
- KRICHAK, S. O., P. ALPERT, 2005a: Decadal trends in the east Atlantic-west Russia pattern and Mediterranean precipitation. – *International Journal of Climatology* **25**(2), 183–192.
- KRICHAK, S. O., P. ALPERT, 2005b: Signatures of the NAO in the atmospheric circulation during wet winter months over the Mediterranean region. – *Theoretical and Applied Climatology* **82**(1-2), 27–39.
- KUGLITSCH, F. G., A. TORETI, E. XOPLAKI, P. M. DELLA-MARTA, C. S. ZEREFOS, M. TÜRKES, J. LUTERBACHER, 2010: Heat wave changes in the eastern Mediterranean since 1960. – *Geophysical Research Letters* **37**(4), 1–5.
- KUNSTMANN, H., A. HECKL, A. RIMMER, 2006: Physically based distributed hydrological modelling of the Upper Jordan catchment and investigation of effective model equations. – *Advances in Geosciences* **9**, 123–130.
- KYSELY, J., M. DUBROVSKY, 2005: Simulation of extreme temperature events by a stochastic weather generator: effects of interdiurnal and interannual variability reproduction. – *International Journal of Climatology* **25**, 251–269.
- LANA, X., M. D. MARTINEZ, A. BURGUENO, C. SERRA, J. MARTIN-VIDE, L. GOMEZ, 2006: Distributions of long dry spells in the iberian peninsula, years 1951-1990. – *International Journal of Climatology* **26**(14), 1999–2021.
- LEANDER, R., A. BUIHAND, P. AALDERS, M. DE WIT, 2005: Estimation of extreme floods of the river Meuse using a stochastic weather generator and a rainfall-runoff model. – *Hydrological Sciences Journal* **50**(6), 1089–1103.
- LIBERATO, M. L. R., J. G. PINTO, I. F. TRIGO, R. M. TRIGO, 2011: Klaus - an exceptional winter storm over northern Iberia and southern France. – *Royal Meteorological Society* **66**(12), 330–334.
- LIONELLO, P., J. BHEND, A. BUZZI, P. M. DELLA-MARTA, S. O. KRICHAK, A. JANSÀ, P. MAHERAS, A. SANNA, I. F. TRIGO, R. TRIGO, 2006a: Chapter 6 Cyclones in the Mediterranean region: Climatology and effects on the environment. – In: P. LIONELLO, P. MALANOTTE-RIZZOLI, and R. BOSCOLO (Eds.), *Mediterranean Climate Variability, Developments in Earth and Environmental Sciences 4*, Elsevier, Amsterdam, 325–372.

- LIONELLO, P., P. MALANOTTE-RIZZOLI, R. BOSCOLO, P. ALPERT, V. ARTALE, L. LI, J. LUTERBACHER, W. MAY, R. TRIGO, M. TSIMPLIS, U. ULBRICH, E. XOPLAKI, 2006b: The Mediterranean climate: An overview of the main characteristics and issues. – In: P. LIONELLO, P. MALANOTTE-RIZZOLI, and R. BOSCOLO (Eds.), *Mediterranean Climate Variability, Developments in Earth and Environmental Sciences* 4, Elsevier, Amsterdam, 1–26.
- LIONELLO, P., U. BOLDRIN, F. GIORGI, 2008: Future changes in cyclone climatology over Europe as inferred from a regional climate simulation. – *Climate Dynamics* **30**(6), 657–671.
- LISTER, D., 2007: EMULATE. European and North Atlantic daily to MULTidecadal climATE variability. <http://www.cru.uea.ac.uk/projects/emulate/>, last accessed on 04.08.2011.
- LÓPEZ-MORENO, J. I., S. M. VICENTE-SERRANO, M. ANGULO-MARTÍNEZ, S. BEGUERÍA, A. KENAWY, 2010: Trends in daily precipitation on the northeastern Iberian Peninsula, 1955-2006. – *International Journal of Climatology* **30**(7), 1026–1041.
- LUTERBACHER, J., D. DIETRICH, E. XOPLAKI, M. GROSJEAN, H. WANNER, 2004: European seasonal and annual temperature variability, trends, and extremes since 1500. – *Science* **303**(5663), 1499–1503.
- MAJEWSKI, D., 1991: The Europa-Modell of the Deutscher Wetterdienst. – In: ECMWF Seminar on numerical methods in atmospheric models, volume 2, 147–191.
- MARIOTTI, A., 2002: Euro-Mediterranean rainfall and ENSO—a seasonally varying relationship. – *Geophysical Research Letters* **29**(12), 2–5.
- MARIOTTI, A., J. BALLABRERA-POY, N. ZENG, 2005: Tropical influence on Euro-Asian autumn rainfall variability. – *Climate Dynamics* **24**(5), 511–521.
- MARIOTTI, A., N. ZENG, J.-H. YOON, V. ARTALE, A. NAVARRA, P. ALPERT, L. Z. X. LI, 2008: Mediterranean water cycle changes: transition to drier 21st century conditions in observations and CMIP3 simulations. – *Environmental Research Letters* **3**(4), 044001.
- MARSLAND, S., 2003: The Max-Planck-Institute global ocean/sea ice model with orthogonal curvilinear coordinates. – *Ocean Modelling* **5**(2), 91–127.

- MARTIN-VIDE, J., J. LOPEZ-BUSTINS, 2006: The western mediterranean oscillation and rainfall in the iberian peninsula. – *International Journal of Climatology* **26**, 1455–1475.
- MEARNS, L. O., F. GIORGI, L. MCDANIEL, C. SHIELDS, 1995: Analysis of daily variability of precipitation in a nested regional climate model: comparison with observations and doubled CO₂ results. – *Global and Planetary Change* **10**(94), 55–78.
- MEDCLIVAR, 2011: MedCLIVAR. Mediterranean CLImate and VARIability and Predictability. <http://www.medclivar.eu/>, last accessed on 04.08.2011.
- MEEHL, G. A., C. TEBALDI, 2004: More intense, more frequent, and longer lasting heat waves in the 21st century.. – *Science* **305**(5686), 994–997.
- MEEHL, G. A., F. ZWIERS, J. EVANS, T. KNUTSON, L. MEARNS, P. WHETTON, 2000: Trends in extreme weather and climate events: issues related to modeling extremes in projections of future climate change. – *Bulletin of the American Meteorological Society* **81**(3), 427–436.
- MICHAELSEN, J., 1987: Cross-validation in statistical climate forecast models. – *Journal of Climate and Applied Meteorology* **26**(11), 1589–1600.
- MILLÁN, M. M., M. J. ESTRELA, M. J. SANZ, E. MANTILLA, M. MARTÍN, F. PASTOR, R. SALVADOR, R. VALLEJO, L. ALONSO, G. GANGOITI, J. L. ILARDIA, M. NAVAZO, A. ALBIZURI, B. ARTIÑANO, P. CICCIOI, G. KALLOS, R. A. CARVALHO, D. ANDRÉS, A. HOFF, J. WERHAHN, G. SEUFERT, B. VERSINO, 2005a: Climatic Feedbacks and Desertification: The Mediterranean Model. – *Journal of Climate* **18**(5), 684–701.
- MILLÁN, M. M., M. J. ESTRELA, J. MIRÓ, 2005b: Rainfall Components: Variability and Spatial Distribution in a Mediterranean Area (Valencia Region). – *Journal of Climate* **18**(14), 2682–2705.
- MIRANDA, P. M. A., A. R. TOMÉ, 2009: Spatial structure of the evolution of surface temperature (1951–2004). – *Climatic Change* **93**(1-2), 269–284.
- MITCHELL, T., 2011: CRU TS 2.1. Tyndall Centre for Climate Change Research. http://www.cru.uea.ac.uk/cru/data/hrg/timm/grid/CRU_TS_2_1.html, last accessed on 02.08.11.

- MITCHELL, T., P. JONES, 2005: An improved method of constructing a database of monthly climate observations and associated high-resolution grids. – *International Journal of Climatology* **25**(6), 693–712.
- MOBERG, A., P. D. JONES, 2005: Trends in indices for extremes in daily temperature and precipitation in central and western Europe, 1901-99. – *International Journal of Climatology* **25**(9), 1149–1171.
- MOBERG, A., P. D. JONES, D. LISTER, A. WALTHER, M. BRUNET, J. JACOBET, L. V. ALEXANDER, P. M. DELLA-MARTA, J. LUTERBACHER, P. YIOU, D. CHEN, A. M. G. KLEIN TANK, O. SALADIÉ, J. SIGRÓ, E. AGUILAR, H. ALEXANDERSSON, C. ALMARZA, I. AUER, M. BARRIENDOS, M. BEGERT, H. BERGSTRÖM, R. BÖHM, C. J. BUTLER, J. CAESAR, A. DREBS, D. FOUNDA, F.-W. GERSTENGARBE, G. MICELA, M. MAUGERI, H. ÖSTERLE, K. PANDZIC, M. PETRAKIS, L. SRNEC, R. TOLASZ, H. TUOMENVIRTA, P. C. WERNER, H. LINDERHOLM, A. PHILIPP, H. WANNER, E. XOPLAKI, 2006: Indices for daily temperature and precipitation extremes in Europe analyzed for the period 1901-2000. – *Journal of Geophysical Research* **111**(D22).
- MODEL&DATA, 2008: IPCC Experiments. IPCC ECHAM5-MPI-OM experiments. <http://www.mad.zmaw.de/service-support/consortium-model-runs/ipcc-experiments/index.html>, last accessed on 15.07.2011.
- MPIM, 2005: ECHAM5 MPI-OM. Model Information of Potential Use to the IPCC Lead Authors and the AR4. Max Planck Institute for Meteorology Hamburg. Model&Data. http://www.mad.zmaw.de/fileadmin/extern/documents/ECHAM5_MPI-OM.pdf, last accessed on 03.02.2012.
- MPIM, 2011a: ECHAM5. Max Planck Institute for Meteorology Hamburg. <http://www.mpimet.mpg.de/en/science/models/echam/echam5.html>, last accessed on 15.07.2011.
- MPIM, 2011b: MPIOM. Max Planck Institute for Meteorology Hamburg. <http://www.mpimet.mpg.de/en/science/models/mpiom.html>, last accessed on 15.07.2011.
- MUNICH RE, 2004: TOPICS geo 2003. Münchner Rückversicherungs-Gesellschaft, Munich.
- MUNICH RE, 2010: Analyses, assessments, positions. Topics GEO. Münchner Rückversicherungs-Gesellschaft, Munich.

- NAKICENOVIC, N., R. SWART, 2000: Emissions Scenarios – Cambridge University Press, Cambridge, UK.
- NATIONAL GEOPHYSICAL DATA CENTER, 1988: Digital relief of the surface of the Earth. Data Announcement 88-MGG-02. NOAA, Boulder, CO.
- NEW, M., M. HULME, P. JONES, 1999: Representing Twentieth-Century Space–Time Climate Variability. Part I: Development of a 1961-90 Mean Monthly Terrestrial Climatology. – *Journal of Climate* **12**(3), 829–856.
- NEW, M., M. HULME, P. JONES, 2000: Representing Twentieth-Century Space–Time Climate Variability. Part II: Development of 1901-96 Monthly Grids of Terrestrial Surface Climate. – *Journal of Climate* **13**(13), 2217–2238.
- NOAA-CPC, 2010: Northern Hemisphere Teleconnection Patterns. NOAA National Weather Service Climate Prediction Center. <http://www.cpc.noaa.gov/data/teledoc/telecontents.shtml>, last accessed on 26.06.2010.
- NOGAJ, M., P. YIOU, S. PAREY, F. MALEK, P. NAVEAU, 2006: Amplitude and frequency of temperature extremes over the North Atlantic region. – *Geophysical Research Letters* **33**(10), 2–5.
- NORRANT, C., A. DOUGUÉDROIT, 2006: Monthly and daily precipitation trends in the Mediterranean (1950-2000). – *Theoretical and Applied Climatology* **83**(1-4), 89–106.
- OSBORN, T., 2004: Simulating the winter North Atlantic Oscillation: the roles of internal variability and greenhouse gas forcing. – *Climate Dynamics* **22**(6-7), 605–623.
- PAETH, H., 2005: The climate of tropical and northern Africa - a statistical-dynamical analysis of the key factors in climate variability and the role of human activity in future climate change. – *Bonner Meteorologische Abhandlungen* **61**, 316.
- PAETH, H., 2010: Postprocessing of simulated precipitation for impact research in West Africa. Part I: model output statistics for monthly data. – *Climate Dynamics* **36**(7-8), 1321–1336.
- PAETH, H., M. DIEDERICH, 2010: Postprocessing of simulated precipitation for impact research in West Africa. Part II: A weather generator for daily data. – *Climate Dynamics* **36**(7-8), 1337–1348.

- PAETH, H., A. HENSE, 2002: Sensitivity of climate change signals deduced from multi-model Monte Carlo experiments. – *Climate Research* **22**, 189–204.
- PAETH, H., A. HENSE, 2003: Seasonal forecast of sub-sahelian rainfall using cross validated model output statistics. – *Meteorologische Zeitschrift* **12**(3), 157–173.
- PAETH, H., A. HENSE, 2005: Mean versus extreme climate in the Mediterranean region and its sensitivity to future global warming conditions. – *Meteorologische Zeitschrift* **14**(3), 329–347.
- PAETH, H., F. POLLINGER, 2010: Enhanced evidence in climate models for changes in extratropical atmospheric circulation. – *Tellus A* **62**(5), 647–660.
- PAETH, H., K. BORN, R. PODZUN, D. JACOB, 2005: Regional dynamical downscaling over West Africa: model evaluation and comparison of wet and dry years. – *Meteorologische Zeitschrift* **14**(3), 349–367.
- PAETH, H., R. GIRMES, G. MENZ, A. HENSE, 2006: Improving Seasonal Forecasting in the Low Latitudes. – *Monthly Weather Review* **134**(7), 1859–1879.
- PAETH, H., K. BORN, R. GIRMES, R. PODZUN, D. JACOB, 2009: Regional Climate Change in Tropical and Northern Africa due to Greenhouse Forcing and Land Use Changes. – *Journal of Climate* **22**(1), 114.
- PAL, J. S., F. GIORGI, X. BI, 2004: Consistency of recent European summer precipitation trends and extremes with future regional climate projections. – *Geophysical Research Letters* **31**(13), 20–23.
- PALMER, T. N., J. RÄISÄNEN, 2002: Quantifying the risk of extreme seasonal precipitation events in a changing climate. – *Nature* **415**(6871), 512–4.
- PARK, J.-S., H.-S. JUNG, R.-S. KIM, J.-H. OH, 2001: Modelling summer extreme rainfall over the Korean peninsula using Wakeby distribution. – *International Journal of Climatology* **21**(11), 1371–1384.
- PAULING, A., J. LUTERBACHER, C. CASTY, H. WANNER, 2006: Five hundred years of gridded high-resolution precipitation reconstructions over Europe and the connection to large-scale circulation. – *Climate Dynamics* **26**(4), 387–405.
- PAXIAN, A., E. HERTIG, G. VOGT, S. SEUBERT, J. JACOB, H. PAETH, 2011: Greenhouse gas related predictability of regional climate model trends in the Mediterranean area. – *International Journal of Climatology* (submitted).

- PENNER, J. E., C. C. CHUANG, K. GRANT, 1998: Climate forcing by carbonaceous and sulfate aerosols. – *Climate Dynamics* **14**, 839–851.
- PLAN BLEU, 2005: A Sustainable Future for the Mediterranean: The Blue Plan's Environment and Development Outlook – Earthscan, 464.
- PLAN BLEU, 2009: State of the Environment and Development. UNEP/MAP-Plan Bleu. http://www.planbleu.org/publications/SoED2009_EN.pdf, last accessed on 03.02.2012.
- PLAN BLEU, EUROPEAN INVESTMENT BANK (EIB), 2008: Climate Change and Energy in the Mediterranean. http://www.planbleu.org/publications/changement_clim_energie_med_EN.pdf, last accessed on 03.02.2011.
- PRICE, C., L. STONE, A. HUPPERT, B. RAJAGOPALAN, P. ALPERT, 1998: A possible link between El Nino and precipitation in Israel. – *Geophysical Research Letters* **25**(21), 3963–3966.
- QUADRELLI, R., V. PAVAN, F. MOLteni, 2001: Wintertime variability of Mediterranean precipitation and its links with large-scale circulation anomalies. – *Climate Dynamics* **17**(5-6), 457–466.
- RAICICH, F., N. PINARDI, A. NAVARRA, 2003: Teleconnections between Indian monsoon and Sahel rainfall and the Mediterranean. – *International Journal of Climatology* **23**(2), 173–186.
- RÄISÄNEN, J., U. HANSSON, A. ULLERSTIG, R. DÖSCHER, L. P. GRAHAM, C. JONES, H. E. M. MEIER, P. SAMUELSSON, U. WILLEN, 2004: European climate in the late twenty-first century: regional simulations with two driving global models and two forcing scenarios. – *Climate Dynamics* **22**(1), 13–31.
- RAMIREZ, E., 2009: Shuttle Radar Topography Mission. The Mission to Map the World. NASA Jet Propulsion Laboratory.. <http://www2.jpl.nasa.gov/srtm/>, last accessed on 15.08.2011.
- REALE, O., P. DIRMEYER, 2000: Modeling the effects of vegetation on Mediterranean climate during the Roman Classical Period Part I: Climate history and model sensitivity. – *Global and Planetary Change* **25**(3-4), 163–184.
- REALE, O., J. SHUKLA, 2000: Modeling the effects of vegetation on Mediterranean climate during the Roman Classical Period: Part II. Model simulation. – *Global and Planetary Change* **25**(3-4), 185–214.

- RINNE, H., 2008: Taschenbuch der Statistik – Verlag Harri Deutsch, Frankfurt am Main, 1060.
- RODRIGO, F. S., 2010: Changes in the probability of extreme daily precipitation observed from 1951 to 2002 in the Iberian Peninsula. – *International Journal of Climatology* **30**(10), 1512–1525.
- RODRIGO, F. S., R. M. TRIGO, 2007: Trends in daily rainfall in the Iberian Peninsula from 1951 to 2002. – *International Journal of Climatology* **27**(4), 513–529.
- RODRÍGUEZ-PUEBLA, C., A. H. ENCINAS, L. A. GARCÍA-CASADO, S. NIETO, 2010: Trends in warm days and cold nights over the Iberian Peninsula: relationships to large-scale variables. – *Climatic Change* **100**(3-4), 667–684.
- RODWELL, M. J., B. J. HOSKINS, 1996: Monsoons and the dynamics of deserts. – *Quarterly Journal of the Royal Meteorological Society* **122**(534), 1385–1404.
- ROECKNER, E., K. ARPE, L. BENGTSSON, M. CHRISTOPH, M. CLAUSSEN, L. DUMENIL, M. ESCH, M. GIORGETTA, U. SCHLESE, U. SCHULZWEIDA, 1996: The atmospheric general circulation model ECHAM-4: Model description and simulation of present-day climate. Max-Planck-Institute for Meteorology Report 218, Hamburg.
- ROECKNER, E., L. BONAVENTURA, R. BROKOPF, M. ESCH, M. GIORGETTA, S. HAGEMANN, I. KIRCHNER, L. KORNBLUEH, E. MANZINI, A. RHODIN, U. SCHLESE, U. SCHULZWEIDA, A. TOMPKINS, 2003: The atmospheric general circulation model ECHAM5. PART I: Model description. MPI-Report 349. Max-Planck-Institute for Meteorology, Hamburg.
- ROECKNER, E., R. BROKOPF, M. ESCH, M. GIORGETTA, S. HAGEMANN, L. KORNBLUEH, E. MANZINI, U. SCHLESE, U. SCHULZWEIDA, 2006: Sensitivity of Simulated Climate to Horizontal and Vertical Resolution in the ECHAM5 Atmosphere Model. – *Journal of Climate* **19**(16), 3771–3791.
- ROGUE WAVE SOFTWARE, 2011: IMSL (International Mathematics and Statistics Library) Numerical Libraries. <http://www.roguewave.com/products/imsl-numerical-libraries.aspx>, last accessed on 01.12.2011.
- ROWELL, D. P., R. G. JONES, 2006: Causes and uncertainty of future summer drying over Europe. – *Climate Dynamics* **27**(2-3), 281–299.

-
- SACHS, L., 1997: *Angewandte Statistik. Anwendung statistischer Methoden* – Springer Verlag, Berlin, 884.
- SÁENZ, J., J. FERNANDEZ, J. ZUBILLAGA, C. RODRIGUEZ-PUEBLA, 2001: Interpretation of interannual winter temperature variations over southwestern Europe. – *Journal of Geophysical Research* **106**(20), 641–20.
- SALATHE, E. P., 2005: Downscaling simulations of future global climate with application to hydrologic modelling. – *International Journal of Climatology* **25**(4), 419–436.
- SANCHEZ-GOMEZ, E., S. SOMOT, A. MARIOTTI, 2009: Future changes in the Mediterranean water budget projected by an ensemble of regional climate models. – *Geophysical Research Letters* **36**(21), 1–5.
- SCHÖNWIESE, C., 2006: *Praktische Statistik für Meteorologen und Geowissenschaftler* – Borntraeger, Berlin, Stuttgart, 302.
- SEMENOV, M. A., 2008: Simulation of extreme weather events by a stochastic weather generator. – *Climate Research* **35**(2008), 203–212.
- SEMENOV, M. A., E. M. BARROW, 1997: Use of a stochastic weather generator in the development of climate change scenarios. – *Climatic Change* **35**, 397–414.
- SEMMLER, T., D. JACOB, 2004: Modeling extreme precipitation events—a climate change simulation for Europe. – *Global and Planetary Change* **44**(1-4), 119–127.
- SENEVIRATNE, S. I., D. LÜTHI, M. LITSCHI, C. SCHÄR, 2006: Land-atmosphere coupling and climate change in Europe.. – *Nature* **443**(7108), 205–9.
- SEUBERT, S., 2010: *Telekonnektionen des Niederschlags im Mittelmeerraum zur Zirkulation in den Tropen*. Phd thesis, University of Augsburg.
- SIMMONS, A. J., D. M. BURRIDGE, M. JARRAUD, C. GIRARD, W. WERGEN, 1989: The ECMWF Medium-Range Prediction Models Development of the Numerical Formulations and the Impact of Increased Resolution. – *Meteorol. Atmos. Phys.* **40**, 28–60.
- SMITH, R., 2003: Chapter 1 Statistics of extremes, with applications in environment, insurance and finance. – In: B. FINKENSTADT and H. ROOTZEN (Eds.), *Extreme Values in Finance, Telecommunications and the Environment*, Chapman and Hall/CRC Press, London, 1–78.

- SOTILLO, M. G., A. W. RATSIMANDRESY, J. C. CARRETERO, A. BENTAMY, F. VALERO, F. GONZÁLEZ-ROUCO, 2005: A high-resolution 44-year atmospheric hindcast for the Mediterranean Basin: contribution to the regional improvement of global reanalysis. – *Climate Dynamics* **25**(2-3), 219–236.
- STEPHENSON, D. B., V. PAVAN, M. COLLINS, M. M. JUNGE, R. QUADRELLI, 2006: North Atlantic Oscillation response to transient greenhouse gas forcing and the impact on European winter climate: a CMIP2 multi-model assessment. – *Climate Dynamics* **27**(4), 401–420.
- STOTT, P. A., D. A. STONE, M. R. ALLEN, 2004: Human contribution to the European heatwave of 2003. – *Nature* **432**, 610–614.
- SZ, 2011: Der Tsunami von Genua. *Sueddeutsche Zeitung* 07.11.2011. <http://archiv.sueddeutsche.de/b5238h/298721/Der-Tsunami-von-Genua.html/>, last accessed on 10.01.12.
- TEBALDI, C., K. HAYHOE, J. M. ARBLASTER, G. A. MEEHL, 2006: Going to the Extremes. – *Climatic Change* **79**(3-4), 185–211.
- TIEDTKE, M., 1989: A comprehensive mass flux scheme for cumulus parameterization in large-scale models. – *Monthly Weather Review* **117**(8), 1779–1800.
- TORETI, A., 2010: Extreme events in the Mediterranean: analysis and dynamics. Phd thesis, University of Bern, Switzerland.
- TORETI, A., F. DESIATO, 2008: Changes in temperature extremes over Italy in the last 44 years. – *International Journal of Climatology* **28**(6), 733–745.
- TORETI, A., E. XOPLAKI, D. MARAUN, F. G. KUGLITSCH, H. WANNER, J. LUTERBACHER, 2010: Characterisation of extreme winter precipitation in Mediterranean coastal sites and associated anomalous atmospheric circulation patterns. – *Natural Hazards and Earth System Science* **10**(5), 1037–1050.
- TRENBERTH, K., P. JONES, P. AMBENJE, R. BOJARIU, D. EASTERLING, A. KLEIN TANK, D. PARKER, F. RAHIMZADEH, J. RENWICK, M. RUSTICUCCI, B. SODEN, P. ZHAI, 2007: Observations: Surface and Atmospheric Climate Change. – In: S. SOLOMON, D. QIN, M. MANNING, Z. CHEN, M. MARQUIS, K. AVERYT, M. TIGNOR, and H. MILLER (Eds.), *Climate Change 2007: The Physical Science Basis. Contribution of Working Group I to the Fourth Assessment Report of the Intergovernmental Panel on Climate Change*, Cambridge University Press, Cambridge, New York.

- TRIGO, I. F., T. D. DAVIES, G. R. BIGG, 2000: Decline in Mediterranean rainfall caused by weakening of Mediterranean cyclones. – *Geophysical Research Letters* **27**(18), 2913–2916.
- TRIGO, R., T. OSBORN, J. CORTE-REAL, 2002: The North Atlantic Oscillation influence on Europe: climate impacts and associated physical mechanisms. – *Climate Research* **20**, 9–17.
- TRIGO, R. M., D. POZO-VÁZQUEZ, T. J. OSBORN, Y. CASTRO-DÍEZ, S. GÁMIZ-FORTIS, M. J. ESTEBAN-PARRA, 2004: North Atlantic oscillation influence on precipitation, river flow and water resources in the Iberian Peninsula. – *International Journal of Climatology* **24**(8), 925–944.
- TRIGO, R. M., J. M. C. PEREIRA, M. G. PEREIRA, B. MOTA, T. J. CALADO, C. C. DACAMARA, F. E. SANTO, 2006a: Atmospheric conditions associated with the exceptional fire season of 2003 in Portugal. – *International Journal of Climatology* **26**(13), 1741–1757.
- TRIGO, R. M., E. XOPLAKI, E. ZORITA, J. LUTERBACHER, S. KRICHAK, P. ALPERT, J. JACOBET, J. SÁENZ, J. FERNÁNDEZ, F. GONZÁLEZ-ROUCO, R. GARCIA-HERRERA, X. RODO, M. BRUNETTI, T. NANNI, M. MAUGERI, M. TÜRKES, L. GIMENO, P. RIBERA, M. BRUNET, I. TRIGO, M. CREPON, A. MARIOTTI, 2006b: Chapter 3 Relations Between Variability in the Mediterranean Region and Mid-Latitude Variability. – In: P. LIONELLO, P. MALANOTTE-RIZZOLI, and R. BOSCOLO (Eds.), *Mediterranean Climate Variability, Developments in Earth and Environmental Sciences 4*, Elsevier, Amsterdam, 179–226.
- TSIMPLIS, M. N., V. ZERVAKIS, S. A. JOSEY, E. L. PENEVA, M. V. STRUGLIA, E. V. STANEV, A. THEOCHARIS, P. LIONELLO, P. MALANOTTE-RIZZOLI, V. ARTALE, E. TRAGO, T. OGUZ, 2006: Chapter 4 Changes in the oceanography of the Mediterranean Sea and their link to climate variability. – In: P. LIONELLO, P. MALANOTTE-RIZZOLI, and R. BOSCOLO (Eds.), *Mediterranean Climate Variability, Developments in Earth and Environmental Sciences 4*, Elsevier, Amsterdam, 227–282.
- TURATO, B., O. REALE, F. SICCARDI, 2004: Water Vapor Sources of the October 2000 Piedmont Flood. – *Journal of Hydrometeorology* **5**, 693–712.

- TÜRKEŞ, M., E. ERLAT, 2005: Climatological responses of winter precipitation in Turkey to variability of the North Atlantic Oscillation during the period 1930-2001. – *Theoretical and Applied Climatology* **81**(1-2), 45–69.
- ULBRICH, U., M. CHRISTOPH, 1999: A shift of the NAO and increasing storm track activity over Europe due to anthropogenic greenhouse gas forcing. – *Climate Dynamics* **15**(7), 551–559.
- ULBRICH, U., M. CHRISTOPH, J. PINTO, J. CORTE-REAL, 1999: Dependence of winter precipitation over Portugal on NAO and baroclinic wave activity. – *International Journal of Climatology* **19**(4), 379–390.
- UPPALA, S. M., P. W. KALLBERG, A. J. SIMMONS, U. ANDRAE, V. D. C. BECHTOLD, M. FIORINO, J. K. GIBSON, J. HASELER, A. HERNANDEZ, G. A. KELLY, X. LI, K. ONOGI, S. SAARINEN, N. SOKKA, R. P. ALLAN, E. ANDERSSON, K. ARPE, M. A. BALMASEDA, A. C. M. BELJAARS, L. VAN DE BERG, J. BIDLOT, N. BORMANN, S. CAIRES, F. CHEVALLIER, A. DETHOF, M. DRAGOSAVAC, M. FISHER, M. FUENTES, S. HAGEMANN, E. HÓLM, B. J. HOSKINS, L. ISAKSEN, P. A. E. M. JANSSEN, R. JENNE, A. P. MCNALLY, J.-F. MAHFOUF, J.-J. MORCRETTE, N. A. RAYNER, R. W. SAUNDERS, P. SIMON, A. STERL, K. E. TRENBERTH, A. UNTCH, D. VASILJEVIC, P. VITERBO, J. WOOLLEN, 2005: The ERA-40 re-analysis. – *Quarterly Journal of the Royal Meteorological Society* **131**(612), 2961–3012.
- USGS EROS, 2011: Shuttle Radar Topography Mission (SRTM) - "Finished". Earth Resources Observation and Science Center of the United States Geological Survey. http://eros.usgs.gov/#/Find_Data/Products_and_Data_Available/SRTM, last accessed on 10.08.11.
- VALCKE, S., A. CAUBEL, D. DECLAT, L. TERRAY, 2003: OASIS3 Ocean Atmosphere Sea Ice Soil User's Guide. Technical Report TR/CMGC/03/69. CERFACS, Toulouse.
- VAN ULDEN, A. P., G. J. VAN OLDENBORGH, 2006: Large-scale atmospheric circulation biases and changes in global climate model simulations and their importance for climate change in Central Europe. – *Atmospheric Chemistry and Physics* **6**, 863–881.
- VON STORCH, H., F. ZWIERS, 1999: Statistical analysis in climate research – Cambridge University Press, Cambridge, 496.

- VON STORCH, H., S. GÜSS, M. HEIMANN, 1999: Das Klimasystem und seine Modellierung – Springer-Verlag, Berlin, Heidelberg, New York, 255.
- VOSS, R., W. MAY, E. ROECKNER, 2002: Enhanced resolution modelling study on anthropogenic climate change: changes in extremes of the hydrological cycle. – *International Journal of Climatology* **22**(7), 755–777.
- WANG, Y., L. LEUNG, J. MCGREGOR, D.-K. LEE, W.-C. WANG, Y. DING, F. KIMURA, 2004: Regional Climate Modeling: Progress, Challenges, and Prospects. – *Journal of the Meteorological Society of Japan* **82**(6), 1599–1628.
- WEISCHET, W., W. ENDLICHER, 2008: Einführung in die Allgemeine Klimatologie – Borntraeger, Berlin, Stuttgart, 342.
- WIJNGAARD, J. B., A. M. G. KLEIN TANK, G. P. KOENNEN, 2003: Homogeneity of 20th century European daily temperature and precipitation series. – *International Journal of Climatology* **23**(6), 679–692.
- WILKS, D., 1999: Multisite downscaling of daily precipitation with a stochastic weather generator. – *Climate Research* **11**(2), 125–136.
- WILKS, D., 2006: Statistical methods in the atmospheric sciences – Elsevier Academic Press, Amsterdam, 648.
- WOLFF, J.-O., E. MAIER-REIMER, S. LEGUTKE, 1997: The Hamburg Ocean Primitive Equation Model HOPE. Technical Report No. 13. German Climate Computing Center (DKRZ), Hamburg, 98.
- XOPLAKI, E., 2002: Climate Variability over the Mediterranean. Phd thesis, University of Bern, Switzerland.
- XOPLAKI, E., J. GONZALEZ-ROUCO, J. LUTERBACHER, H. WANNER, 2003: Mediterranean summer air temperature variability and its connection to the large-scale atmospheric circulation and SSTs. – *Climate Dynamics* **20**(7), 723–739.
- XOPLAKI, E., J. GONZALEZ-ROUCO, J. LUTERBACHER, H. WANNER, 2004: Wet season Mediterranean precipitation variability: influence of large-scale dynamics and trends. – *Climate Dynamics* **23**(1), 63–78.
- ZAMPIERI, M., P. LIONELLO, 2011: Anthropogenic land use causes summer cooling in Central Europe. – *Climate Research* **46**(3), 255–268.

- ZHANG, X., G. HEGERL, F. W. ZWIERS, J. KENYON, 2005: Avoiding Inhomogeneity in Percentile-Based Indices of Temperature Extremes. – *Journal of Climate* **18**(11), 1641–1651.
- ZIV, B., H. SAARONI, P. ALPERT, 2004: The factors governing the summer regime of the eastern Mediterranean. – *International Journal of Climatology* **24**(14), 1859–1871.
- ZOLINA, O., A. KAPALA, C. SIMMER, S. GULEV, 2004: Analysis of extreme precipitation over Europe from different reanalyses: a comparative assessment. – *Global and Planetary Change* **44**(1-4), 129–161.

Acknowledgement

The present study was carried out at the Institute of Geography and Geology of the University of Würzburg within the framework of the research project KLIWEX-MED (Klimawandel und Extremereignisse im Mediterranen Großraum - Climate change and Extreme events in the Mediterranean Basin). In this context, I would like to acknowledge the German Research Foundation (Deutsche Forschungsgemeinschaft DFG) for the financial support and the providers of the observational and climate model datasets applied in this study. First of all, I would like to thank my supervisor Prof. Dr. Heiko Paeth for enabling this study, professional advice, focussed guidance, continuous support and loyal cooperation over the whole time. Particularly, I strongly appreciate that he made it possible for me to present my work and exchange knowledge and experience with other scientists at several national and international conferences and summer schools. Furthermore, I am very grateful that Prof. Dr. Jucundus Jacobeit agreed to become the co-corrector of my thesis and I would like to thank him for good scientific cooperation and helpful suggestions during several project meetings. Additionally, I would like to show my gratitude to Elke Hertig and Stefanie Seubert for great teamwork, fruitful discussions and helpful support. I owe a special thanks to Elke Hertig for carefully and efficiently proofreading my manuscript. I thank Gernot Vogt and Sebastian Mutz for being my closest workmates over the last three years, spending lots of time working together, discussing, supporting, encouraging and helping each other and being friends over the whole time. Gernot, it was a great pleasure for me to be your team member and join several conferences and summer schools together with you. I am very grateful to the whole working group at the Institute of Geography and Geology, especially to Birgit Mannig, Anja Scholten, Daniel Schwindt, Kai-Oliver Heuer, Felix Pollinger, Doro Schill, Christian Büdel, Tobias, Rödder, Christian Steger and Hervé Awoyé for good teamwork, a friendly working atmosphere, helpful advice, friendship and for taking the strain off me during the final phase. Finally, I deeply thank my parents and my girlfriend Friederike Becker for continuous encouragement, assistance and support at any time. Particularly, I am very grateful to Friederike for proofreading my manuscript and helping me out of any problem during the final weeks.

Erklärung

Hiermit versichere ich, Andreas Paxian, geboren am 30.03.1982 in Heidelberg, dass ich die vorliegende Arbeit selbstständig verfasst und keine anderen als die angegebenen Quellen und Hilfsmittel benutzt habe, dass alle Stellen der Arbeit, die wörtlich oder sinngemäß aus anderen Quellen übernommen wurden, als solche kenntlich gemacht sind und dass die Arbeit in gleicher oder ähnlicher Form noch keiner Prüfungsbehörde vorgelegt wurde.

Würzburg, Februar 2012

PUBLIKATIONEN:

Hertig, E., A. Paxian, G. Vogt, S. Seubert, H. Paeth, J. Jacobeit, 2012: Statistical and dynamical downscaling assessments of precipitation extremes in the Mediterranean area. – Meteorologische Zeitschrift 21, in print.

Paxian, A., E. Hertig, G. Vogt, S. Seubert, J. Jacobeit, H. Paeth, 2011: Greenhouse gas related predictability of regional climate model trends in the Mediterranean area. – International Journal of Climatology, submitted.

Eyring, V., H. Bovensmann, I. Cionni, M. Dall'Amico, K. Franke, I. Khlystova, C. Klinger, A. Lauer, A. Paxian, M. Righi, M. Schreier, 2010: Impact of Ship Emissions on Atmosphere and Climate, SeaKLIM Final Report.

Paxian, A., V. Eyring, W. Beer, R. Sausen, C. Wright, 2010: Present-day and future global bottom-up ship emission inventories including polar routes. – Environmental Science & Technology 44 (4), 1333-1339.